Identification of corneal mechanical properties using optical tomography and digital volume correlation

Jiawei Fu

▶ **To cite this version:**

Jiawei Fu. Identification of corneal mechanical properties using optical tomography and digital volume correlation. Biomechanics [physics.med-ph]. Université de Technologie de Troyes; Loughborough university, 2014. English. NNT : 2014TROY0013 . tel-03356083

HAL Id: tel-03356083
https://theses.hal.science/tel-03356083

Submitted on 27 Sep 2021

HAL is a multi-disciplinary open access archive for the deposit and dissemination of scientific research documents, whether they are published or not. The documents may come from teaching and research institutions in France or abroad, or from public or private research centers.

L'archive ouverte pluridisciplinaire **HAL**, est destinée au dépôt et à la diffusion de documents scientifiques de niveau recherche, publiés ou non, émanant des établissements d'enseignement et de recherche français ou étrangers, des laboratoires publics ou privés.

Thèse
de doctorat
de l'UTT

Jiawei FU

Identification of Corneal Mechanical Properties Using Optical Tomography and Digital Volume Correlation

Spécialité :
Systèmes Mécaniques et Matériaux

2014TROY0013 **Année 2014**

Thèse en cotutelle avec l'Université de Loughborough – Royaume-Uni

Loughborough University

utt
université de technologie
Troyes

THESE

pour l'obtention du grade de

DOCTEUR de l'UNIVERSITE DE TECHNOLOGIE DE TROYES

Spécialité : SYSTEMES MECANIQUES ET MATERIAUX

présentée et soutenue par

Jiawei FU

le 26 mars 2014

Identification of corneal mechanical properties using optical tomography and digital volume correlation

JURY

M. M. FRANCOIS	PROFESSEUR DES UNIVERSITES	Président
M. S. AVRIL	PROFESSEUR ENSM SAINT ETIENNE	Rapporteur
M. S. EVANS	PROFESSOR	Rapporteur
M. J. HUNTLEY	PROFESSOR	Examinateur
M. F. PIERRON	PROFESSOR	Directeur de thèse
M. P. RUIZ	SENIOR LECTURER	Examinateur

To my dear family

À toute ma famille

致我亲爱的家人

ACKNOWLEDGMENTS

First of all, I would like to express my sincere gratitude to my supervisors, Professor Fabrice Pierron and Dr Pablo Ruiz for their continuous support, advice, immense knowledge, caring, and trust throughout the past four PhD years. Their guidance and encouragement helped me in all the research and writing up time as well as my career development.

I would also like to thank Professor Jonathan Huntley for his constructive advice to my thesis, who is the independent assessor during the past years. Many thanks go to my colleague Dr Maryam Haghighi-Abayneh at Loughborough University for her kind help in the experiments. Special thanks are given to the PhD student Sarah Dreuilhe at the University of Southampton for helping me to polish the French extended abstract.

I must also acknowledge my colleagues at Loughborough University, Université de Technologie de Troyes, and Arts et Métiers ParisTech as well as my friends, especially Dr Marco Rossi and Dr Wenjin Zhu, for their kind help over the years.

I am also thankful to the China Scholarship Council and the Wolfson School of Mechanical and Manufacturing Engineering, Loughborough University, for their generous financial support, which made this project possible.

Last but not least, I owe my deepest gratitude to my dear family and my beloved, my mother, father and sister, for their continuous and unconditional love and support as always in my life. Without their support and encouragement, my devotion to this domain of expertise would not have been materialized. I wish you all the best.

TABLE OF CONTENTS

LIST OF FIGURES

LIST OF TABLES

GENERAL INTRODUCTION

The study of the vertebrate eye cornea is an interdisciplinary subject which involves medical science, biology, mechanics, material science, *etc*. The study of corneal biomechanical properties has significant importance in ophthalmology. The present work has been inspired by the following research questions. How are the biomechanical properties of the vertebrate eye cornea such as elastic moduli distributed through the thickness? Would it be possible to establish a 3D map of the cornea with the values of its local properties? These identified properties are of great value as they can be used to examine the corneal pathology, in which the properties of the pathological corneas differ from that of the healthy ones. This would also enable forward numerical models to predict the corneal mechanical behaviour under all sorts of conditions to assist, for example, refractive surgery, and take into account corneal deformation due to removed tissue and thus reduce refractive errors and improve visual acuity.

To study corneal biomechanical properties, it is first necessary to be able to examine the composition and internal structure of the eye cornea. The measurement of depth-resolved 3D (depth-resolved) deformation behaviour of cornea under intraocular pressure is a useful method to study the local corneal biomechanical properties. Robust 3D inverse problem identification methodologies need to be developed to identify the constitutive parameters of the cornea by making use of the experimental measurement techniques such as full-field measurement of displacement/strain. The above research objectives however have some challenges to meet. The examination of the internal features and the measurement of the depth-resolved 3D deformation of the cornea need to be implemented in a non-contact way so that they can be applied to the practical in vivo studies. High resolution and spatial resolution of the deformation measurements are required to enable an accurate identification of the local corneal biomechanical properties. In addition, it would be advantageous if the identification is less time-consuming.

Currently, most of the research that has been undertaken to characterize the corneal biomechanical properties was based on uniaxial tensile tests or corneal surface measurements using digital image correlation in inflation tests. However, depth-resolved 3D deformation

measurements have not been achieved yet, which are essential to better understand the internal corneal biomechanical behaviour. Additionally, current identification of material constitutive parameters is generally based on finite element model updating (FEMU), which often suffers from local optimal results and long processing time. The Virtual Fields Method (VFM) has been developed as an alternative identification method that overcomes the shortcomings of the finite element model updating method. In the present work, a methodology that can be applied to measure depth-resolved 3D displacement and strain fields in semi-transparent light-scattering materials by combining optical coherence tomography (OCT) with digital volume correlation (DVC) is proposed. To the best of our knowledge, this is the first time that volume strain data were derived by performing digital volume correlation on optical coherence tomography reconstructed volumes. The proposed methodology has been applied to measure the depth-resolved 3D deformation of an inflated porcine cornea. In addition, an effective method has been developed to correct the commonly seen refraction induced distortions in optical coherence tomography reconstructions, which is another original contribution of the present study. Moreover, a 3D implementation of the virtual fields method is presented, which enables the identification of material constitutive parameters from the 3D deformation measurements. Even though the cornea has inspired and guided this work, it is valid for other soft tissues as long as their internal structures can be reconstructed by optical coherence tomography with sufficient quality.

This thesis is organized as follows:

Chapter 1 presents a literature review on the background knowledge of the cornea such as corneal structure, its composition, intraocular pressure, *etc*. The state-of-the-art on experimental studies of corneal biomechanics is introduced. Various volume imaging techniques are then reviewed with a view to the corneal internal structure analysis. Different approaches to identify the constitutive parameters are then introduced followed by methodologies to obtain the required full-field deformation measurements.

Chapter 2 details the application of the VFM to 3D strain data with both manually defined and piecewise optimized virtual fields, in the case of linear elasticity. Finite element models (FEM) were introduced to validate the derivation of these 3D virtual fields. Finally, the ability of the manually-defined virtual fields method to retrieve constitutive parameters from strain data corrupted by Gaussian noise was compared against the piecewise-optimized virtual fields.

Chapter 3 presents depth-resolved 3D deformation measurements of silicone rubber phantoms under tension obtained by performing DVC on volume reconstructions of the phantoms obtained with OCT. Using stationary tests and rigid body translations of the phantoms, the strain measurement performance of the system was studied in terms of the sub-volume size, strain noise, interpolation bias and strain induced speckle decorrelation. Finally, the elastic constitutive parameters of the silicone rubber phantoms were identified with the VFM.

In Chapter 4, 3D displacement fields of a silicone rubber phantom and of a porcine cornea were obtained in controlled inflation tests. However, these fields which were obtained from a direct application of DVC onto the OCT reconstructions do not represent the true deformation of the materials due to a refraction distortion that affects the OCT reconstructions and leads to spurious strain.

Chapter 5 presents a method that has been implemented to correct the refraction induced distortions in 2D/3D. Rigid body rotation tests, in which non-zero displacement fields with zero strain were introduced in silicone rubber phantoms, were carried out to evaluate the performance of the refraction correction method and its ability to eliminate the spurious strain. Refraction correction was then applied to the porcine cornea to obtain 3D displacement and strain fields that arose in an inflation test.

In the last chapter, conclusions and perspectives are presented.

CHAPTER 1

LITERATURE REVIEW

1.1 Study of corneal biomechanics

The eye is a complex organ, and its primary function is to refract light through a series of windows and lenses on to the back of the eye and convert it into electrical signals that can be interpreted and understood by the brain via the optic nerve [1]. Among all important parts of the eye, the cornea plays the most important role in refracting light and providing a stiff protective envelope for the inner ocular contents as well as serving to maintain the shape of the eye [2, 3]. The integrity and functionality of the cornea is essential for vision. Any abnormalities in its composition or structure due to disorder or disease such as keratoconus, corneal dystrophy, glaucoma, mass lesions, *etc*. severely degrade vision [4-8]. Refractive surgery is widely performed to improve the refractive state of the eye, with 1.8 million operations in 2001 in US alone [9]. As cornea thickness is used as the criterion to perform refractive surgery without taking into account of the corneal biomechanical properties, residual refractive errors might remain due to the difference in corneal biomechanical properties of different patients. For these reasons, a comprehensive understanding of the biomechanical properties and deformation behaviour of cornea is of great importance in clinical applications [10-13].

1.1.1 Anatomy of the cornea

The cornea is located at the outer front of the eye ball and has a transparent multi-layer structure, as illustrated in Fig 1.1 [1]. It protects the eye from the outer environment, absorbs oxygen and nutrients from the tear film and maintains the shape and stability of the eye by resisting the intraocular pressure. It also plays an important role in the image formation by refracting light to the back of the eye [1, 14, 15].

As can be seen from Fig 1.1, the cornea is composed of five layers, namely epithelium, Bowman's layer, stroma, Descemet's membrane, and endothelium. The epithelium, which is approximately 10% of the total cornea thickness, is the outermost layer of the cornea. It

contains mostly stratified squamous cells and serves as a barrier to protect the eye from the external environment. The innermost layer is the endothelium, which is responsible for the clarity of the cornea by maintaining a balance between the fluid flowing in and out of the cornea. Excess fluid in the cornea can make vision hazy, and thus, the endothelium plays an important role in pumping water against the gradient, which is essential for optical transparency. Bowman's membrane lies below the epithelium, and Descemet's membrane lies above the endothelium. These two membranes are very thin layers and consist of collagen fibrils. They serve as protective barriers against injury and infection. The stroma, which locates between Bowman's and Descemet's membranes, constitutes 90% of the cornea's thickness and thus dominates the cornea's structural performance. It consists of the stacked lamellae of regularly arranged collagen fibrils embedded in a hydrated matrix of proteoglycans, glycoproteins, and keratocytes. The collagen fibrils are arranged in two preferred orientations, which are orthogonal and alternate between the adjacent lamellae. Since the collagen fibril is the stiffest component of the corneal structure, its arrangement and distribution mainly determine the mechanical properties and light transparency of the cornea [16-18].

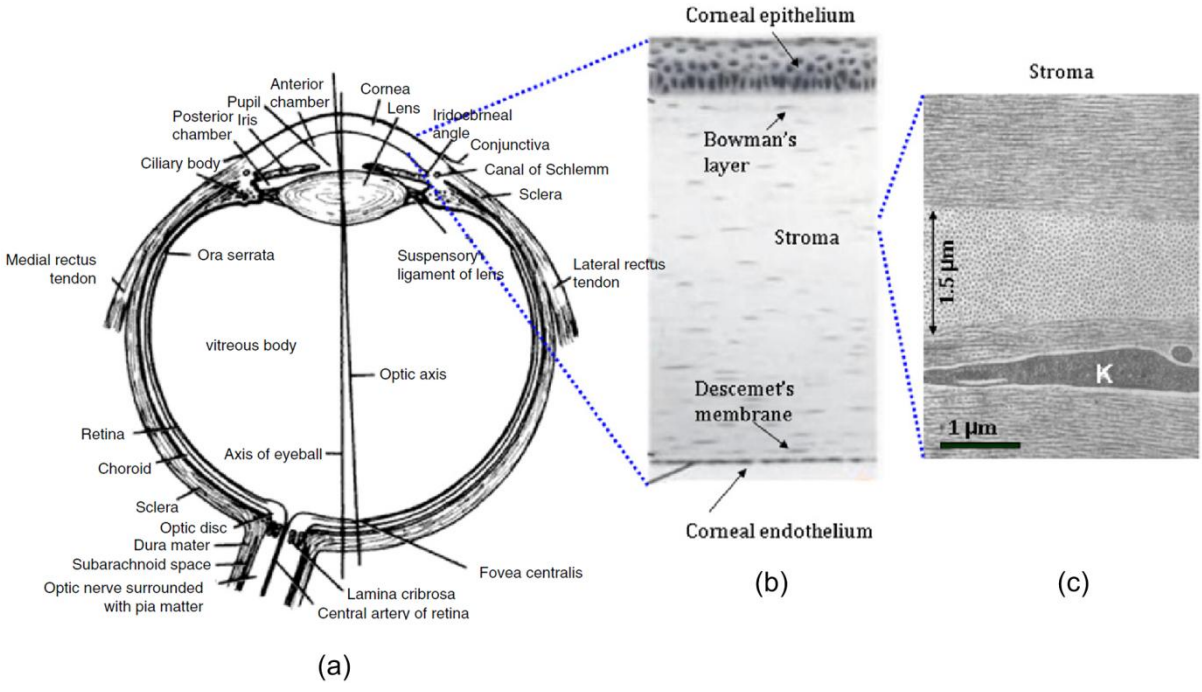

Fig 1.1: Anatomy of cornea: (a) Schematic of the cross-section of human eye. (b) Expanded view of the cornea showing five layers. (c) TEM image of the stroma in the cornea showing two preferred orientations of collagen fibrils. (Reproduced from reference [1], Ambekar *et al*).

1.1.2 Intraocular pressure

Intraocular pressure (IOP) is the fluid pressure inside the eye. It is mainly determined by the coupling of the production and the drainage of aqueous humor mainly through the trabecular network located in the anterior chamber angle. Intraocular pressure is usually measured in millimeters of mercury (mmHg) or kilo-Pascal (kPa). Accumulated evidences indicate that IOP is positively correlated with age, sex, race, blood pressure, obesity and other cardiac risk variables [19, 20]. It is generally accepted that in the total population, the normal IOP reading is 15-16 mmHg (2.0-2.1 kPa) on average, with standard deviation of 2.5-3.0 mmHg (0.33-0.4 kPa). Although the value increases with age, 21-22 mmHg (2.8-2.9 kPa) is generally considered the approximate upper limit of the normal value [21, 22].

Intraocular pressure is related to some eye diseases such as glaucoma. Glaucoma is an eye disease in which the optic nerve is damaged as a consequence of the elevation of intraocular pressure above the physiological level of individuals. Intraocular pressure may become elevated due to anatomical problems, inflammation of the eye, genetic factors, or as a side-effect from medication. Therefore, it serves as an indication of the physical status of the eye. Measuring and monitoring intraocular pressure and its influence in the corneal deformation is therefore an extremely important aspect of diagnosis, treatment, and management of glaucoma [23, 24].

1.1.3 Corneal pathology

There are several types of corneal pathologies that are usually seen by ophthalmologists. The first one is keratoconus and related non-inflammatory corneal thinning disorders [8]. It is a degenerative disorder of the eye in which structural changes occur within the cornea causing it to thin and change to a more conical shape than a normal gradual curve, which distorts and decreases vision. The second one is corneal dystrophy. It is a group of disorders, defined as a non-inflammatory, inherited, bilateral opacity of the cornea. It appears as grayish white lines, circles, or clouding of the cornea [25]. Another one is the inflammation of the cornea such as keratitis and corneal ulcer. It is an inflamed condition of the cornea commonly resulting from viral infection. It represents a break or disruption in the corneal epithelium or even stroma, which can cause a loss of corneal transparency and potentially significant loss of vision in serious cases [26, 27].

Since these corneal pathologies are generally associated with the changes in the shape and the composition of the cornea, they are essentially associated with the changes in the corneal biomechanical properties as well. Therefore, a method of identifying the corneal biomechanical properties would be very useful as it could be utilized in evaluating and diagnosing corneal pathology by comparing the identified biomechanical properties of the normal and the pathological corneas.

1.1.4 Experimental study of corneal biomechanical properties

Many experimental studies have been carried out in order to characterize the biomechanical properties of the cornea. Generally, there are two types of tests that are usually adopted to examine the mechanical response of the cornea under pressure, which are the inflation and strip tensile tests.

1.1.4.1 Inflation testing method

The inflation testing method has been applied by many researchers as it can provide a physiologically representative mechanical characterization of the cornea. Fig 1.2 shows a schematic of a typical inflation test rig which was developed by Anderson *et al* [28]. In this experimental setup, the cornea specimen is fixed by mechanical clamps and glued to the fixture along its ring of sclera tissue to provide watertight edge connection and avoid fluid leakage during the inflation tests. The cornea specimen is subjected to a changeable posterior pressure provided by adjusting a small vertically moveable reservoir. The pressure in the chamber is measured using a pressure unit. A water tank equipped with a temperature controller is added between the chamber and the reservoir to ensure the temperature in the pressure chamber remains constant throughout the test. During the tests, a laser displacement sensor is used to measure the displacement at the apex of the cornea from which the corneal biomechanical properties can be evaluated through the Pressure-Apical rise relation. Beside this, two digital cameras can be positioned in the plane of the cornea-scleral intersection to continually record changes in corneal profile during the tests as described by El-sheikh *et al* [29].

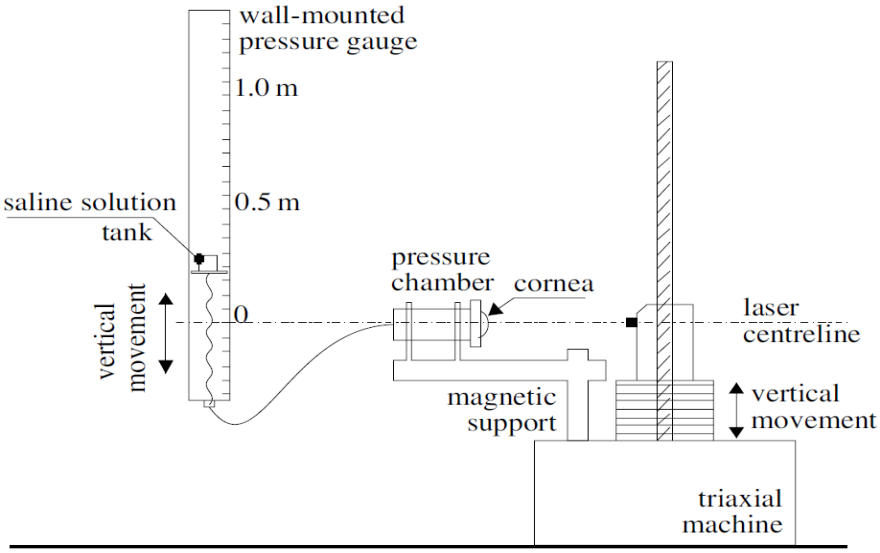

Fig 1.2: Schematic of a typical cornea inflation test rig from literature (Reproduced from reference [28], Anderson *et al*).

The nonlinear material properties of the cornea were studied by Woo *et al* [30] and were confirmed by Anderson *et al* [28]. In Anderson's study, inflation tests were carried out to measure the apical rise of porcine cornea specimens subjected to a gradually increasing posterior pressure up to a maximum of 105 mmHg. The results show that the stress-strain relation experiences two phases: an initial phase of linear behaviour, followed by sudden stiffening at about 30 mmHg. The explanation is that the cornea is mainly composed of corneal matrix and collagen fibril layers. In the first phase, the collagen fibril layers remain loose and the mechanical behaviour is dominated by the corneal matrix. Thus, apical rise increases linearly with the pressure, and the cornea shows low stiffness. After the pressure has increased to a relatively large value, the collagen fibril layers become taut. Due to the higher stiffness of the collagen fibril layers, they start to dominate the corneal mechanical behaviour, and thus the cornea shows higher stiffness. Therefore, the nonlinear behaviour of the cornea is due to material property rather than geometry, and it can be characterized by a matrix regulated initial phase followed by a collagen regulated phase, as shown in Fig 1.3 [28].

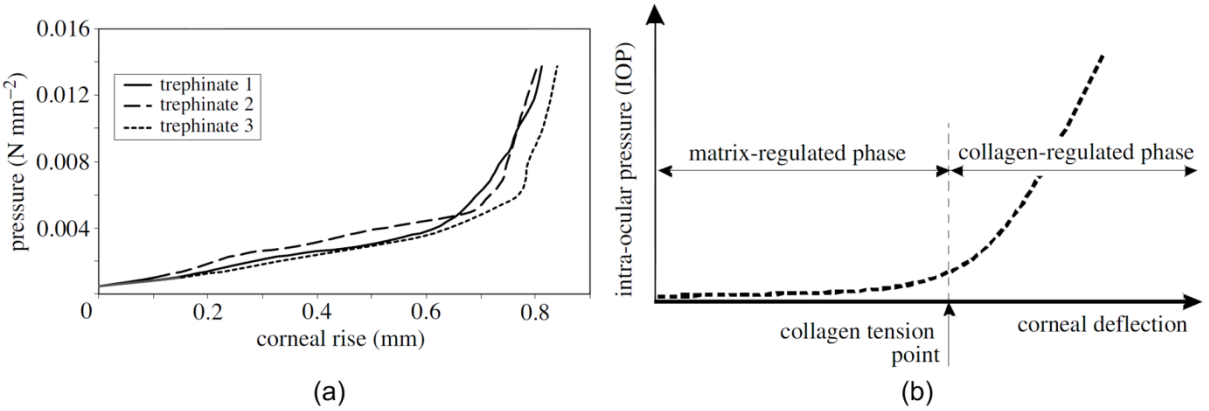

Fig 1.3: Nonlinear behaviour of cornea specimens under inflation conditions: (a) Curves of corneal Pressure-Apical rise, and (b) The two phases of corneal behaviour. (Reproduced from reference [28], Anderson *et al*).

Elsheikh *et al* compared mechanical properties of human and porcine corneas using inflation tests [29]. They divided the human cornea specimens into 3 groups according to the age of the donors and with a single group of the porcine corneas all within the same age range. The results showed that when subjected to an increasing posterior inflation pressure of up to 170 mmHg, both human and porcine corneas exhibit nonlinear behaviour, with all specimens demonstrating low initial stiffness and sudden stiffening after a certain pressure level. Although human and porcine corneas show differences in the pressure at which they start to stiffen, their overall mechanical behaviour is consistent with Fig 1.3. The stress-strain curves of the four groups are compared in Fig 1.4 [29]. It shows that cornea stiffens with age and human corneas are generally stiffer than porcine corneas.

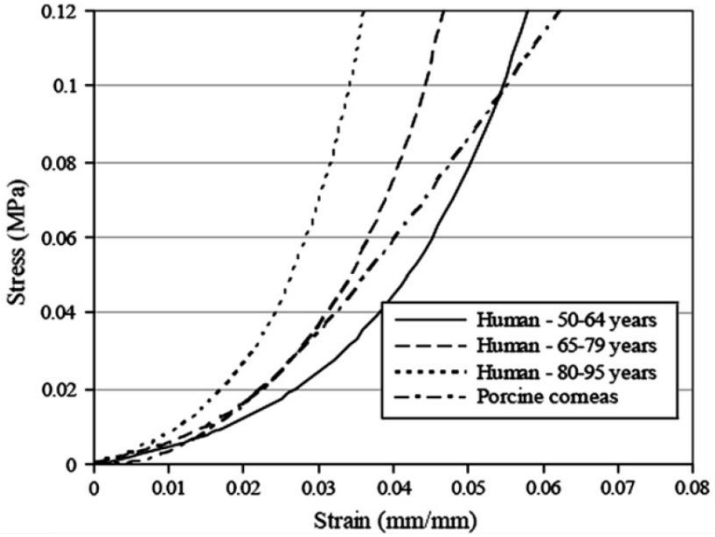

Fig 1.4: Comparison of the stress-strain relation between human and porcine corneas (Reproduced from reference [29], El-sheikh *et al*).

Another experiment was carried out by Elsheikh *et al* to evaluate the epithelium's contribution to corneal biomechanics [31]. Two groups of corneas with and without epithelium were tested under inflation conditions. Based on the results, they concluded that the stiffness of the epithelium was considerably lower than that of the stroma, and might therefore be ignored in numerical simulation studies.

The viscoelastic properties of bovine cornea and sclera were studied using inflation tests coupled with digital image correlation by Boyce *et al* [32, 33]. They obtained the full-field surface deformation maps over a certain pressure range through digital image correlation. They found that for pressures near and above the IOP, the majority of the deformation localized in the limbus and peripheral regions, and the central cornea remained largely undeformed. This result can be explained by the well-known preferred circumferential alignment of collagen fibrils in the peripheral regions. Viscoelastic behaviours such as hysteresis, creep and relaxation were observed in a broad pressure range of 0-32 kPa. In the range of 3.6-8 kPa, which represents the physiological pressure range, small viscoelastic deformation was observed, and the cornea within this range can be approximated as a linear viscoelastic or linear pseudo-elastic material.

1.1.4.2 Strip tensile testing method

Strip tensile tests have been extensively used by researchers to determine the mechanical properties of cornea and other soft biological tissues due to their evident implementation simplicity [34-37]. Fig 1.5 gives the schematics of the excised cornea strip specimen and the strip tensile test as studied by El-sheikh *et al* [34].

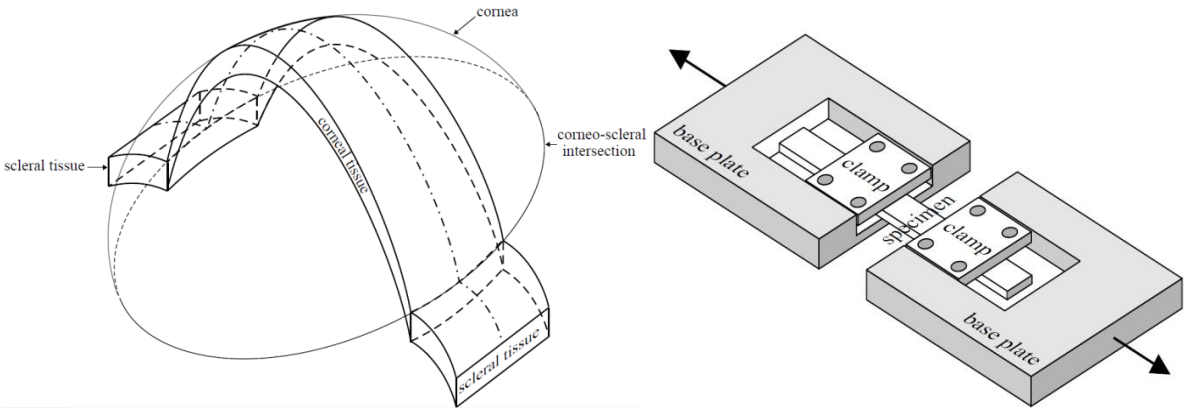

Fig 1.5: Schematics of the excised cornea strip specimen and the strip tensile test (Reproduced from reference [34], El-sheikh *et al*).

Compared with the inflation test, the strip tensile test has three inherent limitations due to the excised cornea strip specimen. The first limitation is the effect of variation in length in the strip specimen as the original cornea has a spherical configuration. Therefore, the central length is longer than that of the two sides. This limitation leads to a non-uniform stress distribution during the tensile test. When flattening the originally curved specimen, strains are generated, which will superimpose to the tensile strain under the test conditions. This is the second limitation. In addition, the variation of corneal thickness also influences the identification results as constant thickness is generally assumed. Elsheikh *et al* verified these effects by comparing the results of the inflation and strip tensile tests. They found that the stress-strain relations derived from the tensile tests exhibited larger stiffness than that from the inflation tests [34].

The inflation test is a physiologically representative method for determining the mechanical properties of the cornea, as can be concluded from the above discussions. Therefore, this testing method was selected in the current project when studying the ex-vivo depth-resolved mechanical behaviour of the cornea.

As the cornea has a complex composite structure, in addition to the fact that some pathologies can locally change the internal corneal biomechanical properties, surface measurements are not adequate to address the complete mechanical behaviour of the cornea. Therefore, it would be useful to develop a method that be used to characterize the internal corneal biomechanical properties and the 3D deformation behaviour.

1.2 Tomographic techniques for structure analysis

The analysis of the internal microstructure of a material is important for the study of the material mechanical properties. Instead of traditional surface imaging, imaging techniques that can look within the materials are needed, which are referred to as Tomography. Various tomographic techniques based on different mechanisms have been developed, such as X-ray computed tomography, magnetic resonance imaging, confocal microscopy, optical coherence tomography, *etc*. These will be introduced in this section.

1.2.1 X-ray computed tomography

X-ray computed tomography (X-ray CT) is a technology that utilizes computer-processed series of X-ray projections to produce tomographic volume of a scanned object. It enables the

user to see the internal structure of an object in a non-invasive and non-destructive way. X-ray CT is based on X-ray absorption contrast. The attenuation is characterized by Beer's Law, which defines the intensity attenuation as a function of incident and detected X-ray intensities, path length, and material attenuation coefficient. During a scan, a series of 1D projections of the attenuation through an object are obtained by rotating the X-ray source and the detector array (mounted on opposite sides of the scanned object) at various angles. These projections are then processed by the computer using a specialized algorithm to produce a cross-sectional 2D distribution of X-ray attenuations (2D X-ray CT image). A 3D volume distribution of X-ray attenuations can then be obtained by scanning different cross-sections of the object along the axis of rotation. This technique has been widely used in medical imaging (e.g. shown in Fig 1.6 (a) for a brain CT image) which is very useful for diagnostic and therapeutic purposes [38-40]. It is also applied in industrial areas for internal inspection such as structural analysis, flaw detection, failure analysis, deformation analysis, *etc* [41-43]. Fig 1.6 (b) gives an example of the 2D view of X-ray CT image of a low density polymeric foam which was previously developed by Pierron *et al* [41].

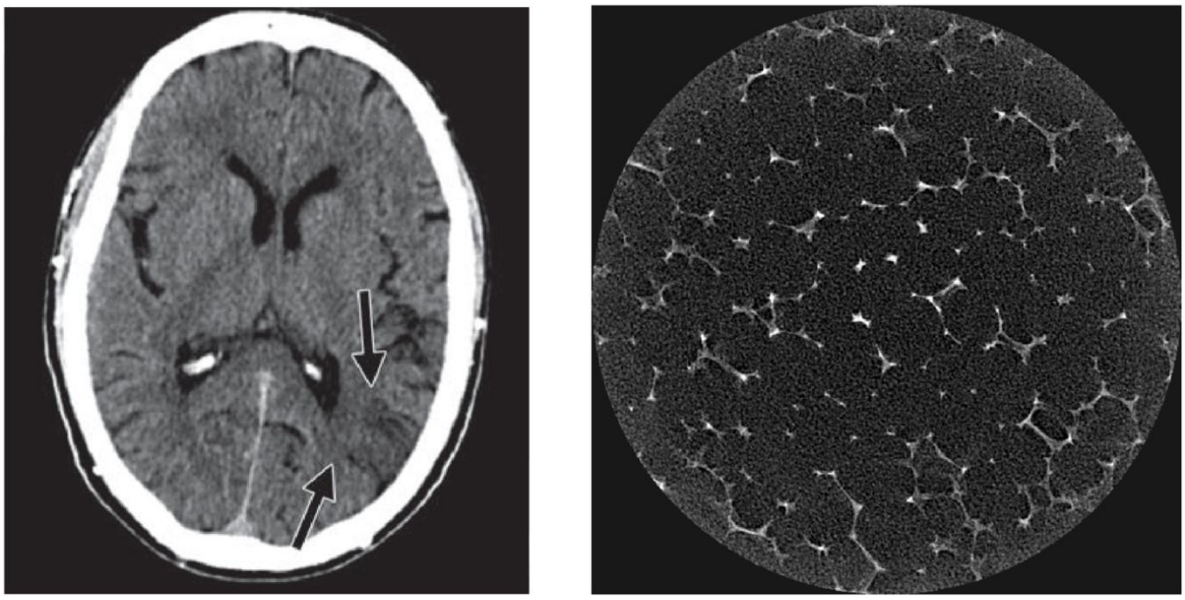

(a) (b)

Fig 1.6: Examples of the X-ray CT images: (a) Brain CT image with aphasia and headache, arrows show acute infarct (Reproduced from reference [38], Jordan *et al*) (b) X-ray CT image of low density polymeric foam (Reproduced from reference [41], Pierron *et al*).

X-ray CT, however, has some limitations. Not all the scanned objects have sufficient X-ray absorption contrast for effective imaging. Some image artefacts such as ring artefact, beam hardening, *etc* can pollute the image acquisition and interpretation. Ring artefacts commonly occur due to miscalibration or failure of individual detector elements. They appear in the reconstructed images as a number of concentric rings superimposed on the object's structure. Beam hardening is another common artefact. It arises when the average energy of a polychromatic X-ray beam passing through an object increases (becomes harder) as low energy photons are absorbed more readily than high energy ones. X-rays passing through the central region of the object are said to be 'hardened' more than those passing through the edges because more material is traversed. This can cause a cup appearance in the image which differs from the ideal case when there is no beam hardening. Apart from the image artefacts, when reconstructing a volume with high spatial resolution, the acquisition can be very time-consuming. Although high spatial resolution X-ray CT (with spatial resolution about 1 μm) has been developed for industrial applications, most of the medical applications of X-ray CT are millimetre scales because a limited dose of low-energy X-rays is coupled with high-efficiency detector to meet the requirements of optimized tissue differentiation and optimized patient exposure time for medical research as described by Helliwell *et al* [44]. High cost of the machine is another drawback. Due to these limitations, X-ray CT is not a suitable technique for imaging cornea.

1.2.2 Magnetic resonance imaging

For biological tissues with high water content such as brain, eye or artery tissues, *etc*. magnetic resonance imaging (MRI) is a useful tomographic technique to investigate the anatomy and function of these tissues. MRI is based on the nuclear magnetic resonance (NMR) phenomenon. During MRI, a strong magnetic field is applied across the tissue to be examined. The magnetic field is then oscillated at an appropriate resonance frequency to excite the nuclear spins of the hydrogen nuclei. The radio frequency signal emitted by these excited hydrogen nuclei in the tissue (e.g. from water, fat molecules) is then detected when they relax from the magnetic interaction. As the frequency of the emitted signal is dependent on the tissue and the pulse used to excite the spins, locations with different signal frequency indicate different amount of hydrogen nuclei. This provides a method to map the tissue in terms of hydrogen nuclei density. Thus, for tissues with different hydrogen densities, images showing contrast can be obtained. MRI is widely applied in medical areas. It is particularly

well suited for the imaging and diagnosis of soft tissues such as brain, heart, eye, *etc*. as shown in Fig 1.7 [45-47]. However, it can only be used for materials that present MR signal. MRI is a safe technique as it does not involve harmful ionizing radiations compared with X-ray CT. This technique also has limitations. Although many MRI scanners have spatial resolution better than 100 μm, only a small number are better than 10 μm as described by Glover *et al* [48]. The machine makes tremendous noise during scanning, and it usually requires a long scanning time. In addition, MRI equipment is very expensive. Thus, this technique is not suitable for the present study.

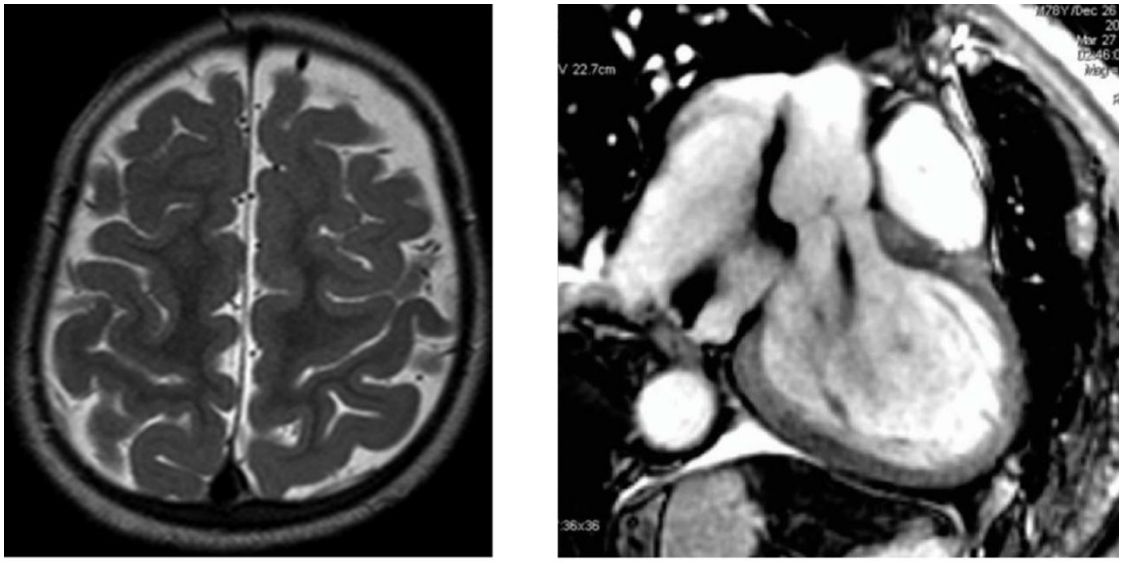

(a) (b)

Fig 1.7: Examples of the MRI images: (a) Brain MRI image showing generalized cerebral atrophy (Reproduced from reference [45], Lee *et al*) (b) A heart MRI image (Reproduced from reference [46], Sommer *et al*).

1.2.3 Confocal microscopy

Confocal microscopy (CM) is a point by point illumination optical imaging technique that can provide sharp and high resolution images of a scanned sample. Different from the conventional microscopy, CM increases the optical resolution and contrast by using point illumination of the specimen and excluding the out of focus light in the specimen. As illustrated in Fig 1.8(a), this is implemented by placing a pinhole in the optically conjugate plane (conjugates to the focal point of the lens) in front of the detector. As CM uses point illumination, less light can be collected for each point. To avoid too much image noise, enough light needs to be collected for each point. This is achieved nowadays using laser light

sources. By combining the point illuminations (in short and regular intervals), 2D and 3D imaging can be implemented. The achievable depth is determined by the wavelength of the light source and the aperture of the objective lens. It is also determined by the optical property of the specimen. CM is popular in the medical and industrial communities and typically applied for imaging biological tissues, glass fibre composites, *etc*. A few examples are shown in Fig 1.8 [49, 50].

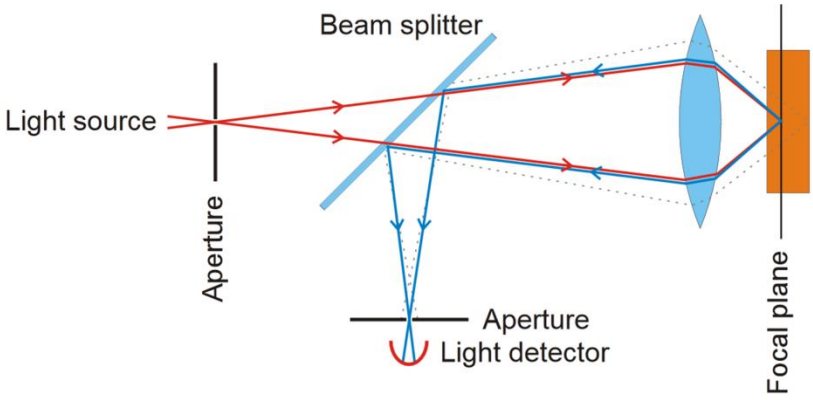

(a)

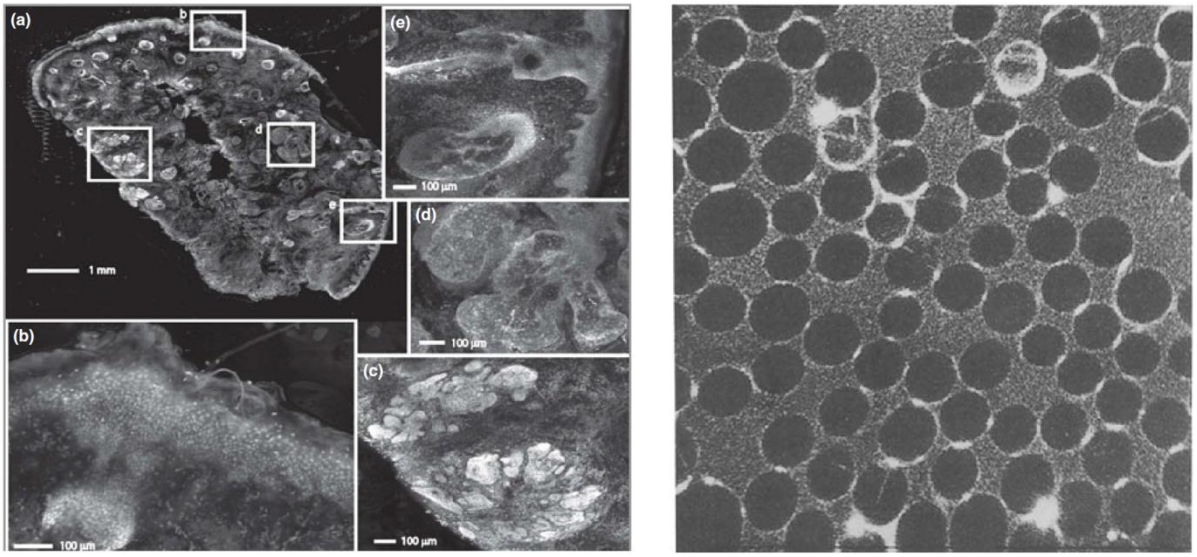

(b) (c)

Fig 1.8: (a) Schematic of CM and examples of CM images, (b) Histological images of tissue excised from Mohs surgery for skin cancer (Reproduced from reference [49], Larson *et al*), (c) Cross-section of a glass-epoxy composite (Reproduced from reference [50], Thomason *et al*).

CM has very high submicrometre spatial resolution, approximately 200 nm in lateral and 400 nm in axial depending on the NA of the objective and the wavelength of the emitted light as

described by Croixl *et al* [51]. The imaging depth however is limited to submillimetre scales, e.g. 240 μm for a non-compensated setup and 800 μm for a compensated setup which was previously studied by McConnell [52]. To image tissues that are thicker than a millimetre such as cornea, artery, *etc*., a technique with larger imaging depth would be more suitable.

1.2.4 Optical coherence tomography

Optical coherence tomography (OCT) is a non-invasive, non-contacting imaging technique that can acquire micrometer resolution, cross sectional images from within semi-transparent, light scattering media such as biological tissues. It is based on low coherence interferometry through the use of broadband light sources that can emit light over a broad range of frequencies [53]. Basically, OCT can be divided into two types, time domain OCT (TD-OCT) and frequency domain OCT (FD-OCT).

A typical schematic for the two types of OCT is shown in Fig 1.9 [54]. The light generated from the broadband light source is split by the beam splitter into two arms, namely reference and object arms. One light beam goes through the reference arm and reflects back from a reference mirror. The other light beam in the object arm is moved across the sample by the galvanometer scanner and lenses. This beam of light penetrates the sample and backscatters from the inner structure. This reflected light then interferes with the light reflected from the reference arm. For FD-OCT, the interference signal is recorded and analysed by the spectrometer. The light backscattered from different depths in the sample and which interferes with the reference light modulates the spectra. The depth information can be directly calculated by a Fourier transformation of the acquired spectra. Different from the fixed reference mirror and spectrometer in FD-OCT, TD-OCT uses a translating mirror and a simple photodiode as the photo detector. The reference mirror is scanned over the imaging depth and the time dependent signal is recorded. By demodulating the interference signal a reflectivity profile of the sample called A-scan can be obtained.

There are mainly two types of FD-OCT. One is the spectral domain OCT (SD-OCT) as discussed above. The other is called swept source OCT (SS-OCT). Both of them use a fixed reference mirror, but in SS-OCT a frequency scanning light source is used instead of the broad band light source. The spectral components are not encoded by spectral separation, but encoded by time. Thus, a simple photodiode is used as the photo detector instead of a spectrometer, which enables faster imaging.

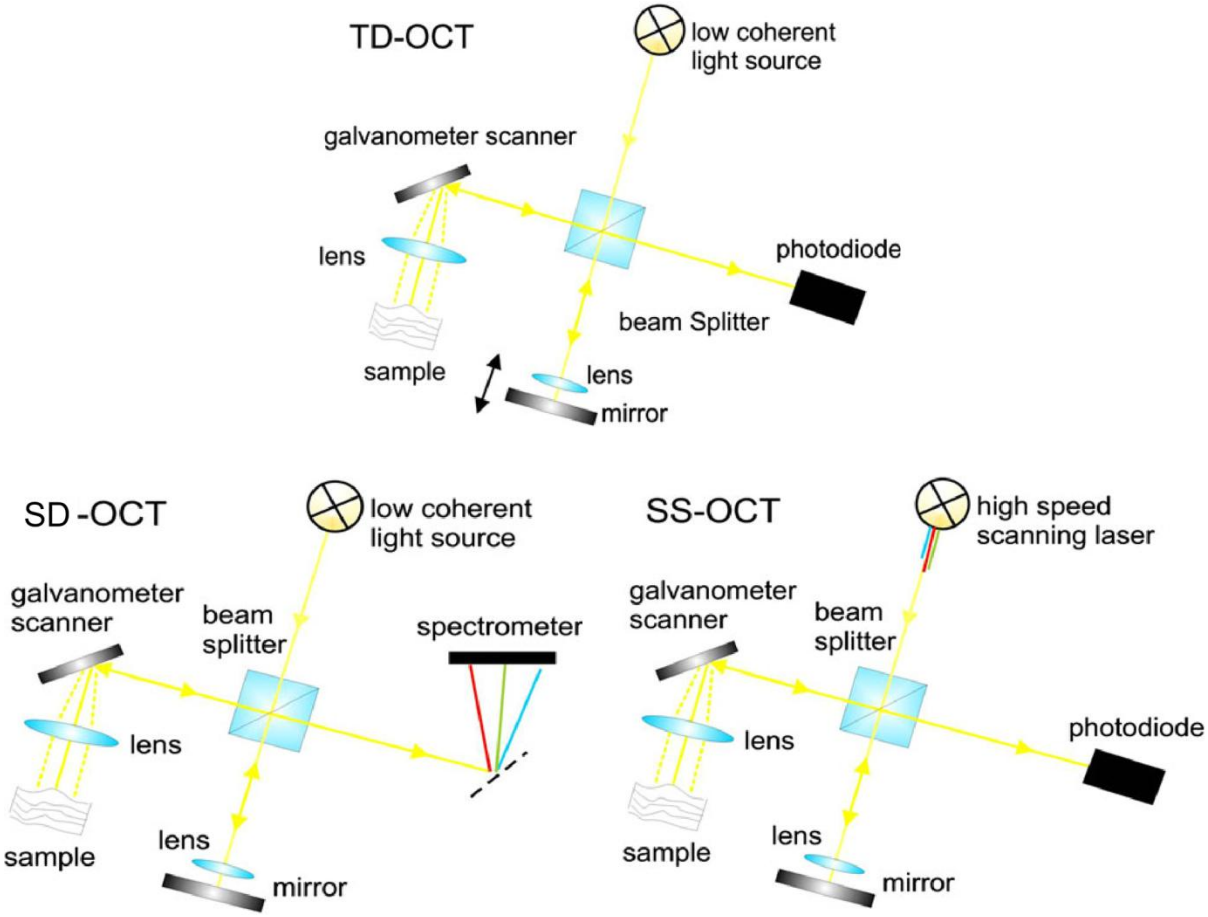

Fig 1.9: Schematics of TD-OCT and FD-OCT systems (Reproduced from reference [54], Gambichler *et al*).

Compared to TD-OCT, FD-OCT has the advantages of faster signal acquisition and higher signal-to-noise ratio [55]. Currently, many commercial OCT systems, especially SD-OCT, are available [56]. This rapidly developing imaging technique has already been applied in many areas, ranging from diagnostics medicine such as ophthalmology, cardiology, gastroenterology and dermatology [53-58] to industrial applications such as the study of glass fibre reinforced composites, adhesives, polymers [59-62], *etc*. Examples of OCT images are given in Fig 1.10.

Compared to X-ray CT, MRI and CM, OCT is more suitable for the depth-resolved 3D imaging of thin soft biological tissues such as cornea, skin, artery, *etc*. X-ray CT requires the scanned objects to have sufficient X-ray absorption contrast for effective imaging, and the spatial resolution for medical application is typically millimetre scale. Although MRI is used for imaging biological tissues such as brain, heart, *etc*., its relatively poor spatial resolution (<100 μm) is not sufficient for thin tissues such as cornea. In addition, the high cost of X-ray

CT and MRI confines the applicability of these techniques. CM can provide very high spatial resolution (e.g. 200 nm in lateral and 400 nm in axial), the imaging depth of this technique however is limited to submillimetre scale. OCT is more suitable as it can provide larger imaging depth (~ 3 mm in air) as well as high spatial resolution (~1 μm in lateral and axial) as studied by Safrani *et al* [63]. Therefore, in the present study, OCT was selected for the reconstruction of the soft tissues such as cornea.

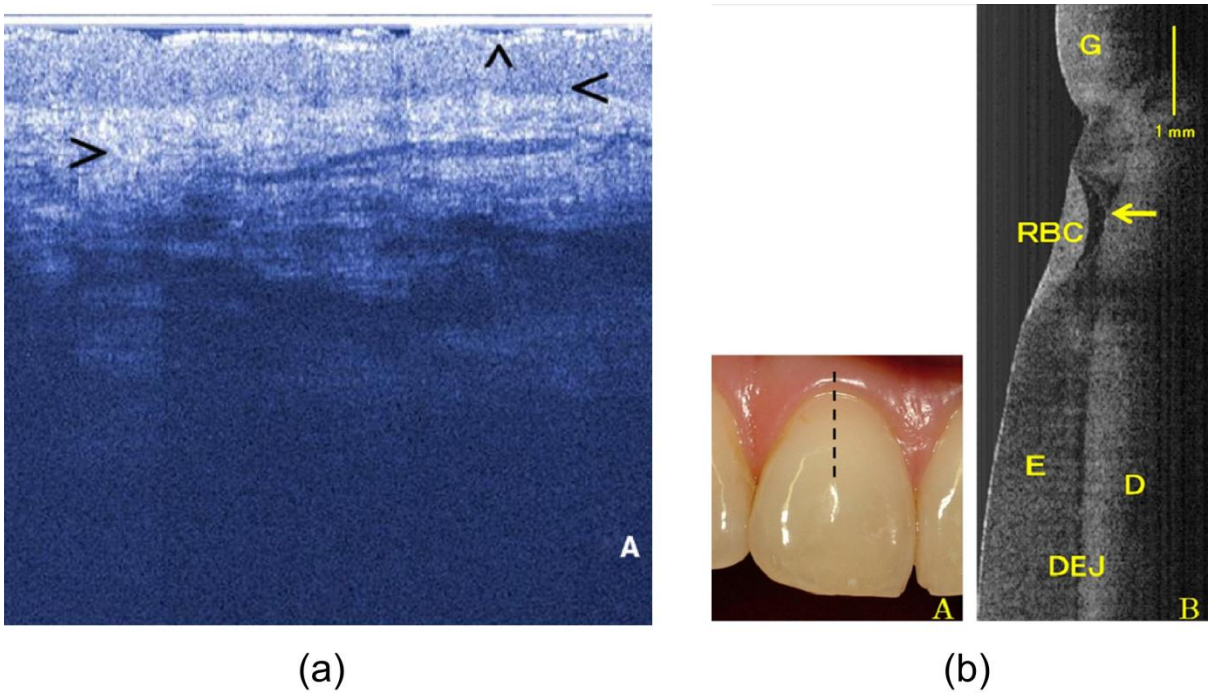

Fig 1.10: Examples of OCT images: (a) Healthy human skin on upper back (Reproduced from reference [54], Gambichler *et al*) (b) Photo and OCT image of restoration in the central incisor, and arrow shows gap formation beneath resin-based composites material (Reproduced from reference [59], Ishibashi *et al*).

1.3 Inverse problem to identify material constitutive parameters

Traditional approaches for the identification of the material constitutive parameters involve simple mechanical tests such as tensile or bending tests. They allow the identification of constitutive parameters based on analytical relations between these parameters and measured data such as local strains and applied load. However, these approaches are usually based on some stringent assumptions such as uniform or linear stress distributions, which are difficult to ensure experimentally. Therefore, alternative methods are currently being developed to relax some of the limitations of these simple tests. The most promising rely on

displacement/strain fields obtained from suitable full-field measurement techniques coupled with numerical processing and a robust identification strategy that can extract the parameters from the strain field.

The classical direct problem consists in determining the displacement, strain and stress fields assuming that the constitutive equations, the constitutive parameters, the load, the boundary conditions and the geometry are known. Using the same set of equations, another problem aims at finding the constitutive parameters that govern the constitutive equations assuming the displacement/strain fields are known. The displacement/strain fields are usually obtained using suitable full-field measurement techniques coupled with numerical processing methods such as tomography plus digital volume correlation. The load is measured through traditional load sensors. The geometry and the constitutive equations are known *a priori*. This is referred to as an inverse problem. Several methods have been developed to solve the inverse problem including finite element model updating (FEMU) [10, 28, 64-66, 71] and the virtual fields method (VFM) [67-71]. These methods were reviewed by Avril *et al* in [71].

1.3.1 Finite element model updating

FEMU is the most widely accepted approach for inverse problem solution. It compares the mechanical measurements collected on the specimen with their numerical counterparts obtained from a finite element (FE) model. A cost function is built up using the difference between the numerical and the experimental values in terms of force and/or displacement or strain. The cost function is then minimized with respect to the sought constitutive parameters iteratively, and finally provides a solution to the problem.

Different constitutive models have been used by the researchers to characterize the mechanical properties of cornea using FEMU. Early research applied isotropic constitutive models such as linear elastic isotropy, linear transverse isotropy, nonlinear elastic isotropy, and hyperelastic isotropy to predict the mechanical response of the cornea under inflation conditions [10, 28]. More recently, researchers have studied anisotropic properties of the cornea using FEMU. Anisotropic hyperelastic models are often chosen to characterize the anisotropic nonlinear behaviour of the cornea [64-66].

FEMU however exhibits some shortcomings. It is iterative by essence, even in the simplest case of linear elasticity. Therefore, initial values must be provided to start the iteration procedure. The choice of the initial values generally affects the convergence rate and

the quality of the results as local minima of the cost function may appear. In addition, at least one FE model needs to be run for each cost-function evaluation, resulting in computationally intensive routines, particularly for highly non-linear problems (large deformation, hyperelasticity, *etc*.

The VFM has been developed specifically to solve this inverse problem when full-field measurements are available. It avoids the drawbacks of FEMU by taking maximum advantage of the availability of full-field deformation measurements.

1.3.2 The virtual fields method

The VFM is based on the principle of virtual work as described by Pierron *et al* [67]. It utilizes the full-field deformation measurement data to retrieve the unknown constitutive parameters. For VFM, the stress fields are substituted as a function of the unknown parameters, and the identification is achieved by making the stress fields validate the equilibrium equation of the principle of virtual work with preselected test functions. A thorough explanation for the VFM will be given in Chapter 2.

The method for identifying the constitutive parameters depends on the nature of the material. For linear elastic materials, the equilibrium equation of the principle of virtual work depends linearly on the sought parameters. Therefore, a direct identification of the constitutive parameters is available by choosing proper test functions and solving the correspondent linear equation system. This strategy has been applied to the identification of the in-plane, through-thickness and bending stiffness components of linear elastic anisotropic materials such as composites [72-75]. It should be noted that certain non-linear constitutive models can still be explicitly and linearly expressed as functions of the unknown constitutive parameters, which has previously been described [76-78].

For other materials, the constitutive equations of which are not linear functions of the constitutive parameters such as anisotropic hyperelasticity or elasto-plasticity, direct identification is not feasible. Therefore, an iterative procedure minimizing the residual of the equilibrium equation of the principle of virtual work needs to be applied. It has been used to identify the elasto-plastic constitutive parameters of metals [79-81] and has been verified to be feasible to identify the anisotropic hyperelastic constitutive parameters of the soft and biological materials such as arteries [82, 83].

1.4 Full-field deformation measurement techniques

According to the discussions above, it is obvious that the acquisition of the deformation field and the corresponding strain field is a prerequisite for the identification of material constitutive parameters. Recent advances in surface/volume deformation measurement techniques such as the grid method, wavelength scanning interferometry, digital image/volume correlation, *etc.* enable the 2D and/or 3D deformation measurements. These techniques are reviewed in this section.

1.4.1 The grid method

The grid method is an optical method developed to measure surface deformation which was previously studied by Surrel [84]. It is based on the use of a spatial carrier to characterize the surface of a specimen. The spatial carrier is made up of a grid pattern with a set of horizontal and vertical lines bonded at the surface of the specimen. The intensity pattern reflected by the grid is captured by a high resolution camera to extract the phase fields using the spatial phase shifting methods. The displacement fields from the reference to the deformed state are then calculated from the corresponding phase differences introduced by the deformation. Fig 1.11 shows typical displacement and strain maps for a glass fibre reinforced epoxy open-hole tensile specimen studied by Pierron *et al* [85]. The specimen was bonded a grid pattern and loaded up to surface ply cracking in a tensile machine under controlled displacement. A CCD camera was positioned in front of the specimen to record the grid pattern of the specimen under various loading conditions. Then, the phase changes between each two consecutive images were calculated from which the displacements can be determined incrementally. By adding up this series of displacement increments the total displacement field at any load where an image was recorded can be determined, In the left column of Fig 1.11, displacement fields for both in-plane components U_x and U_y under a load of 4.84 kN are shown. From the displacement field, the strain field was then calculated using local differentiation, as illustrated in the right bottom of Fig 1.11 for the strain component ε_{yy}. The grid method however is limited to surface deformation measurement. For tests such as bending as studied by Avril *et al* [86], surface measurement would suffice as deformation is homogeneous through the width. For more heterogeneous through-thickness deformations, volume deformation measurement is needed.

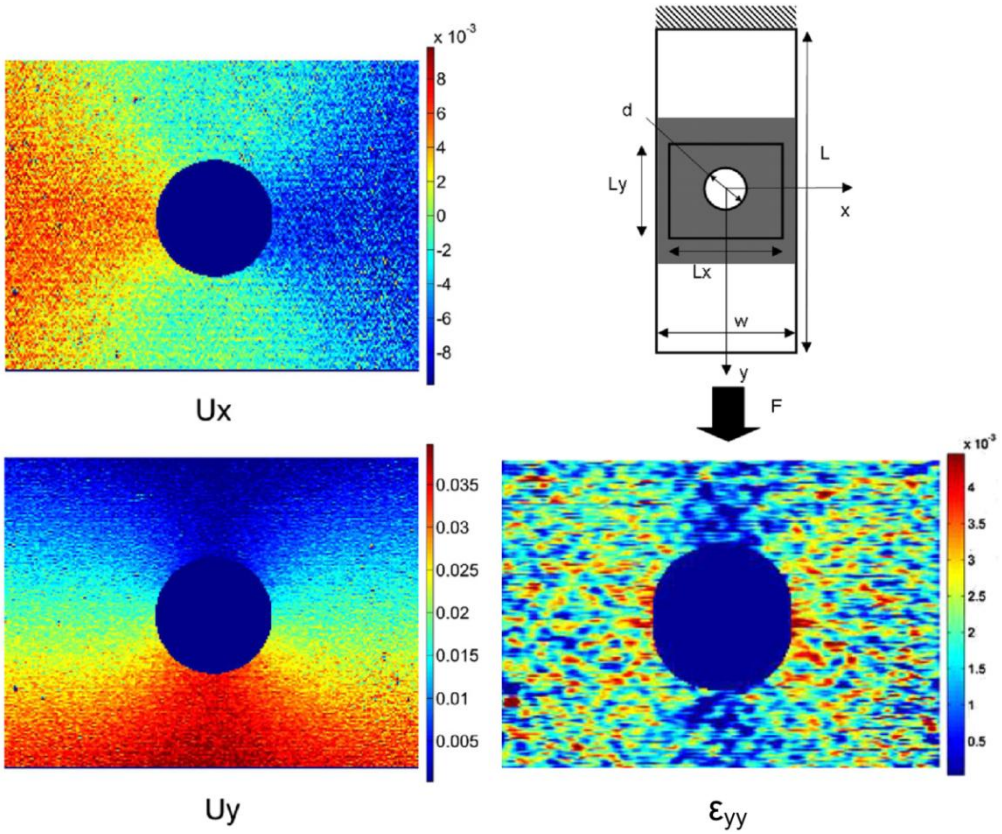

Fig 1.11: Displacement and strain maps from the grid method for a glass fibre reinforced epoxy open-hole tensile specimen (Reproduced from reference [85], Pierron *et al*).

1.4.2 Wavelength scanning interferometry

Interferometric techniques such as wavelength scanning interferometry (WSI) have been applied to the measurement of depth-resolved displacement fields by Ruiz *et al* [87-89]. WSI is a volume imaging technique in which 2D image sequences are recorded as the wavenumber of the light source changes over time. It uses a tunable light source to illuminate the sample. First, the phase can be extracted by measuring the light intensity when phase shifts are introduced between two interfering waves. The phase shifts are a function of the temporal carrier which is introduced by the changing wavenumber and with a frequency that is related to the optical path difference. Through Fourier transformation the signal is separated into different depth-resolved bands. Then, the phase distribution is used to measure the in-depth displacement fields, which is carried out first by calculating the phase change between the two phase volumes of the reference and deformed states of the sample. After that, the resulting phase difference maps are unwrapped to produce the 3D displacement field by

an unwrapping algorithm that connects the phase change to the change in optical path length due to the deformation.

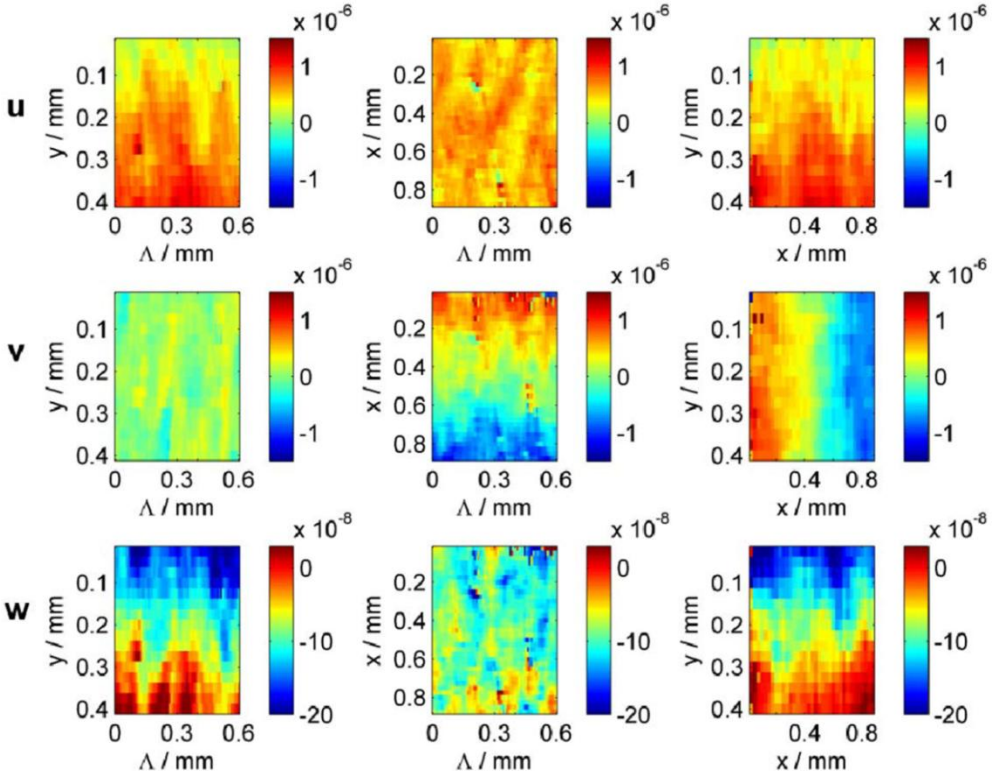

Fig 1.12: Cross sections of the measured 3D displacement fields from WSI for an epoxy sample under in-plane rotation and out-of-plane tilt (displacement unit: meters). The rows from top to bottom indicate the displacement components along the 3 orthogonal directions. The columns from left to right indicate sections of the data volume on different planes (Reproduced from reference [89], Chakraborty *et al*).

A latest WSI system that can measure all orthogonal components of displacement in the volume of scattering materials was developed by Chakraborty and Ruiz [89]. In their study, an optical setup was developed which used a tunable laser and had three illumination beams to illuminate the sample from three non-coplanar directions. Using this optical setup, all the displacement components in each voxel of the data volume were obtained by simultaneously measuring the interference signal from the different illumination directions during a wavelength scan. These interference signals were separated for the different illumination directions in the frequency domain by introducing different optical paths between the reference and illumination beams so that interference signals from different illumination directions will have a different carrier frequency in the spectral domain. To evaluate the

performance of the WSI system, an epoxy sample was moved by an in-plane rotation and out-of-plane tilt, and the displacement fields were measured using the WSI system. First, the change in the 3D phase distributions before and after moving the sample was measured. The displacement fields were then calculated from the measured phase change. Fig 1.12 gives an example of the measured 3D displacement fields. The rows from top to bottom illustrate the three displacement components, while the columns from left to right illustrate different sections of the data volume. Chakraborty and Ruiz observed excellent agreement between the measured and reference displacements.

1.4.3 Elastography

Elastography is a medical imaging technique for the mapping of strain and elastic modulus in soft tissues. Different ways can be employed to perform elastography including ultrasound elasticity imaging [90], magnetic resonance elastography (MRE) [91], and OCT-based elastography (OCE) [92-95].

Generally, OCE determines the deformation in the OCT image sequences (B-scans) by applying 2D cross-correlation algorithms (CCOCE) to calculate the speckle motion due to applied forces. Fig 1.13 gives an example of the OCE map for a multi-layer silicone phantom under compression. The map clearly shows the difference in stiffness between the two layers. Another type of OCE determines the deformation by measuring the phase change between successive A-scans or B-scans due to tissue motion, which is called phase-sensitive OCT-based elastography (PSOCE). Compared with CCOCE, PSOCE is capable of detecting very small sub-wavelength deformation, and is faster (capable of real time imaging of instantaneous tissue deformations) as described by Wang *et al* [92]. OCE is a useful method to quantify the elastic behaviour of soft tissues. However, most of the applications have so far focused on the measurements with only axial sensitivity, especially for PSOCE. For a more comprehensive study of the material behaviour (e.g. deformation in anisotropic material) as well as the prerequisite for the identification of 3D constitutive parameters using FEMU or VFM, measurement of the depth-resolved 3D deformation is highly desirable. This can be implemented by either 1) using a system with sensitivity to all deformation components based on a wavelength scanning OCT system with multiple illumination directions as introduced by Chakraborty and Ruiz [89] or 2) using a single channel OCT system coupled with digital volume correlation to provide deformation fields with all components.

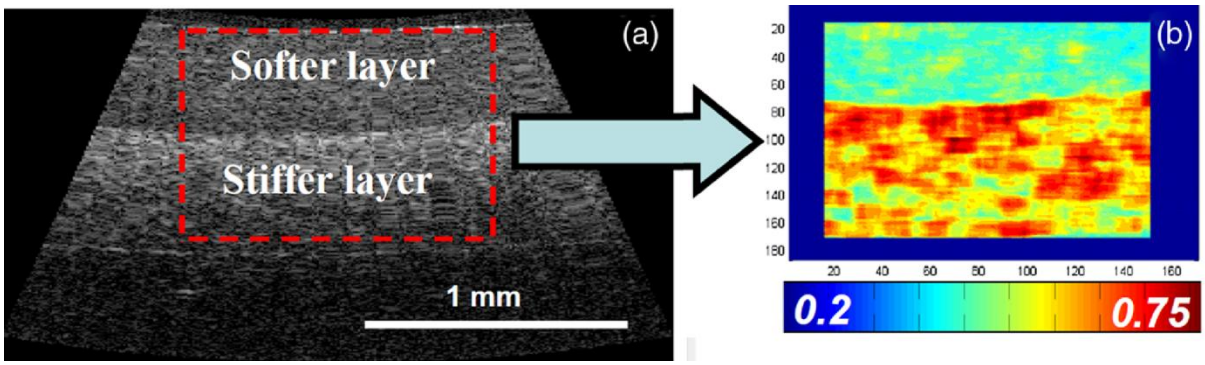

Fig 1.13: Elastographic correlation stability map indicating the stiffness distribution of a multi-layer silicone phantom (Reproduced from reference [93], Zaitsev *et al*).

1.4.4 Digital image/volume correlation

1.4.4.1 Digital image correlation

Digital image correlation (DIC) is a popular measurement technique to measure surface deformation of a specimen under load. This method was introduced in the early 1980s by Chu *et al* [96]. It is based on recent advances in computer technology and digital cameras. DIC determines the deformation field by tracking and matching the patterns between two digital images acquired from the surface of a specimen in the reference and deformed states. To be able to perform DIC, the measured surface must present patterns (surface contrast) so that they can be tracked. The pattern can be provided either by the intrinsic surface texture of the specimen or application of markers such as spray painting and powders, *etc*. to provide a diffusively reflective surface. For DIC, two approaches have been mainly used to quantify the surface deformation. The first one, which is the most widely used, is a local approach. In this case, the images in the reference and deformed states are first divided into subsets. These subsets are then correlated individually through a cross-correlation algorithm between the two loading states to determine the displacement vector of each subset. This is realized by maximizing the correlation coefficient that measures the degree of similarity of the grey level distributions in the subsets of the reference and deformed states. The best prediction of the displacement relates to the highest degree of similarity of the grey level distributions thus, to the maximal correlation coefficient. Fig 1.14 shows the front views of a tensile bar with applied speckle pattern under subsequent load steps and the axial strain maps obtained with DIC studied by Parsons *et al* [97]. The other approach quantifies the deformation field based on a continuous global field using a large number of degree of freedom determined at the

same time rather than sequentially for the local approach. This is referred to as global approach as described by Hild *et al* [98]. DIC has been widely applied in many disciplines such as mechanical engineering, material science, medical science, *etc*. [32, 33, 99-102]. This method however is limited to surface deformation measurement. Thanks to the development of the various tomographic techniques, volume deformation measurement based on the same principle as DIC becomes possible.

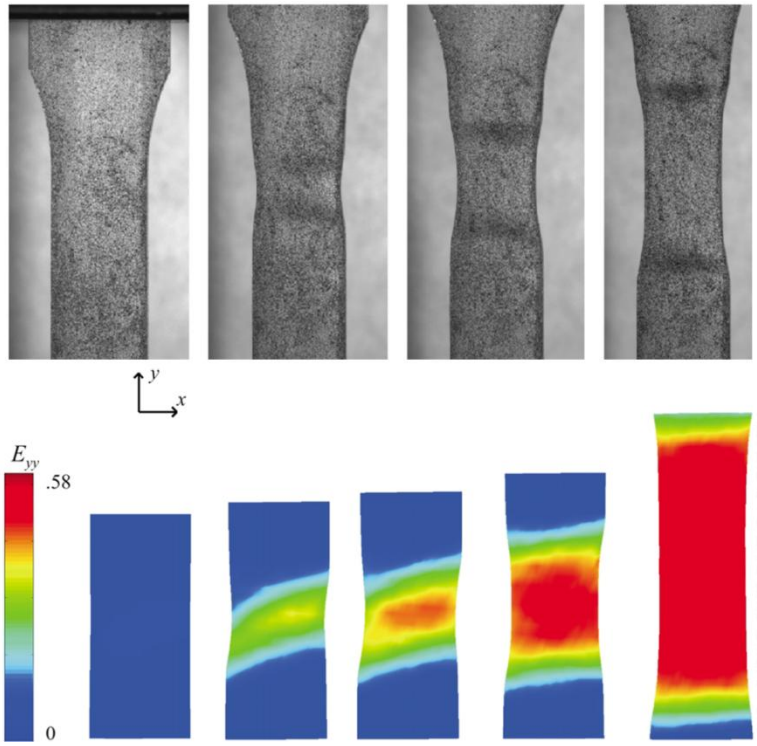

Fig 1.14: Front views of a tensile bar with applied speckle pattern in different load steps and the strain maps for E_{yy} obtained with DIC (Reproduced from reference [97], Parsons *et al*).

1.4.4.2 Digital volume correlation

Digital volume correlation (DVC) is effectively a 3D extension of DIC. DVC was developed to measure the internal 3D deformation behavior of materials by tracking internal features that resemble 3D speckle patterns contained in the reconstructed volumes, which was introduced by Bay *et al* [103]. Instead of pixels for DIC, the reconstructed volume consists of voxels. Similar to DIC, during DVC, a volume is first divided into sub-volumes (for local approach), and the displacement vector of each sub-volume is individually determined by a 3D cross-correlation algorithm.

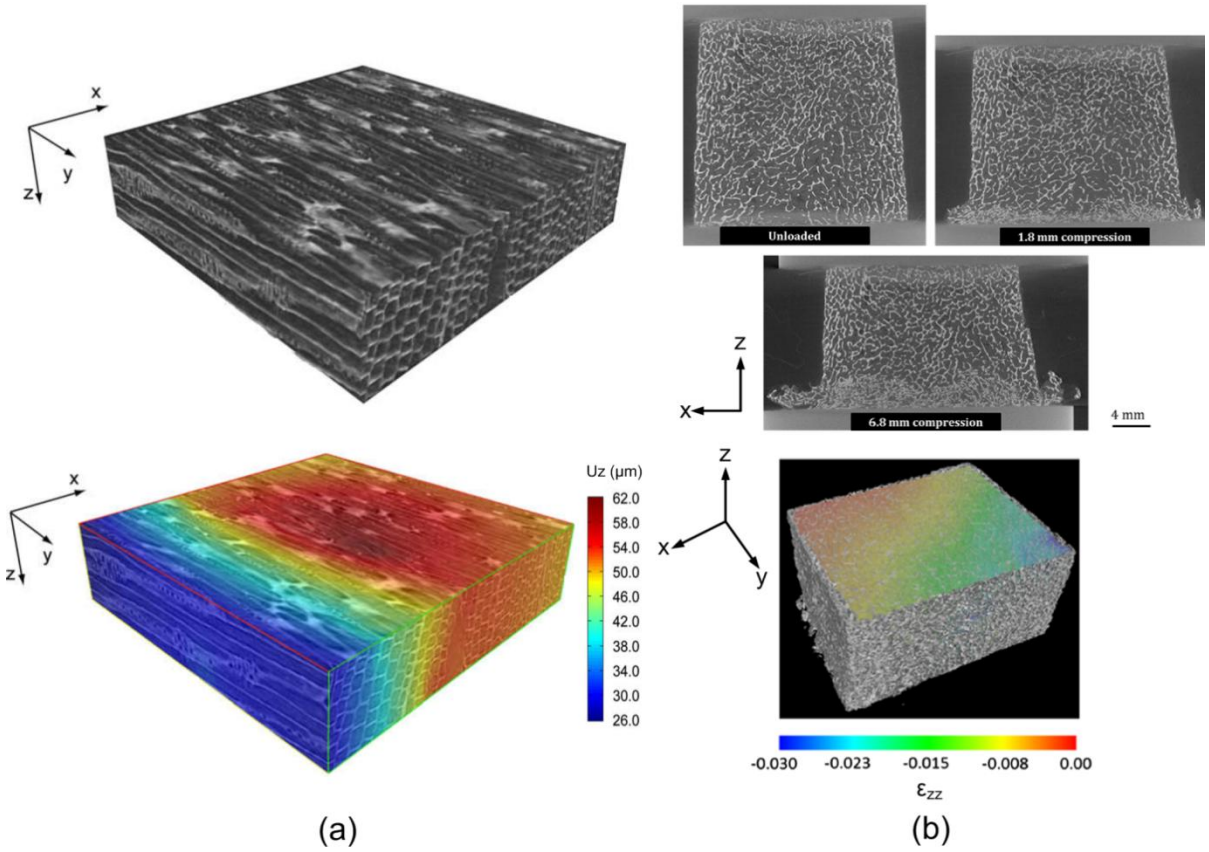

Fig 1.15: X-ray CT reconstructions and deformation distributions obtained with DVC for: (a) Wood specimen under three-point bending (Reproduced from reference [104], Forsberg *et al*) and (b) Trabecular bone under compression (Reproduced from reference [105], Gillard *et al*).

Like DIC, DVC requires sufficient speckle contrast in the reconstructed volumes to ensure that the correlation algorithm runs successfully. For solid materials with cellular or granular structures, such as trabecular bone, wood, *etc*., X-ray CT is suitable for the volume reconstruction as these materials present X-ray absorption contrast, as illustrated in Fig 1.15. These volume reconstructions are suitable for application of DVC for internal deformation measurement [104-107]. Engineering materials such as metals, composites, foams *etc*. have also been studied using X-ray CT coupled with DVC [41, 42, 108, 109]. In some cases, small particles need to be seeded into the material during the manufacturing process in order to provide sufficient pattern contrast. The application of DVC coupled with X-ray CT requires the materials to present proper X-ray absorption contrast. For soft semi-transparent materials such as biological tissues (cornea, skin, artery, *etc*.), more suitable techniques can be used. CM is one option for these types of material, which can provide high resolution (submicron) volume data. It has been coupled with DVC by Franck *et al* [110] to measure the internal 3D deformation of agarose gel under compression, and showing reasonable results. CM is

however limited to very small fields of view. As the penetration depth for CM is generally restricted to submillimetre, for thicker specimens such as cornea, skin, artery, *etc*. this technique is not adequate for mapping the whole through-thickness deformation field. It has been shown in the previous sections that OCT is capable of obtaining larger penetration depths compared to CM, and is widely used to image soft biological tissues. To measure the internal 3D deformation of soft biological tissues such as cornea, it would be interesting to combine OCT reconstructed volume data with DVC.

1.5 Conclusions

Cornea plays a very important role in the optical function of the eye. It has a complex composite structure, and is composed of five layers. Different corneal pathologies can cause changes in the corneal biomechanical properties, and corneal surgery such as refractive surgery requires a comprehensive understanding of the corneal deformation behaviour. Therefore, the study of the corneal biomechanical properties and its deformation behaviour is of great importance in clinical applications. A number of studies have been undertaken by researchers to characterize the corneal biomechanical properties using experimental testing methods such as inflation test, tensile test, *etc*. These studies however are based on surface measurement, which are not adequate to fully address the through-thickness information.

Tomographic imaging techniques are useful methods for the internal structure analysis of materials. Many types of tomographic techniques are available nowadays for depth-resolved imaging, such as X-ray CT, MRI, CM, and OCT. Among these techniques, OCT is the most suitable for imaging biological tissues such as cornea, skin, artery, *etc*. considering its relatively good resolution and deeper penetration. FEMU is the most widely used approach for the identification of material constitutive parameters, which however exhibits limitations such as local minima and longer processing time. The VFM is an alternative method specifically developed for processing full-field measurements, which overcomes these drawbacks to a certain point. To identify material parameters using FEMU or the VFM, full-field deformation measurements must be provided *a priori*. DVC is a popular method developed to determine the volume deformation, which is generally applied nowadays by coupling with X-ray CT reconstructed volume data. To determine the internal 3D deformation of soft biological tissues such as cornea, DVC will be performed on the OCT reconstructions.

CHAPTER 2

3D VIRTUAL FIELDS METHOD FOR LINEAR ELASTICITY

2.1 Introduction

The virtual fields method (VFM) is a useful method for solving identification problems which was developed by Pierron *et al* [67]. It is based on the principle of virtual work and retrieves material constitutive parameters by utilizing the full-field deformation measurements. This method is less time consuming compared with finite element model updating (FEMU) since for the latter at least one FE model needs to be run for each cost-function evaluation, resulting in computationally intensive routines, particularly for highly non-linear problems. So far, the VFM has been applied successfully to the identification of constitutive parameters for linear elastic materials such as composites, elasto-plasticity for metals as well as hyperelasticity for soft and biological tissues such as arterial walls, *etc*. However, most of these applications are based on surface deformation measurements and 2D VFM (usually with assumption of plane stress or thin plate). For materials with more complex structures and stress states, surface deformation measurement and 2D VFM are not able to address the complete mechanical property of such materials. In this case, 3D VFM in connection with volume deformation measurements would be highly desirable.

In this chapter, the derivation of the 3D manually defined VFM and the 3D optimized piecewise VFM for linear elasticity is presented in detail. A strategy to select suitable virtual fields that enable direct identification and minimize the influence of noise is adopted for the optimized piecewise VFM, which has already been proved successful in 2D identification [67]. Simple FE models were produced to verify the feasibility of the established 3D virtual fields. Finally, the manually defined virtual fields are benchmarked against the piecewise optimized virtual fields to compare their performance in retrieving constitutive parameters from noise corrupted strain data.

2.2 3D virtual fields method in linear elasticity

The virtual fields method, developed to identify the material constitutive parameters, is based on the principle of virtual work. This equation, provided below, is the integral form of the

global equilibrium equation for the standard deformable continuous solid model. It describes the balance between the virtual works of internal and external forces.

$$-\int_V \boldsymbol{\sigma} : \boldsymbol{\varepsilon}^* dV + \int_{\partial V} \overline{\boldsymbol{T}} \cdot \boldsymbol{u}^* dS + \int_V \boldsymbol{b} \cdot \boldsymbol{u}^* dV = \int_V \rho \boldsymbol{a} \cdot \boldsymbol{u}^* dV \tag{2.1}$$

In this equilibrium equation, $\boldsymbol{\sigma}$ is the actual stress tensor, $\boldsymbol{\varepsilon}^*$ is the virtual strain tensor, $\boldsymbol{u}^*$ is the virtual displacement vector, $\overline{\boldsymbol{T}}$ is the applied stress vector on the boundary ∂V of the solid volume V, $\boldsymbol{b}$ is the volume force vector, $\boldsymbol{a}$ is the acceleration vector and ρ is the mass per unit volume. The "." Is the vector dot product and ":" is the contracted product for second order tensors (or the matrix dot product). In this study, the solid will be assumed to be subjected to quasi-static deformation and body forces will be neglected. Therefore, their contribution to the virtual work can be canceled out. Thus, the equilibrium equation becomes

$$-\int_V \boldsymbol{\sigma} : \boldsymbol{\varepsilon}^* dV + \int_{\partial V} \overline{\boldsymbol{T}} \cdot \boldsymbol{u}^* dS = 0 \tag{2.2}$$

This equilibrium equation is valid for any continuous and differentiable virtual displacement field. The actual strain field and the load information are provided by the experiment. The stress components can be substituted by the material constitutive parameters and the strain components through an appropriate constitutive equation. The stress and strain components can be denoted in columns as follows

$$\boldsymbol{\sigma} : \begin{Bmatrix} \sigma_{11} \\ \sigma_{22} \\ \sigma_{33} \\ \sigma_{23} \\ \sigma_{13} \\ \sigma_{12} \end{Bmatrix} \qquad \boldsymbol{\varepsilon} : \begin{Bmatrix} \varepsilon_{11} \\ \varepsilon_{22} \\ \varepsilon_{33} \\ 2\varepsilon_{23} \\ 2\varepsilon_{13} \\ 2\varepsilon_{12} \end{Bmatrix} \tag{2.3}$$

In this chapter, the standard contracted notation is used as follows for the sake of legibility.

$$\boldsymbol{\sigma} : \begin{Bmatrix} \sigma_1 \\ \sigma_2 \\ \sigma_3 \\ \sigma_4 \\ \sigma_5 \\ \sigma_6 \end{Bmatrix} \qquad \boldsymbol{\varepsilon} : \begin{Bmatrix} \varepsilon_1 \\ \varepsilon_2 \\ \varepsilon_3 \\ \varepsilon_4 \\ \varepsilon_5 \\ \varepsilon_6 \end{Bmatrix} \tag{2.4}$$

The engineering shear strain is equal to twice the tensorial shear strain component. Thus, $\varepsilon_4 = 2\varepsilon_{23},\ \varepsilon_5 = 2\varepsilon_{13},\ \varepsilon_6 = 2\varepsilon_{12}$.

After introducing the constitutive relation into the equilibrium equation (2.2) of the principle of virtual work, the stress components can be replaced by the actual strain components and the sought constitutive parameters. Thus, the equilibrium equation (2.2) becomes

$$\int_V Q_{ij}\varepsilon_j\varepsilon_i^* dV = \int_{\partial V} \overline{\boldsymbol{T}} \cdot \boldsymbol{u}^* dS, \quad (i,j) \in [1,2,\ldots,6] \tag{2.5}$$

Assuming the material to be homogeneous, the equation above becomes

$$Q_{ij}\int_V \varepsilon_j\varepsilon_i^* dV = \int_{\partial V} \overline{\boldsymbol{T}} \cdot \boldsymbol{u}^* dS \tag{2.6}$$

For 3D orthotropic elasticity, the stress and strain components are related by the stiffness matrix as

$$\begin{pmatrix} \sigma_1 \\ \sigma_2 \\ \sigma_3 \\ \sigma_4 \\ \sigma_5 \\ \sigma_6 \end{pmatrix} = \begin{bmatrix} Q_{11} & Q_{12} & Q_{13} & 0 & 0 & 0 \\ Q_{12} & Q_{22} & Q_{23} & 0 & 0 & 0 \\ Q_{13} & Q_{23} & Q_{33} & 0 & 0 & 0 \\ 0 & 0 & 0 & Q_{44} & 0 & 0 \\ 0 & 0 & 0 & 0 & Q_{55} & 0 \\ 0 & 0 & 0 & 0 & 0 & Q_{66} \end{bmatrix} \begin{pmatrix} \varepsilon_1 \\ \varepsilon_2 \\ \varepsilon_3 \\ \varepsilon_4 \\ \varepsilon_5 \\ \varepsilon_6 \end{pmatrix} \tag{2.7}$$

If the material is isotropic

$$\begin{cases} Q_{11} = Q_{22} = Q_{33} \\ Q_{12} = Q_{13} = Q_{23} \\ Q_{44} = Q_{55} = Q_{66} = \dfrac{Q_{11} - Q_{12}}{2} \end{cases} \tag{2.8}$$

where Q_{11} and Q_{12} are the two stiffness components relating to Young's modulus E and Poisson's ratio ν through

$$\begin{cases} Q_{11} = \dfrac{(1-\nu)E}{(1+\nu)(1-2\nu)} \\ Q_{12} = \dfrac{\nu E}{(1+\nu)(1-2\nu)} \end{cases} \tag{2.9}$$

Therefore, for isotropic elasticity, after introducing equations (2.7) and (2.8) into equation (2.6), the equilibrium equation (2.6) can be written as

$$Q_{11}\int_V\left(\varepsilon_1\varepsilon_1^*+\varepsilon_2\varepsilon_2^*+\varepsilon_3\varepsilon_3^*+\frac{1}{2}\varepsilon_4\varepsilon_4^*+\frac{1}{2}\varepsilon_5\varepsilon_5^*+\frac{1}{2}\varepsilon_6\varepsilon_6^*\right)dV+Q_{12}\int_V\left(\varepsilon_1\varepsilon_3^*+\varepsilon_3\varepsilon_1^*+\varepsilon_2\varepsilon_3^*+\varepsilon_3\varepsilon_2^*+\right.$$
$$\left.\varepsilon_1\varepsilon_2^*+\varepsilon_2\varepsilon_1^*-\frac{1}{2}\varepsilon_4\varepsilon_4^*-\frac{1}{2}\varepsilon_5\varepsilon_5^*-\frac{1}{2}\varepsilon_6\varepsilon_6^*\right)dV=\int_{\partial V}\overline{\boldsymbol{T}}\cdot\boldsymbol{u}^*dS \tag{2.10}$$

For orthotropic elasticity, the equilibrium equation (2.6) becomes

$$Q_{11}\int_V\varepsilon_1\varepsilon_1^*dV+Q_{22}\int_V\varepsilon_2\varepsilon_2^*dV+Q_{33}\int_V\varepsilon_3\varepsilon_3^*dV+Q_{12}\int_V\left(\varepsilon_1\varepsilon_2^*+\varepsilon_2\varepsilon_1^*\right)dV+Q_{13}\int_V\left(\varepsilon_1\varepsilon_3^*+\varepsilon_3\varepsilon_1^*\right)dV$$
$$+Q_{23}\int_V\left(\varepsilon_3\varepsilon_2^*+\varepsilon_2\varepsilon_3^*\right)dV+Q_{44}\int_V\varepsilon_4\varepsilon_4^*dV+Q_{55}\int_V\varepsilon_5\varepsilon_5^*dV+Q_{66}\int_V\varepsilon_6\varepsilon_6^*dV=\int_{\partial V}\overline{\boldsymbol{T}}\cdot\boldsymbol{u}^*dS \tag{2.11}$$

Each new virtual field leads to an independent linear equation. Therefore, choosing as many virtual fields as the number of unknowns leads to a linear equation system

$$\boldsymbol{AQ}=\boldsymbol{B} \tag{2.12}$$

where $\boldsymbol{A}$ is a square matrix, $\boldsymbol{Q}$ is a vector containing the sought constitutive parameters Q_{ij}, and $\boldsymbol{B}$ is a vector whose components are the external virtual works done by the applied force for each virtual field. For the isotropic case, only two virtual fields are needed as there are only two unknowns to identify. Thus,

$$\boldsymbol{A}:\begin{bmatrix}\int_v\left(\varepsilon_1\varepsilon_1^{*(1)}+\varepsilon_2\varepsilon_2^{*(1)}+\varepsilon_3\varepsilon_3^{*(1)}+\frac{1}{2}\varepsilon_4\varepsilon_4^{*(1)}\right.\\ \left.+\frac{1}{2}\varepsilon_5\varepsilon_5^{*(1)}+\frac{1}{2}\varepsilon_6\varepsilon_6^{*(1)}\right)dV & \int_v\left(\varepsilon_1\varepsilon_2^{*(1)}+\varepsilon_2\varepsilon_1^{*(1)}+\varepsilon_1\varepsilon_3^{*(1)}+\varepsilon_3\varepsilon_1^{*(1)}+\varepsilon_2\varepsilon_3^{*(1)}+\right.\\ \left.\varepsilon_3\varepsilon_2^{*(1)}-\frac{1}{2}\varepsilon_4\varepsilon_4^{*(1)}-\frac{1}{2}\varepsilon_5\varepsilon_5^{*(1)}-\frac{1}{2}\varepsilon_6\varepsilon_6^{*(1)}\right)dV\\ \int_v\left(\varepsilon_1\varepsilon_1^{*(2)}+\varepsilon_2\varepsilon_2^{*(2)}+\varepsilon_3\varepsilon_3^{*(2)}+\frac{1}{2}\varepsilon_4\varepsilon_4^{*(2)}\right.\\ \left.+\frac{1}{2}\varepsilon_5\varepsilon_5^{*(2)}+\frac{1}{2}\varepsilon_6\varepsilon_6^{*(2)}\right)dV & \int_v\left(\varepsilon_1\varepsilon_2^{*(2)}+\varepsilon_2\varepsilon_1^{*(2)}+\varepsilon_1\varepsilon_3^{*(2)}+\varepsilon_3\varepsilon_1^{*(2)}+\varepsilon_2\varepsilon_3^{*(2)}+\right.\\ \left.\varepsilon_3\varepsilon_2^{*(2)}-\frac{1}{2}\varepsilon_4\varepsilon_4^{*(2)}-\frac{1}{2}\varepsilon_5\varepsilon_5^{*(2)}-\frac{1}{2}\varepsilon_6\varepsilon_6^{*(2)}\right)dV\end{bmatrix}$$

$$\boldsymbol{Q}:\begin{bmatrix}Q_{11}\\Q_{12}\end{bmatrix}\qquad\boldsymbol{B}:\begin{bmatrix}\int_{\partial v}\overline{\boldsymbol{T}}.\boldsymbol{u}^{*(1)}dS\\\int_{\partial v}\overline{\boldsymbol{T}}.\boldsymbol{u}^{*(2)}dS\end{bmatrix} \tag{2.13}$$

Similarly, for orthotropic elasticity, nine virtual fields need to be chosen for the nine unknown constitutive parameters. Thus, the corresponding $\boldsymbol{A}$ is a 9×9 square matrix, and $\boldsymbol{Q}$ and $\boldsymbol{B}$ are vectors with 9 components.

It should be pointed out that due to the discrete nature of the deformation measurement, the integrals above must be approximated in practice by discrete sums. This is the reason why full-field measurements are necessary for the VFM. If the spatial density of the strain measurement points is not large enough to faithfully reproduce the strain gradients, this approximation will cause errors that will lead to biases on the identified stiffness components. In practice, this is an important problem to consider but it will not be addressed here. For instance, the integral $\int_V \varepsilon_1 \varepsilon_1^* dV$ can be approximated by $\sum_{i=1}^{n} \varepsilon_1^{(i)} \varepsilon_1^{*(i)} v^{(i)}$, where n is the number of measurement points, $\varepsilon_1^{(i)}$ is the actual strain ε_1 at measurement point (i), $\varepsilon_1^{*(i)}$ the virtual strain ε_1^* at measurement point (i) and $v^{(i)}$ the volume associated to measurement point (i). In this way, matrix A in (2.12) becomes

$$\boldsymbol{A}: \begin{bmatrix} \sum_{i=1}^{n} \left(\varepsilon_1^{(i)} \varepsilon_1^{*(i)(1)} + \varepsilon_2^{(i)} \varepsilon_2^{*(i)(1)} + \varepsilon_3^{(i)} \varepsilon_3^{*(i)(1)} + \frac{1}{2} \varepsilon_4^{(i)} \varepsilon_4^{*(i)(1)} + \frac{1}{2} \varepsilon_5^{(i)} \varepsilon_5^{*(i)(1)} + \frac{1}{2} \varepsilon_6^{(i)} \varepsilon_6^{*(i)(1)} \right) v^{(i)} & \sum_{i=1}^{n} \left(\varepsilon_1^{(i)} \varepsilon_2^{*(i)(1)} + \varepsilon_2^{(i)} \varepsilon_1^{*(i)(1)} + \varepsilon_1^{(i)} \varepsilon_3^{*(i)(1)} + \varepsilon_3^{(i)} \varepsilon_1^{*(i)(1)} + \varepsilon_2^{(i)} \varepsilon_3^{*(i)(1)} + \varepsilon_3^{(i)} \varepsilon_2^{*(i)(1)} - \frac{1}{2} \varepsilon_4^{(i)} \varepsilon_4^{*(i)(1)} - \frac{1}{2} \varepsilon_5^{(i)} \varepsilon_5^{*(i)(1)} - \frac{1}{2} \varepsilon_6^{(i)} \varepsilon_6^{*(i)(1)} \right) v^{(i)} \\ \sum_{i=1}^{n} \left(\varepsilon_1^{(i)} \varepsilon_1^{*(i)(2)} + \varepsilon_2^{(i)} \varepsilon_2^{*(i)(2)} + \varepsilon_3^{(i)} \varepsilon_3^{*(i)(2)} + \frac{1}{2} \varepsilon_4^{(i)} \varepsilon_4^{*(i)(2)} + \frac{1}{2} \varepsilon_5^{(i)} \varepsilon_5^{*(i)(2)} + \frac{1}{2} \varepsilon_6^{(i)} \varepsilon_6^{*(i)(2)} \right) v^{(i)} & \sum_{i=1}^{n} \left(\varepsilon_1^{(i)} \varepsilon_2^{*(i)(2)} + \varepsilon_2^{(i)} \varepsilon_1^{*(i)(2)} + \varepsilon_1^{(i)} \varepsilon_3^{*(i)(2)} + \varepsilon_3^{(i)} \varepsilon_1^{*(i)(2)} + \varepsilon_2^{(i)} \varepsilon_3^{*(i)(2)} + \varepsilon_3^{(i)} \varepsilon_2^{*(i)(2)} - \frac{1}{2} \varepsilon_4^{(i)} \varepsilon_4^{*(i)(2)} - \frac{1}{2} \varepsilon_5^{(i)} \varepsilon_5^{*(i)(2)} - \frac{1}{2} \varepsilon_6^{(i)} \varepsilon_6^{*(i)(2)} \right) v^{(i)} \end{bmatrix} \tag{2.14}$$

If the selected virtual fields are independent, then the determinant of $\boldsymbol{A}$ is different from zero. Thus, the linear system is invertible and $\boldsymbol{Q}$ can be directly obtained by

$$\boldsymbol{Q} = \boldsymbol{A}^{-1} \boldsymbol{B} \tag{2.15}$$

2.3 Manually defined virtual fields in 3D case and example for validation

In this section, manually defined virtual fields were selected for the identification of the material constitutive parameters based on the method described in the previous section 2.2. A

simple case of a cube in compression was designed to illustrate the practical implementation of the virtual fields method in 3D. Linear isotropic elasticity was chosen for the sake of simplicity.

2.3.1 Simulation of strain data

A simple finite element model was produced to supply precise actual strain values and applied force from which the constitutive parameters can be extracted using the 3D VFM. If the identified values match the theoretical input values, then the 3D VFM is validated. Here, a model of a cube with one surface fixed and subjected to a concentrated force at point A was developed using ABAQUS® as shown in Fig 2.1. The dimensions and force were chosen arbitrarily. The dimensions of the cube are $30\times30\times30$ mm^3. The components of the concentrated force are equal to 9000 N along the x_1, x_2 and x_3 directions. The model uses 8-noded linear brick elements and has $15\times15\times15$ elements (measurement points) along each direction. Linear isotropic elasticity was set for this model. Therefore, Q_{11} and Q_{12} are the sought quantities. They are related to the Young's modulus E and Poisson's ratio ν through equation (2.9). The input material constitutive parameters were arbitrarily chosen as in Table 2.1.

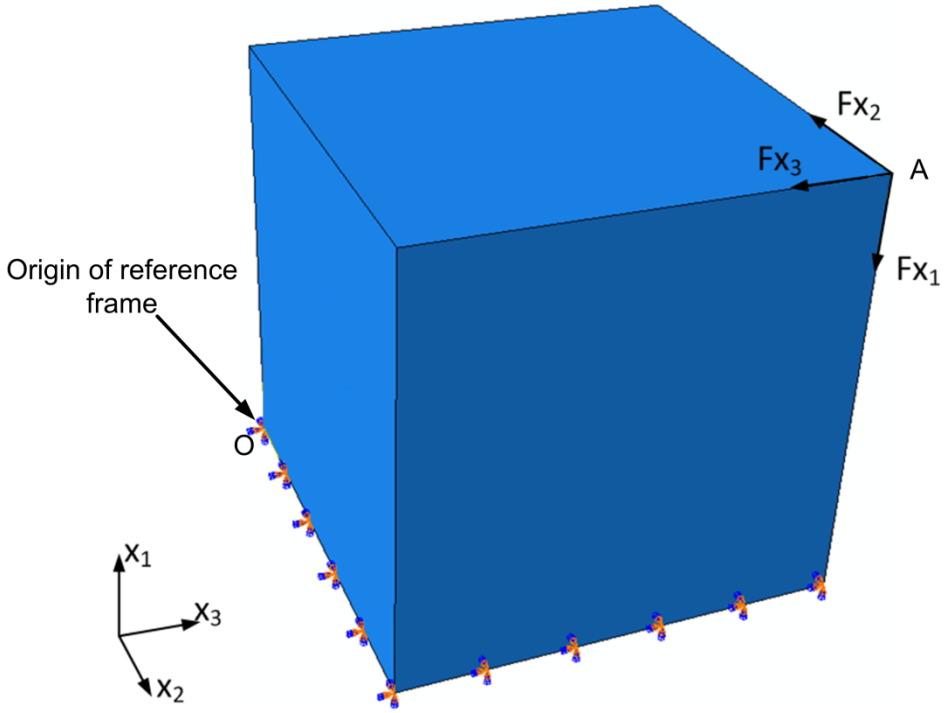

Fig 2.1: Cube under compression/shear.

Table 2.1: Input constitutive parameters for isotropic elasticity.

Q_{11} (GPa)	Q_{12} (GPa)	Young's modulus E (GPa)	Poisson's ratio v
134.6	57.7	100.0	0.3

After running the simulation, the strain data were exported from ABAQUS for each element. The coordinates of the centroid of each element were also output. These quantities were then utilized to characterize the constitutive parameters using 3D VFM.

2.3.2 3D manually defined virtual fields

As stated in section 2.2, two different virtual fields need to be selected to retrieve the Young's modulus and Poisson's ratio for isotropic elasticity. Since the reaction forces on the clamped surface are hard to measure in practice, the selected virtual fields on this surface need to be set to 0 so that the contribution of these reaction forces to the external virtual work can be cancelled out from the VFM equations. Here, two groups of virtual fields were chosen among an infinity of possibilities. For the first group, the virtual displacement field and the corresponding virtual strain field are

$$\textit{Virtual field 1:} \begin{cases} u_1^{*(1)} = x_1 \\ u_2^{*(1)} = 0 \\ u_3^{*(1)} = 0 \end{cases} \qquad \begin{cases} \varepsilon_1^{*(1)} = 1 \\ \varepsilon_2^{*(1)} = 0 \\ \varepsilon_3^{*(1)} = 0 \\ \varepsilon_4^{*(1)} = 0 \\ \varepsilon_5^{*(1)} = 0 \\ \varepsilon_6^{*(1)} = 0 \end{cases} \tag{2.16}$$

$$\textit{Virtual field 2:} \begin{cases} u_1^{*(2)} = 0 \\ u_2^{*(2)} = x_1 x_2 x_3 \\ u_3^{*(2)} = 0 \end{cases} \qquad \begin{cases} \varepsilon_1^{*(2)} = 0 \\ \varepsilon_2^{*(2)} = x_1 x_3 \\ \varepsilon_3^{*(2)} = 0 \\ \varepsilon_4^{*(2)} = x_1 x_2 \\ \varepsilon_5^{*(2)} = 0 \\ \varepsilon_6^{*(2)} = x_2 x_3 \end{cases} \tag{2.17}$$

After introducing the above two virtual fields (2.16) and (2.17) into the equilibrium (2.10), a linear equation system can be formed to directly determine the sought stiffness components Q_{11} and Q_{12}.

For virtual field 1, the left-hand side of the equilibrium equation (2.10) becomes

$$Q_{11}\int_V\left(\varepsilon_1\varepsilon_1^*+\varepsilon_2\varepsilon_2^*+\varepsilon_3\varepsilon_3^*+\frac{1}{2}\varepsilon_4\varepsilon_4^*+\frac{1}{2}\varepsilon_5\varepsilon_5^*+\frac{1}{2}\varepsilon_6\varepsilon_6^*\right)dV+Q_{12}\int_V\left(\varepsilon_1\varepsilon_3^*+\varepsilon_3\varepsilon_1^*+\varepsilon_2\varepsilon_3^*+\varepsilon_3\varepsilon_2^*+\right.$$
$$\left.\varepsilon_1\varepsilon_2^*+\varepsilon_2\varepsilon_1^*-\frac{1}{2}\varepsilon_4\varepsilon_4^*-\frac{1}{2}\varepsilon_5\varepsilon_5^*-\frac{1}{2}\varepsilon_6\varepsilon_6^*\right)dV=Q_{11}\int_V\varepsilon_1dV+Q_{12}\int_V\left(\varepsilon_2+\varepsilon_3\right)dV \tag{2.18}$$

The virtual displacement at point A is equal to $u_1^*(A)=L$, $u_2^*(A)=0$, $u_3^*(A)=0$. Therefore, the external virtual work at the right-hand side of the equilibrium equation (2.10) is equal to

$$\int_{\partial V}\overline{\boldsymbol{T}}\cdot\boldsymbol{u}^*dS=-F_{x_1}L \tag{2.19}$$

So the equilibrium equation (2.10) becomes

$$Q_{11}\int_V\varepsilon_1dV+Q_{12}\int_V\left(\varepsilon_2+\varepsilon_3\right)dV=-F_{x_1}L \tag{2.20}$$

Similarly, for virtual field 2, the equilibrium equation (2.10) becomes

$$Q_{11}\int_V(\varepsilon_2x_1x_3+\frac{1}{2}\varepsilon_4x_1x_2+\frac{1}{2}\varepsilon_6x_2x_3)dV+Q_{12}\int_V\left(\left(\varepsilon_1+\varepsilon_3\right)x_1x_3-\frac{1}{2}\varepsilon_4x_1x_2-\frac{1}{2}\varepsilon_6x_2x_3\right)dV=-F_{x_2}L^3 \tag{2.21}$$

Thus, the linear equation system is equal to

$$\boldsymbol{AQ}=\boldsymbol{B} \tag{2.22}$$

$$\boldsymbol{A}:\begin{bmatrix}\int_V\varepsilon_1dV & \int_V\left(\varepsilon_2+\varepsilon_3\right)dV\\ \int_V(\varepsilon_2x_1x_3+\frac{1}{2}\varepsilon_4x_1x_2+\frac{1}{2}\varepsilon_6x_2x_3)dV & \int_V\left(\left(\varepsilon_1+\varepsilon_3\right)x_1x_3-\frac{1}{2}\varepsilon_4x_1x_2-\frac{1}{2}\varepsilon_6x_2x_3\right)dV\end{bmatrix}$$

$$\boldsymbol{Q}:\begin{Bmatrix} Q_{11} \\ Q_{12} \end{Bmatrix} \qquad \boldsymbol{B}:\begin{Bmatrix} -F_{x_1}L \\ -F_{x_2}L^3 \end{Bmatrix}$$

After approximating the above integrals by discrete sums over the whole measurement data points, matrix $\boldsymbol{A}$ in the linear equation system (2.22) becomes

$$\begin{cases} \boldsymbol{A}(1,1) = \sum_{i=1}^{n} \varepsilon_1^{(i)} v^{(i)} \\ \boldsymbol{A}(1,2) = \sum_{i=1}^{n} \left(\varepsilon_2^{(i)} + \varepsilon_3^{(i)}\right) v^{(i)} \\ \boldsymbol{A}(2,1) = \sum_{i=1}^{n} \left(\varepsilon_2^{(i)} x_1^{(i)} x_3^{(i)} + \frac{1}{2}\varepsilon_4^{(i)} x_1^{(i)} x_2^{(i)} + \frac{1}{2}\varepsilon_6^{(i)} x_2^{(i)} x_3^{(i)} \right) v^{(i)} \\ \boldsymbol{A}(2,2) = \sum_{i=1}^{n} \left(\left(\varepsilon_1^{(i)} + \varepsilon_3^{(i)}\right) x_1^{(i)} x_3^{(i)} - \frac{1}{2}\varepsilon_4^{(i)} x_1^{(i)} x_2^{(i)} - \frac{1}{2}\varepsilon_6^{(i)} x_2^{(i)} x_3^{(i)} \right) v^{(i)} \end{cases} \tag{2.23}$$

For this FE model, because the mesh is regular, $v^{(i)}$ is constant and equal to $\frac{V}{n}$, where V is the volume of the object and n is the number of elements. Therefore, $v^{(i)}$ can be taken out of the sum, and a sum in matrix $\boldsymbol{A}$, for instance, becomes

$$\sum_{i=1}^{n} \varepsilon_1^{(i)} v^{(i)} = \frac{V}{n} \sum_{i=1}^{n} \varepsilon_1^{(i)} = V\bar{\varepsilon}_1 \tag{2.24}$$

where $\bar{\varepsilon}_1$ denotes the arithmetic spatial average of ε_1 over the whole volume of the solid. Finally, the linear equation system (2.22) to solve can be written as follows

$$\begin{bmatrix} \bar{\varepsilon}_1 & \overline{\varepsilon_2 + \varepsilon_3} \\ \overline{\varepsilon_2 x_1 x_3} + \frac{1}{2}\overline{\varepsilon_4 x_1 x_2} + \frac{1}{2}\overline{\varepsilon_6 x_2 x_3} & \overline{(\varepsilon_1 + \varepsilon_3) x_1 x_3} - \frac{1}{2}\overline{\varepsilon_4 x_1 x_2} - \frac{1}{2}\overline{\varepsilon_6 x_2 x_3} \end{bmatrix} \begin{Bmatrix} Q_{11} \\ Q_{12} \end{Bmatrix} = \begin{Bmatrix} -\frac{F_{x_1}L}{V} \\ -\frac{F_{x_2}L^3}{V} \end{Bmatrix} \tag{2.25}$$

Young's modulus and Poisson's ratio can then be calculated through the relation (2.9). The identification results were obtained after introducing the simulated strain results into the Matlab program of the 3D VFM. The identified values were compared to the reference ones in Table 2.2 and the relative errors were calculated using the following equations

$$\begin{cases} error\_E = \left| \dfrac{E_{identified} - E_{reference}}{E_{reference}} \right| \times 100\% \\ error\_\nu = \left| \dfrac{\nu_{identified} - \nu_{reference}}{\nu_{reference}} \right| \times 100\% \end{cases} \tag{2.26}$$

It can be seen that the identified results are nearly exactly the same as the input values.

Table 2.2: Identification results for virtual fields 1 and 2.

Constitutive parameters	**Reference**	**Identified**	**Error**
Young's modulus *E* (GPa)	100.000	100.008	0.008%
Poisson's ratio *v*	0.300	0.300	0.0%

Two more complicated virtual fields using sine and exponential functions were also chosen for identification, which are

$$\textit{Virtual field 3:} \begin{cases} u_1^{*(3)} = \sin(x_1) \\ u_2^{*(3)} = 0 \\ u_3^{*(3)} = 0 \end{cases} \qquad \begin{cases} \varepsilon_1^{*(3)} = \cos(x_1) \\ \varepsilon_2^{*(3)} = 0 \\ \varepsilon_3^{*(3)} = 0 \\ \varepsilon_4^{*(3)} = 0 \\ \varepsilon_5^{*(3)} = 0 \\ \varepsilon_6^{*(3)} = 0 \end{cases} \tag{2.27}$$

$$\textit{Virtual field 4:} \begin{cases} u_1^{*(4)} = 0 \\ u_2^{*(4)} = x_1 e^{x_2} \\ u_3^{*(4)} = 0 \end{cases} \qquad \begin{cases} \varepsilon_1^{*(4)} = 0 \\ \varepsilon_2^{*(4)} = x_1 e^{x_2} \\ \varepsilon_3^{*(4)} = 0 \\ \varepsilon_4^{*(4)} = 0 \\ \varepsilon_5^{*(4)} = 0 \\ \varepsilon_6^{*(4)} = e^{x_2} \end{cases} \tag{2.28}$$

For these virtual fields, for $x_1 = 0$, all the virtual displacement components are zero, as required to filter out the bottom reaction forces. Using the same analysis as for virtual fields 1 and 2, another linear equation system can be formed for the identification of stiffness

components Q_{11} and Q_{12}. The elements of matrix $\boldsymbol{A}$ in the linear equation system for virtual fields 3 and 4 is equal to

$$\begin{cases} \boldsymbol{A}(1,1) = \sum_{i=1}^{n} \varepsilon_1^{(i)} \cos\left(x_1\right)^{(i)} v^{(i)} \\ \boldsymbol{A}(1,2) = \sum_{i=1}^{n} \left(\varepsilon_2^{(i)} + \varepsilon_3^{(i)}\right) \cos\left(x_1\right)^{(i)} v^{(i)} \\ \boldsymbol{A}(2,1) = \sum_{i=1}^{n} \left(\varepsilon_2^{(i)} x_1^{(i)} e^{x_2(i)} + \frac{1}{2} \varepsilon_6^{(i)} e^{x_2(i)} \right) v^{(i)} \\ \boldsymbol{A}(2,2) = \sum_{i=1}^{n} \left(\left(\varepsilon_1^{(i)} + \varepsilon_3^{(i)}\right) x_1^{(i)} e^{x_2(i)} - \frac{1}{2} \varepsilon_6^{(i)} e^{x_2(i)} \right) v^{(i)} \end{cases} \tag{2.29}$$

Thus, the linear equation system can be expressed as

$$\begin{bmatrix} \overline{\varepsilon_1 \cos\left(x_1\right)} & \overline{\left(\varepsilon_2 + \varepsilon_3\right) \cos\left(x_1\right)} \\ \overline{\varepsilon_2 x_1 e^{x_2}} + \frac{1}{2} \overline{\varepsilon_6 e^{x_2}} & \overline{\left(\varepsilon_1 + \varepsilon_3\right) x_1 e^{x_2}} - \frac{1}{2} \overline{\varepsilon_6 e^{x_2}} \end{bmatrix} \begin{Bmatrix} Q_{11} \\ Q_{12} \end{Bmatrix} = \begin{Bmatrix} -\dfrac{F_{x_1} \sin(L)}{V} \\ -\dfrac{F_{x_2} L e^{L}}{V} \end{Bmatrix} \tag{2.30}$$

The identification results are listed in Table 2.3. One can see that the identified E and ν are even closer to the input values.

Table 2.3: Identification results for virtual fields 3 and 4.

Constitutive parameters	**Reference**	**Identified**	**Error**
Young's modulus E (GPa)	100.000	100.000	0.0%
Poisson's ratio ν	0.300	0.300	0.0%

Another two virtual fields with higher degrees were selected, which are

$$\textit{Virtual field } 5\text{: } \begin{cases} u_1^{*(5)} = x_1^3 \\ u_2^{*(5)} = 0 \\ u_3^{*(5)} = 0 \end{cases} \qquad \begin{cases} \varepsilon_1^{*(5)} = 3x_1^2 \\ \varepsilon_2^{*(5)} = 0 \\ \varepsilon_3^{*(5)} = 0 \\ \varepsilon_4^{*(5)} = 0 \\ \varepsilon_5^{*(5)} = 0 \\ \varepsilon_6^{*(5)} = 0 \end{cases} \tag{2.31}$$

$$\textit{Virtual field } 6:\ \begin{cases} u_1^{*(6)} = 0 \\ u_2^{*(6)} = x_1^3 x_2^5 \\ u_3^{*(6)} = 0 \end{cases} \qquad \begin{cases} \varepsilon_1^{*(6)} = 0 \\ \varepsilon_2^{*(6)} = 5x_1^3 x_2^4 \\ \varepsilon_3^{*(6)} = 0 \\ \varepsilon_4^{*(6)} = 0 \\ \varepsilon_5^{*(6)} = 0 \\ \varepsilon_6^{*(6)} = 3x_1^2 x_2^5 \end{cases} \tag{2.32}$$

Matrix $\boldsymbol{A}$ is equal to

$$\begin{cases} \boldsymbol{A}(1,1) = \sum_{i=1}^{n} 3\varepsilon_1^{(i)} {x_1^{2}}^{(i)} v^{(i)} \\ \boldsymbol{A}(1,2) = \sum_{i=1}^{n} 3\left(\varepsilon_2^{(i)} + \varepsilon_3^{(i)}\right) {x_1^{2}}^{(i)} v^{(i)} \\ \boldsymbol{A}(2,1) = \sum_{i=1}^{n} \left(5\varepsilon_2^{(i)} x_1^{3(i)} x_2^{4(i)} + \frac{3}{2}\varepsilon_6^{(i)} {x_1^{2}}^{(i)} {x_2^{5}}^{(i)} \right) v^{(i)} \\ \boldsymbol{A}(2,2) = \sum_{i=1}^{n} \left(5\left(\varepsilon_1^{(i)} + \varepsilon_3^{(i)}\right) x_1^{3(i)} x_2^{4(i)} - \frac{3}{2}\varepsilon_6^{(i)} {x_1^{2}}^{(i)} {x_2^{5}}^{(i)} \right) v^{(i)} \end{cases} \tag{2.33}$$

Similarly, a linear equation system can be formed using the above two virtual fields, which writes

$$\begin{bmatrix} 3\overline{\varepsilon_1 x_1^2} & 3\overline{(\varepsilon_2 + \varepsilon_3) x_1^2} \\ 5\overline{\varepsilon_2 x_1^3 x_2^4} + \frac{3}{2}\overline{\varepsilon_6 x_1^2 x_2^5} & 5\overline{(\varepsilon_1 + \varepsilon_3) x_1^3 x_2^4} - \frac{3}{2}\overline{\varepsilon_6 x_1^2 x_2^5} \end{bmatrix} \begin{Bmatrix} Q_{11} \\ Q_{12} \end{Bmatrix} = \begin{Bmatrix} -\frac{F_{x_1} L^3}{V} \\ -\frac{F_{x_2} L^8}{V} \end{Bmatrix} \tag{2.34}$$

The identified E and ν are shown in Table 2.4. Although the results are very close to the references, larger error can be seen. It indicates that this set of virtual fields is less stable and more sensitive to noise. This is caused by the higher order polynomial functions which amplify the small numerical errors from the FE model.

Table 2.4: Identification results for virtual fields 5 and 6.

Constitutive parameters	**Reference**	**Identified**	**Error**
Young's modulus E (GPa)	100.000	103.416	3.42%
Poisson's ratio ν	0.300	0.294	2.07%

The above results show that the exact strain data from simulation can yield very good identification results. However, in practice strain measurements are corrupted by different sources of noise. This will degrade the identification accuracy. To illustrate this, Gaussian white noise with standard deviation of 10^{-4} was added to the exact strain data, which is tens of percent of the actual strain values. The strain data with noise were then used to extract E and ν using the previously defined sets of virtual fields 1 and 2, 3 and 4, 5 and 6, respectively. The results are given in Table 2.5. It can be seen that the error becomes much larger especially for the set of virtual fields 5 and 6. This is not surprising when looking at the condition number of matrix $\boldsymbol{A}$ in the linear equation system for each set of virtual fields, which is 907.07, 3.26, 1.03×10^{8}, for virtual fields 1 and 2, 3 and 4, 5 and 6, respectively. The reason for this is that error in $\boldsymbol{B}$ will introduce larger error in the solution $\boldsymbol{Q}$ when the condition number of $\boldsymbol{A}$ is larger. Thus, the choice of virtual fields can be critical and virtual fields that can minimize noise effect become highly desirable.

Table 2.5: Identification results for strain data polluted by Gaussian white noise with amplitude of 10^{-4}.

Constitutive parameters	**Reference**	**VFM 1, 2**	**VFM 3, 4**	**VFM 5, 6**
Young's modulus E (GPa)	100.000	102.026	98.535	119.066
Poisson's ratio ν	0.300	0.294	0.298	0.256

2.4 Special virtual fields

Due to the fact that the principle of virtual work is valid for any continuous and differentiable virtual displacement field, there are infinite choices for such virtual fields. Therefore, it is desirable to add some constraints so that better choices of the virtual fields can be reached.

As stated in section 2.3.2, the condition number of $\boldsymbol{A}$ in the linear equation (2.15) generally indicates how inaccurate the solution $\boldsymbol{Q}$ will be after inversion of the linear system. If the square matrix $\boldsymbol{A}$ is equal to the identity matrix $\boldsymbol{I}$, then its condition number is equal to one. This condition number indicates that the matrix $\boldsymbol{A}$ is the best conditioned and the solution $\boldsymbol{Q}$ can be less sensitive to the errors in $\boldsymbol{B}$. In addition, the problem of independence of the virtual fields can be solved when the matrix $\boldsymbol{A}$ is equal to the identity matrix $\boldsymbol{I}$. Such

virtual fields are referred to as special virtual fields as stated by Pierron *et al* in [67]. In this case

$$\boldsymbol{Q} = \boldsymbol{A}^{-1}\boldsymbol{B} = \boldsymbol{I}^{-1}\boldsymbol{B} = \boldsymbol{B} \tag{2.35}$$

These special virtual fields can be obtained by defining the diagonal components of $\boldsymbol{A}$ as one and the other components as zero. In the isotropic case for instance, $\boldsymbol{A}(1,1) = 1$, $\boldsymbol{A}(1,2) = 0$ for the first special virtual field $\boldsymbol{u}^{*(1)}$ and $\boldsymbol{A}(2,1) = 0$, $\boldsymbol{A}(2,2) = 1$ for the second special virtual field $\boldsymbol{u}^{*(2)}$. Analogously, the special virtual fields for the orthotropic case can be obtained by defining the virtual fields so that nine diagonal components are equal to one and all the others to zero. The special virtual fields can lead to a straightforward solution.

2.5 Piecewise virtual fields

Virtual fields can be constructed using various types of functions such as polynomials, sine functions or piecewise functions. Similar to the approach that is used to construct the actual displacement field in the finite element method, the virtual displacement of a point in an element can be expressed as a function of the virtual displacement at the nodes of this element as

$$\boldsymbol{u}^{*} = \boldsymbol{N}\boldsymbol{u}^{*(e)} \tag{2.36}$$

where $\boldsymbol{u}^{*}$ is a vector containing the virtual displacements u_1^*, u_2^* and u_3^* of any point within element (e). $\boldsymbol{N}$ is the matrix containing the shape functions serving as interpolation functions, and $\boldsymbol{u}^{*(e)}$ is the vector of nodal virtual displacements of given element (e) in the defined mesh. For the 3D case here, an 8-noded brick element was selected, which is shown in Fig 2.2. The shape functions are

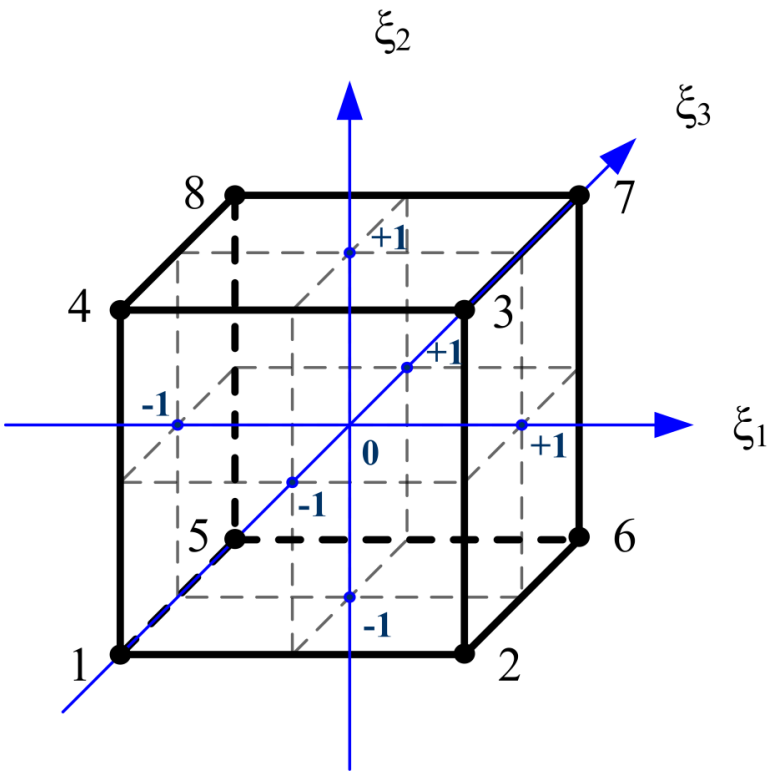

Fig 2. 2 Local coordinate system for the 8-noded brick element

$$\begin{cases} N^{(1)} = \frac{1}{8}(1-\xi_1)(1-\xi_2)(1-\xi_3) \\ N^{(2)} = \frac{1}{8}(1+\xi_1)(1-\xi_2)(1-\xi_3) \\ N^{(3)} = \frac{1}{8}(1+\xi_1)(1+\xi_2)(1-\xi_3) \\ N^{(4)} = \frac{1}{8}(1-\xi_1)(1+\xi_2)(1-\xi_3) \\ N^{(5)} = \frac{1}{8}(1-\xi_1)(1-\xi_2)(1+\xi_3) \\ N^{(6)} = \frac{1}{8}(1+\xi_1)(1-\xi_2)(1+\xi_3) \\ N^{(7)} = \frac{1}{8}(1+\xi_1)(1+\xi_2)(1+\xi_3) \\ N^{(8)} = \frac{1}{8}(1-\xi_1)(1+\xi_2)(1+\xi_3) \end{cases} \tag{2.37}$$

where (ξ_1, ξ_2, ξ_3) are the parametric coordinates of a point in the reference element. For an 8-noded element, each node has three degrees of freedom. Thus, $\boldsymbol{u}^{*(e)}$ contains 24 components and $\boldsymbol{N}$ is a 3×24 matrix

$$\boldsymbol{u}^{*}:\begin{Bmatrix} u_1^{*} \\ u_2^{*} \\ u_3^{*} \end{Bmatrix} \tag{2.38}$$

$$\boldsymbol{N}:\begin{bmatrix} N^{(1)} & 0 & 0 & N^{(2)} & 0 & 0 & \cdots & N^{(8)} & 0 & 0 \\ 0 & N^{(1)} & 0 & 0 & N^{(2)} & 0 & \cdots & 0 & N^{(8)} & 0 \\ 0 & 0 & N^{(1)} & 0 & 0 & N^{(2)} & \cdots & 0 & 0 & N^{(8)} \end{bmatrix} \tag{2.39}$$

$$\boldsymbol{u}^{*(e)}:\begin{Bmatrix} u_1^{*(1)} \\ u_2^{*(1)} \\ u_3^{*(1)} \\ \vdots \\ u_1^{*(8)} \\ u_2^{*(8)} \\ u_3^{*(8)} \end{Bmatrix} \tag{2.40}$$

Virtual strains in the element can be calculated using the derivatives of the virtual displacement components and expressed as

$$\boldsymbol{\varepsilon}^{*} = \boldsymbol{S}^{(e)}\boldsymbol{u}^{*(e)} \tag{2.41}$$

where $\boldsymbol{\varepsilon}^{*}$ is a vector containing the six virtual strain components of any point within the virtual element (e). $\boldsymbol{S}^{(e)}$ is a 6×24 matrix which contains the partial derivatives of the shape functions.

$$\boldsymbol{\varepsilon}^{*}:\begin{Bmatrix} \varepsilon_1^{*} \\ \varepsilon_2^{*} \\ \varepsilon_3^{*} \\ \varepsilon_4^{*} \\ \varepsilon_5^{*} \\ \varepsilon_6^{*} \end{Bmatrix} \tag{2.42}$$

$$\boldsymbol{S}^{(e)}:\begin{bmatrix} \frac{\partial N^{(1)}}{\partial x_1} & 0 & 0 & \frac{\partial N^{(2)}}{\partial x_1} & 0 & 0 & \cdots & \frac{\partial N^{(8)}}{\partial x_1} & 0 & 0 \\ 0 & \frac{\partial N^{(1)}}{\partial x_2} & 0 & 0 & \frac{\partial N^{(2)}}{\partial x_2} & 0 & \cdots & 0 & \frac{\partial N^{(8)}}{\partial x_2} & 0 \\ 0 & 0 & \frac{\partial N^{(1)}}{\partial x_3} & 0 & 0 & \frac{\partial N^{(2)}}{\partial x_3} & \cdots & 0 & 0 & \frac{\partial N^{(8)}}{\partial x_3} \\ 0 & \frac{\partial N^{(1)}}{\partial x_3} & \frac{\partial N^{(1)}}{\partial x_2} & 0 & \frac{\partial N^{(2)}}{\partial x_3} & \frac{\partial N^{(2)}}{\partial x_2} & \cdots & 0 & \frac{\partial N^{(8)}}{\partial x_3} & \frac{\partial N^{(8)}}{\partial x_2} \\ \frac{\partial N^{(1)}}{\partial x_3} & 0 & \frac{\partial N^{(1)}}{\partial x_1} & \frac{\partial N^{(2)}}{\partial x_3} & 0 & \frac{\partial N^{(2)}}{\partial x_1} & \cdots & \frac{\partial N^{(8)}}{\partial x_3} & 0 & \frac{\partial N^{(8)}}{\partial x_1} \\ \frac{\partial N^{(1)}}{\partial x_2} & \frac{\partial N^{(1)}}{\partial x_1} & 0 & \frac{\partial N^{(2)}}{\partial x_2} & \frac{\partial N^{(2)}}{\partial x_1} & 0 & \cdots & \frac{\partial N^{(8)}}{\partial x_2} & \frac{\partial N^{(8)}}{\partial x_1} & 0 \end{bmatrix} \tag{2.43}$$

Results for each element are assembled, and the global virtual strains can be calculated by

$$\boldsymbol{\varepsilon}^{*} = \boldsymbol{S}\boldsymbol{u}^{*(g)} \tag{2.44}$$

where $\boldsymbol{S}$ is the global matrix assembled from the elemental $\boldsymbol{S}^{(e)}$ matrices of each element and expressed in the global coordinate system. $\boldsymbol{u}^{*(g)}$ is the global vector that contains the virtual displacements at all the virtual nodes of the body.

For both isotropic and orthotropic elasticity, there are 12 different types of integrals for the internal virtual work as shown in the equilibrium equations (2.10) and (2.11). Based on the above discussion, these integrals can be approximated by discrete sums. Take $\int_V \varepsilon_1 \varepsilon_1^* dV$ for example

$$\int_V \varepsilon_1 \varepsilon_1^* dV \approx \sum_{i=1}^{n} \varepsilon_1\left(x_1^{(i)}, x_2^{(i)}, x_3^{(i)}\right) \boldsymbol{S}_1\left(x_1^{(i)}, x_2^{(i)}, x_3^{(i)}\right) \boldsymbol{u}^{*(g)} v^{(i)} \tag{2.45}$$

where n is the number of measurement points. $\boldsymbol{S}_1$ is a vector that contains the components of the first line of the global matrix $\boldsymbol{S}$. $\left(x_1^{(i)}, x_2^{(i)}, x_3^{(i)}\right)$ is the coordinate of measurement point (*i*). Similarly, other integrals can also be calculated.

Compared to other forms of virtual fields expansions, piecewise virtual fields have the main advantage of flexibility. When specific virtual displacements are required in certain areas for the purposes of simple calculation of the external virtual work or meeting the

requirements of different boundary conditions, these conditions are more easily expressed with piecewise virtual fields.

2.6 Virtual fields minimizing noise effect

Due to the noise and measurement uncertainties, the measured strain values are different from the actual ones. This can influence the identification results depending on the sensitivity of the identified parameters to the noise. In addition, as there is an infinity of special virtual fields that can be chosen to identify constitutive parameters, some extra constraints need to be added to enable a better identification. In this case, the virtual fields that minimize the effect of noise on the identification results would be useful. The procedure for developing such virtual fields in 2D has been presented by Avril *et al* in [111]. In this section, this approach is extended to 3D. In reality, the noise structure of the measured strain is very complex considering the interpolation errors, speckle decorrelation, change of illumination, possible smoothing, *etc*. For the sake of simplicity, a simple zero-mean Gaussian noise model with standard deviation of γ is assumed here. The measured strain thus is composed of the actual strain plus the noise. Since the principle of virtual work is only rigorously true for the actual strain values, the expression of the principle of virtual work in equation (2.35) with special virtual fields is only verified when the noise is subtracted from the strain measurements. Therefore, a matrix indicating the deviation from the actual values due to noise is subtracted from the identity matrix in equation (2.35), and equation (2.35) becomes

$$(\boldsymbol{I} - \boldsymbol{D})\boldsymbol{Q} = \boldsymbol{B} \tag{2.46}$$

where $\boldsymbol{D}$ is the matrix indicating the deviation from the actual values due to noise. Thus, the identified stiffness is

$$\boldsymbol{Q} = \boldsymbol{B} + \boldsymbol{D}\boldsymbol{Q} \tag{2.47}$$

If noise exists but is not considered, the approximate $\boldsymbol{Q}$ is identified and written as

$$\boldsymbol{Q}^{app} = \boldsymbol{B} \tag{2.48}$$

An important assumption is that the amplitude of noise γ is negligible compared to the L^2 norm of the strain components, $\gamma << \min(\|\varepsilon_i\|)$.Under this assumption, equation (2.47) can be approximated as

$$\boldsymbol{Q} \approx \boldsymbol{Q}^{app} + \boldsymbol{DQ}^{app} \tag{2.49}$$

Therefore, the variance of $\boldsymbol{Q}$ can be written as follows

$$V(\boldsymbol{Q}) = E\left((\boldsymbol{Q} - E(\boldsymbol{Q}))^2\right) = E\left(\left(\boldsymbol{DQ}^{app}\right)^2\right) \tag{2.50}$$

where $E(X)$ is the mathematical expectation of X, and $\boldsymbol{Q}^{app}$ is assumed to be equal to the mathematical expectation of $\boldsymbol{Q}$.

For the 3D isotropic case, the variances of Q_{11} and Q_{12} are as follows

$$V(Q_{(i)}) = \gamma^2\left[\left(Q_{11}^{app}\right)^2\left(\int_V \left(\varepsilon_1^{*(i)}\right)^2 dV + \int_V \left(\varepsilon_2^{*(i)}\right)^2 dV + \int_V \left(\varepsilon_3^{*(i)}\right)^2 dV + \frac{1}{4}\int_V \left(\varepsilon_4{}^{(i)}\right)^2 dV + \right.\right.$$

$$\left.\frac{1}{4}\int_V \left(\varepsilon_5{}^{(i)}\right)^2 dV + \frac{1}{4}\int_V \left(\varepsilon_6{}^{(i)}\right)^2 dV\right) + 2Q_{11}^{app}Q_{12}^{app}\left(2\left(\int_V \varepsilon_1^{*(i)}\varepsilon_2^{*(i)} dV + \int_V \varepsilon_1^{*(i)}\varepsilon_3^{*(i)} dV + \int_V \varepsilon_2^{*(i)}\varepsilon_3^{*(i)} dV\right) - \right.$$

$$\left.\frac{1}{4}\int_V \left(\varepsilon_4{}^{(i)}\right)^2 dV - \frac{1}{4}\int_V \left(\varepsilon_5{}^{(i)}\right)^2 dV - \frac{1}{4}\int_V \left(\varepsilon_6{}^{(i)}\right)^2 dV\right) + \left(Q_{12}^{app}\right)^2\left(2\left(\int_V \left(\varepsilon_1^{*(i)}\right)^2 dV + \int_V \left(\varepsilon_2^{*(i)}\right)^2 dV + \right.\right.$$

$$\left.\int_V \left(\varepsilon_3^{*(i)}\right)^2 dV + \int_V \varepsilon_1^{*(i)}\varepsilon_2^{*(i)} dV + \int_V \varepsilon_1^{*(i)}\varepsilon_3^{*(i)} dV + \int_V \varepsilon_2^{*(i)}\varepsilon_3^{*(i)} dV\right) + \frac{1}{4}\int_V \left(\varepsilon_4{}^{(i)}\right)^2 dV + \frac{1}{4}\int_V \left(\varepsilon_5{}^{(i)}\right)^2 dV + $$

$$\left.\left.\frac{1}{4}\int_V \left(\varepsilon_6{}^{(i)}\right)^2 dV\right)\right] \tag{2.51}$$

when i=1, $Q_{(1)}$ represents Q_{11}, when i=2, $Q_{(2)}$ represents Q_{12}.

For the orthotropic case, the variances of the nine stiffness components are as follows

$$V(Q_{(i)}) = \gamma^2 \Bigg[\left(\left(Q_{11}^{app}\right)^2 + \left(Q_{12}^{app}\right)^2 + \left(Q_{13}^{app}\right)^2 \right) \int_V \left(\varepsilon_1^{*(i)}\right)^2 dV + \left(\left(Q_{22}^{app}\right)^2 + \left(Q_{12}^{app}\right)^2 + \left(Q_{23}^{app}\right)^2 \right) \int_V \left(\varepsilon_2^{*(i)}\right)^2 dV +$$

$$\left(\left(Q_{33}^{app}\right)^2 + \left(Q_{13}^{app}\right)^2 + \left(Q_{23}^{app}\right)^2 \right) \int_V \left(\varepsilon_3^{*(i)}\right)^2 dV + \left(Q_{44}^{app}\right)^2 \int_V \left(\varepsilon_4^{*(i)}\right)^2 dV + \left(Q_{55}^{app}\right)^2 \int_V \left(\varepsilon_5^{*(i)}\right)^2 dV +$$

$$\left(Q_{66}^{app}\right)^2 \int_V \left(\varepsilon_6^{*(i)}\right)^2 dV + 2\left(Q_{11}^{app}Q_{12}^{app} + Q_{22}^{app}Q_{12}^{app} + Q_{13}^{app}Q_{23}^{app}\right) \int_V \varepsilon_1^{*(i)} \varepsilon_2^{*(i)} dV +$$

$$2\left(Q_{11}^{app}Q_{13}^{app} + Q_{33}^{app}Q_{13}^{app} + Q_{12}^{app}Q_{23}^{app}\right) \int_V \varepsilon_1^{*(i)} \varepsilon_3^{*(i)} dV +$$

$$2\left(Q_{22}^{app}Q_{23}^{app} + Q_{33}^{app}Q_{23}^{app} + Q_{12}^{app}Q_{13}^{app}\right) \int_V \varepsilon_2^{*(i)} \varepsilon_3^{*(i)} dV \Bigg]$$

(2.52)

where i=1:9, and $Q_{(1)}$, $Q_{(2)}$, $Q_{(3)}$, $Q_{(4)}$, $Q_{(5)}$, $Q_{(6)}$, $Q_{(7)}$, $Q_{(8)}$, $Q_{(9)}$ represent Q_{11}, Q_{22}, Q_{33}, Q_{23}, Q_{13}, Q_{12}, Q_{44}, Q_{55}, Q_{66}, respectively.

Due to the discrete nature of the measurement, the integrals above in functions (2.51) and (2.52) must be approximated by discrete sums. Therefore, for the isotropic case, equation (2.51) becomes

$$V(Q_{(i)}) = \gamma^2 \left(\frac{V}{n}\right)^2 \Bigg[\left(Q_{11}^{app}\right)^2 \left(\sum_{k=1}^{n} \left(\varepsilon_1^{*(i)}(k)\right)^2 + \sum_{k=1}^{n} \left(\varepsilon_2^{*(i)}(k)\right)^2 + \sum_{k=1}^{n} \left(\varepsilon_3^{*(i)}(k)\right)^2 + \frac{1}{4}\sum_{k=1}^{n} \left(\varepsilon_4^{*(i)}(k)\right)^2 + \right.$$

$$\left. \frac{1}{4}\sum_{k=1}^{n} \left(\varepsilon_5^{*(i)}(k)\right)^2 + \frac{1}{4}\sum_{k=1}^{n} \left(\varepsilon_6^{*(i)}(k)\right)^2 \right) + 2Q_{11}^{app}Q_{12}^{app} \left(2\left(\sum_{k=1}^{n} \varepsilon_1^{*(i)}(k)\varepsilon_2^{*(i)}(k) + \sum_{k=1}^{n} \varepsilon_1^{*(i)}(k)\varepsilon_3^{*(i)}(k) + \right. \right.$$

$$\left. \sum_{k=1}^{n} \varepsilon_2^{*(i)}(k)\varepsilon_3^{*(i)}(k) \right) - \frac{1}{4}\sum_{k=1}^{n} \left(\varepsilon_4^{*(i)}(k)\right)^2 - \frac{1}{4}\sum_{k=1}^{n} \left(\varepsilon_5^{*(i)}(k)\right)^2 - \frac{1}{4}\sum_{k=1}^{n} \left(\varepsilon_6^{*(i)}(k)\right)^2 \Bigg) +$$

$$\left(Q_{12}^{app}\right)^2 \Bigg(2\Bigg(\sum_{k=1}^{n} \left(\varepsilon_1^{*(i)}(k)\right)^2 + \sum_{k=1}^{n} \left(\varepsilon_2^{*(i)}(k)\right)^2 + \sum_{k=1}^{n} \left(\varepsilon_3^{*(i)}(k)\right)^2 + \sum_{k=1}^{n} \varepsilon_1^{*(i)}(k)\varepsilon_2^{*(i)}(k) +$$

$$\sum_{k=1}^{n} \varepsilon_1^{*(i)}(k)\varepsilon_3^{*(i)}(k) + \sum_{k=1}^{n} \varepsilon_2^{*(i)}(k)\varepsilon_3^{*(i)}(k) \Bigg) + \frac{1}{4}\sum_{k=1}^{n} \left(\varepsilon_4^{*(i)}(k)\right)^2 + \frac{1}{4}\sum_{k=1}^{n} \left(\varepsilon_5^{*(i)}(k)\right)^2 +$$

$$\left. \frac{1}{4}\sum_{k=1}^{n} \left(\varepsilon_6^{*(i)}(k)\right)^2 \Bigg) \Bigg]$$

(2.53)

where k is the number of measurement points.

For the orthotropic case, equation (2.52) now becomes

$$
\begin{aligned}
V(Q_{(i)}) = \gamma^2\left(\frac{V}{n}\right)^2\Bigg[&\left(\left(Q_{11}^{app}\right)^2+\left(Q_{12}^{app}\right)^2+\left(Q_{13}^{app}\right)^2\right)\sum_{k=1}^{n}\left(\varepsilon_1^{*(i)}(k)\right)^2+\\
&\left(\left(Q_{22}^{app}\right)^2+\left(Q_{12}^{app}\right)^2+\left(Q_{23}^{app}\right)^2\right)\sum_{k=1}^{n}\left(\varepsilon_2^{*(i)}(k)\right)^2+\\
&\left(\left(Q_{33}^{app}\right)^2+\left(Q_{13}^{app}\right)^2+\left(Q_{23}^{app}\right)^2\right)\sum_{k=1}^{n}\left(\varepsilon_3^{*(i)}(k)\right)^2+\left(Q_{44}^{app}\right)^2\sum_{k=1}^{n}\left(\varepsilon_4^{*(i)}(k)\right)^2+\\
&\left(Q_{55}^{app}\right)^2\sum_{k=1}^{n}\left(\varepsilon_5^{*(i)}(k)\right)^2+\left(Q_{66}^{app}\right)^2\sum_{k=1}^{n}\left(\varepsilon_6^{*(i)}(k)\right)^2+\\
&2\left(Q_{11}^{app}Q_{12}^{app}+Q_{22}^{app}Q_{12}^{app}+Q_{13}^{app}Q_{23}^{app}\right)\sum_{k=1}^{n}\varepsilon_1^{*(i)}(k)\varepsilon_2^{*(i)}(k)+\\
&2\left(Q_{11}^{app}Q_{13}^{app}+Q_{33}^{app}Q_{13}^{app}+Q_{12}^{app}Q_{23}^{app}\right)\sum_{k=1}^{n}\varepsilon_1^{*(i)}(k)\varepsilon_3^{*(i)}(k)+\\
&2\left(Q_{22}^{app}Q_{23}^{app}+Q_{33}^{app}Q_{23}^{app}+Q_{12}^{app}Q_{13}^{app}\right)\sum_{k=1}^{n}\varepsilon_2^{*(i)}(k)\varepsilon_3^{*(i)}(k)\Bigg]
\end{aligned}
\tag{2.54}
$$

The variances of the stiffness components can be written as

$$V(Q_{(i)}) = \gamma^2\left(\eta^{(i)}\right)^2 \tag{2.55}$$

Since the $\left(\eta^{(i)}\right)^2$ depend on the choice of virtual fields that are chosen to extract the stiffness components Q_{ij}, minimizing the coefficients $\left(\eta^{(i)}\right)^2$ will lead to the optimal choice of virtual fields in terms of stability with respect to noise.. Here, $\left(\eta^{(i)}\right)^2$ can be rewritten as equation (2.56).

$$\left(\eta^{(i)}\right)^2 = \frac{1}{2}\boldsymbol{Y}^{*(i)T}\boldsymbol{H}\boldsymbol{Y}^{*(i)} \tag{2.56}$$

where $\boldsymbol{Y}^{*(i)}$ is the vector containing all the nodal virtual displacements and $\boldsymbol{H}$ is a square matrix obtained by rewriting equation (2.53) (for the isotropic case) or equation (2.54) (for the orthotropic case) after introducing the definition of virtual strain components given in equation (2.44). It has been proved in reference [67] that $\left(\eta^{(i)}\right)^2$ is strictly convex and exhibits a unique minimum. The best choice of the virtual displacements $\boldsymbol{Y}^{*(i)}$ is the solution of a

minimization problem. The minimization must be performed under constraints, which are the boundary conditions to eliminate the contribution of reaction forces at the supports (KA) and the special conditions to directly provide the constitutive parameters. These two types of constraints can be merged and presented in a more compact form

$$\boldsymbol{A}\boldsymbol{Y}^{*(i)} = \boldsymbol{z}^{(i)} \tag{2.57}$$

where $\boldsymbol{z}^{(i)}$ is a vector containing only zeros apart from one component which is equal to 1, and the location of this "1" component depends on *i*. This is the 'speciality' condition, one for each virtual field associated to each stiffness component to identify.

Using Lagrangian multipliers this constrained optimization problem becomes

$$\boldsymbol{\Lambda}^{(i)} = \frac{1}{2}\boldsymbol{Y}^{*(i)^T}\boldsymbol{H}\boldsymbol{Y}^{*(i)} + \boldsymbol{\lambda}^{(i)^T}\left(\boldsymbol{A}\boldsymbol{Y}^{*(i)} - \boldsymbol{z}^{(i)}\right) \tag{2.58}$$

Minimizing $\boldsymbol{\Lambda}^{(i)}$ leads to the linear system

$$\begin{bmatrix} \boldsymbol{H} & \boldsymbol{A}^T \\ \boldsymbol{A} & \boldsymbol{0} \end{bmatrix} \begin{Bmatrix} \boldsymbol{Y}^{(i)} \\ \boldsymbol{\lambda}^{(i)} \end{Bmatrix} = \begin{Bmatrix} \boldsymbol{0} \\ \boldsymbol{z}^{(i)} \end{Bmatrix} \tag{2.59}$$

Since the sought quantities $Q_{(i)}$ are unknown and involved in the $\left(\eta^{(i)}\right)^2$, the linear system is solved iteratively and a random first set of $Q_{(i)}$ is chosen to start the iteration. The whole algorithm was implemented using the MATLAB® program. The finite element model described in section 2.3.1 was used to validate the above described identification approach by providing exact strain data.

2.7 Verification of the 3D piecewise optimized virtual fields method

2.7.1 Finite element models for validation

In addition to the isotropic model of section 2.3.1, an orthotropic model was developed to study the performance of the 3D piecewise optimized VFM in identifying the nine orthotropic stiffness components. The dimensions, the applied force, the type and number of elements are all the same as for the isotropic model, just the material properties differ. The nine input stiffness components for the orthotropic model are shown in Table 2.6, which were chosen somewhat arbitrarily.

Table 2.6: Input stiffness components for orthotropic elasticity.

Q_{11} (GPa)	Q_{22} (GPa)	Q_{33} (GPa)	Q_{12} (GPa)	Q_{13} (GPa)	Q_{23} (GPa)	Q_{44} (GPa)	Q_{55} (GPa)	Q_{66} (GPa)
90.0	50.0	70.0	29.0	38.0	12.0	20.0	25.0	15.0

2.7.2 Identification results

A mesh with 3×3×3 virtual elements was considered here. As illustrated in Fig 2.3, it has 64 nodes and 192 degrees of freedom. In this case, the vector of global nodal virtual displacement $\boldsymbol{Y}^*$ is

$$\boldsymbol{Y}^* : \left\{ u_1^{*(1)} \quad u_2^{*(1)} \quad u_3^{*(1)} \quad u_1^{*(2)} \quad u_2^{*(2)} \quad u_3^{*(2)} \quad \cdots\cdots \quad u_1^{*(64)} \quad u_2^{*(64)} \quad u_3^{*(64)} \right\}^T \tag{2.60}$$

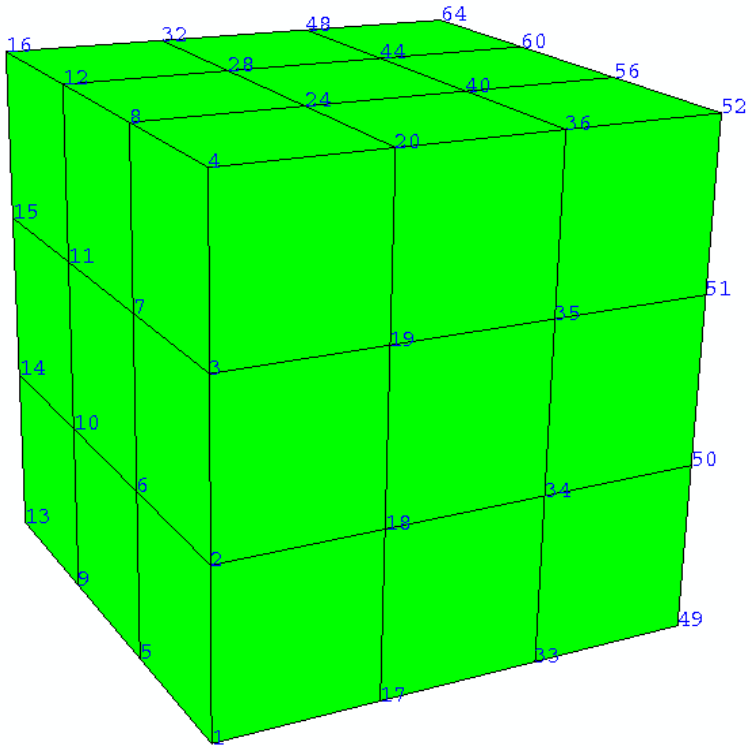

Fig 2.3: Schematic of the 3D virtual mesh.

For this model, the traction at the fixed bottom is unknown. Therefore, boundary conditions must be added to eliminate their contribution to the external virtual work. This can be easily achieved by setting all virtual degrees of freedom at the bottom nodes to zero.

Table 2.7 and Table 2.8 list the identification results for the isotropic and orthotropic case, respectively.

It can be seen that the identified values are nearly the same as the theoretical input values. For both isotropic and orthotropic cases, the errors of all the stiffness components are much smaller than 1%.

Table 2.7: Identification results for isotropic elasticity using 3D piecewise optimized VFM.

Constitutive parameters	**Reference**	**Identified**	**Error**
Young's modulus E (GPa)	100.0	100.053	0.053%
Poisson's ratio v	0.3	0.3003	0.1%

Table 2.8: Identification results for orthotropic elasticity using 3D piecewise optimized VFM.

Constitutive parameters	**Reference**	**Identified**	**Error**
Q_{11} (GPa)	90.0	90.057	0.063%
Q_{22} (GPa)	50.0	50.088	0.176%
Q_{33} (GPa)	70.0	70.131	0.187%
Q_{12} (GPa)	29.0	29.026	0.090%
Q_{13} (GPa)	38.0	38.031	0.082%
Q_{23} (GPa)	12.0	12.026	0.217%
Q_{44} (GPa)	20.0	20.006	0.030%
Q_{55} (GPa)	25.0	25.006	0.024%
Q_{66} (GPa)	15.0	15.007	0.047%

To verify that the 3D virtual fields are the truly optimized virtual fields, the sensitivity to noise of each identified stiffness component has been studied. This was implemented by studying the coefficients of variation of each stiffness component for strain noises with increasing standard deviations. The coefficient of variation (CV) is defined in equation (2.61), which represents the ratio of the standard deviation $\eta^{(i)}\gamma$ to the identified stiffness component $Q_{(i)}$ for a strain noise with standard deviation γ.

$$CV\left(Q_{(i)}\right)=\frac{\eta^{(i)}}{Q_{(i)}}\gamma \tag{2.61}$$

If the predicted $\frac{\eta^{(i)}}{Q_{(i)}}$ is equal to the theoretical mean $\frac{\eta^{(i)}}{Q_{(i)}}$ calculated by adding noise to the strain data and working out the scatter of the identified distributions, the virtual fields are confirmed to be the optimized ones. To validate this, a range of Gaussian white noise was added to the simulated strain data, of which the standard deviation γ changes from 5×10^{-6} to 1×10^{-4} with an increment of 5×10^{-6}. For each value of γ, 30 identifications were run and distributions of stiffness components identified. To verify equation (2.61), coefficients of variations for different stiffness components as a function of γ were plotted. The points were fitted by a line to compute the slope which can then be compared to the theoretical value of $\frac{\eta^{(i)}}{Q_{(i)}}$. For the isotropic case, the coefficients of variation for the two stiffness components are plotted as a function of γ in Fig 2.4. It can be seen that the *CV* of Q_{11} is smaller than that of Q_{12}, which indicates that Q_{11} is more stable than Q_{12} as expected as Poisson's ratio has a smaller influence on the actual material deformation. The points are fitted by a line and the fitted slope $\frac{\eta^{(i)}}{Q_{(i)}}$ are compared with the theoretical values in Table 2.9. The results show that the fitted values match the theoretical values. When the noise amplitude increases to a large value like 1×10^{-4}, which is tens of percent of the actual strain values, the fit is less adequate. This is not surprising because such a large noise amplitude does not fit the precondition that the noise amplitude should be small compared with the strain values.

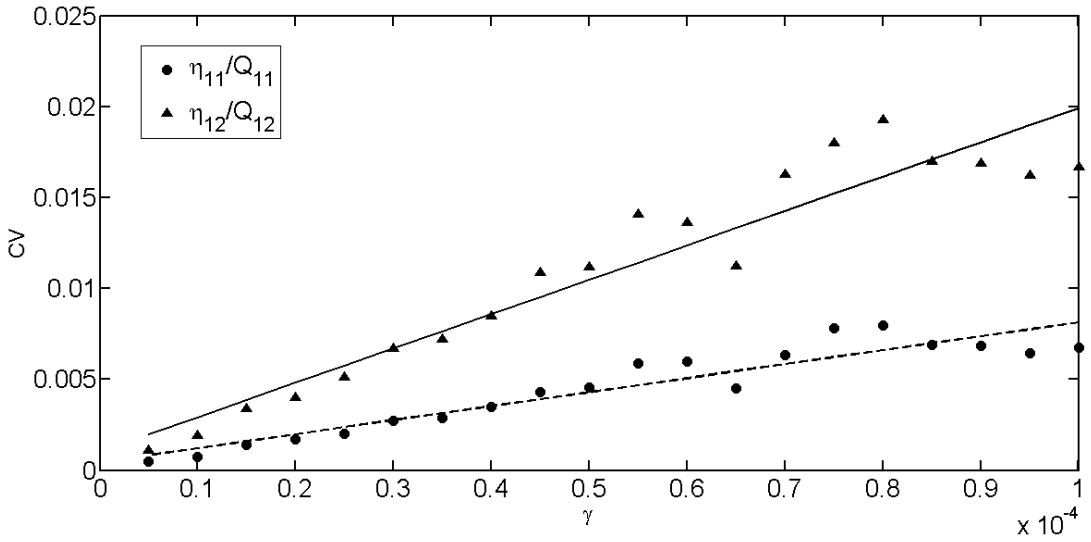

Fig 2.4: Coefficients of variation of the different stiffness components as a function of γ for isotropic elasticity, 3D piecewise optimized VFM.

Table 2.9: Comparison of the fitted slope $\frac{\eta^{(i)}}{Q_{(i)}}$ with the theoretical values for isotropic elasticity, 3D piecewise optimized VFM.

	Fitted	**Theoretical**
η_{11}/Q_{11}	77.0	81.4
η_{12}/Q_{12}	189	198

The same procedure was carried out for the orthotropic case, and the coefficients of variation for the nine stiffness components are plotted as a function of γ in Fig 2.5. As can be seen from Fig 2.5, Q_{44}, Q_{55} and Q_{66} are the most stable stiffness components and they all have very small coefficients of variation. Q_{11}, Q_{22} and Q_{33} have intermediate coefficients of variation, while the last three components Q_{23}, Q_{12} and Q_{13} have the largest scatter and are the most sensitive to noise.

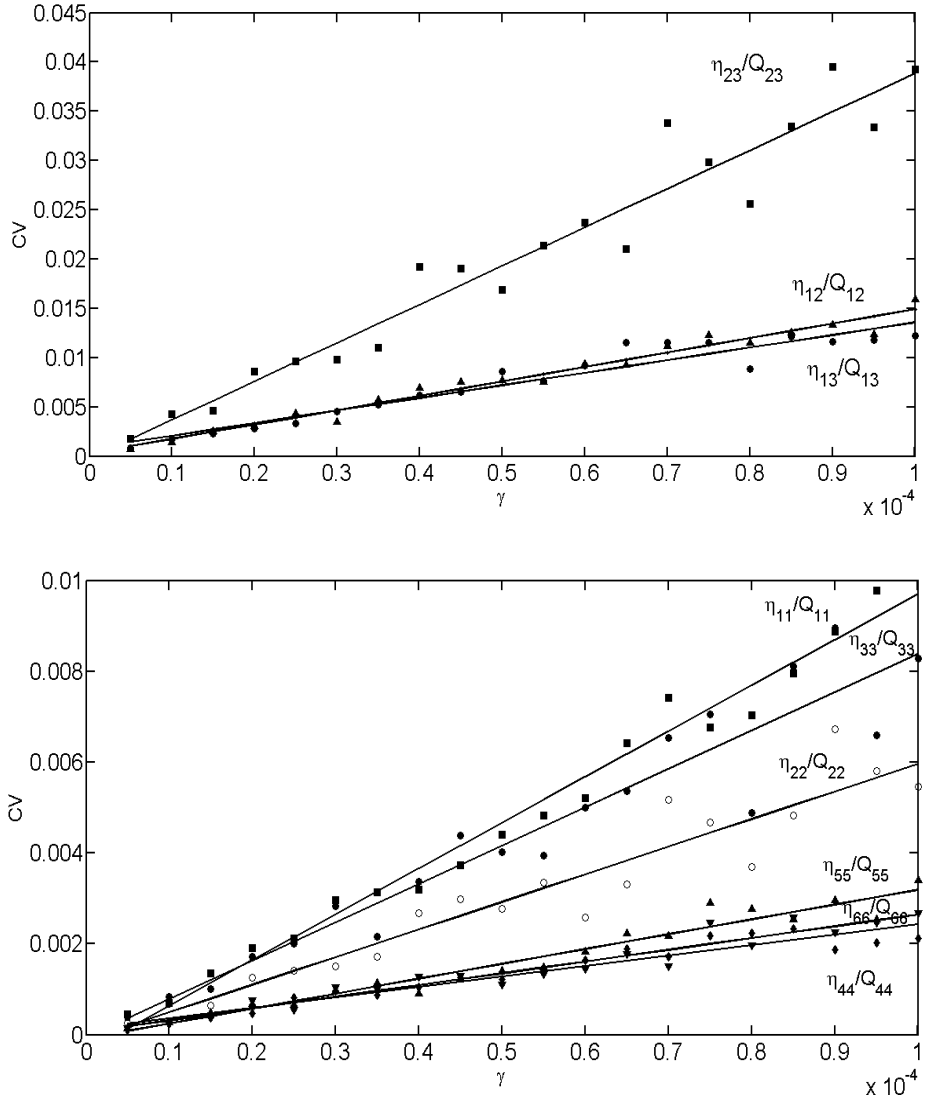

Fig 2.5: Coefficients of variation of the different stiffness components plotted as a function of γ for orthotropic elasticity, 3D piecewise optimized VFM.

The fitted slope $\frac{\eta^{(i)}}{Q_{(i)}}$ for the nine stiffness components are compared with theoretical values in Table 2.10. Similarly to the isotropic case, it can be seen that the fitted values match the theoretical values.

The above results validate that the 3D piecewise optimized VFM can extract the constitutive parameters successfully for both isotropic and orthotropic elasticity even the noise amplitude is relatively large. This is the first time that optimized virtual fields have been generated for a 3D problem.

Table 2.10: Comparison of the fitted slope $\frac{\eta^{(i)}}{Q_{(i)}}$ with the theoretical values for orthotropic elasticity, 3D piecewise optimized VFM.

	Fitted	**Theoretical**
η_{11}/Q_{11}	100	88.6
η_{22}/Q_{22}	60.8	57.7
η_{33}/Q_{33}	84.5	80.9
η_{12}/Q_{12}	146	147
η_{13}/Q_{13}	128	151
η_{23}/Q_{23}	391	384
η_{44}/Q_{44}	23.0	25.6
η_{55}/Q_{55}	32.7	30.9
η_{66}/Q_{66}	26.0	27.2

2.8 Benchmarking optimized against manual virtual fields

In this section, the 3D manually defined VFM developed in section 2.3 is compared to the 3D piecewise optimized VFM. The idea is to evaluate the performance of both methods in retrieving Young's modulus and Poisson's ratio from noise polluted strain data. The same FE model with isotropic elasticity as introduced in previous sections is used here. As the set of manually defined virtual fields 5 and 6 are very unstable and expected to have very large error in the identification results for the noise polluted strain data, here, only the sets of virtual fields 1 & 2 and 3 & 4 are compared to the piecewise optimized VFM. The identification results are then compared with each other and critically discussed.

A range of Gaussian white noises were added to the exact simulated strain data. The noise amplitude γ ranges from 0 to 2×10^{-4} with an increment of 1×10^{-5}. For each amplitude value of γ, 30 copies of noise were added to the simulated strain data. Thus, 30 identifications were run for each γ using both the optimized and manually defined VFM. The mean and standard deviation of the identified Young's modulus *E* are plotted versus the noise amplitude γ in Fig 2.6 using symmetric error bars that are two standard deviation units in length. It can be seen from the figure that all three VFM implementations yield near-exact identification of Young's modulus when there is no noise (when $\gamma = 0$). However, when noise increases identification results for all three VFM implementations become less stable especially for the set of virtual fields 1 and 2. Clearly, for all noise amplitudes, virtual fields 1 and 2 yield the least accurate mean values and the largest standard deviations. Better results can be found for virtual fields 3 and 4, which have smaller standard deviations than virtual fields 1 and 2. The piecewise optimized VFM obviously has the smallest standard deviations and is the least affected by noise. Even when the noise amplitude reaches 2×10^{-4}, which is already tens of percent of the strain values, the identification results are still rather reasonable. Similar results were found for the identification of Poisson's ratio ν in Fig 2.7. Again, virtual fields 1 and 2 yield the least accurate identified Poisson's ratio, while the piecewise optimized VFM yields the best results, which is what was expected.

The relative identification error for Young's modulus and Poisson's ratio were then calculated using equation (2.26). For each noise amplitude γ, the mean of the relative errors of the 30 identifications was obtained and plotted as a function of γ in Fig 2.8 and Fig 2.9, for Young's modulus and Poisson's ratio, respectively. As expected from Fig 2.6 and Fig 2.7, virtual fields 1 and 2 yield the largest identification error for both Young's modulus and Poisson's ratio, while the optimized virtual fields have the smallest error.

Based on the above discussions, it can be concluded that both the optimized and manually defined VFM can yield very good identification results. However, when the strain measurements are polluted by noise, the optimized VFM is much more stable and able to give much more accurate identification results.

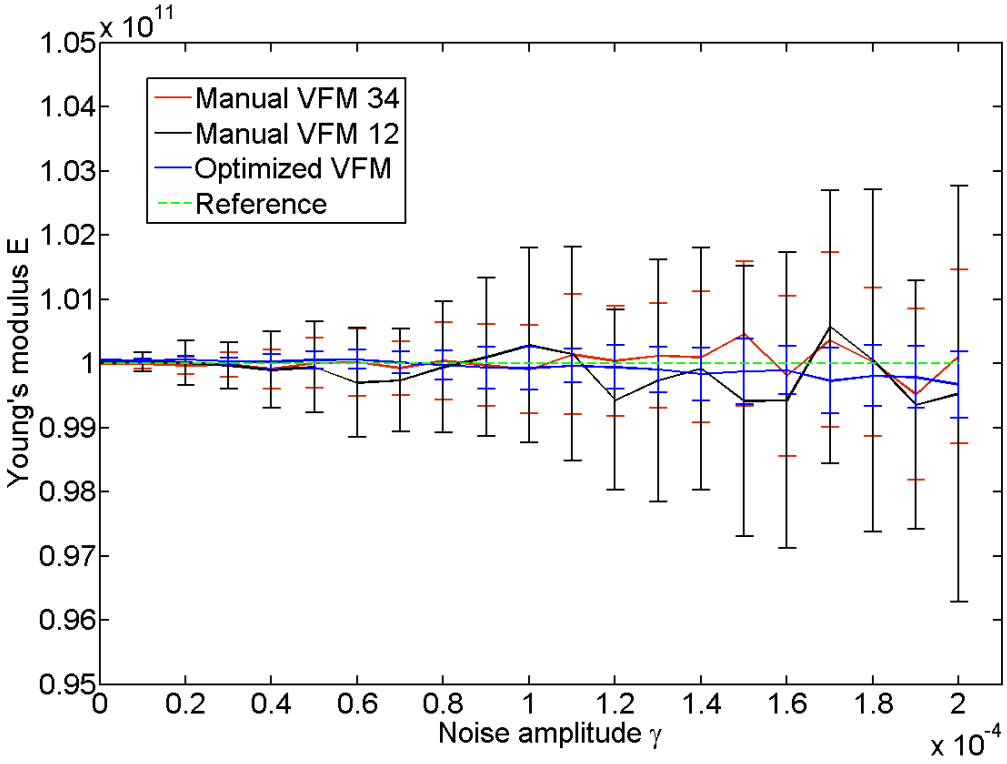

Fig 2.6: Symmetric error bars for Young's modulus E plotted as a function of noise amplitude γ for isotropic elasticity.

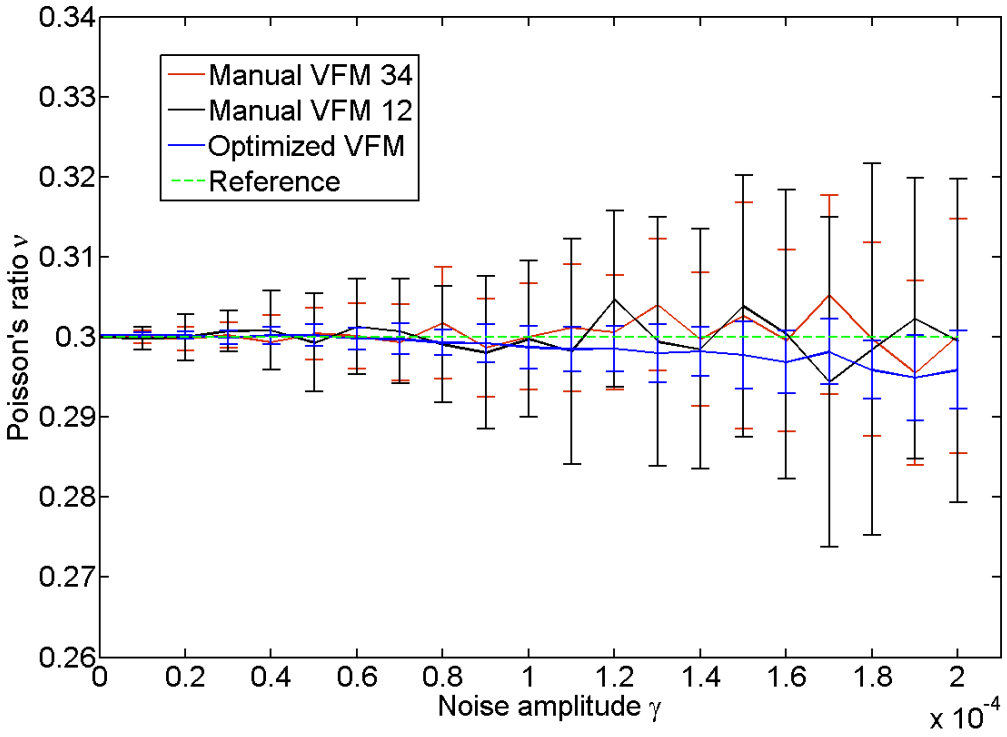

Fig 2.7: Symmetric error bars for Poisson's ratio ν plotted as a function of noise amplitude γ for isotropic elasticity.

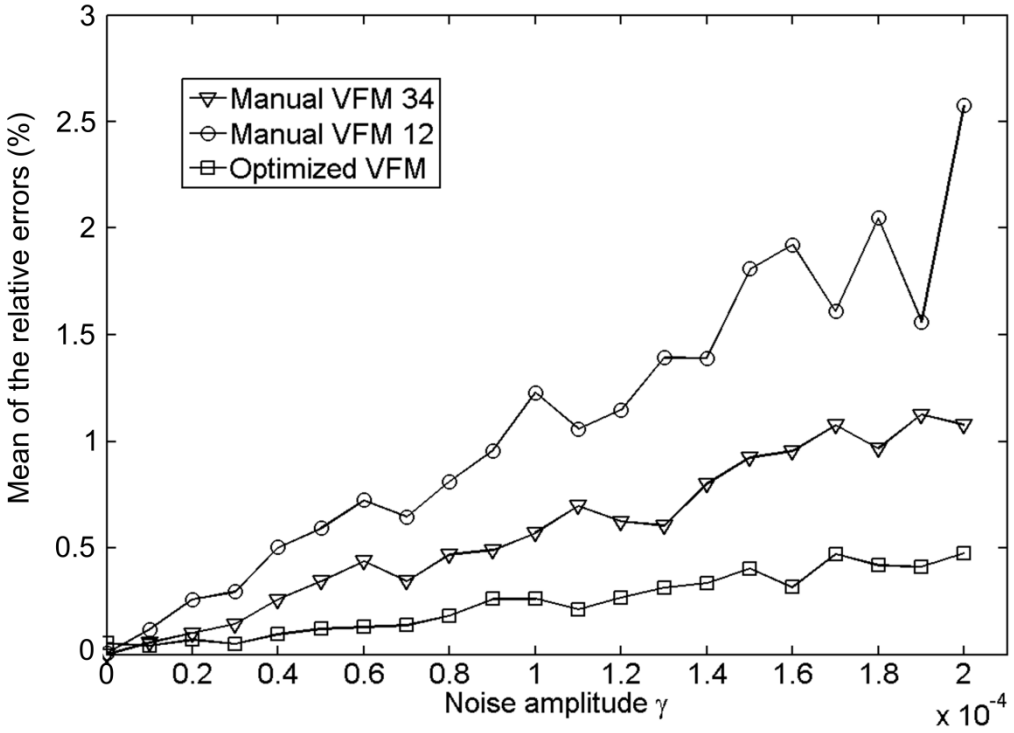

Fig 2.8: Mean of the relative errors for the identified Young's modulus E plotted as a function of γ for isotropic elasticity.

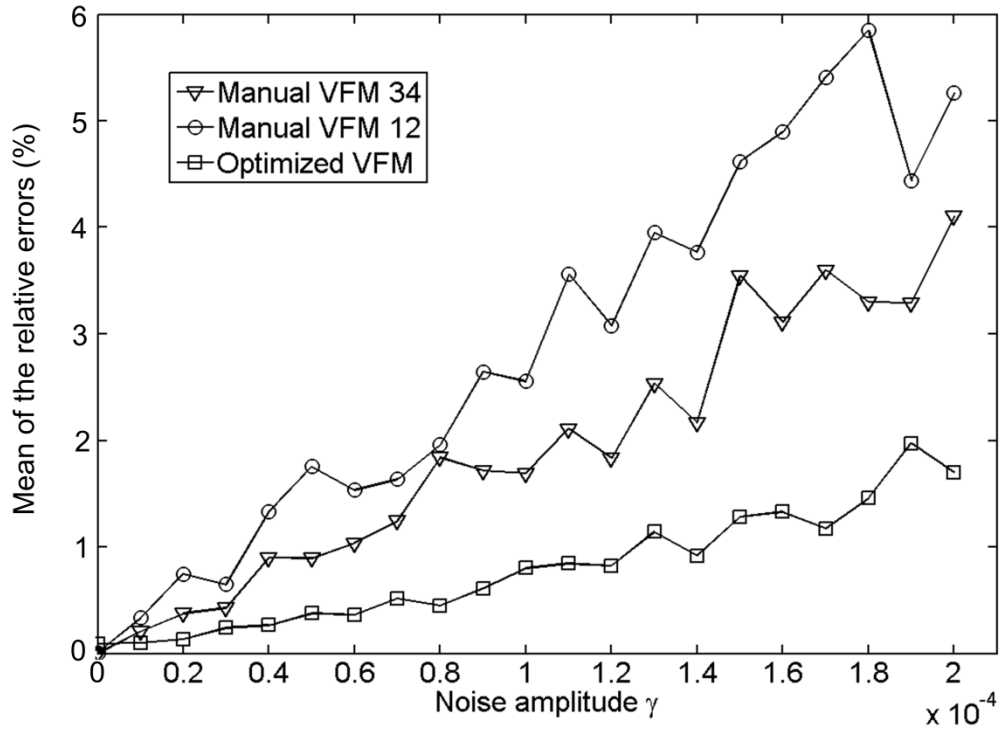

Fig 2.9: Mean of the relative errors for the identified Poisson's ratio ν plotted as a function of γ for isotropic elasticity.

2.9 Conclusions

In this chapter, 3D manually defined VFM was first developed for the identification of 3D elasticity from volume strain data. It was validated using the simulated strain data from a FE model with isotropic elasticity. The results showed that the different sets of virtual fields have different sensitivity to strain noise and the choice of virtual fields can be critical. 3D optimized VFM was then developed in detail. Piecewise virtual fields were selected here. The optimization was implemented using Lagrangian multipliers under boundary conditions constraints that eliminate the contribution of reaction forces at the supports (KA) and the special conditions constraints that directly provide the constitutive parameters. This 3D piecewise optimized VFM was validated using simulated strain data from FE models with both isotropic and orthotropic elasticity material models. Similar to the manually defined VFM, the identified stiffness components from the piecewise optimized VFM are also nearly identical to the input reference values, thus verifying the method. Finally, the manually defined VFM was compared to the piecewise optimized VFM when the strain data were polluted by Gaussian white noise. The idea was to benchmark both approaches in terms of sensitivity to noise. The results showed that both methods yielded good identification results. However, when the noise amplitude becomes larger, the piecewise optimized VFM led to much more stable results, as expected. It was also shown that the standard deviation predicted by the optimized approach matched the ones calculated directly from the stiffness distributions obtained with different copies of noise with increasing amplitude, thus validating the analytical expressions of the variance provided here for the first time for 3D elasticity.

To identify the constitutive parameters of a material using the VFM, strain data need to be obtained. For 3D VFM, depth-resolved full-field deformation measurement is needed. This issue is addressed in the following chapter.

CHAPTER 3

3D DEFORMATION MEASUREMENT USING OPTICAL COHERENCE TOMOGRAPHY AND DIGITAL VOLUME CORRELATION FOR ELASTIC MODULI IDENTIFICATION

3.1 Introduction

A wide variety of techniques have been developed to measure the deformation of materials under load, ranging from point-wise sensors such as the resistive strain gauge [112] and optical fibre Bragg gratings [113] to 2D full-field measurements including DIC [93], the grid method [81], speckle interferometry [114] and Moiré interferometry [115], to name a few. For homogeneous and isotropic materials, these techniques usually provide enough information to investigate their mechanical behaviour. However, for materials with more complex structures such as biological tissues and composites, surface measurements are much less adequate to address their complete mechanical behaviour since the deformation may vary significantly between the bulk and the surface. In this case, a depth-resolved 3D measurement (Depth-resolved represents through the thickness, while 3D refers to the 3 components of the displacement vector for each volume element in the sample) of the deformation would be highly desirable.

Thanks to the development of the various tomographic techniques, DVC has become a popular measurement technique for depth-resolved 3D deformation fields. DVC has made its way into clinical and industrial applications [103-110], where it is mainly applied on X-ray CT data of materials such as composites, metals, foams and trabecular bones. However, for soft biological tissues dominated by collagen, such as cornea, artery or skin, OCT is a more suitable technique to reconstruct the material microstructure. With the aid of OCT, the micro structure of the scanned sample can be reconstructed as a data cube which can then be utilized for structure analysis or deformation analysis using DVC. To the best of our knowledge, this is the first time that measurements of depth-resolved deformations have been undertaken combining OCT and DVC.

In this chapter a methodology for stiffness identification of semi-transparent and light scattering materials from depth-resolved 3D deformation fields is presented. These were obtained by performing digital volume correlation on optical coherence tomography volume reconstructions of silicone rubber phantoms. The effect of noise and reconstruction uncertainties on the performance of the correlation algorithm was first evaluated through stationary and rigid body translation tests to give an indication of the minimum strain that can be reliably measured. The phantoms were then tested under tension and the 3D deformation fields were used to identify the elastic constitutive parameters using 3D manually defined VFM. The identification results for the cases of uniform and heterogeneous strain fields were compared with those calculated analytically through a constant uniaxial stress assumption and also measured independently using a tensile testing machine.

3.2 Sample preparation

In the present study, two rectangular flat phantom strips were fabricated using silicone rubber (MM240-TV), one of them with a notch. The material comprises of two parts, a rubber base and a hardener. They were mixed to a ratio of 10:1. The nominal Young's modulus of the silicone rubber is 1.88 MPa, which can change with the proportion of hardener. Since the silicone rubber does not present suitable speckle contrast for the application of DVC, copper particles (with an average particle size of about 1 μm) were seeded into the silicone rubber mixture to provide the speckle contrast. The mixture was then put into molds and left to cure at room temperature for approximately 24 hours. The flat strips were cut from a larger piece using a scalpel to $60 \times 1.4 \times 10$ mm^3 ($length \times thickness \times width$). Fig 3.1 shows the phantom specimen after the manufacturing process.

3.3 Experimental set-up and image acquisition

The experimental set-up consists of a tensile test fixture and a swept-source OCT system (SS-OCT, Thorlabs OCS1300SS, lateral resolution 25 μm, depth resolution 12 μm in air), as shown in Fig 3.2. For the test, the phantom strip was mounted with one end fixed to the fixture and the other end loaded by a dead weight. At first, a dead weight of 50 g was applied as a preload to insure the phantom strip was taut and vertical. This is a necessary step since the silicone rubber is rather compliant. The preload state was taken as the reference state. A 10 g dead weight was then added to the preload and considered as the deformed state, referred to as 'load step 1' hereafter.

For both reference and deformed states, a 3D volume reconstruction of the specimen was generated using the SS-OCT system. It uses a rapidly tuned narrowband light source with central wavelength of 1325 nm and spectral bandwidth of 100 nm and records the information with a single photo detector. The frequency of the interference signal is proportional to the optical path difference between the sample and reference arms of an interferometer. Depth profiles (A-scans) of the sample are obtained by evaluating the Fourier transform of the signal for each wavelength scan. The 5-6 mm coherence length of the laser enables a depth range of approximately 3 mm. Adjacent A-scans are then synthesized to create an image in the *xy* plane. Multiple adjacent 2D images in the *z*-direction then form the reconstructed 3D volume. In the present work, a region with dimensions of $11\times3\times11$ mm^3 was scanned, corresponding to *x*, *y* and *z* directions, respectively. A 3D data volume of $1024\times512\times1024$ voxels was obtained. The acquisition time for each 3D volume is approximately 5 minutes. It should be pointed out that each time, before acquiring the volume data, the specimen was left 10 minutes under load to accommodate significant short term viscoelastic creep. Along the lateral scanning directions *x* and *z*, the image voxel size was determined by dividing the 11 mm dimension by the number of corresponding 1024 voxels, which is equal to 10.7 μm. Regarding the through-thickness *y*-direction, which corresponds to optical path, the voxel size depends on the refractive index of the medium. For the silicone rubber phantom the voxel size inside the medium along the *y*-direction is 4.1 μm determined by dividing its thickness 1.4 mm by the number of corresponding voxels, here 345. The reconstructed volume and a typical central transverse *z*-slice (1024×512 voxels) of the specimen are given in Fig. 3.3 (a) and (b), respectively. Due to light saturation, the voxels at the top surface exhibit very high intensity values, as can be seen from the white line at the top of the phantom in Fig. 3.3(b). It should be pointed out that all the regions outside the phantom strip and the saturated voxels at the top surface were masked out in Fig. 3.3 (a) for a better visualization of the 3D reconstructed volume. The reconstructed volumes for the reference and deformed states were recorded and DVC was then used to compute the 3D displacement and strain fields.

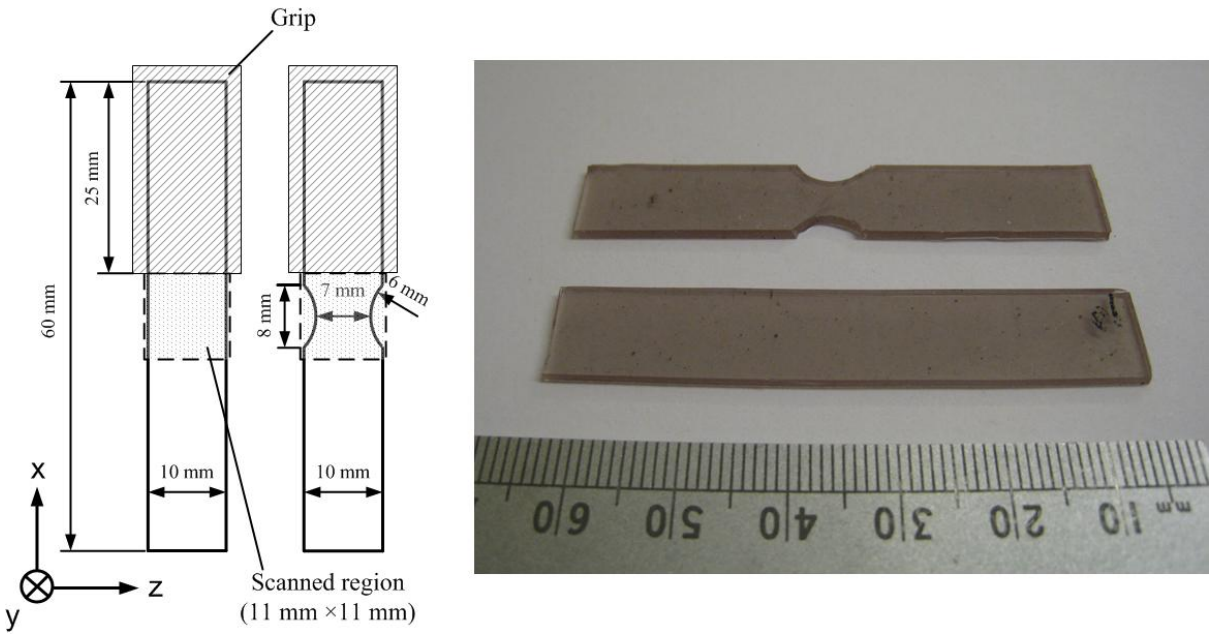

Fig 3.1: Image of the fabricated silicone rubber phantom specimen.

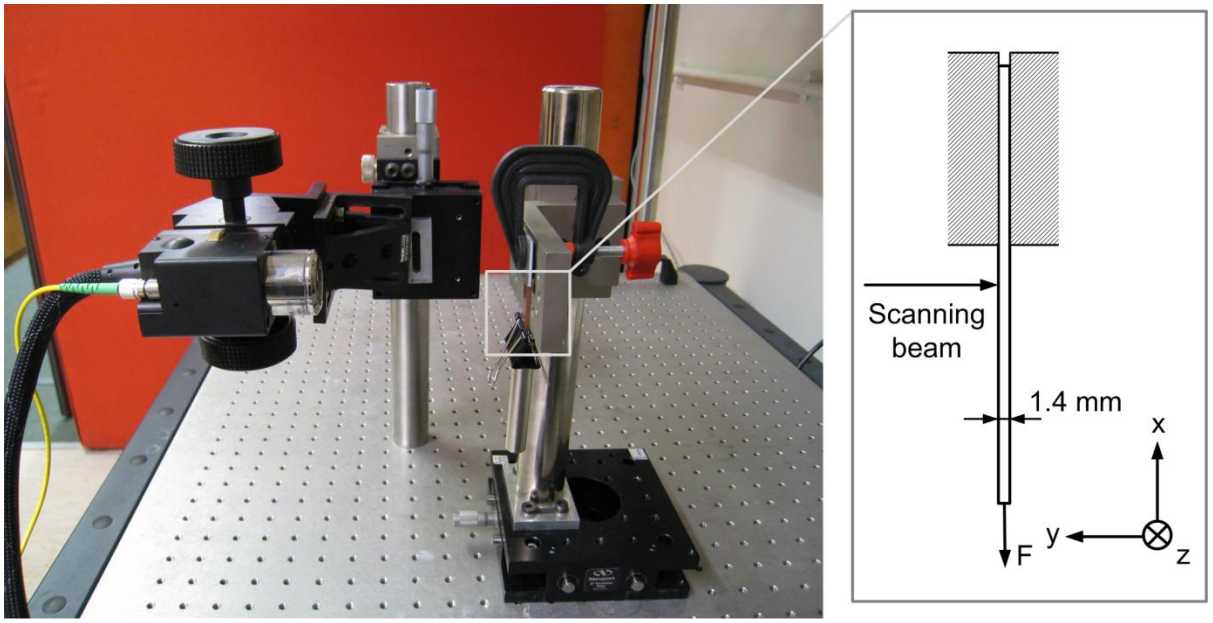

Fig 3.2: Schematic and image of the experimental set-up.

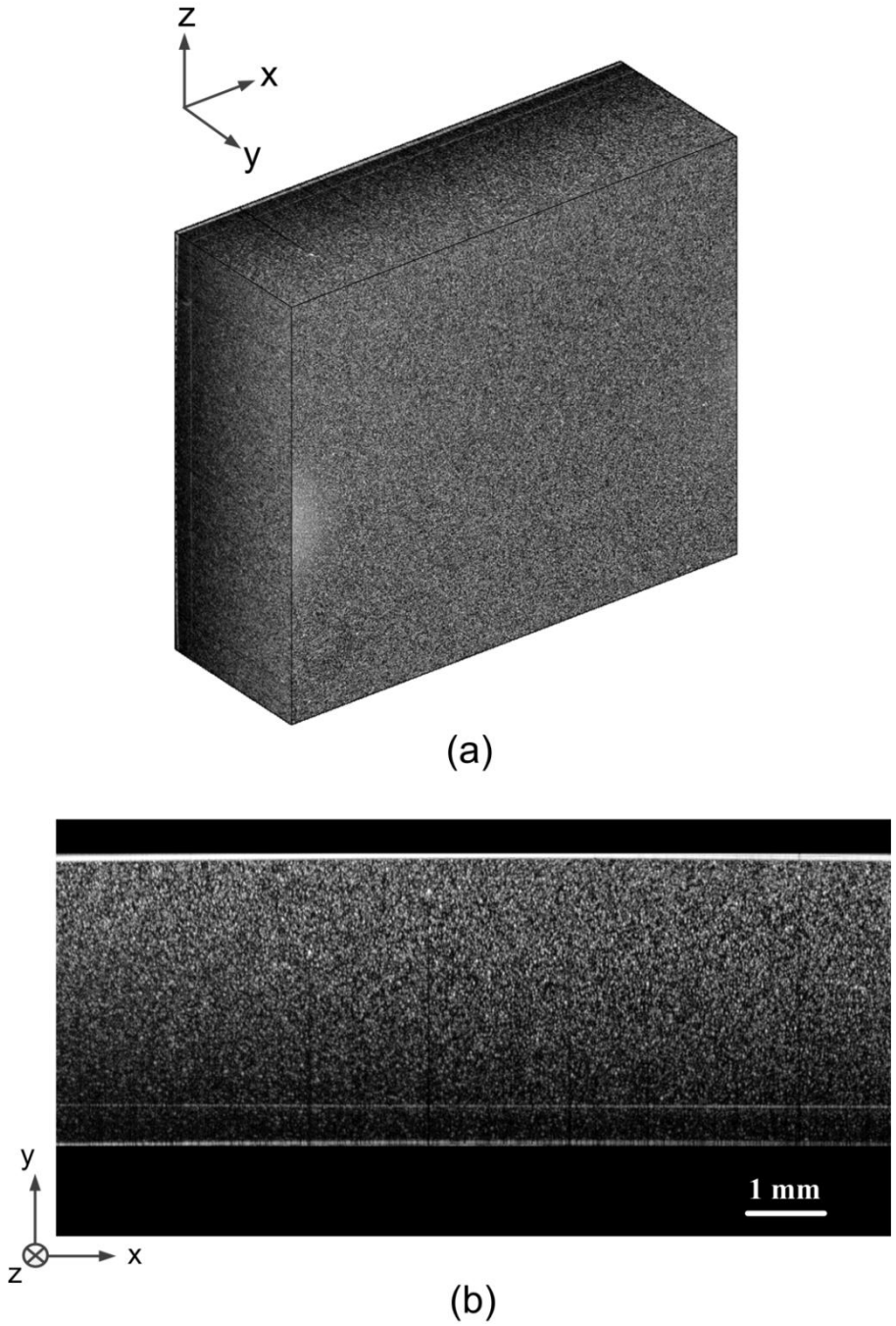

Fig 3.3: OCT reconstructions of the rectangular silicone rubber phantom strip: (a) 3D view of the reconstructed volume and (b) 2D view of the central transverse *z*-slice generated through the SS-OCT system.

3.4 Digital volume correlation

DVC is the 3D extension of the widely applied DIC used to measure surface deformations. During the DVC procedure, the correlated volumes are first divided into sub-volumes. The displacement vector of each sub-volume is determined by tracking and matching the voxels

of the sub-volumes in the reference and deformed states. This is performed by maximizing the correlation coefficient which measures the degree of similarity of the grey level distributions in the sub-volumes in the reference and deformed states. The best prediction of the displacement leads to the highest degree of similarity of the grey level distributions thus the maximal correlation coefficient (a correlation coefficient value close to 1 indicates a perfect match). In the present study, the displacement fields were calculated using the DaVis® (LaVision) software package based on a fast Fourier transform (FFT) algorithm. It evaluates a normalized cross-correlation coefficient (NCC) defined as

$$C = \frac{\sum\sum\sum F(x,y,z)G(\hat{x},\hat{y},\hat{z})}{\sqrt{\sum\sum\sum [F(x,y,z)]^2 \sum\sum\sum [G(\hat{x},\hat{y},\hat{z})]^2}} \tag{3.1}$$

where $F(x,y,z)$ represents the grey level at a voxel (x,y,z) in the sub-volume of the reference state, while $G(\hat{x},\hat{y},\hat{z})$ represents the grey level at a point $(\hat{x},\hat{y},\hat{z})$ in the sub-volume of the deformed state. The coordinates (x,y,z) and $(\hat{x},\hat{y},\hat{z})$ stand for the same material point in the reference and deformed states, respectively, and are related by the 3D affine transformation in the form of rigid body motion combined with displacement gradients

$$\begin{aligned}
\hat{x} &= x + u_x + \frac{\partial u_x}{\partial x}\Delta x + \frac{\partial u_x}{\partial y}\Delta y + \frac{\partial u_x}{\partial z}\Delta z \\
\hat{y} &= y + u_y + \frac{\partial u_y}{\partial x}\Delta x + \frac{\partial u_y}{\partial y}\Delta y + \frac{\partial u_y}{\partial z}\Delta z \\
\hat{z} &= z + u_z + \frac{\partial u_z}{\partial x}\Delta x + \frac{\partial u_z}{\partial y}\Delta y + \frac{\partial u_z}{\partial z}\Delta z
\end{aligned} \tag{3.2}$$

where u_x, u_y, and u_z are the rigid body displacement components of the sub-volume centre in the x, y and z-direction, respectively. Δx, Δy and Δz, represent the distance between the sub-volume centre and the point (x,y,z). A double-pass approach was used whereby large sub-volumes were initially used to capture large displacements. Subsequent to this, these initially calculated displacements were used to displace smaller sub-volumes, and thus ensure the pattern was followed and the signal to noise ratio increased. Gaussian curve-fitting of the correlation function peak was used to detect the position of the displacement with sub-voxel resolution. The strains were then determined from the centred finite difference of the calculated displacement fields, without any additional smoothing.

3.5 Evaluation of measurement performance

A fundamental condition in image correlation techniques is that the changes in the intensity pattern are in one-to-one correspondence with the displacements of the surface. DVC results from OCT volume reconstructions of the reference and deformed states are likely to be affected by a variety of factors such as: 1) electronic noise of the detectors; 2) light source stability; 3) reconstruction algorithms; 4) contrast reduction through the sample thickness due to material absorption, scattering, dispersion, defocusing and spectral roll-off; and 5) strain-induced speckle decorrelation due to "speckle boiling", a phenomenon in which the intensity of the speckle pattern changes considerably due to large, uncorrelated phase changes; speckle grains change from dark to bright and vice versa. We studied the combined effect of 1-4 by performing a stationary test and a rigid body translation test of the phantoms. The effect of strain induced speckle decorrelation was explored through a numerical simulation described below in section 3.5.4.

3.5.1 Influence of sub-volume size

The DVC algorithm requires sufficient contrast in a sub-volume in order to determine a displacement vector. The size of the sub-volumes influences the value of the correlation coefficient and thus the displacement and strain uncertainties. In the present study, four different sub-volume sizes were selected and compared to determine an optimal size considering the displacement and strain spatial variation as well as the spatial resolution. A double-pass approach used initial sub-volumes sizes 24^3, 48^3, 72^3 and 96^3 in the first pass, followed by 12^3, 24^3, 36^3 and 48^3 in the second path and each had 50% overlap with the six adjacent neighbours. Thus, the distance between each sub-volume centre with its immediate neighbours is 6, 12, 18 and 24 voxels, respectively.

From the DVC results on the OCT reconstructions of the stationary specimen, the influence of sub-volume size was analysed quantitatively by comparing the standard deviations of the strain components for a central *z*-slice (x, y) for the four final sub-volume sizes. All the six strain components were derived from the centred finite difference of the spurious displacements as follows without any smoothing

$$\varepsilon_{ij} = \frac{1}{2}\left(u_{i,j} + u_{j,i}\right) \tag{3.3}$$

where the commas stand for the partial derivatives. The standard deviations over the whole field of view are compared in Fig 3.4 for ε_{xx}, ε_{xy} and ε_{yy} only, for the sake of legibility. From the figure, one can see that the standard deviations of the strain components drop from $\sim 3\times10^{-3}$ to about 5×10^{-4} when the sub-volume size increases from 12^3 to 24^3. When the sub-volume size is further increased to 36^3 and 48^3 –see Fig 3.5, the strain std fluctuations further reduced to about 2×10^{-4}. This is not surprising when analysing the 3D views of the four sub-volumes in Fig 3.5. As it can be seen, the 48^3 sub-volume contains the largest number of features which assist the convergence of the volume correlation algorithm and enable more accurate tracking of the sub-volume deformation. A smaller number of features in the 12^3 sub-volume lead to bigger tracking errors. However, although 48^3 sub-volumes provide the highest strain resolution among the four, it is not necessarily the optimal choice because the spatial resolution must also be taken into consideration. This is important especially for those specimens with very small thickness compared to the spatial resolution of the SS-OCT system such as the porcine cornea studied by Fu *et al* in [116]. For the flat phantom in the present study, 36^3 sub-volumes were found to be a good compromise between strain resolution and spatial resolution. As a consequence, a sub-volume size of 36^3 was kept for this study. Depending on the OCT spatial sampling rate, the speckle field may be under-sampled, leading to interpolation bias [117]. This issue will be discussed later on in the chapter.

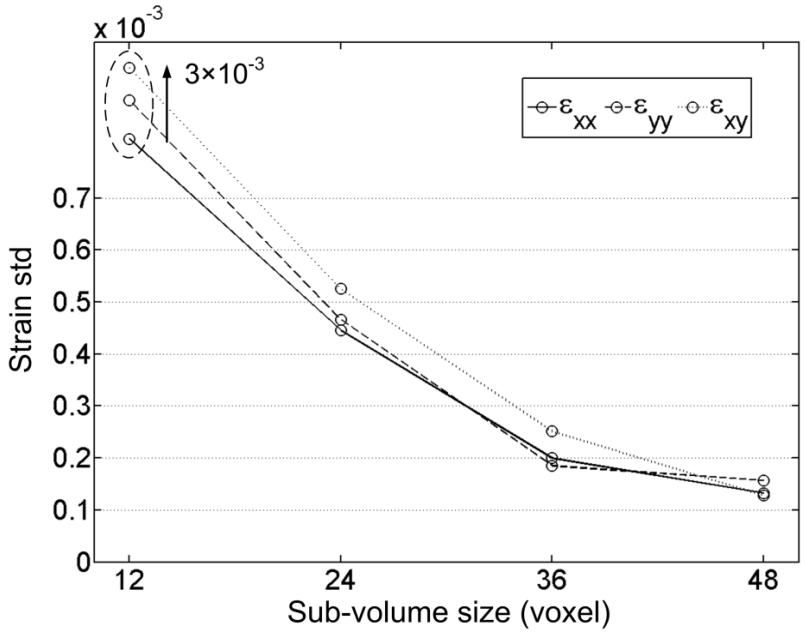

Fig 3.4: Comparison of the strain standard deviations for different sub-volume sizes, calculated for a stationary rectangular phantom strip.

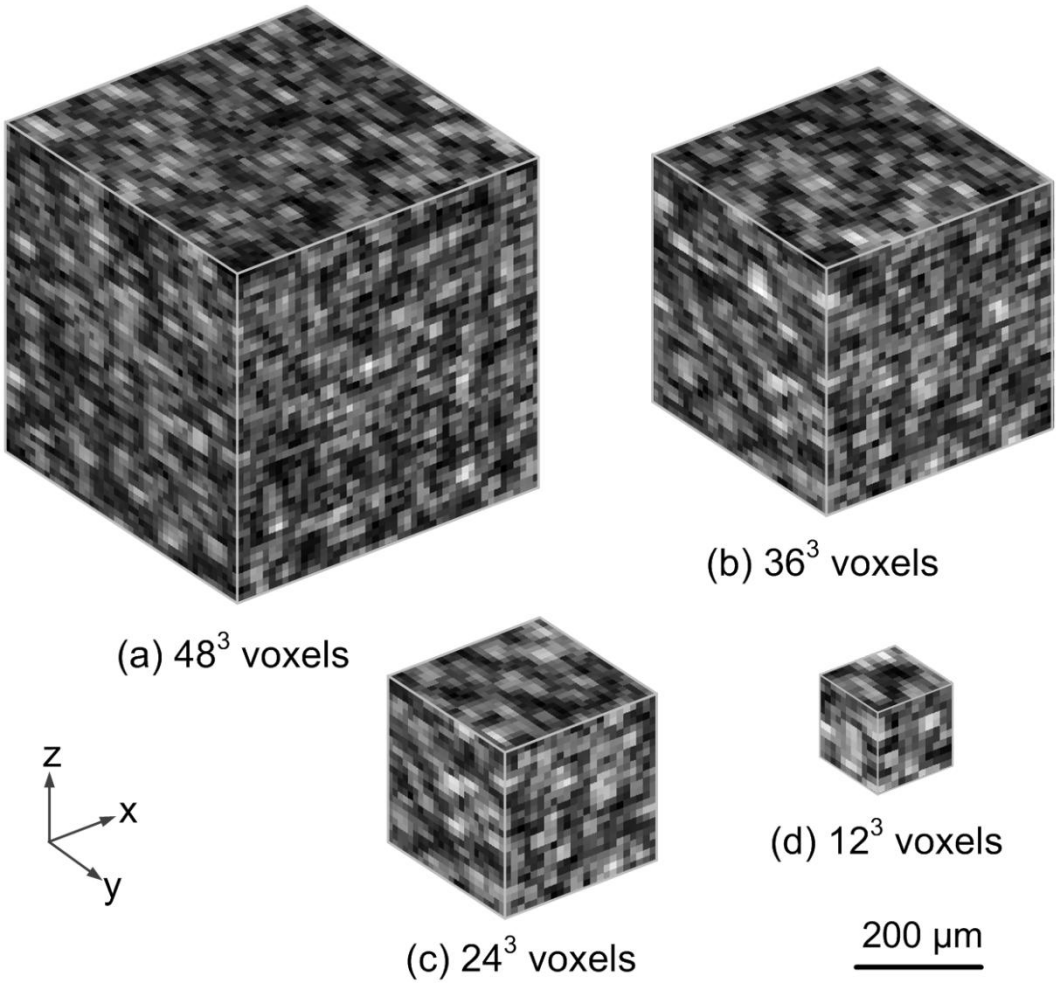

Fig 3.5: 3D views of the OCT sub-volumes with different sizes. The granular structure corresponds to the 3D speckle.

3.5.2 Stationary test

Prior to performing tests that induce deformation of the sample, it is necessary to evaluate the errors caused by all sources of noise and reconstruction uncertainties. This can be done by performing DVC on two reconstructed volumes of the stationary phantom strip. Since the stationary specimen was not subjected to any applied force, the correlation results should show zero displacement and strain fields over the whole field of view. This is not the case in practice due to the influence of electronic noise in the SS-OCT system, environmental vibration, the volume reconstruction algorithm, *etc*. Therefore, any non-zero results should be attributed to the contribution of noise and other reconstruction uncertainties. The standard deviations of the spurious strains were calculated to evaluate the resolution (uncertainty) of the strain measurement.

Based on the volume strain fields of the stationary test, the standard deviation of each strain component was calculated for each *z*-slice and the results are plotted in Fig 3.6. It can be observed that the standard deviations of all the strain components generally remain stable along the different *z*-slices, with a slight increase towards the ends. This is expected as the DVC results are usually noisier near edges due to the lack of data. Although with fluctuation, all the standard deviations are generally between 1.5×10^{-4} and 2.5×10^{-4} without any smoothing, which is considered as satisfactory compared with the strain levels in the tensile tests later on.

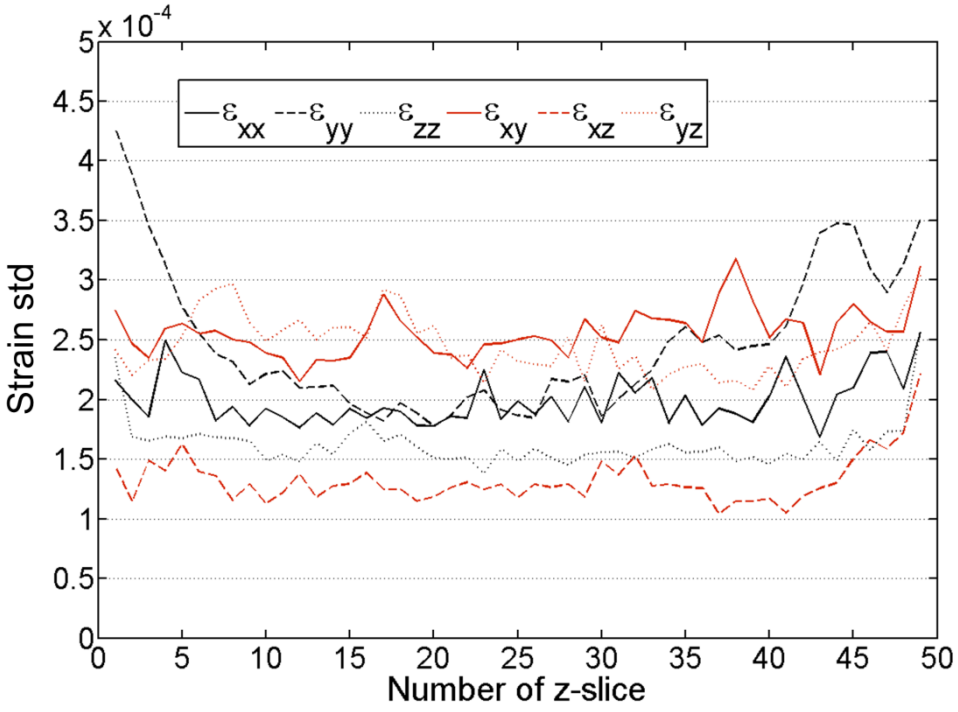

Fig 3.6: Standard deviation of the spurious strain obtained with 36^3 voxels sub-volume and 50% overlap in a stationary test.

3.5.3 Rigid body translation test

Two reconstructed volumes were recorded after introducing a rigid body translation of 40 μm (about 10 voxels) in the *y*-direction between the two volumes. This not only tests the effect of all sources of noise but also tests the performance of DVC sub-voxel interpolation (tri-linear in the present study) and accuracy of the correlation algorithm in determining the displacement fields for a translated specimen. The same procedure of data processing used for the stationary test was applied to the rigid body translation test and the strain

measurement resolution was computed. The above tests give an overall idea of the resolution of the whole set-up so that the significance of the tensile test results can be better analysed.

Slightly larger values of strain std, between 2×10^{-4} and 3.5×10^{-4}, were obtained for the rigid body translation test – see Fig 3.7. Compared with the results of the stationary test, the strain std for the translation test have larger fluctuation. This is so as the errors not only come from all the error sources presented in the stationary test, but also arise from the sub-voxel interpolation error as the DVC algorithm tracks the sub-volumes between the reference and displaced states as well as defocusing and spectral roll-off. Therefore, higher noise levels can be expected. It was observed that lateral translations (in the *xz* plane) lead to strain standard deviations values between those obtained for the stationary and the axial translation tests. Although the strain standard deviations for the rigid body translation test are larger than those for the stationary test, these noise levels are still low compared to the strain levels of approximately ~1% in the tensile tests and were thus considered satisfactory.

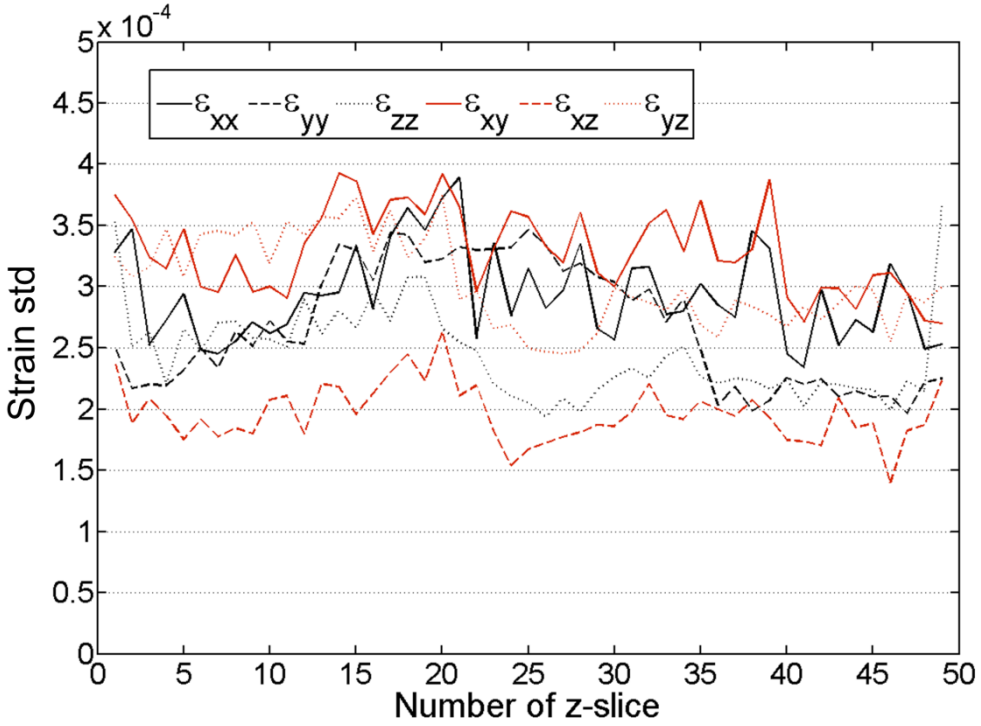

Fig 3.7: Standard deviation of the spurious strain obtained with 36^3 voxels sub-volume and 50% overlap in a rigid body translation test.

3.5.4 Strain-induced speckle decorrelation

Due to the backscatter illumination/observation configuration, the complex 3D point spread function (PSF) of the OCT system has ~18 fringes across it along the axial direction (ratio between the depth resolution, 8.3 μm, and the half wavelength of the light source in the medium of refractive index 1.45, i.e. 1.325 μm/(2×1.45)=0.457 μm). The magnitude of the measured OCT signal corresponds to the convolution between the 3D PSF and the scattering particles within the phantom. This magnitude, which determines the brightness of the 3D speckle grain at any particular position within the sample, does not change with rigid body motion of the sample as relative phase differences between scatterers within the 3D PSF remain constant. In case of strain, however, there is a limit within which the magnitude of the speckle remains nearly unchanged and beyond which an incremental DVC approach would be required.

In order to estimate the level of OCT speckle decorrelation due to strain, we performed a 2D (on the *xy* plane) numerical simulation involving the following steps:

1. Generate a 2D random distribution of scatterers such that there are many of them (~100) inside the point spread function of the OCT system.
2. Evaluate the 2D speckle field due to the spatial distribution of scatterers considering the numerical aperture of the system, the central wavelength and bandwidth of the source, and the refractive index of the medium. This was done by Coupland *et al* using linear systems theory [118, 119] by first calculating the transfer function of the OCT system, then evaluating the complex PSF and convolving it with the scatterers. The speckle field was oversampled to recover phase information within the PSF. In this way, the correlation coefficient evaluation is free from under-sampling effects. We used images of 1024×1024 pixels with a speckle size given by the dimensions of the PSF (~1024/4 pixels in the axial direction *y* and ~1024/2 pixels in the lateral direction *x*). Using the Rayleigh resolution criteria, this leads to ~8×4=32 speckles in the simulated subset, as shown in Fig 3.8, which compares well with the number of speckles observed on the *xy* face of the 36^3 sub-volume shown in Fig 3.5.

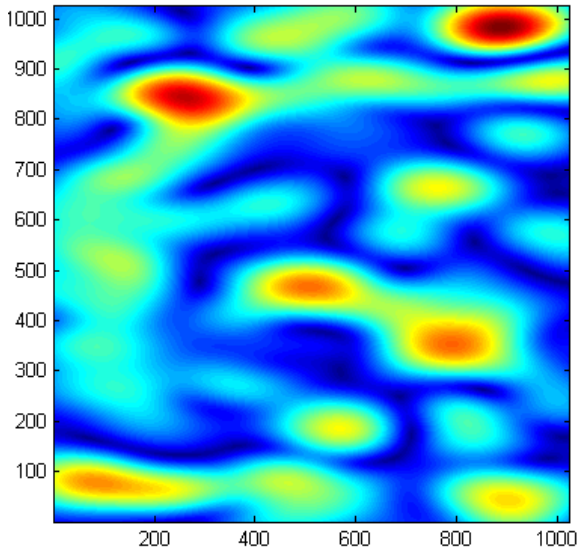

Fig 3.8: Simulated speckle field in a sub-set or sub-image: horizontal axis is *x*, vertical axis is observation axis *y*.

3. Deform the spatial distribution of scatterers with a horizontal strain ε_{xx} from 0 to 0.5 in steps of 0.001 from 0 to 0.02 and steps of 0.05 thereafter. Poisson's contraction in the vertical direction was also considered, using $\nu = 0.42$ as estimated for our phantoms in Section 3.7. For each deformation state, the intensity of the corresponding speckle field was calculated.
4. Finally, the normalized cross correlation as defined in equation (3.1) was evaluated between the first speckle field for $\varepsilon_{xx} = 0$ and all others in the sequence.

Figure 3.9 shows that NCC drops to ~0.987 for $\varepsilon_{xx} = 1\%$ and to ~0.961 for $\varepsilon_{xx} = 2\%$. This latter strain corresponds to a total maximum through-thickness relative displacement of the scatterers in the PSF of ~70nm. This is equivalent to ~1/6th of the fringe period inside the PSF and is inversely proportional to the Poisson's ratio. NCC drops to ~0.9 for ε_{xx} ~ 4%, which corresponds to ε_{yy} ~1.7% using $\nu = 0.42$. This strain level is probably a good estimate to the maximum strain that we can measure with OCT and DVC without using an incremental approach. Above this level, the correlation coefficient is too low to guarantee a good estimate of displacements. When the changes in the magnitude of the interference of light scattered by particles within the PSF are large, the speckle is said to '*boil*', i.e. its structure changes while only the average speckle size is preserved. Even though these results correspond to a 2D case (B-scan), a 3D simulation is expected to render similar results to those reported here. Zaitsev *et al* [93] have found similar results performing a numerical simulation and evaluating the

zero mean normalized cross correlation coefficient (ZMNCC) as a function of strain. They report that speckle boiling fully decorrelates the speckle for axial strain levels of ~1.5%, which compares well with our figure of ~1.7% mentioned above.

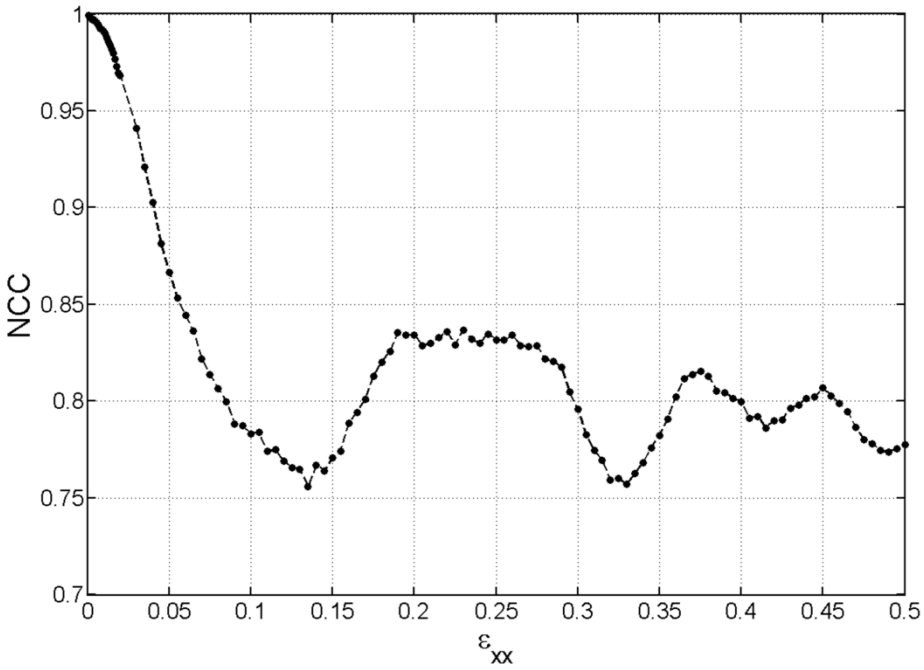

Fig 3.9: Normalized cross correlation of a speckle field in a simulated B-scan as a function of longitudinal strain ε_{xx}.

3.6 DVC results for tensile tests

3.6.1 Correlation coefficient maps

The 3D deformation field was measured under tension after performing DVC on the OCT reconstructed volume data for the rectangular and notched phantom strips. As DVC was performed using the sub-volume size of 36^3-voxel and 50% overlap, the reconstructed volume of interest thus contained $55\times18\times50$ measurement points, corresponding to dimensions of $10.5\times1.4\times10$ mm^3. The reliability of the deformation measurements was assessed in terms of the 3D correlation coefficient maps, shown in Figs. 3.10 (a) and (b) for the rectangular and notched phantom strips, respectively. In order to see the correlation coefficients within the specimens, sub-volumes of the whole fields are represented here obtained by cutting the volumes in the *xy* plane at *z*-slice 25. For both specimens, it can be observed that the correlation coefficient is larger in regions at the top of the samples and smaller in regions at the bottom (along *y*-direction). For *y*-slice 18 at the top of the

rectangular specimen, the mean value of the correlation coefficient is 0.95, while it is 0.92 for *y*-slice 1 at the bottom. Similar results were obtained for the notched specimen: 0.95 and 0.84, respectively. This decrease in correlation coefficient through the thickness can be attributed to a depth-dependent speckle contrast reduction as a result of signal attenuation due to light scattering, defocusing and spectral roll-off. In our experiments, the maximum ε_{xx} was ~1.4% (see results for 'load step 2' in Section 3.6.2) and therefore speckle boiling was not an issue. The correlation coefficient is considered as satisfactory.

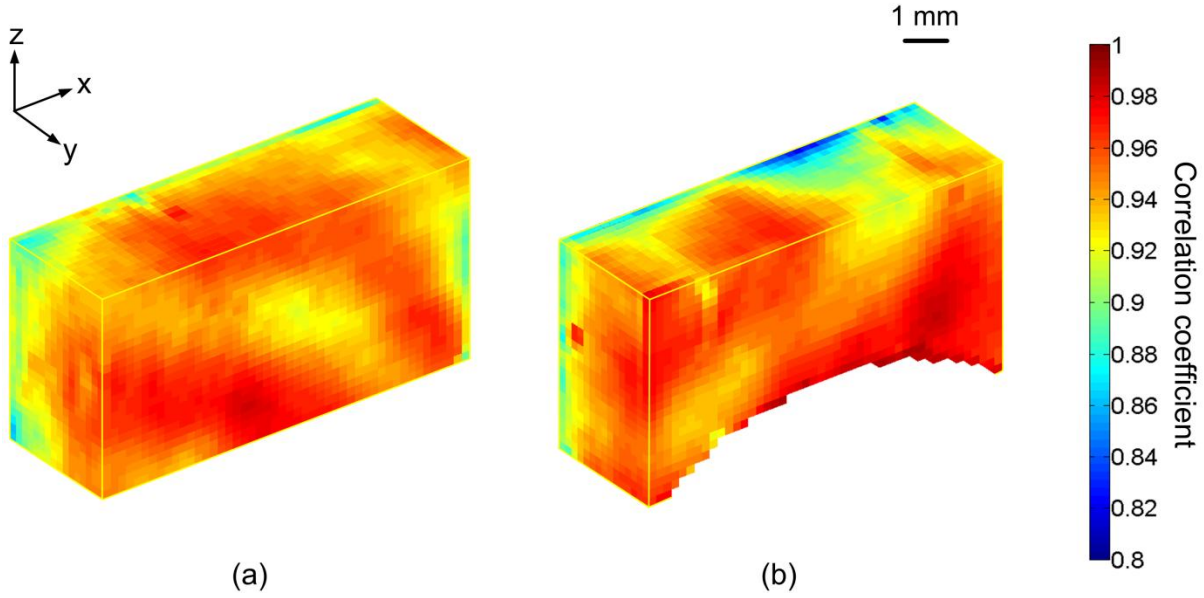

Fig 3.10: 3D views of the correlation coefficient maps for: (a) Rectangular phantom strip and (b) Notched phantom strip, cut at the position $z = 25$, load step 1.

3.6.2 Results for the rectangular phantom strip

u_x displacement maps for the rectangular phantom strip, which denote the displacement along the tension direction, are shown in Fig 3.11. Changes of u_x in cross sections cut at different *z*-slices can be seen along the *x*-axis. It can be observed that the absolute value of u_x increases continuously along the *x*-direction from the fixed side to the other, ranging from 0 to 0.07 mm, as expected from the loading configuration. When plotting the mean value of u_x in each cross section *yz* along the *x* direction in Fig 3.12(a), one can see that generally the mean value evolves linearly along the *x*-direction. Nevertheless a sinusoidal oscillation is apparent when the difference between the actual values and a linear fit is plotted as a function

of x in Fig. 3.12(b). An analysis of these displacement oscillations is provided below in this Section.

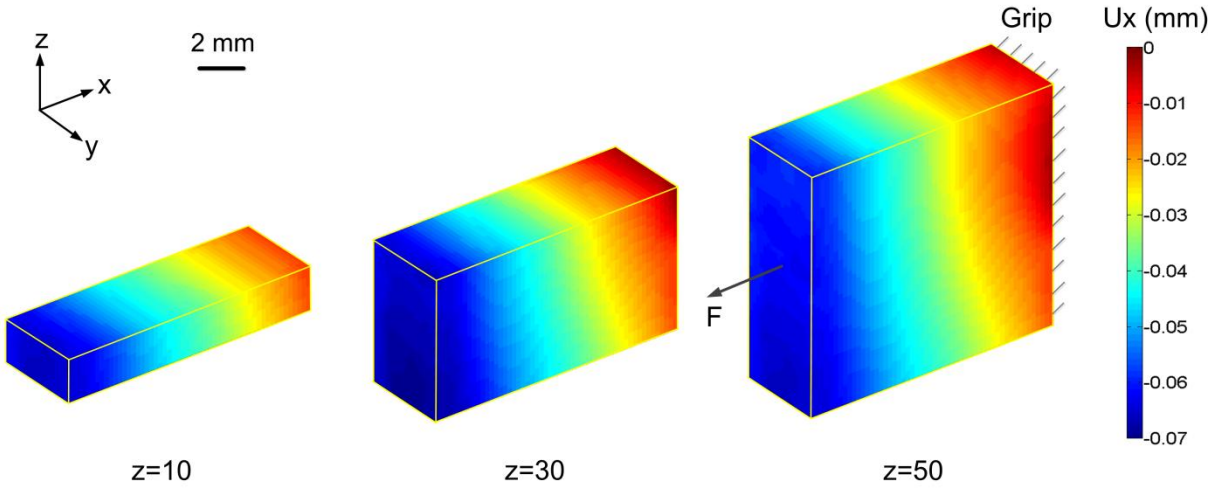

Fig 3.11: u_x displacement distribution obtained for a rectangular phantom strip under tension (load step 1), showing different sub-regions of the data volume.

The strain maps were derived using the same procedure as for the noise analysis (centred finite difference of the displacement data, without any smoothing). All six strain components for central *z*-slice 25 and central *y*-slice 10 are shown in Figs. 3.13 and 3.14, respectively. As expected from the loading configuration, the ε_{xx} strain maps for both *z*- and *y*- slices show positive values around 0.007. Strain maps ε_{yy} and ε_{zz} show negative values indicating a Poisson's contraction along the corresponding directions. It is interesting to note that ε_{zz} is very small (close to zero) at the right-hand side, where the grip prevents Poisson's contraction in the *z*- direction. Regarding ε_{yy}, it is not zero at the right-hand side because the constraint from the grip acts only at the surface. The reason why ε_{yy} is actually larger in magnitude may be from some material non-linearity due to the compression in the grip. Figure 3.15 shows that the measured strain components are significantly larger than the corresponding strain noise obtained for the stationary test. Since this is a pure tensile test for the rectangular strip, all the shear strain components should be close to noise level, as confirmed in Figs 3.13 and 3.14. Some irregularities, however, can be seen from these strain maps. In the ε_{xx} strain component, apparent fringes can be observed in Fig 3.13 and Fig 3.14, which is expected from the oscillation in the u_x displacement. The fringes observed in the ε_{xx} strain component

in Figs 3.13 and 3.14 could be due to either: 1) a spatial variation of the elastic modulus, or 2) interpolation bias [117].

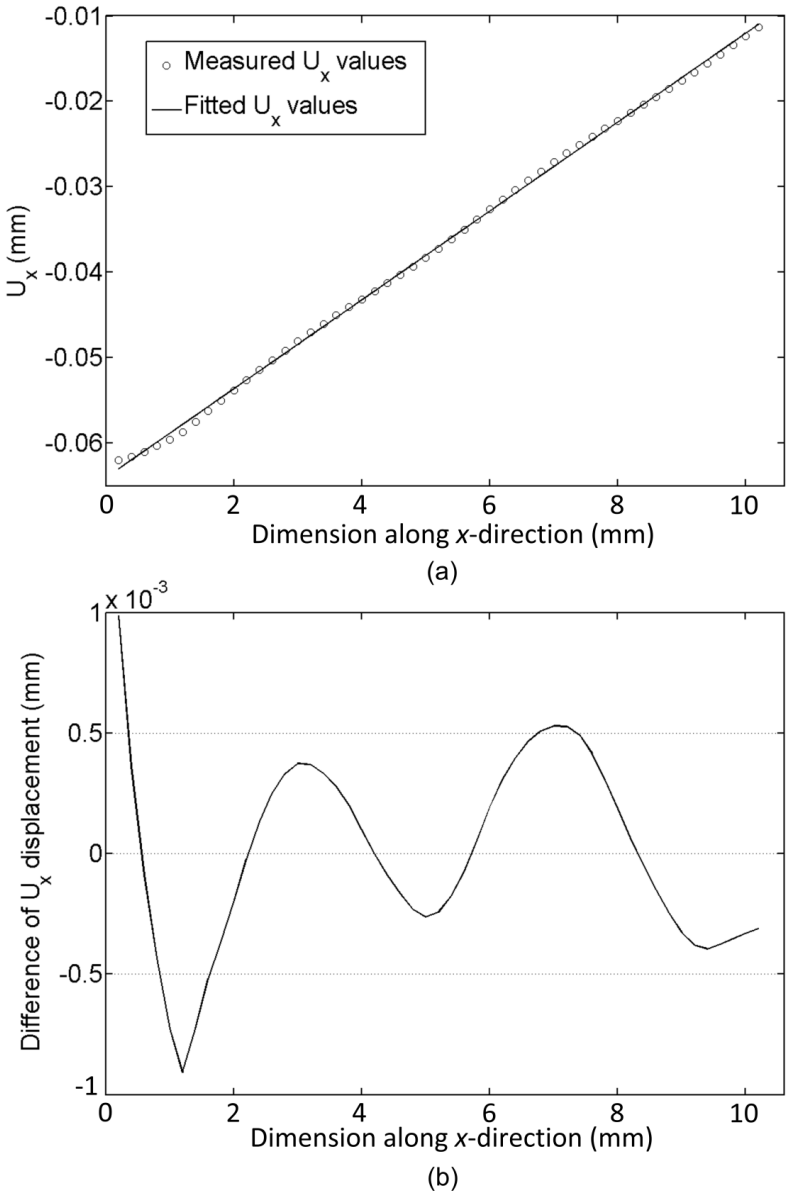

Fig 3.12: (a) u_x displacement averaged within *yz*-cross sections along the *x*-direction and a linear data fit obtained for a rectangular phantom strip under tension (load step 1); (b) Difference between the averaged u_x and the linear fit shown in (a).

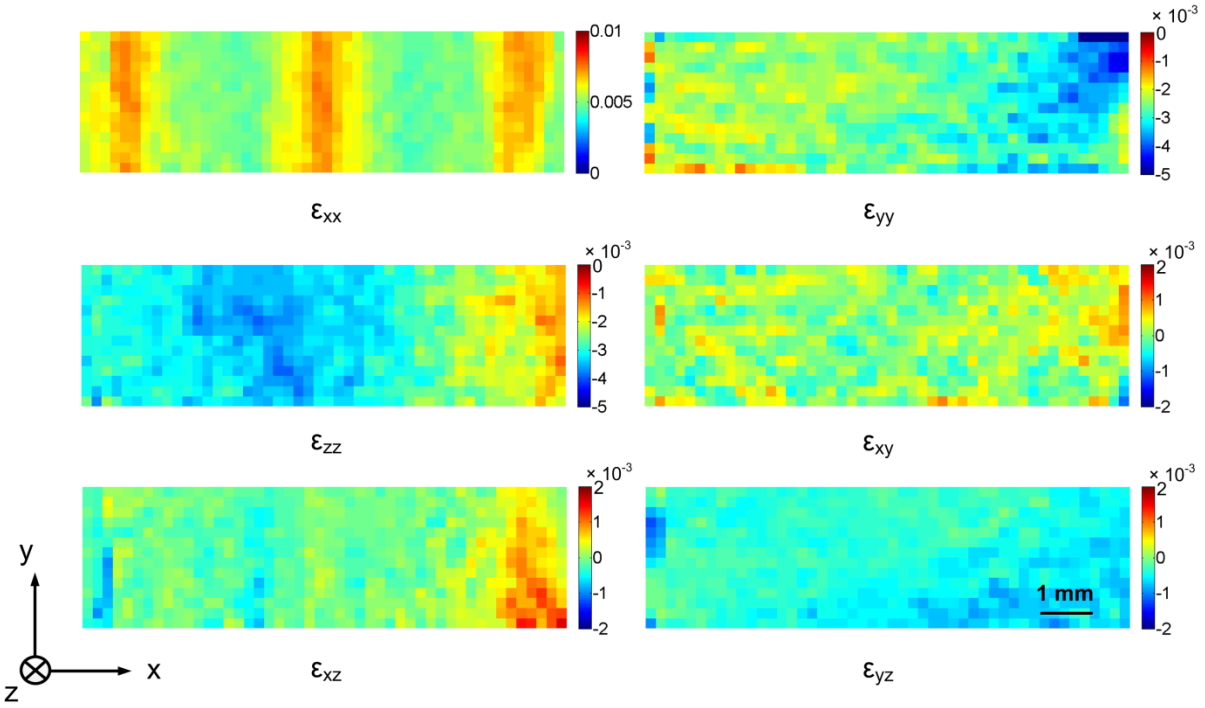

Fig 3.13: Spatial distribution of the strain components obtained for a rectangular phantom strip under tension (load step 1). The central *z*-slice 25 is shown.

To analyse the sinusoidal oscillation in the displacement and strain results, the study of interpolation bias in digital image correlation from reference [117] by Sutton *et al* is cited here. In the reference, 20 images were produced by the authors, corresponding to sub-pixel shift increments of 0.05 pixel between images. The displacement of each image with respect to the original image was determined using DIC that implements different interpolation filters. The plot of interpolation bias is cited here in Fig 3.16. It can be seen that the general shapes of the errors are the same for all interpolation filters, which are sinusoidal, only the magnitudes of the errors being different. In the present study, it is apparent that the sinusoidal oscillation in Fig 3.12 for the rectangular phantom strip is consistent with the results stated in reference [117], indicating that it is the result of interpolation bias. In the case of the FFT based DIC algorithm used here, the period of the oscillation due to interpolation bias has been proved to correspond to a displacement equivalent to 2 voxels [107, 120, 121]. This is consistent with 2.5 fringes observed in Fig 3.12(b) for a total deformation corresponding to 5 voxels.

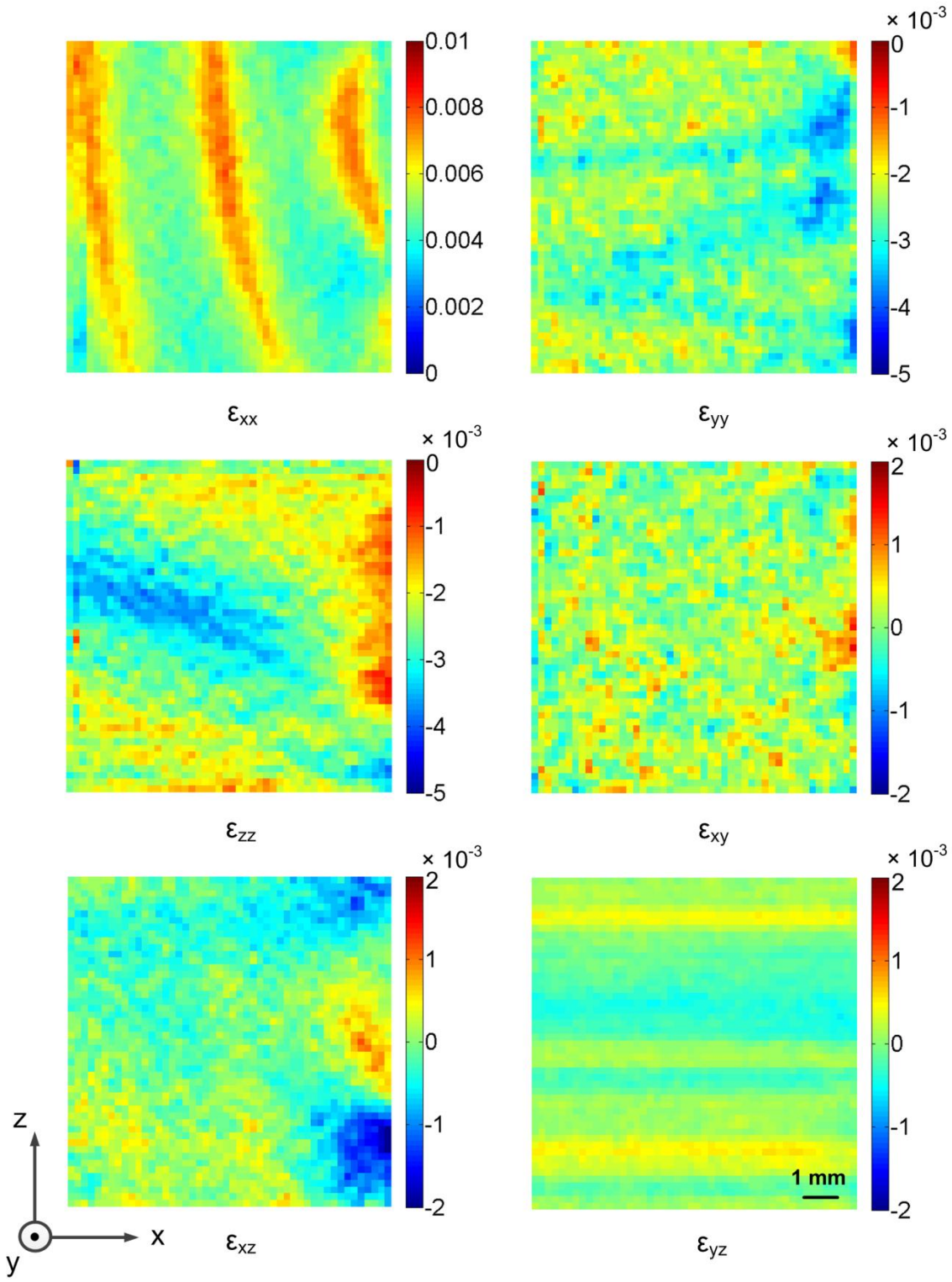

Fig 3.14: Spatial distribution of the strain components obtained for a rectangular phantom strip under tension (load step 1). The central *y*-slice 10 is shown.

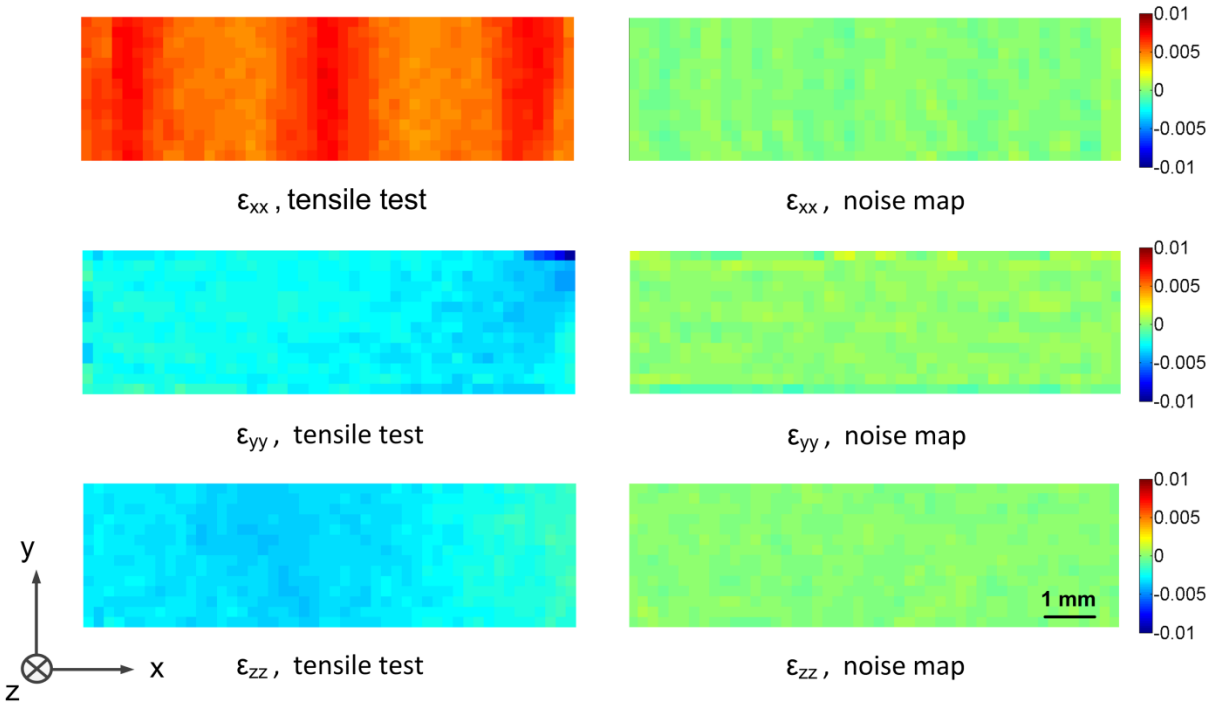

Fig 3.15: Normal strain components obtained at *z*-slice 25 for a rectangular phantom strip under tension (load step 1) and the corresponding strain noise obtained in the stationary test.

A bias in displacement directly leads to bias in strain, proportional to the slope of the displacement bias. For OCT reconstructions with fine speckle patterns e.g. for the present phantom strips, the displacement values obtained when comparing sub-volumes between reference and deformed states are likely to suffer from larger interpolation bias due to under-sampling of the speckle patterns which is further amplified when strain is calculated. It has been shown that the correlation results for the under-sampled images typically show up as a moiré-like fringe pattern in the displacement and strain fields and that it is more obvious in the latter.

In order to bring more evidence to the above discussions, a second load step was performed on the same rectangular phantom strip with an extra 10 g dead weight (we refer to this case as 'load step 2'). The idea is to see the strain maps after the tension load is doubled. Ideally, when the load is doubled, the deformation should also be doubled assuming the material is elastic. Therefore, the number of fringes for ε_{xx} as shown in Figs 3.13 and 3.14 are expected to double according to the above discussion. This is confirmed by the ε_{xx} strain maps in Fig 3.17, in which (a) central *z*-slice 25 and (b) central *y*-slice 10 are illustrated. Around 5 fringes can be observed confirming that these are due to interpolation bias in this

elastic material. It should also be pointed out that there are fewer fringes in the strain map of the other lateral strain component ε_{zz} in Fig 3.14, showing about 1.5 fringes. The reason why there are more fringes in ε_{xx} is because it is the tension direction (larger deformation in *x*-direction). As stated in the text, 2 voxels deformation corresponds to 1 bias fringe. Since the deformation along *z* is smaller than in *x*, it is not surprising that fewer fringes are observed. It has been found that after the tension load was doubled, the number of fringes in both ε_{xx} and ε_{zz} was doubled.

One way to reduce interpolation bias is to perform pre-smoothing (before the correlation) on both the reference and deformed volume data using a Gaussian low-pass filter to reduce high spatial frequency components [122, 123]. Another way is to increase the sampling density of the OCT reconstruction. These will be further discussed in Section 3.7.

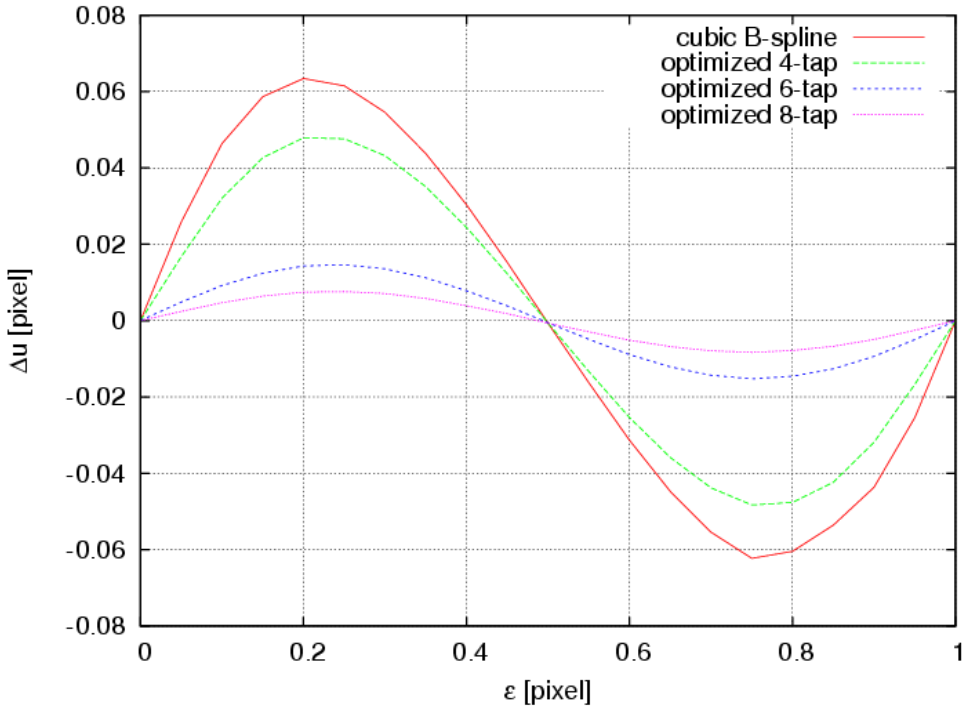

Fig 3.16: Interpolation bias as a function of sub-pixel position for different interpolation filters (Reproduced from reference [117], Sutton *et al*).

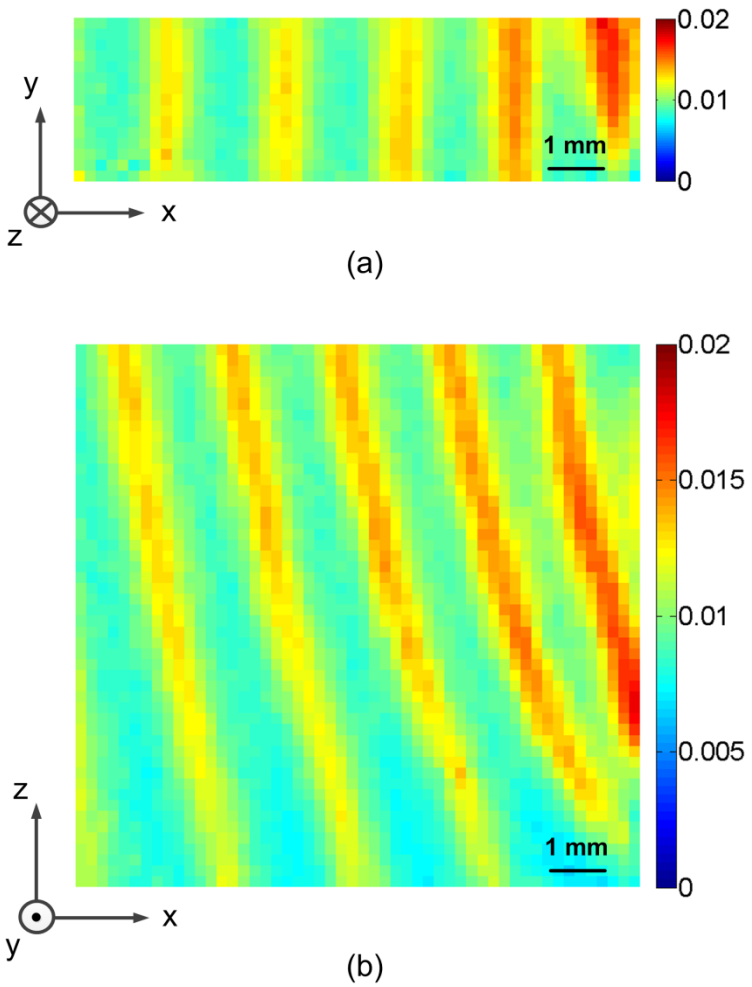

Fig 3.17: Spatial distribution of the normal strain ε_{xx} obtained for a rectangular phantom strip under tension (load step 2): (a) central *z*-slice 25 and (b) central *y*-slice 10.

3.6.3 Results for the notched phantom strip

u_x displacement maps for the notched phantom strip are shown in Fig 3.18. The left hand side shows the internal u_x displacement in a cross section cut at the central *z* position (*z*-slice 25), while the right had side shows the whole volume. It can be seen that in each *z*-slice the absolute value of u_x increases continuously along the *x*-direction from the fixed side to the other, as expected from the loading configuration and consistent with the displacement maps for the rectangular phantom strip as shown in Fig 3.11. In Fig 3.18, a slight bending of the strip can be observed from the larger u_x displacement values at the top half of the strip compared to those at the bottom half. This is probably due to the slight geometrical

asymmetry between the two notches. The geometrical asymmetry was induced during the manufacturing process when cutting the strip to a notched shape from a larger piece.

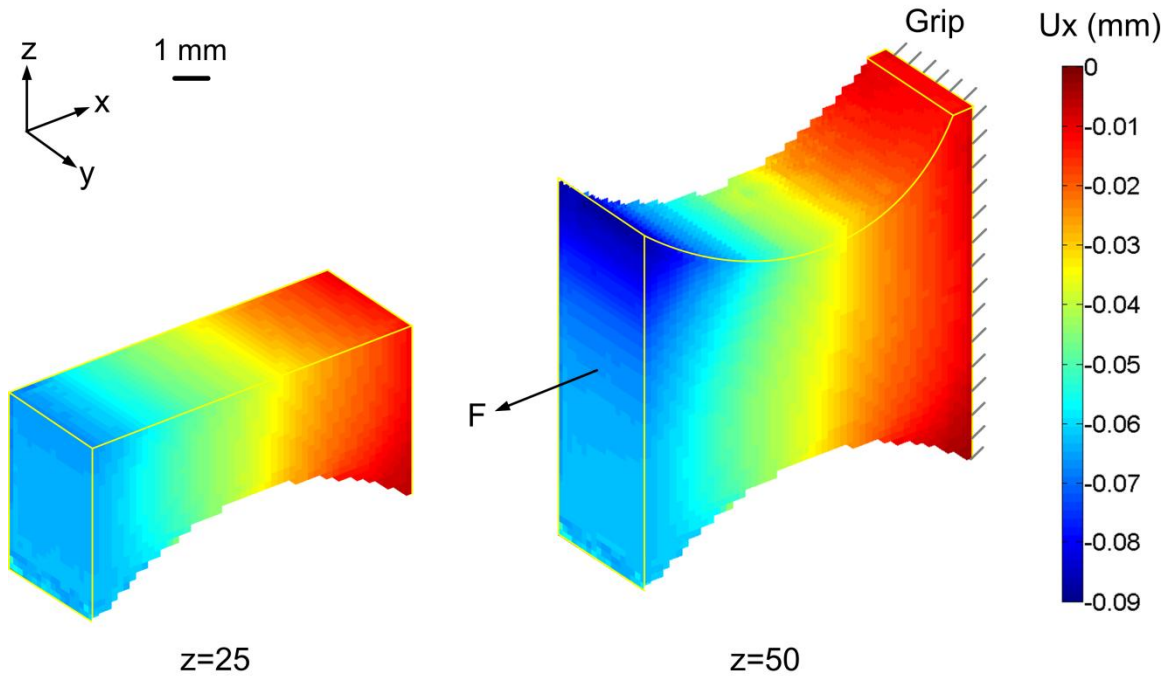

Fig 3.18: u_x displacement distribution obtained for a notched phantom strip under tension (load step 1), showing different sub-regions of the data volume.

For the notched phantom strip, all six strain components for a central *z*-slice (slice *z*=25) and a central *y*-slice (slice $y=10$) are shown in Figs 3.19 and 3.20, respectively. The ε_{xx} strain map shows positive values while the ε_{yy} and ε_{zz} strain maps show negative (compressive) values. The analysis is the same as for the strain results of the rectangular phantom strip. Due to the notched shape of the strip, larger deformation is expected in the notched region. This can be observed in the maps of normal strain components in Figs 3.19 and 3.20. In addition, strain concentration is observed near the top notch tip of the strip in Figs 3.20. This is consistent with the larger u_x displacement found near the top notch in Fig 3.18. The explanation for this local strain concentration is the geometrical asymmetry of the notched strip, which has already been stated earlier. In Fig 3.20, the ε_{xz} strain map shows an anti-symmetric shear strain distribution. Regarding the other two shear strain components, they are close to zero. These results are consistent for this type of test. It should be pointed out

however that these results also suffer from large interpolation bias, especially evident in ε_{xx}. Although the fringes are not as visible in Fig 3.20 compared with Fig 3.14, about 3 fringes still can be observed in the ε_{xx} strain map. The reason why these fringes are not so regular is because of the relatively more complex stress state (with more spatial variation) in the notched phantom compared with the rectangular phantom under uniaxial tension.

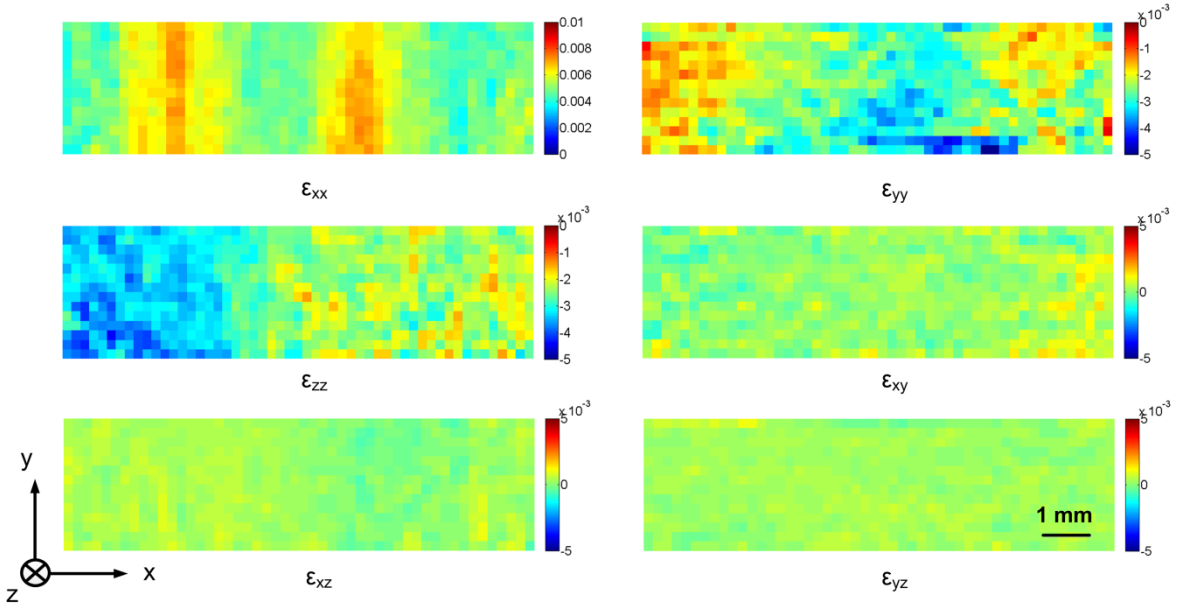

Fig 3.19: Spatial distribution of the strain components obtained for a notched phantom strip under tension (load step 1). The central *z*-slice 25 is shown.

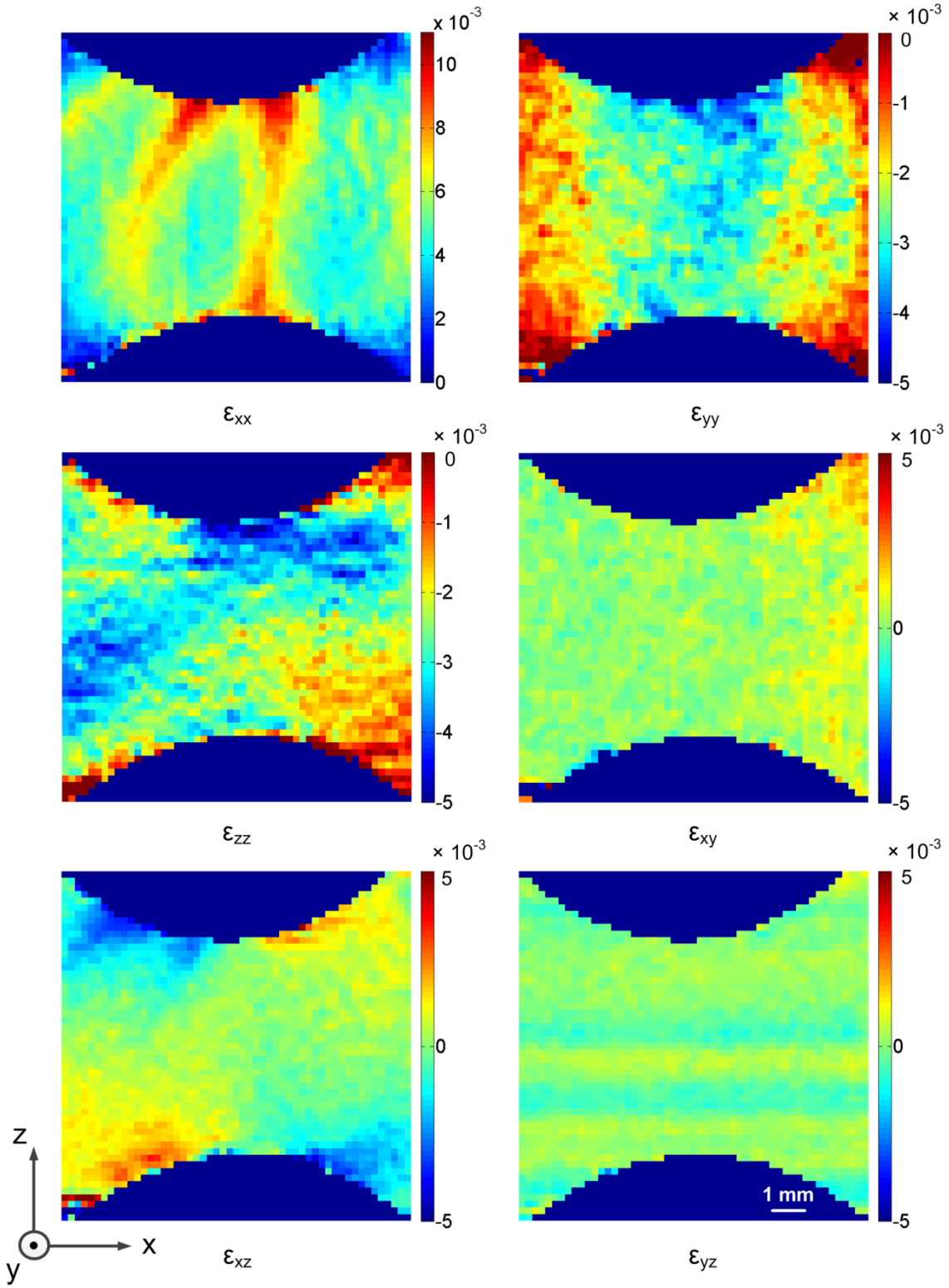

Fig 3.20: Spatial distribution of the strain components obtained for a notched phantom strip under tension (load step 1). The central *y*-slice 10 is shown.

3.7 Reduction of interpolation bias

3.7.1 Bias reduction using Gaussian pre-smoothing

Pre-smoothing of the grey level images before performing DIC using e.g. a Gaussian filter has proved effective in reducing interpolation bias [122, 123]. This is because Gaussian pre-smoothing can blur an image and reduce high-frequency components, which improves the image sampling and thus reduces the interpolation bias due to image under-sampling. A 3D Gaussian low-pass filter is expressed as

$$f(x_1, x_2, x_3) = \frac{1}{\left(\sqrt{2\pi}\sigma\right)^3} e^{-\frac{x_1^2+x_2^2+x_3^2}{2\sigma^2}} \tag{3.4}$$

where x_1, x_2, x_3 are the distances from the origin in the 3 directions, respectively. σ is the standard deviation of the Gaussian distribution. Gaussian smoothing is achieved by using the 3D distribution in Eqn. (3.4) as PSF and convolving it with the original OCT data cube. As the data cube is stored as a set of discrete voxels, a discrete approximation of the Gaussian distribution function is required. Since the Gaussian distribution is non-zero everywhere, it would require an infinitely large convolution kernel. However, in practice it is considered effectively zero for pixels at a distance more than about three standard deviations. Therefore, the kernel can be truncated at this point, and contributions from pixels outside that range can be ignored. Once a suitable kernel has been selected, the Gaussian smoothing can be performed using standard convolution methods. Gaussian smoothing outputs a new value for each pixel using a weighted average of that pixel's neighbourhood. The value of the original pixel receives the heaviest weight and values of the neighbouring pixels receive smaller weights as their distance to the original pixel increases.

To determine a proper Gaussian filter that can reduce the interpolation bias due to image under-sampling, 4 Gaussian filters were selected with the kernel size increasing successively. The four Gaussian filters are defined as: $\sigma = 0.65$ with kernel size $3\times3\times3$, $\sigma = 1.0$ with kernel size $5\times5\times5$, $\sigma = 1.5$ with kernel size $7\times7\times7$ and $\sigma = 2.0$ with kernel size $9\times9\times9$, respectively. These filters were applied to the reconstructed volume data for both the reference and deformed states prior to correlation. Figure 3.21 shows a transverse *z*-slice of the rectangular phantom strip in the reference state before and after pre-smoothing. It can be

observed that the image is apparently blurred for the Gaussian filter with $\sigma = 2.0$ and kernel size $9 \times 9 \times 9$ and also the larger filter. High-frequency details are attenuated.

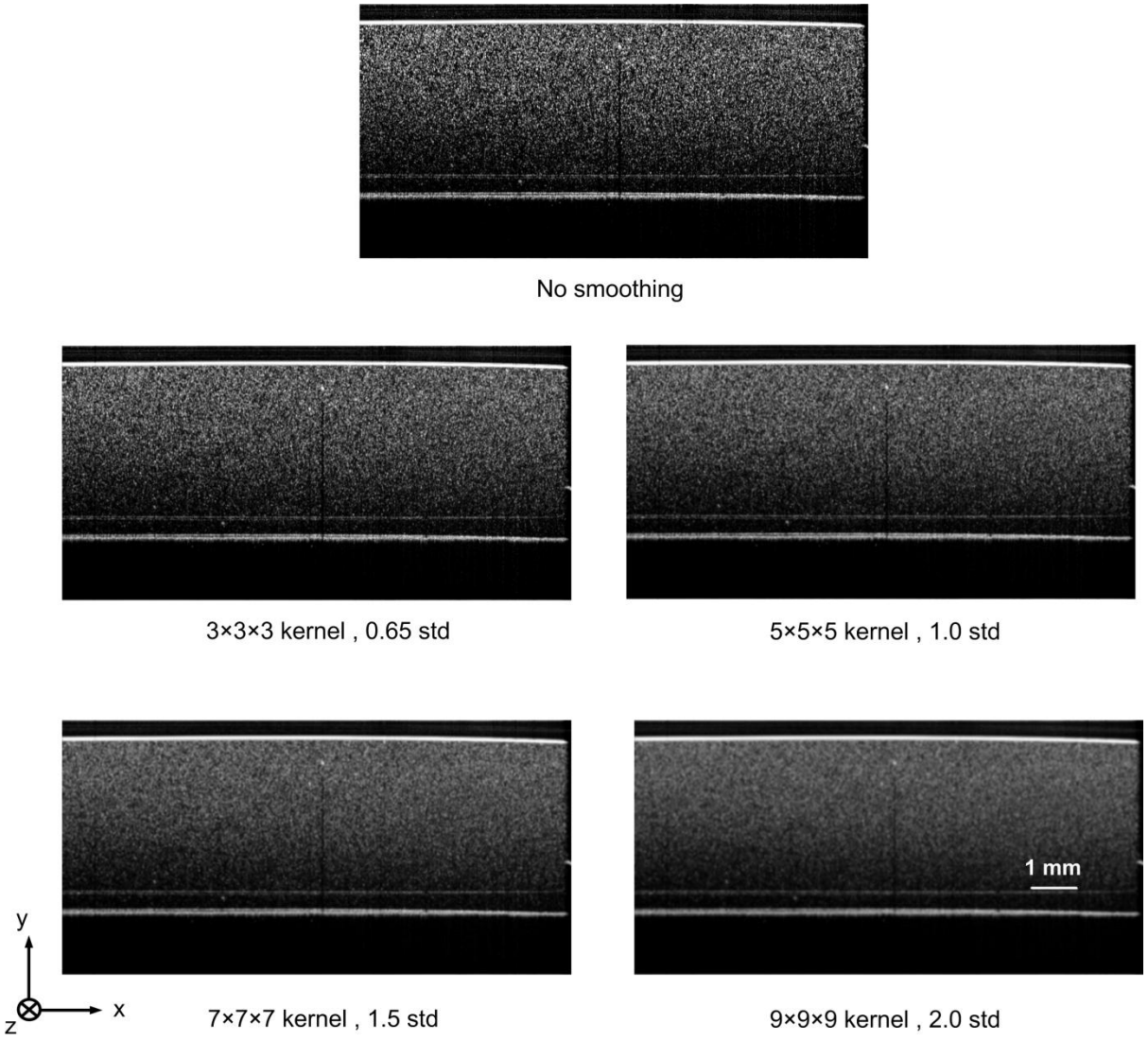

Fig 3.21: 2D views of a transverse *z*-slice of the reference state of the rectangular phantom strip before and after Gaussian pre-smoothing.

The smoothed data volume was then used to perform DVC. The resulting ε_{xx} strain maps with and without pre-smoothing are shown in Fig 3.22 for a transverse *z*-slice. One can see that the fringes become less evident as the Gaussian filter becomes larger. However, this also leads to an increase in the strain standard deviation, as can be seen from the ε_{xx} strain map with the $9 \times 9 \times 9$ Gaussian filter. The reason for this increase has been explained by Pan in [123], which states that the sum of squares of subset intensity gradient (SSSIG) is reduced

after smoothing, and the standard deviation error is inversely proportional to the SSSIG value. In this case, the Gaussian filter with $\sigma = 1.5$ and kernel size $7 \times 7 \times 7$ was kept for this study.

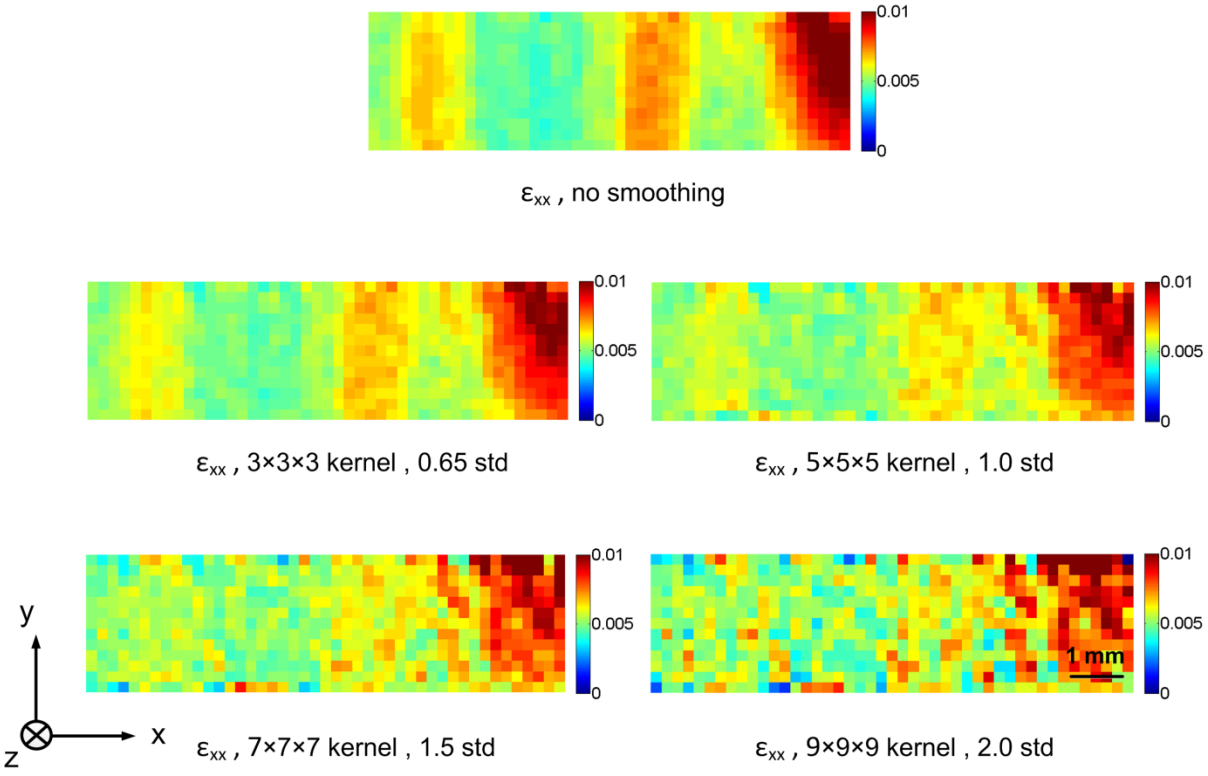

Fig 3.22: ε_{xx} strain maps with and without pre-smoothing for a transverse *z*-slice.

The difference between the measured and the fitted mean u_x displacement of each *yz*-cross section as a function of *x*-position with and without pre-smoothing are compared in Fig 3.23 for the rectangular phantom strip. The difference is substantially reduced after pre-smoothing, which is expected according to [122, 123]. Gaussian smoothing was also applied to the volume data of the stationary and rigid body translation tests in order to check its influence in the strain resolution. The results show an increase in the strain standard deviations with pre-smoothing, generally ranging from 4×10^{-4} to 8×10^{-4}, as shown in Figs 3.24 (a) and (b) for the stationary and rigid body translation tests, respectively. The reason for this increase has been explained earlier for the ε_{xx} strain maps for the different Gaussian filters in Fig 3.22. In any case, these noise levels may still be considered as acceptable compared with the strain levels of the tensile tests (about one order of magnitude larger). Fig 3.25 shows the central *y*-slice 10 for the ε_{xx} strain maps with and without pre-smoothing for the rectangular and

notched phantom strips. The fringes due to interpolation bias are eliminated after pre-smoothing.

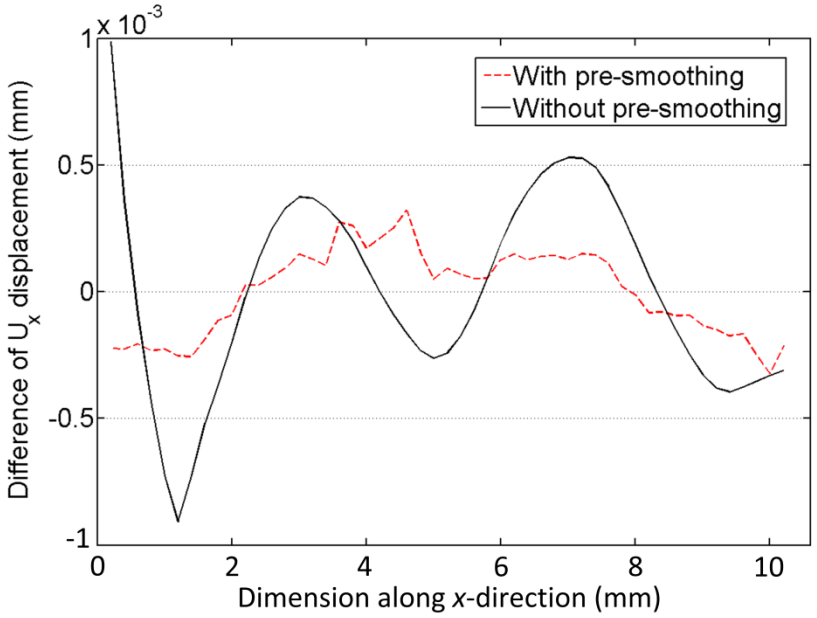

Fig 3.23: Difference between the u_x displacement averaged within yz-cross sections along the x-direction and a linear data fit obtained for a rectangular phantom strip under tension (load step 1), with and without pre-smoothing.

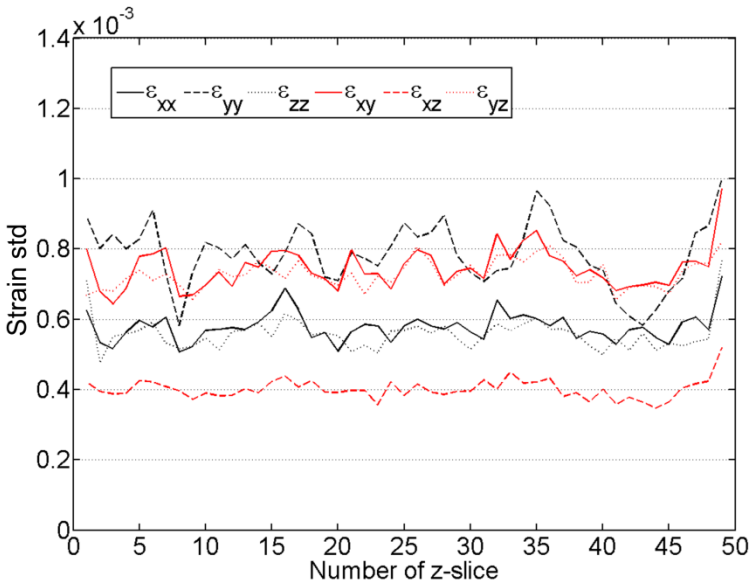

(a)

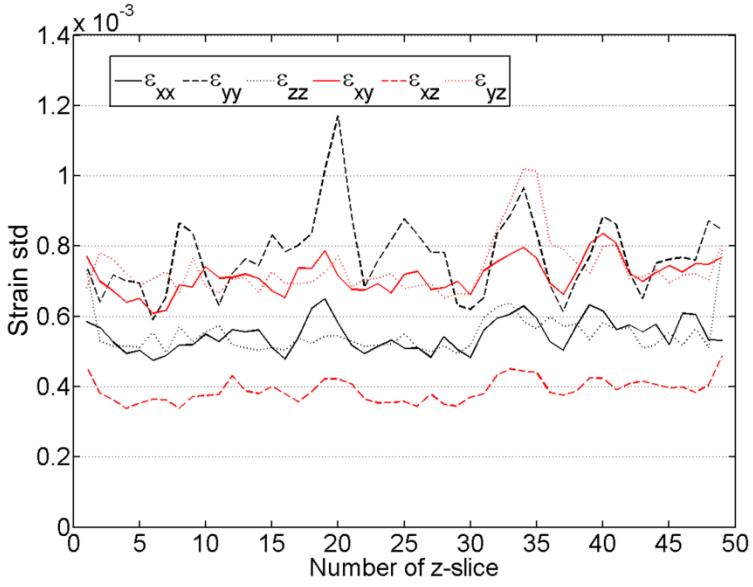

(b)

Fig 3.24: Strain standard deviations obtained with 36^3 voxels sub-volume, 50% overlap and Gaussian pre-smoothing for: (a) Stationary test and (b) Rigid body translation test.

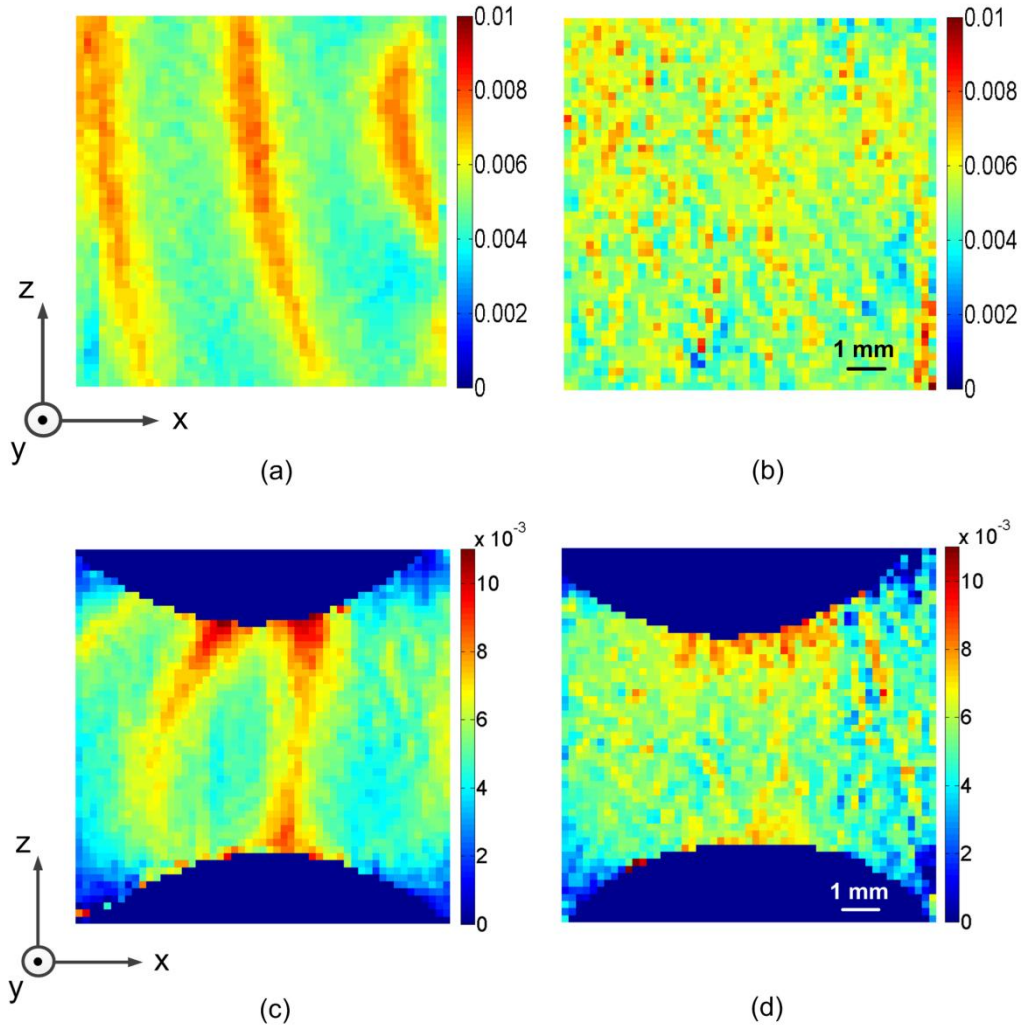

Fig 3.25: Spatial distributions of the normal strain ε_{xx} obtained at central *y*-slice 10 for phantom strips under tension (load step 1): (a) Rectangular, without pre-smoothing (b) Rectangular, with pre-smoothing, (c) Notched, without pre-smoothing, (d) Notched, with pre-smoothing.

3.7.2 Bias reduction by increasing sampling density

It was stated in section 3.6.2 that for the samples studied in this work, the reconstructed OCT images are under-sampled due to the fine speckle patterns. In this section, two tensile tests were performed on two rectangular silicone rubber phantom strips of different dimensions. Larger copper particles with an average particle size of about 10 μm, about 10 times larger than the fine particles stated in section 3.2, were used with the hope that this would increase the OCT signal. This choice, however, is not recommended as the speckle field could turn too sparse as the particles are close to the resolving power of the OCT system (a situation

common in particle image velocimetry) with a loss of spatial resolution in the displacement fields. Another drawback of using large scattering particles is that they can increase wavefront distortion of the imaging beam, which compromises image quality as stated by Wang *et al* [124]. The average speckle size corresponds to the 3D PSF of the SS-OCT system, which is 8.3 μm (axial) × 25 μm (transverse) and is a function of the source central wavelength and the effective NA of the OCT objective.

In the first test, a $60\times1.4\times10$ mm^3 rectangular phantom strip ($length\times thickness\times width$) as the one in section 3.2 was tested. A $11\times3\times11$ mm^3 region was scanned, corresponding to *x*, *y* and *z* directions, respectively. A 3D data volume of $1024\times512\times1024$ voxels was obtained. In the second test, a narrower strip $60\times1.4\times5$ mm^3 ($length\times thickness\times width$) was tested. The scanned region for this second strip was $5.5\times2.5\times5.5$ mm^3, corresponding to *x*, *y* and *z* directions, respectively. The corresponding voxel dimensions of this scanned region remained the same at $1024\times512\times1024$ voxels. For both tests, the same loading configuration as 'load step 1' was applied (50 g dead weight preload plus 10 g dead weight load). Thus, in the first test the lateral image voxel size remained unchanged (10.7 μm) as in the tests described in section 3.3, only the average particle size becoming larger. In the second test, the lateral voxel size was reduced to 5.35 μm as the sampling density was doubled.

Fig 3.26 (a) shows the 2D view of a transverse *z*-slice in the $60\times1.4\times10$ mm^3 phantom strip while Fig 3.26 (b) shows the $60\times1.4\times5$ mm^3 strip. It can be observed that the speckle grains appear larger for the second strip in Fig. 3.26(b) as twice as many lateral scans are used to sample them in that direction. Note that the same number of voxels is used in both cases in all directions.

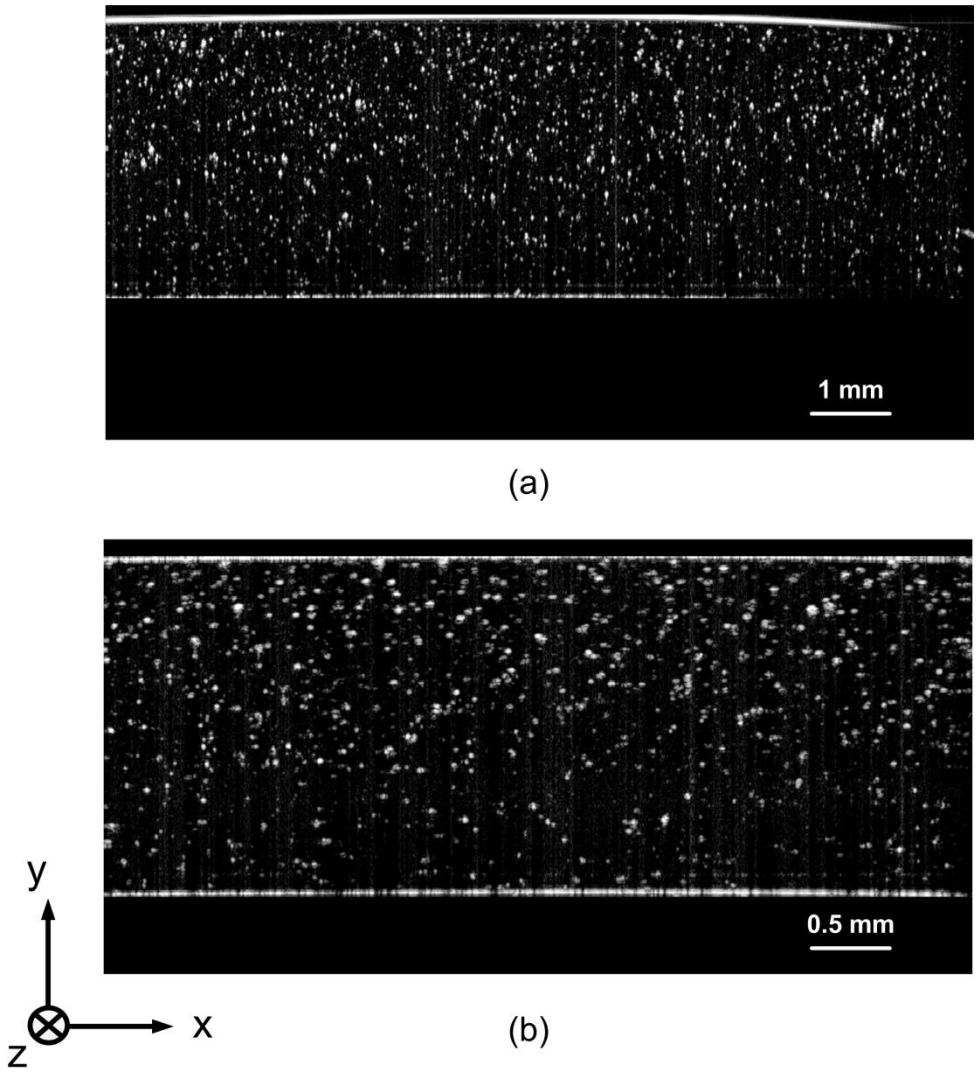

Fig 3.26: 2D views of a transverse *z*-slice of the rectangular phantom strips seeded with 10μm copper particles: (a) $60\times1.4\times10$ mm^3 rectangular phantom strip, $11\times3\times11$ mm^3 region of interest and (b) $60\times1.4\times5$ mm^3 rectangular phantom strip, $5.5\times2.5\times5.5$ mm^3 region of interest. Data cubes in both cases contain $1024\times512\times1024$ voxels.

The spatial distribution of the displacement component u_x and the lateral strain components ε_{xx} and ε_{zz} obtained for the $60\times1.4\times10$ mm^3 phantom strip are shown in Fig 3.27 for the central *y*-slice 10. From the ε_{xx} strain map, one can see about 2.5 fringes, which correspond to about 5 voxels total u_x deformation. Similarly, fringes can also be observed from the ε_{zz} strain map. As compared with the results in section 3.6.2, increasing the size of the seeded particles does not reduce the interpolation bias, as expected.

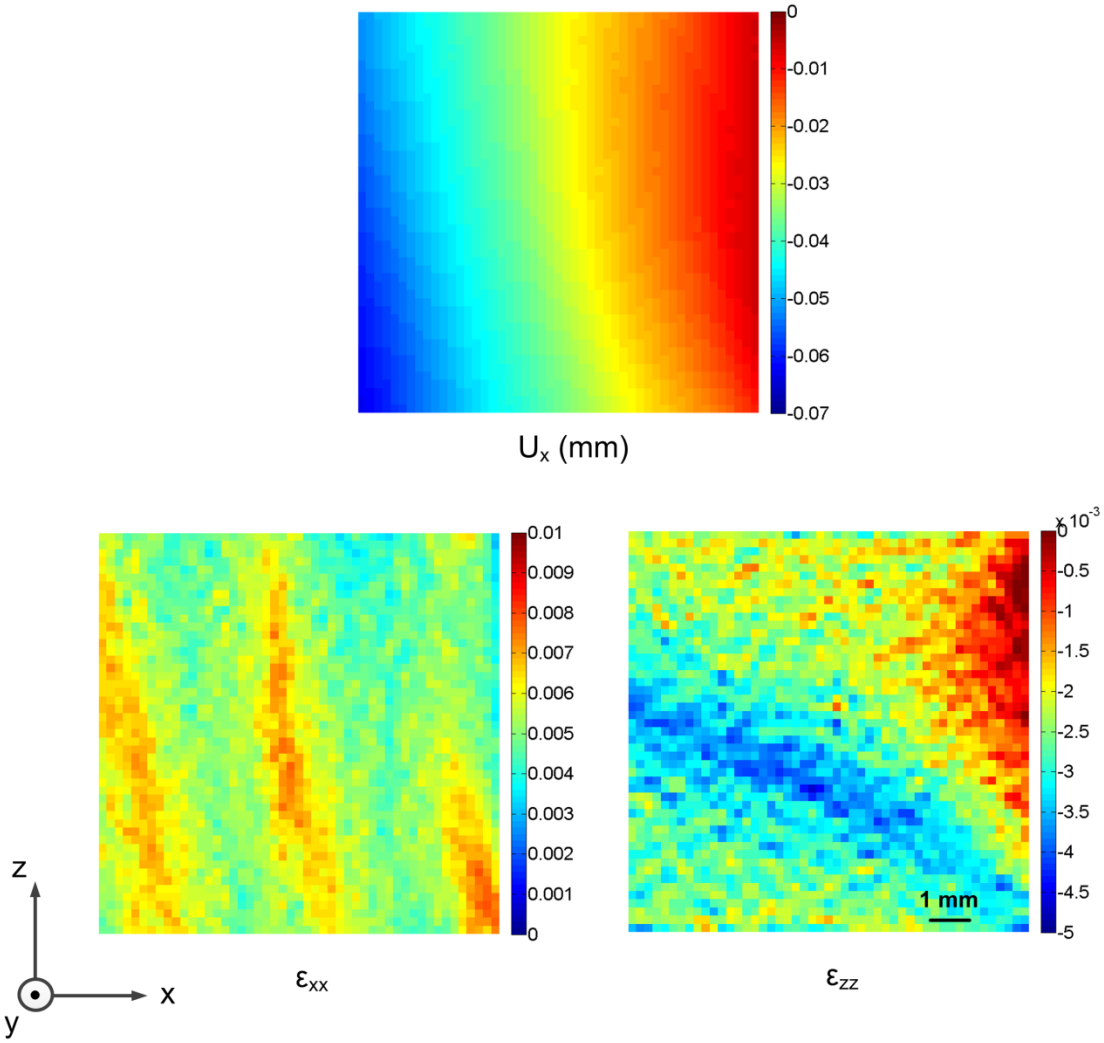

Fig 3.27: Spatial distribution of the displacement component u_x and the lateral strain components ε_{xx} and ε_{zz} obtained for the $60\times1.4\times10$ mm^3 rectangular phantom strip seeded with 10μm copper particles under tension (load step 1). Dimensions of the scanned region are $11\times3\times11$ mm^3 corresponding to $1024\times512\times1024$ voxels. The central *y*-slice 10 is shown.

In Fig 3.28, the spatial distribution of the displacement component u_x and the lateral strain components ε_{xx} and ε_{zz} obtained for the $60\times1.4\times5$ mm^3 phantom strip are shown for the central *y*-slice 10. As the total u_x deformation is about 12 voxels, similar to the strain distribution shown in Fig 3.17, the ε_{xx} strain map here should also show about 6 fringes if the reconstructed images were aliased. However, in Fig 3.28 one can see that there are not apparent fringes in the ε_{xx} strain map nor in the ε_{zz} strain map. Besides, as can be seen in Fig 3.26 (b) the speckle size increases substantially in terms of voxels. The interpolation bias

is thus substantially reduced by doubling the lateral sampling density of the OCT reconstructions.

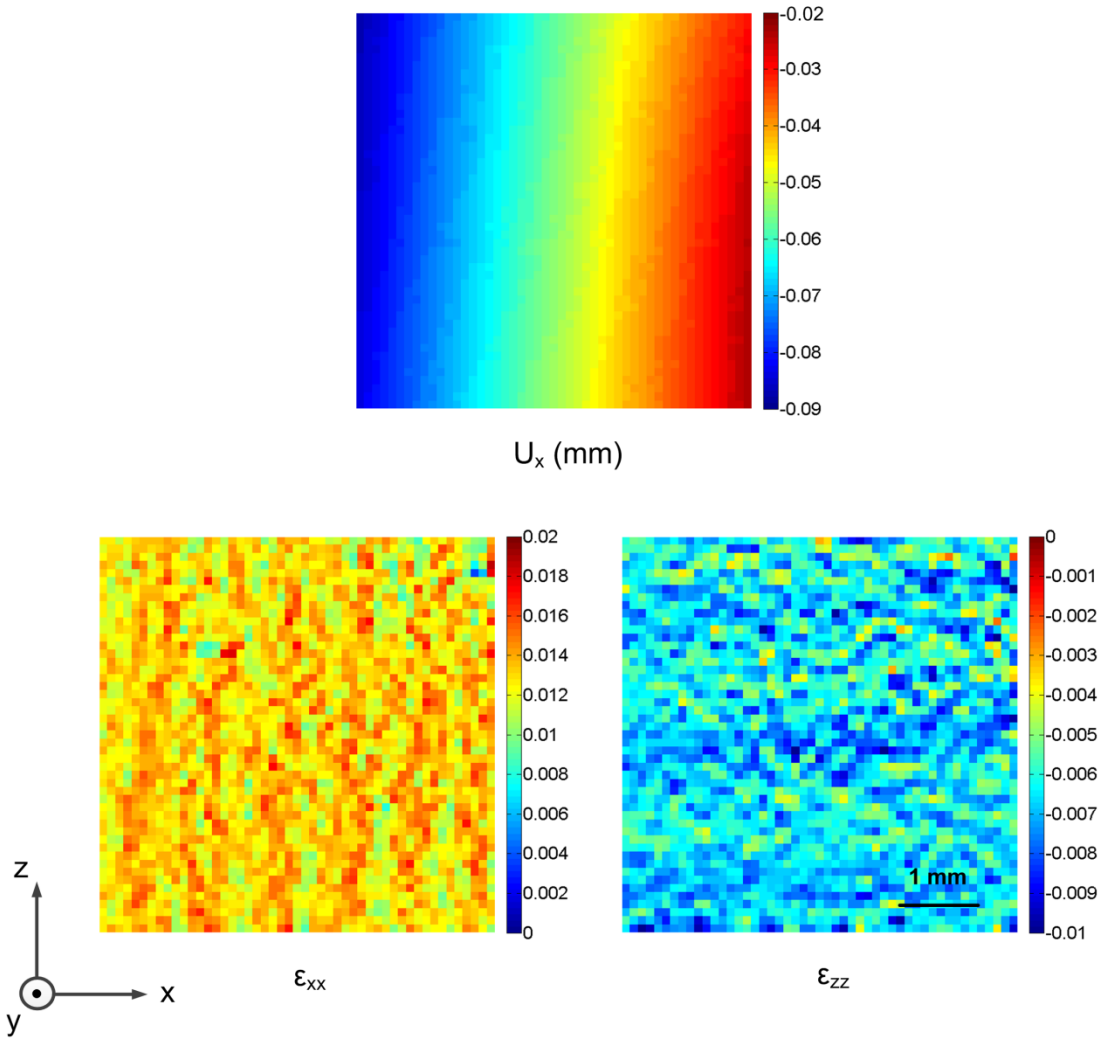

Fig 3.28: Spatial distribution of the displacement component u_x and the lateral strain components ε_{xx} and ε_{zz} obtained for the $60\times1.4\times5$ mm^3 rectangular phantom strip seeded with 10µm copper particles under tension (load step 1). Dimensions of the scanned region are $5.5\times2.5\times5.5$ mm^3 corresponding to $1024\times512\times1024$ voxels. The central *y*-slice 10 is shown.

Therefore, to conclude this section, the interpolation bias due to image under-sampling can be reduced either by performing pre-smoothing (e.g. Gaussian smoothing) to the grey level data volumes prior to the volume correlation or by increasing the sampling density of the OCT reconstructions, even though this latter approach leads to a reduced field of view on the specimen.

3.8 Identification of elasticity for phantom specimens

The objective of this section is to evaluate the availability of utilizing the strain measurements from section 3.6 (for the rectangular and notched phantom strips) to identify the elasticity of the silicone rubber phantoms. Isotropic elasticity was chosen here as the material constitutive model, and Young's modulus E and Poisson's ratio ν are the sought quantities. Since the two specimens were manufactured using the same material, the identification results for all these tensile tests are expected to be consistent with each other. Efforts are also made to identify the shear modulus G and bulk modulus K from the strain results of the rectangular phantom strip tensile test. For all the simple tension configurations, 3D manually defined virtual fields were selected for the identification.

3.8.1 Identification of Young's modulus E and Poisson's ratio ν

3.8.1.1 Selection of 3D manually defined virtual fields

According to section 2.2, two different virtual fields are required to retrieve the Young's modulus E and Poisson's ratio ν for isotropic elasticity. The first virtual displacement fields and the corresponding virtual strain fields are:

$$\begin{cases} u_x^{*(1)} = x - L \\ u_y^{*(1)} = 0 \\ u_z^{*(1)} = 0 \end{cases} \qquad \begin{cases} \varepsilon_{xx}^{*(1)} = 1 \\ \varepsilon_{yy}^{*(1)} = 0 \\ \varepsilon_{zz}^{*(1)} = 0 \\ \varepsilon_{yz}^{*(1)} = 0 \\ \varepsilon_{xz}^{*(1)} = 0 \\ \varepsilon_{xy}^{*(1)} = 0 \end{cases} \tag{3.5}$$

For the second virtual field:

$$\begin{cases} u_x^{*(2)} = 0 \\ u_y^{*(2)} = xy(x - L) \\ u_z^{*(2)} = 0 \end{cases} \qquad \begin{cases} \varepsilon_{xx}^{*(2)} = 0 \\ \varepsilon_{yy}^{*(2)} = x(x - L) \\ \varepsilon_{zz}^{*(2)} = 0 \\ \varepsilon_{yz}^{*(2)} = 0 \\ \varepsilon_{xz}^{*(2)} = 0 \\ \varepsilon_{xy}^{*(2)} = xy - \frac{1}{2} yL \end{cases} \tag{3.6}$$

where L is the length (dimension along the x-direction) of the phantom strips.

After introducing the above two virtual fields (3.5) and (3.6) into the equilibrium equation (2.10), a linear equation system (3.7) can be formed to directly determine the sought stiffness components Q_{xx} and Q_{xy}.

$$\boldsymbol{AQ} = \boldsymbol{B} \tag{3.7}$$

with

$$\boldsymbol{A}: \begin{bmatrix} \int_V \varepsilon_{xx} dV & \int_V (\varepsilon_{yy} + \varepsilon_{zz}) dV \\ \int_V \left(x(x-L)\varepsilon_{yy} + (2xy - yL)\varepsilon_{xy}\right) dV & \int_V \left(x(x-L)(\varepsilon_{xx} + \varepsilon_{zz}) - (2xy - yL)\varepsilon_{xy}\right) dV \end{bmatrix}$$

$$\boldsymbol{Q}: \begin{Bmatrix} Q_{xx} \\ Q_{xy} \end{Bmatrix} \qquad \boldsymbol{B}: \begin{Bmatrix} -FL \\ 0 \end{Bmatrix}$$

where F is the tension load at the position $x = 0$, and $-L$ represents the virtual displacement at the same position calculated from equation (3.5) for the first virtual field. $-FL$ represents the external virtual work done by the tension load.

Finally, similar to the discussion in section 2.3.2, the linear equation system (3.7) can be written as:

$$\begin{bmatrix} \overline{\varepsilon_{xx}} & \overline{\varepsilon_{yy} + \varepsilon_{zz}} \\ \overline{x(x-L)\varepsilon_{yy}} + \overline{(2xy - yL)\varepsilon_{xy}} & \overline{x(x-L)(\varepsilon_{xx} + \varepsilon_{zz})} - \overline{(2xy - yL)\varepsilon_{xy}} \end{bmatrix} \begin{Bmatrix} Q_{xx} \\ Q_{xy} \end{Bmatrix} = \begin{Bmatrix} \dfrac{-FL}{V} \\ 0 \end{Bmatrix} \tag{3.8}$$

3.8.1.2 Identification results

Using the experimental strain results in the linear equation system (3.8), the material stiffness components Q_{xx} and Q_{xy} can then be directly determined for the two tensile tests. The identification results with and without pre-smoothing are listed in Tables 3.1 and 3.2, respectively. From these results Young's modulus E and Poisson's ratio ν can be calculated through the relations stated in equation (2.9). In order to provide a reference for the stiffness parameters obtained through the VFM, Young's modulus and Poisson's ratio were also calculated for the rectangular strip based on the assumption of constant uniaxial stress through the relation:

$$\begin{cases} E = \dfrac{\sigma_x}{\varepsilon_x} \\ \nu = -\dfrac{\varepsilon_y}{\varepsilon_x} \end{cases} \tag{3.9}$$

where uniform stress σ_x in the *yz* cross-section of the rectangular phantom strip was determined through the equation $\sigma_x = \dfrac{F}{A}$. F is the tension load and A is the *yz* cross-sectional area. ε_x and ε_y are the average values of the corresponding strain components over the whole field of view. Thus, both Young's modulus and Poisson's ratio can be derived and the results are listed in Tables 3.1 and 3.2. In both tensile tests the results obtained from the VFM are consistent with each other and also with those calculated from the constant uniaxial stress assumption. They are also consistent with the Young's modulus 1.47 MPa measured with a tensile testing machine for the rectangular phantom strip. This indicates that the 3D VFM is an effective tool to identify the constitutive parameters of materials with non-uniform stress/strain states when the constant uniaxial stress assumption is no longer applicable. Moreover, the identification results with pre-smoothing are in agreement with those without pre-smoothing when comparing Table 3.1 to Table 3.2.

Table 3.1: Identified material elastic stiffness parameters without pre-smoothing.

	Q_{xx} (MPa)	Q_{xy} (MPa)	E (MPa)	ν
VFM (rectangular, load step 1)	3.45	2.44	1.44	0.41
VFM (rectangular, load step 2)	3.48	2.44	1.47	0.41
Constant Stress (rectangular, load step 1)	3.65	2.64	1.43	0.42
VFM (Notched, load step 1)	3.24	2.18	1.49	0.40

Table 3.2: Identified material elastic stiffness parameters with pre-smoothing.

	Q_{xx} (MPa)	Q_{xy} (MPa)	E (MPa)	ν
VFM (rectangular, load step 1)	3.39	2.40	1.40	0.41
VFM (rectangular, load step 2)	3.26	2.23	1.45	0.41
Constant Stress (rectangular, load step 1)	3.55	2.57	1.39	0.42
VFM (Notched, load step 1)	3.18	2.09	1.51	0.40

3.8.2 Identification of shear modulus G and bulk modulus K

3.8.2.1 Equations

In some cases, it might be inconvenient to identify the stiffness components Q_{ij} when the Poisson's ratio of materials is very close to 0.5. As can be seen from the equation (2.9), Q_{ij} will become very large when ν is very close to 0.5. In this case, a small error in ν will lead to a large error in Q_{ij}. Bulk modulus K and shear modulus G are other constitutive parameters for measuring the stiffness of materials. Bulk modulus K measures the material's resistance to uniform compression, while Shear modulus G measures the material's resistance to shear deformation. Instead of identifying Q_{ij}, K and G offer another option for measuring the material properties when ν is very close to 0.5.

For linear elasticity, the general form of Hook's law can be written as

$$\boldsymbol{\sigma} = KTr(\boldsymbol{\varepsilon})\boldsymbol{I} + 2G\left[\boldsymbol{\varepsilon} - \frac{1}{3}Tr(\boldsymbol{\varepsilon})\boldsymbol{I}\right] \tag{3.10}$$

where Tr is the trace operator and $Tr(\boldsymbol{\varepsilon}) = \varepsilon_{11} + \varepsilon_{22} + \varepsilon_{33}$. $\boldsymbol{I}$ is the identity matrix. The stress and strain components are related by K and G as

$$\begin{cases} \sigma_1 = (\varepsilon_1+\varepsilon_2+\varepsilon_3)K + 2G\left(\frac{2}{3}\varepsilon_1 - \frac{1}{3}\varepsilon_2 - \frac{1}{3}\varepsilon_3\right) \\ \sigma_2 = (\varepsilon_1+\varepsilon_2+\varepsilon_3)K + 2G\left(\frac{2}{3}\varepsilon_2 - \frac{1}{3}\varepsilon_1 - \frac{1}{3}\varepsilon_3\right) \\ \sigma_3 = (\varepsilon_1+\varepsilon_2+\varepsilon_3)K + 2G\left(\frac{2}{3}\varepsilon_3 - \frac{1}{3}\varepsilon_1 - \frac{1}{3}\varepsilon_2\right) \\ \sigma_4 = 2G\varepsilon_4 \\ \sigma_5 = 2G\varepsilon_5 \\ \sigma_6 = 2G\varepsilon_6 \end{cases} \tag{3.11}$$

After introducing equation (3.11) into equilibrium equation (2.2), the equilibrium equation (2.2) becomes

$$\int_V K(\varepsilon_1+\varepsilon_2+\varepsilon_3)(\varepsilon_1^*+\varepsilon_2^*+\varepsilon_3^*)dV + \int_V 2G\left[\left(\frac{2}{3}\varepsilon_1 - \frac{1}{3}\varepsilon_2 - \frac{1}{3}\varepsilon_3\right)\varepsilon_1^* + \left(\frac{2}{3}\varepsilon_2 - \frac{1}{3}\varepsilon_1 - \frac{1}{3}\varepsilon_3\right)\varepsilon_2^* + \left(\frac{2}{3}\varepsilon_3 - \frac{1}{3}\varepsilon_1 - \frac{1}{3}\varepsilon_2\right)\varepsilon_3^* + \varepsilon_4\varepsilon_4^* + \varepsilon_5\varepsilon_5^* + \varepsilon_6\varepsilon_6^*\right]dV = \int_{\partial V} \bar{\boldsymbol{T}}\cdot\boldsymbol{u}^* dS \tag{3.12}$$

For homogeneous materials, the equation above becomes

$$K\int_V (\varepsilon_1+\varepsilon_2+\varepsilon_3)(\varepsilon_1^*+\varepsilon_2^*+\varepsilon_3^*)dV + G\int_V 2\left[\left(\frac{2}{3}\varepsilon_1 - \frac{1}{3}\varepsilon_2 - \frac{1}{3}\varepsilon_3\right)\varepsilon_1^* + \left(\frac{2}{3}\varepsilon_2 - \frac{1}{3}\varepsilon_1 - \frac{1}{3}\varepsilon_3\right)\varepsilon_2^* + \left(\frac{2}{3}\varepsilon_3 - \frac{1}{3}\varepsilon_1 - \frac{1}{3}\varepsilon_2\right)\varepsilon_3^* + \varepsilon_4\varepsilon_4^* + \varepsilon_5\varepsilon_5^* + \varepsilon_6\varepsilon_6^*\right]dV = \int_{\partial V} \bar{\boldsymbol{T}}\cdot\boldsymbol{u}^* dS \tag{3.13}$$

Two virtual fields are needed to identify the bulk modulus K and shear modulus G. Thus, similar to the identification for Q_{ij}, a linear equation system can be formed, which is written

$$\boldsymbol{AM} = \boldsymbol{B} \tag{3.14}$$

with

$$\boldsymbol{A} = \begin{bmatrix} A_{11} & A_{12} \\ A_{21} & A_{22} \end{bmatrix} \qquad \boldsymbol{M} = \begin{Bmatrix} K \\ G \end{Bmatrix} \qquad \boldsymbol{B} = \begin{Bmatrix} \int_{\partial v} \bar{T}.u^{*(1)} dS \\ \int_{\partial v} \bar{T}.u^{*(2)} dS \end{Bmatrix}$$

where

$$
\begin{cases}
A_{11} = \int_V (\varepsilon_1 + \varepsilon_2 + \varepsilon_3)(\varepsilon_1^{*(1)} + \varepsilon_2^{*(1)} + \varepsilon_3^{*(1)})dV \\
A_{12} = \int_v 2\left[\left(\frac{2}{3}\varepsilon_1 - \frac{1}{3}\varepsilon_2 - \frac{1}{3}\varepsilon_3\right)\varepsilon_1^{*(1)} + \left(\frac{2}{3}\varepsilon_2 - \frac{1}{3}\varepsilon_1 - \frac{1}{3}\varepsilon_3\right)\varepsilon_2^{*(1)} + \ldots \right. \\
\qquad \left. \ldots + \left(\frac{2}{3}\varepsilon_3 - \frac{1}{3}\varepsilon_1 - \frac{1}{3}\varepsilon_2\right)\varepsilon_3^{*(1)} + \varepsilon_4\varepsilon_4^{*(1)} + \varepsilon_5\varepsilon_5^{*(1)} + \varepsilon_6\varepsilon_6^{*(1)}\right]dV \\
A_{21} = \int_V (\varepsilon_1 + \varepsilon_2 + \varepsilon_3)(\varepsilon_1^{*(2)} + \varepsilon_2^{*(2)} + \varepsilon_3^{*(2)})dV \\
A_{22} = \int_v 2\left[\left(\frac{2}{3}\varepsilon_1 - \frac{1}{3}\varepsilon_2 - \frac{1}{3}\varepsilon_3\right)\varepsilon_1^{*(2)} + \left(\frac{2}{3}\varepsilon_2 - \frac{1}{3}\varepsilon_1 - \frac{1}{3}\varepsilon_3\right)\varepsilon_2^{*(2)} + \ldots \right. \\
\qquad \left. \ldots + \left(\frac{2}{3}\varepsilon_3 - \frac{1}{3}\varepsilon_1 - \frac{1}{3}\varepsilon_2\right)\varepsilon_3^{*(2)} + \varepsilon_4\varepsilon_4^{*(2)} + \varepsilon_5\varepsilon_5^{*(2)} + \varepsilon_6\varepsilon_6^{*(2)}\right]dV
\end{cases}
$$

After introducing the same two virtual fields (3.5) and (3.6) into the linear equation system (3.14) and substituting the integrals using discrete sums, a linear equation system to identify K and G can be formed, which is written

$$
\begin{bmatrix}
\overline{\varepsilon_{xx} + \varepsilon_{yy} + \varepsilon_{zz}} & \overline{2\left(\frac{2}{3}\varepsilon_{xx} - \frac{1}{3}\varepsilon_{yy} - \frac{1}{3}\varepsilon_{zz}\right)} \\
\overline{(\varepsilon_{xx} + \varepsilon_{yy} + \varepsilon_{zz})x(x-L)} & \overline{2\left(\frac{2}{3}\varepsilon_{yy} - \frac{1}{3}\varepsilon_{xx} - \frac{1}{3}\varepsilon_{zz}\right)x(x-L)} - 8\overline{\varepsilon_{xy}\left(xy - \frac{1}{2}yL\right)}
\end{bmatrix}
\begin{Bmatrix} K \\ G \end{Bmatrix} = \begin{Bmatrix} \frac{-FL}{V} \\ 0 \end{Bmatrix}
\tag{3.15}
$$

3.8.2.2 Identification results

It should be pointed out that it is impossible to reliably extract K and G from the strain data of the rectangular phantom strip tensile test because there is no shear deformation in this test configuration. Therefore, only the strain data of the notched phantom strip tensile test (load step 1) was used here for identification. After solving the linear equation system (3.15) in Matlab®, K and G were determined as: $K = 2.56\ MPa$, and $G = 0.53\ MPa$.

In order to provide a reference for the above identification results, K and G were also calculated from the Young's modulus E and Poisson's ratio ν identified for the notched phantom strip (load step 1) using VFM as listed in Table 3.1. K and G are related to E and ν through

$$\begin{cases} K = \dfrac{E}{3(1-2\nu)} \\ G = \dfrac{E}{2(1+\nu)} \end{cases} \tag{3.16}$$

The results from the above equations are $K = 2.54\,MPa$, and $G = 0.53\,MPa$, which are highly consistent with the results calculated from equation (3.15).

3.9 Conclusions

We have shown that DVC can provide, by means of OCT data, multicomponent displacement fields from which all the strain components required by inversion methods such as the 3D VFM can be evaluated. OCT+DVC has low displacement sensitivity compared to phase-sensitive OCT elastography, and seems appropriate for strain as large as ~2% (in the axial direction) above which an incremental approach should be used to avoid speckle decorrelation. A strain uncertainty in the order of $\sim 2\times10^{-4}$ to $\sim 3.5\times10^{-4}$ was observed by performing noise analysis. Strain below this uncertainty level would require an alternative approach such as phase-sensitive OCT, capable of detecting sub-wavelength displacements with low noise. In the cases studied in this work, one fringe across a 10 mm field of view would correspond to a relative axial displacement equal to 0.45 µm and an average strain of 4.5×10^{-5}, an order of magnitude better than the uncertainty we report for OCT+DVC. Even though most phase-sensitive OCT elastography systems have so far focused on phase measurements with only axial sensitivity, a new system with sensitivity to all displacement components has been recently developed by Chakraborty and Pablo based on a wavelength scanning OCT system using multiple illumination directions and a single observation direction [89]. In the present study, strain was evaluated with a centred finite difference operator applied to the displacement field. No displacement smoothing was used before strain calculation in order to achieve maximal spatial resolution with a view to further studies on thin biological tissues such as the vertebrate eye cornea. In cases where strain accuracy is paramount, a weighted-least squares strain estimator would be more appropriate as studied by Kennedy *et al* [125].

The spurious fringes observed in the strain maps were analysed, and interpolation bias in the DVC algorithm was found to be the reason. Two approaches were verified to be feasible to reduce the interpolation bias due to image under-sampling. For the first approach, pre-

smoothing using a Gaussian low-pass filter was performed on the volume data prior to correlation. The results confirmed that pre-smoothing is effective in reducing interpolation bias although it causes slight increase in strain standard deviations (noise increases to a level between ~4×10^{-4} and ~8×10^{-4} after pre-smoothing). For the second approach, no apparent spurious fringes were observed in the strain maps when the sampling density of the SS-OCT was doubled, even though the field of view was halved.

Uniform and non-uniform 3D strain fields measured with OCT+DVC were used to identify the elastic stiffness components Q_{ij} of rectangular and notched silicone rubber phantoms using the VFM with 3D manually defined virtual fields. In order to test the proposed identification methodology, simple uniaxial tensile tests and isotropic materials were used. The material moduli (Young's modulus E and Poisson's ratio ν) extracted from this approach are consistent with those calculated from the constant uniaxial stress approach and the results obtained with a micro tensile machine. Another 3D VFM was also developed to identify the bulk modulus K and shear modulus G by utilizing the strain data obtained from the notched phantom strip tensile test. This offers another option for measuring the material stiffness when ν is very close to 0.5.

The proposed methodology can be applied to study the depth-resolved 3D deformation behaviour of soft biological tissues such as cornea under more complex loading conditions. This will be presented in the following chapter.

CHAPTER 4

DEPTH-RESOLVED FULL-FIELD MEASUREMENT OF CORNEAL DEFORMATION

4.1 Introduction

So far, most of the research work that has been done towards identification of corneal mechanical properties from full-field measurements was based on surface deformation measurements in corneal inflation tests using stereoscopic camera systems and DIC [32]. However, depth-resolved 3D deformation fields have not been undertaken yet, which is essential to better understand the local response of the cornea through its thickness.

In this chapter, DVC was carried out on a series of volume data obtained with the SS-OCT system described in section 3.3. Silicone rubber phantoms as well as porcine corneal trephinates were loaded under inflation in a pressure controlled chamber. The effect of noise and OCT reconstruction uncertainties and the performance of volume correlation were first evaluated in a similar way as described in Chapter 3 for flat samples using static and rigid body translation tests. The 3D displacement fields obtained due to a change in intraocular pressure were then evaluated by applying DVC directly to the OCT data volume. This, however, does not lead to correct results due to the fact that the microstructure reconstructed under the sample surface is distorted due to the refraction of light at the air/sample interface. This Chapter thus illustrates the consequences of ignoring this critical fact and sets the scene for Chapter 5, in which the refraction induced distortion is accounted for and eliminated, thus getting rid of spurious strains.

4.2 Sample preparation for inflation tests

Porcine corneas were used in this study instead of human corneas to avoid wasting corneas from donor banks until the methodology is fully developed and tested. A fresh ocular globe was collected from the local abattoir within 6 hours after slaughter and the corneas were tested within 12 hours post-mortem. The ocular globes were stored in a refrigerator below 4℃

to prevent tissue degeneration. It was then brought to room temperature half an hour before testing to ensure thermal equilibrium with the environment. A corneal trephinate (circular cut-off that includes the cornea and a 2mm sclera ring, shown in Fig 4.1 from different views), was excised from the corneal globe using a pair of scissors and a scalpel and stored in saline solution 0.9% NaCl. The central corneal thickness was measured using a Direct Computer Control (DCC) Coordinate Measuring machine. During the measurement, the coordinates of the apex of a corneal shaped support were first recorded when the touch-point sensor made contact with it. The corneal trephinate was then mounted on the support with its apex over the apex of the support. The coordinates of the corneal apex were recorded and the thickness of the cornea determined by evaluating the axial distance between the two measured points. The corneal trephinate thickness was 1.53±0.03mm, which includes a slight swelling due to water absorption in the sclera.

In order to have a stable sample, an artificial corneal phantom was fabricated using silicone rubber (MM240-TV A/B). A rubber base and a hardener were mixed to a ratio of 10:1. Titanium oxide particles were seeded into the silicone rubber mixture to supply the speckle contrast. The mixture was then put into a special mould designed to replicate the average dimensions of the Arizona eye model [126] and left to cure at room temperature for approximately 24 hours. Fig 4.2 shows one of the corneal phantoms that were fabricated in this way. Its outer edge spherical diameter and central thickness are 15.6 mm and 0.58 mm, respectively.

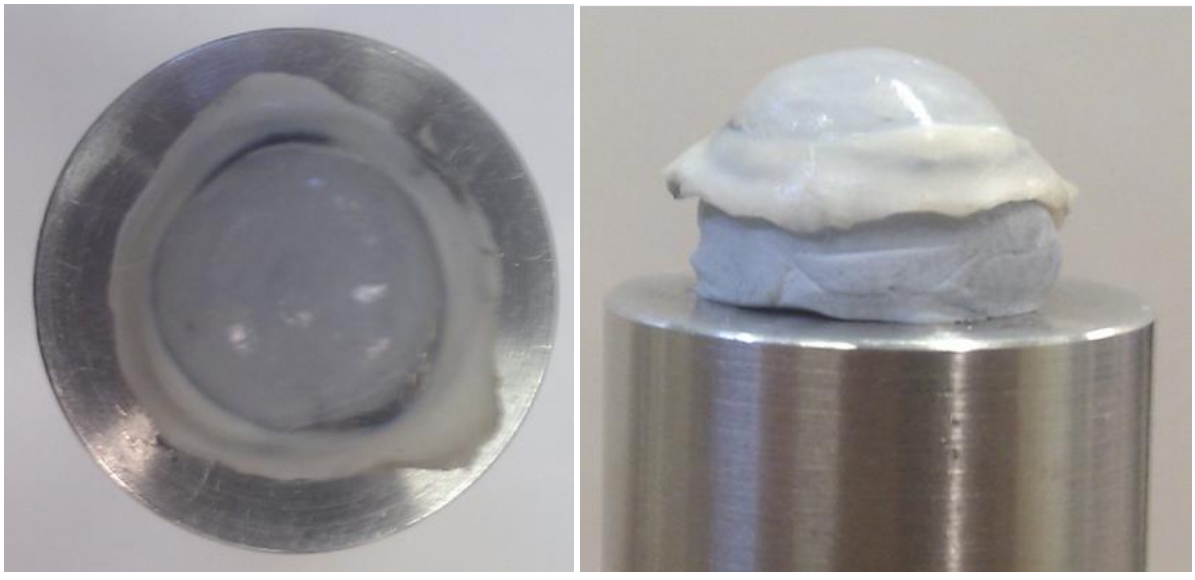

Fig 4.1: Porcine corneal trephinate from different views.

4.3 Experimental set-up and image acquisition

The experimental set-up is illustrated in Fig 4.3, which contains an inflation configuration and the SS-OCT system (Thorlabs OCS1300SS). The samples were mounted and fixed on an artificial anterior chamber (AAC) by a locking ring. This chamber has inlet and outlet ports for the fluid to adjust the internal pressure and another port connected to the pressure transducer. The simulated intraocular pressure was achieved by adjusting a 1 ml micro-syringe. Both the porcine corneal trephinate and the silicone rubber phantom were first inflated to 2 kPa. Under this pressure state the samples maintained a smooth and taut anterior surface and served as the reference configuration. They were then inflated to 2.5 kPa, which is close to the physical porcine intraocular pressure to study the corneal deformation under the pressure change. All the tests were carried out at room temperature.

At each pressure state, a 3D volume data cube of the specimen was acquired using the SS-OCT system. The dimensions of the reconstructed volumes were $1024 \times 512 \times 1024$ voxels, corresponding to a $11 \times 3 \times 11$ mm^3 region of interest. Fig 4.4 shows a quarter of the reconstructed corneal volume. Typical central transverse *z*-slices of the porcine cornea and silicone rubber phantom are shown in Fig 4.5 (a) and (b), respectively. Along the lateral scanning directions *x* and *z*, the voxel size is 10.7 μm. Along the vertical *y* direction, which is the optical path, the voxel size depends on the refractive index of the medium (1.45 for phantom and 1.38 for cornea) and is 4.8 μm and 4.5 μm for the phantom and porcine corneal trephinate, respectively.

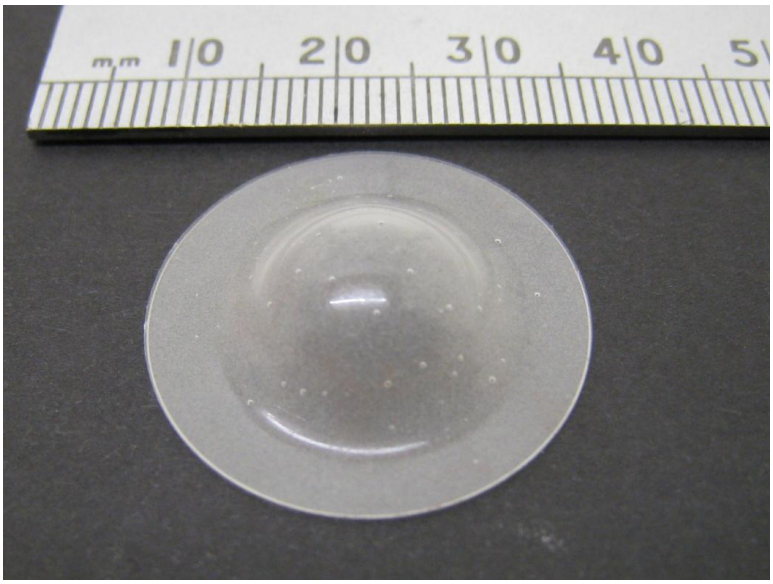

Fig 4.2: Corneal silicone rubber phantom.

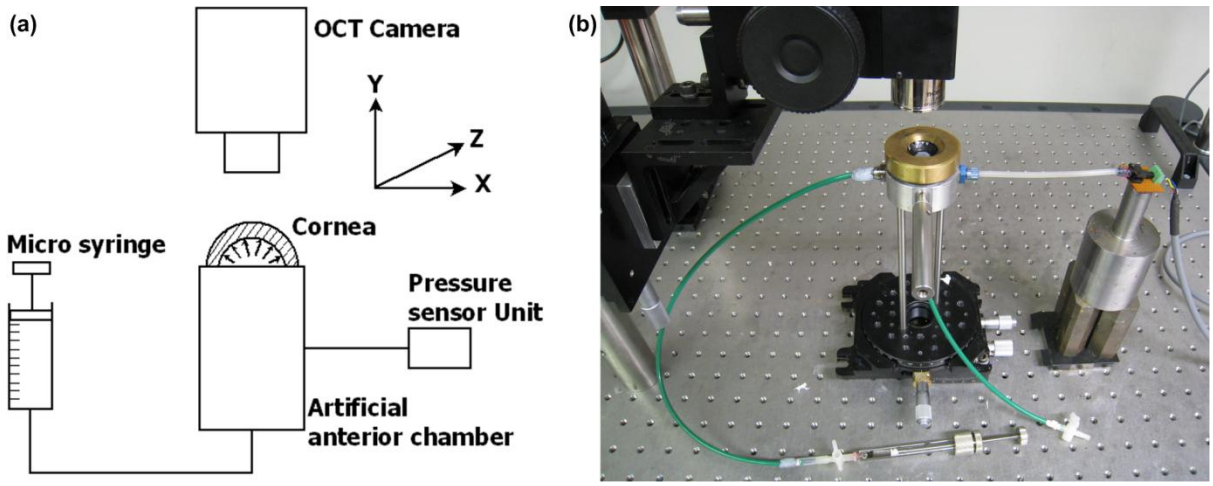

Fig 4.3: (a) Schematic diagram, and (b) experimental set-up.

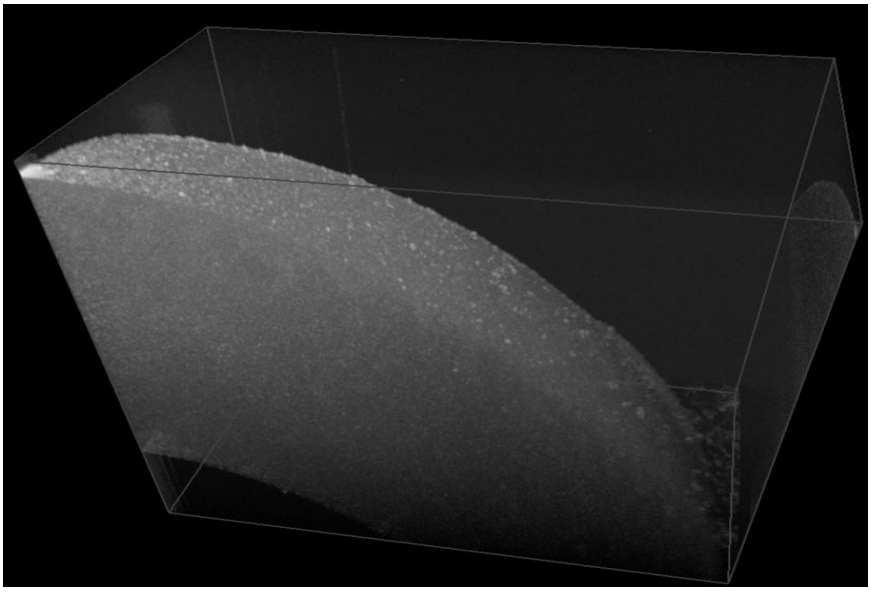

Fig 4.4: Part of the reconstructed porcine corneal trephinate volume obtained with the SS-OCT system.

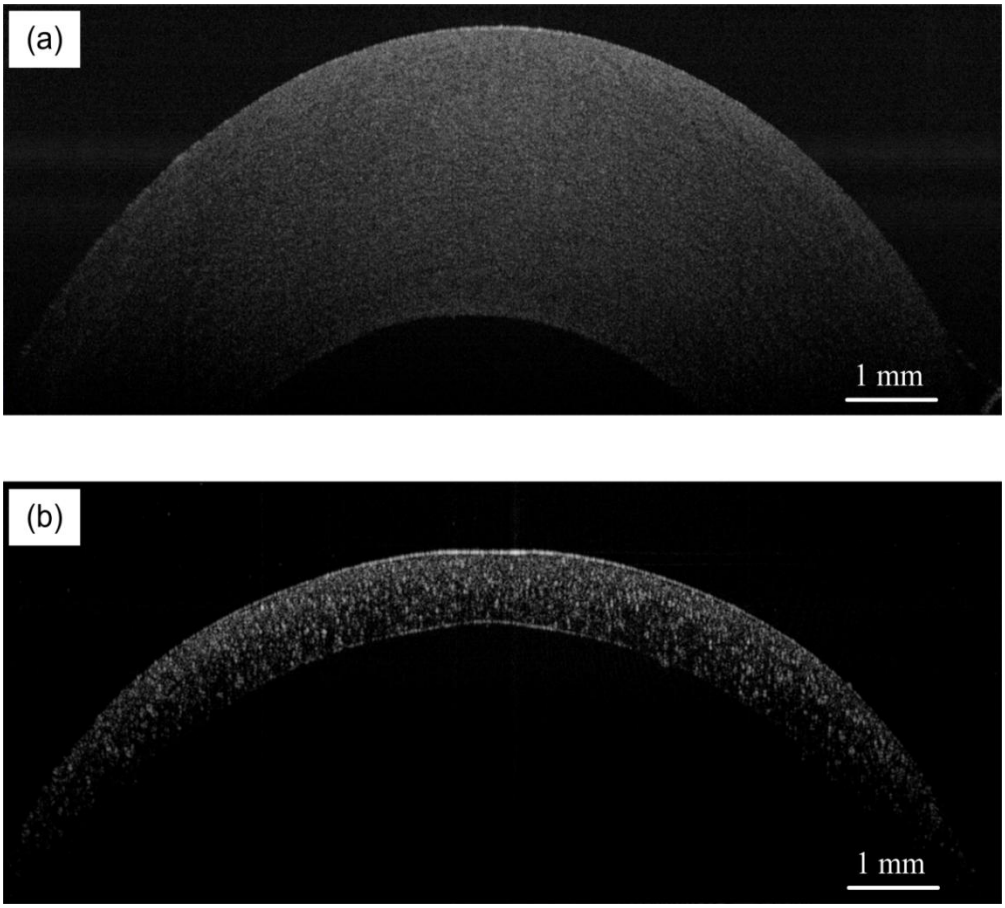

Fig 4.5: Central transverse *z*-slice of the: (a) Porcine corneal trephinate and (b) Silicone rubber phantom obtained with the SS-OCT system.

4.4 Noise analysis

Considering the relatively small thickness of the porcine cornea and corneal phantom to the spatial resolution of the SS-OCT system, 24×24×24-voxel sub-volume with 50% overlap was selected to perform DVC. Based on this sub-volume size, a noise analysis equivalent to the one described in Chapter 3 for the flat phantom was repeated here, i.e. a stationary test in which two reconstructions are compared maintaining a constant pressure and with no displacements, and a controlled rigid body translation of 40 μm in the vertical *y*-direction.

The strain standard deviation (a measure of the strain uncertainty) was evaluated for both cases and this is shown in Fig 4.6. It can be seen that there is an increase in the strain standard deviations compared with those plotted in Fig 3.6 (for stationary test) and Fig 3.7 (for translation test) for the 36×36×36-voxel sub-volume size, which is expected on the basis of a smaller sub-volume size. The strain standard deviations mostly fall in the range between

3×10^{-4} and 8×10^{-4}. These noise levels are about one order of magnitude below the strain levels due to deformation in the inflation tests.

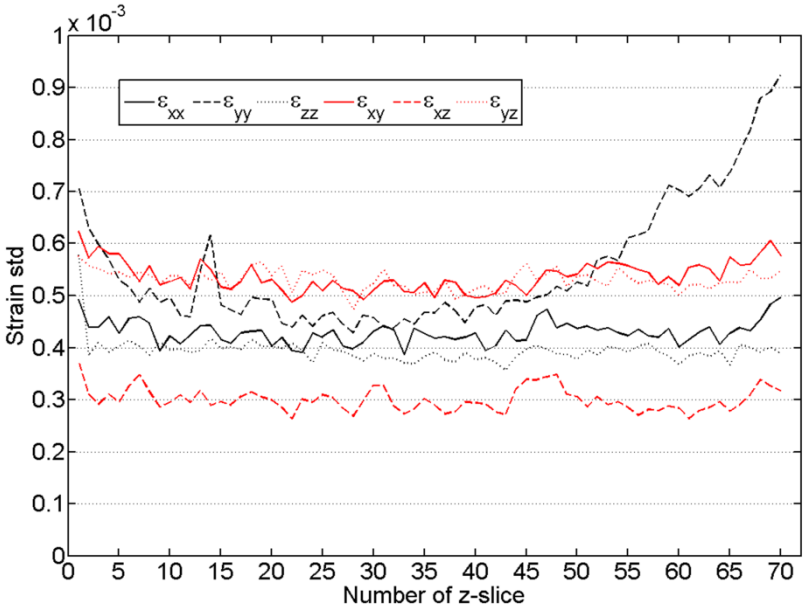

(a)

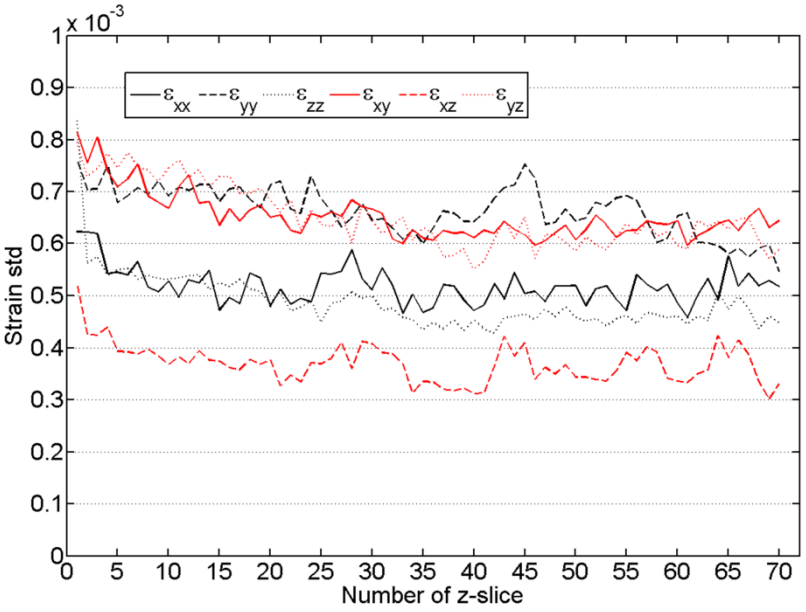

(b)

Fig 4.6: Strain standard deviations obtained with 24^3 voxels sub-volume and 50% overlap for: (a) Stationary test and (b) Rigid body translation test.

4.5 Finite elements modeling of corneal inflation test

In order to visualize what kind of displacement and strain distributions we should expect through the thickness of the cornea under inflation, a simple finite element model was

developed using the commercial software package ABAQUS 6.11®. The simulation results were aimed at a qualitative comparison with those measured with DVC. According to ref. [28], the porcine cornea behaves linearly while the intraocular pressure remains below 4 kPa. Therefore, a linear elastic material with Young's modulus E=0.3 MPa and Poisson's ratio v=0.49 (see ref. [127] by Hamilton and Pye) was chosen for the FE model. A study by Anderson *et al* [28] shows that a model that assumes constant corneal thickness only results in a very small average change in predictions compared to the model with actual thickness variation. Therefore, in the present work, a constant corneal thickness of 1.53 mm was chosen for the sake of simplicity. A hex-dominated first-order reduced-integration element type was selected for the FE model. The corneal volume with FE mesh and a cross section are shown in Fig 4.7. The peripheral boundary was fixed. Uniform normal pressure was applied to the inner surface to simulate the intraocular pressure. The model was inflated from 2 kPa to 2.5 kPa. The displacement and strain simulation results were then exported to compare them against the DVC measurements.

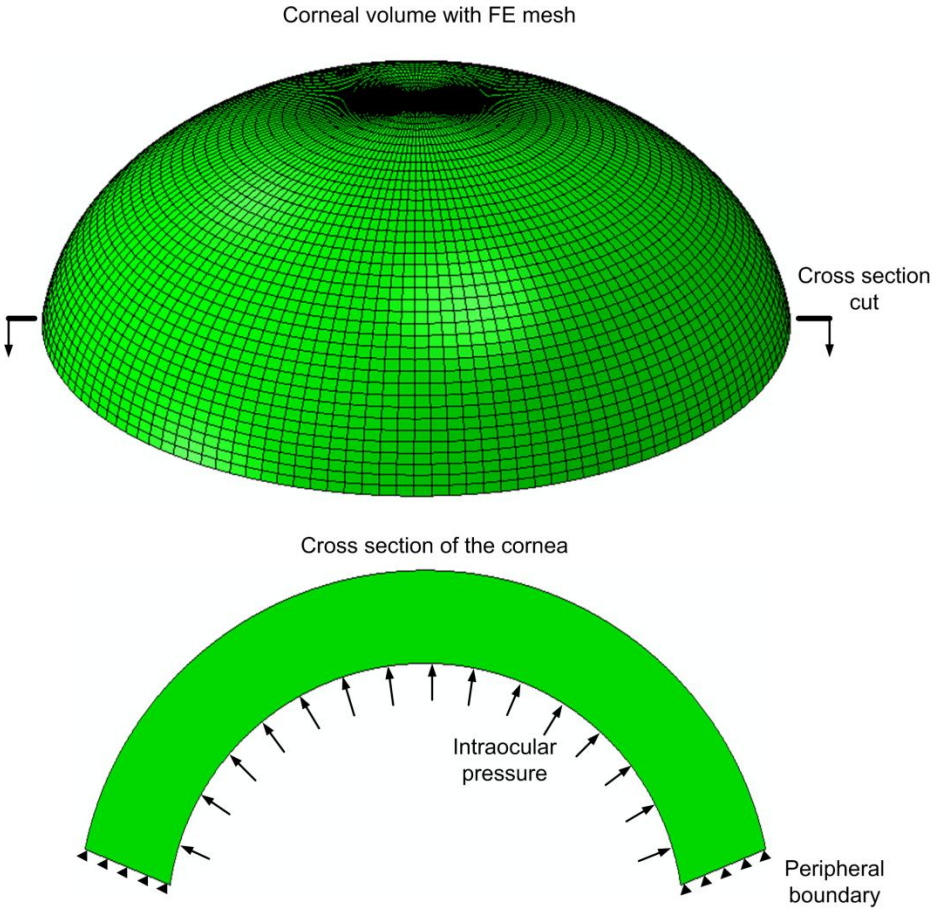

Fig 4.7: FE model of porcine cornea.

4.6 DVC measurements Vs. FE simulations

4.6.1 Porcine corneal trephinate

u_y displacement maps, which represent the axial displacement, for the z-slices of the volume are illustrated in Fig 4.8 from different views. For the sake of legibility, these displacement maps are only plotted every five z-slices. In Fig 4.9, u_x displacement maps, which represent the horizontal displacement along x-direction, for the z-slices are shown. From these maps, continuity of the displacement distribution can be observed. One can see clearly how the corneal volume deforms in different directions when the pressure increases. More detailed analysis for the displacements is given for the central z-slice of the porcine cornea and the FE model in Fig 4.10. Due to the limited A-scan depth of the SS-OCT system, the corneal outer circumference (region where the cornea meets the sclera) was left outside the field of view, leaving only the upper part of the cornea around the apex. The measured displacement maps in Fig 4.10(a) thus correspond to the FE counterparts within the rectangle sketched in Fig 4.10(b). From the DVC results, it can be seen that the horizontal displacement u_x is close to zero near the central region, and increases symmetrically when it moves to two sides. The half positive and half negative displacement distribution is expected from the FE model, which is the result of applying a normal inflation pressure. The distribution of the horizontal displacement u_z is the same as u_x due to the rotational symmetry around the y-axis.

The maximum u_y is located near the centre of the endothelium, and u_y decreases from the endothelium to the epithelium, which is compatible with an compressive state through the thickness. Qualitatively, the measured displacement maps are consistent in terms of the observed spatial distributions with the displacements predicted by the FE model.

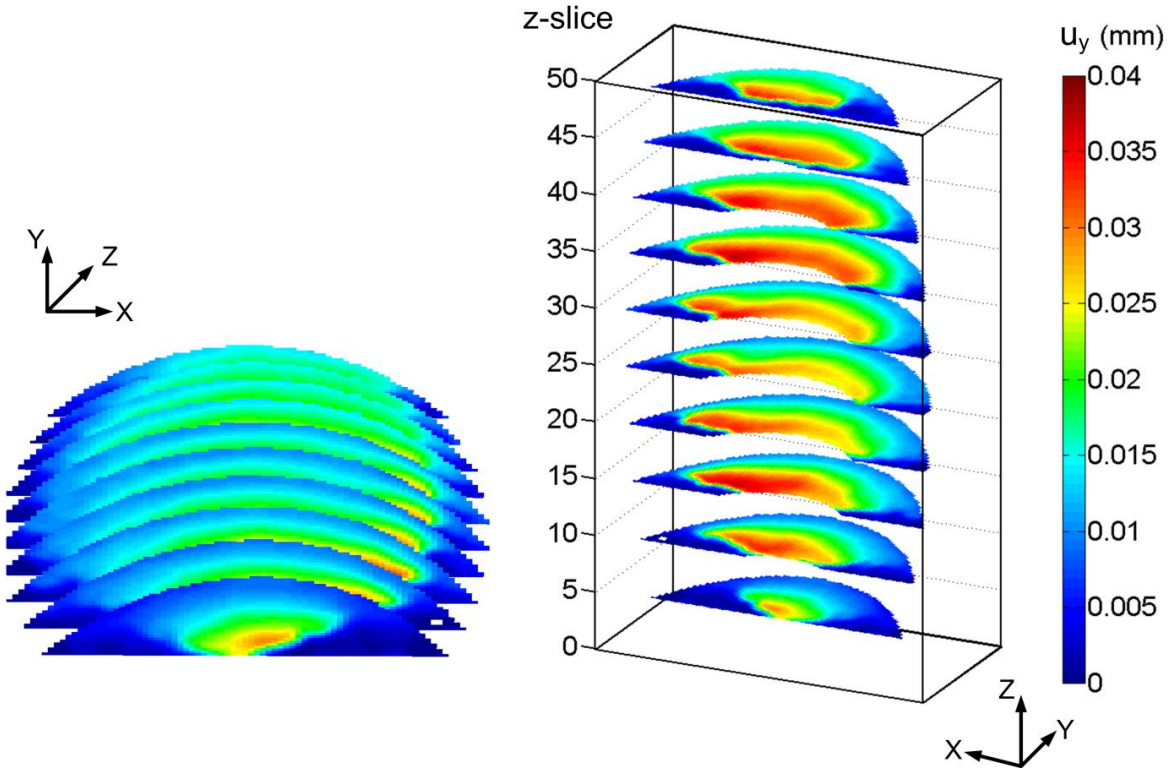

Fig 4.8: u_y displacement maps measured with DVC for different z-slices of the porcine cornea with 24^3 voxels sub-volume and 50% overlap.

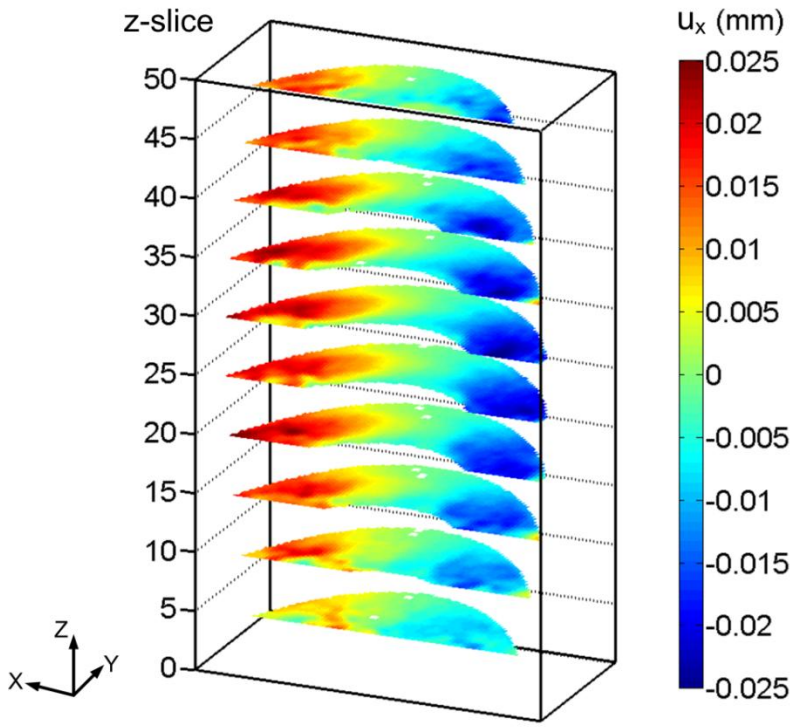

Fig 4.9: u_x displacement maps measured with DVC for different z-slices of the porcine cornea with 24^3 voxels sub-volume and 50% overlap.

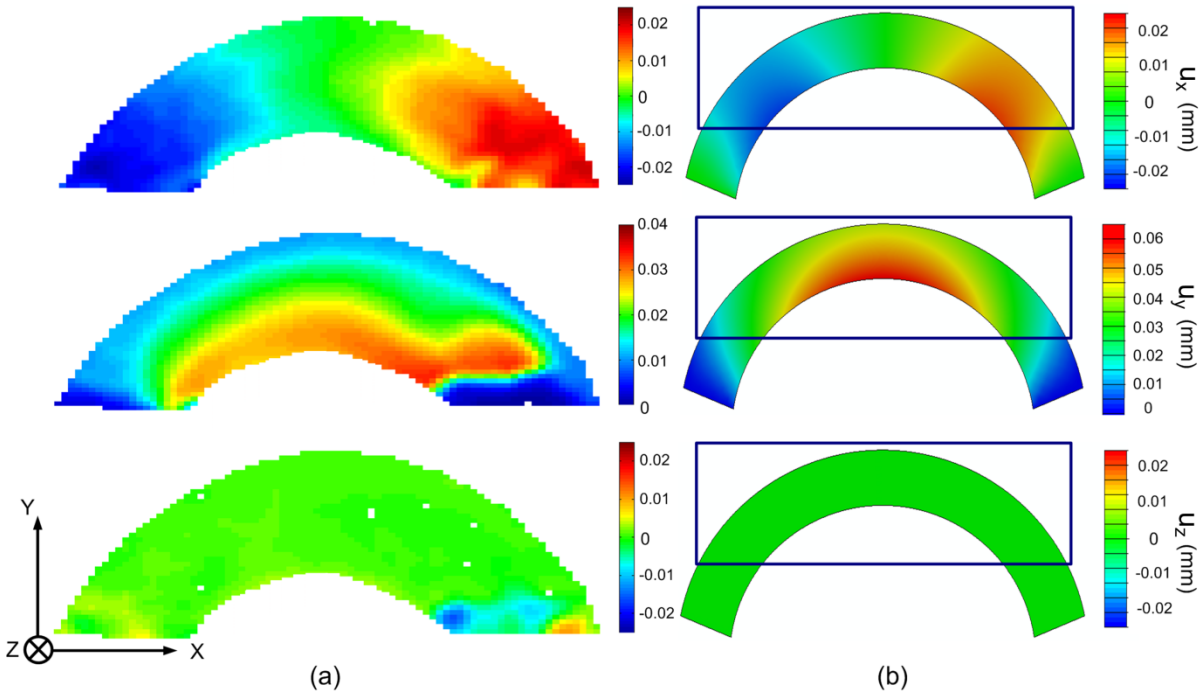

Fig 4.10: (a) Displacement maps measured with DVC for the central *z*-slice of the porcine cornea inflated from 2 to 2.5 kPa with 24^3 voxels sub-volume and 50% overlap, and (b) Simulation results.

The strain maps were obtained from the centred finite difference of the displacement data and are shown in Fig 4.11(a). The measured strains show a good overall agreement in terms of spatial distribution with those predicted by the FE model, as shown in Fig 4.11(b). The distribution of the normal strain components ε_{xx} and ε_{yy} indicates a tensile deformation along the horizontal *x*-axis and a compressive deformation along the vertical *y*-axis which dominates the central region. Near the peripheral regions, however, the cornea experiences considerable shear strains, as illustrated in the ε_{xy} strain maps. It indicates that in the peripheral regions lying between the central region and the fixed support, the cornea primarily experiences shear deformation. The colour bars in Fig 4.11 show maximum absolute strains of about 2%, which exceed the strain standard deviation due to noise of about 0.08% shown in Fig. 4.6. This means that the strain due to the deformation dominates the strain noise floor and therefore these distributions are the results of material behaviour rather than noise artefacts. Positive strain can be observed on the bottom surface of the cornea in ε_{yy} strain map, which is not consistent with the FE model. One explanation for this is that DVC results near the edge are noisier due to lack of data.

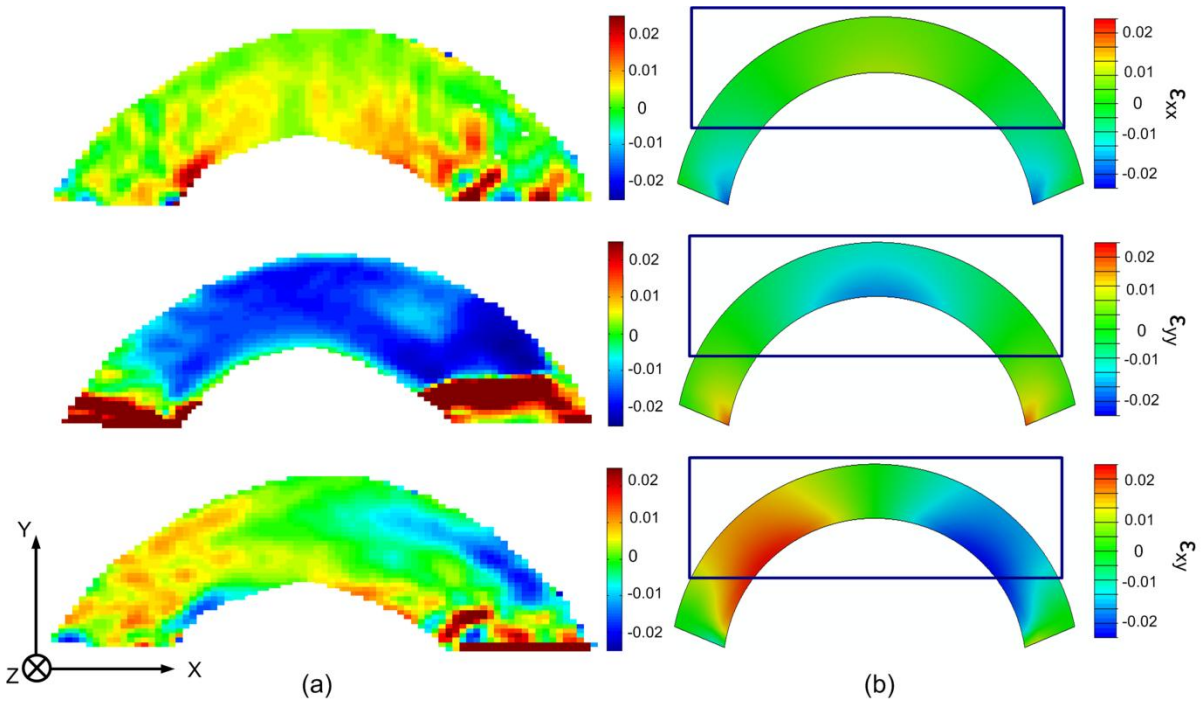

Fig 4.11: (a) Strain maps measured with DVC for the central *z*-slice of the porcine cornea inflated from 2 to 2.5 kPa with 24^3 voxels sub-volume and 50% overlap, and (b) Simulation results.

4.6.2 Silicone rubber phantom

Human corneas are thinner than porcine corneas with the thickness normally ranging from 0.5-0.6 mm in the centre and 0.6-0.8 mm at the periphery. A question that comes to mind is whether the spatial resolution of the measured displacements and strains would be sufficient to capture the spatial variations of the strain field and for the VFM to identify elastic parameters through the thickness of the cornea. Fig 4.12 shows the displacement and strain measured with DVC in the phantom inflation test, in which the phantom with 0.58 mm thickness was inflated from 2 to 2.5 kPa. Qualitatively, the displacement maps of the inflated phantom are consistent with those of the porcine cornea when comparing the displacement maps in Fig 4.12(a) to Fig 4.10. However, since the phantom is almost 1/3 of the thickness of the porcine cornea, it experienced a larger deformation under the same pressure change, especially in the *y*-direction, though the Young's modulus of the silicone rubber (~1.5 MPa) is large than that of the porcine cornea (~0.3 MPa). From Fig 4.12(a), it can be observed that u_y reaches a maximum of about 0.12 mm in the central region. Regarding the strain distributions in Fig. 4.12(b), agreement is also found between the results for the phantom and the porcine cornea. As for the cornea inflation, the central region of the phantom is

dominated by horizontal tension and vertical compression deformations while the peripheral regions are dominated by shear deformation. It should be pointed out that some abnormality of the strain values can be observed on the top and bottom surfaces such as the positive values on the top surface in the ε_{yy} strain map. This is probably due to the edge effect of DVC. Thus, only the values of the internal layers are reliable. This however is the best result one can get from the current OCT system for specimens with such small thickness taking into account the strain resolution and spatial resolution.

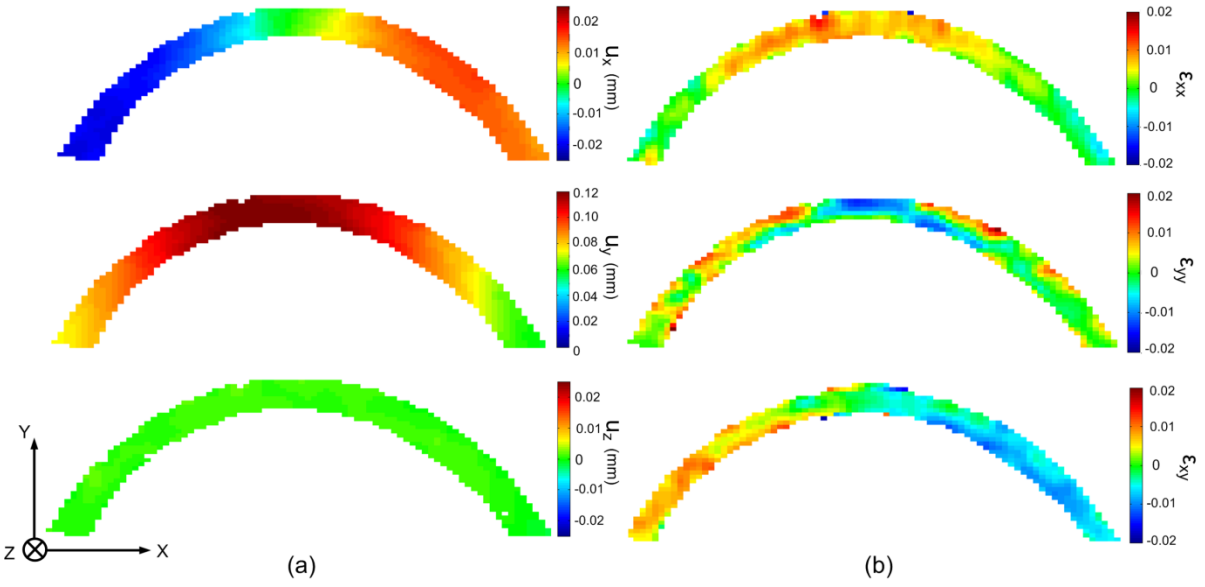

Fig 4.12: (a) Displacement and (b) Strain maps for the central transverse *z*-slice of the silicone rubber phantom inflated from 2 to 2.5 kPa with 24^3 voxels sub-volume and 50% overlap.

4.7 Limitations

As highlighted in Fig 4.13, the strain map of ε_{yy} shows incorrect results at the bottom left and right. This is due to a loss of speckle contrast in those regions (caused by a combination of spectral roll-off, transmission of light at the air/specimen interface and material scattering) which leads to inadequate values of the correlation coefficient in DVC as can be seen from the correlation coefficient map in Fig 4.14. In this correlation coefficient map, values at the peripheral bottom regions are below 0.5 and thus not reliable. Only the central region is reliable where the correlation coefficient values are over 0.8. This limitation of the OCT system is currently unavoidable.

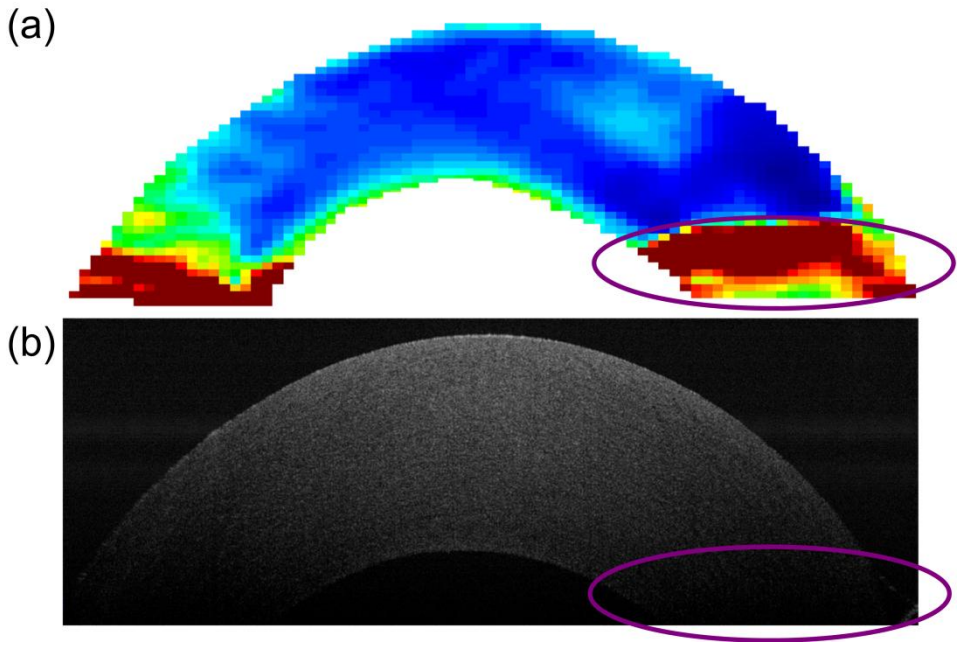

Fig 4.13: Low speckle contrast leads to incorrect displacement and strain values. (a) measured ε_{yy} strain; (b) The same region in the raw OCT image

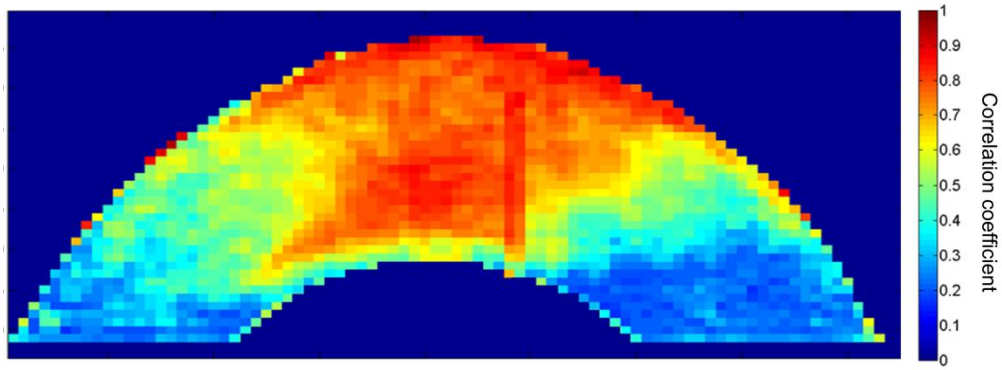

Fig 4. 14 Correlation coefficient map for the central transverse z-slice of the porcine cornea inflated from 2 to 2.5 kPa with 24^3 voxels sub-volume and 50% overlap

Although the experimental results show a good overall agreement with the results from the FE model, differences can still be seen between them, especially in the strain maps. Take the strain maps of ε_{xx} in Fig 4.11 as an example. While the strain distribution in the FE model is smooth and continuous, with the maximal tension strain in the inner central region and decreasing gradually from centre to periphery, the measured strain is dominated by noise with a small background trend that is not clearly observed in the simulated results. Strain noise is also apparent in the strain components ε_{yy} and ε_{xy}.

With regards to the FE model, it was developed to assist a qualitative comparison with the DVC measurements. The material property was defined as homogeneous and isotropic for the sake of simplicity, which, however, is not true in the case of the cornea. The cornea has five different layers and a complex composite structure composed of the corneal matrix and embedded collagen fibrils, which makes it heterogeneous and anisotropic. Moreover, the Young's modulus and Poisson's ratio used here for the FE model were chosen from the literature and represent average values for the porcine corneas. The true modulus of the present cornea can be different from these average values and be position dependent, thus leading to different FE results. Slightly different strain distributions would be expected from a more realistic model, which is beyond the scope of this Thesis.

Due to the time limitation of the present project, added complexity to the VFM in an inflation test with pressure field, and poorer strain results near the bottom regions due to inadequate image quality, constitutive parameters of the porcine cornea have not been identified yet. Future work will be aimed at identifying the constitutive parameters once these issues are solved.

We should not forget that the displacements and strain maps presented in this chapter are fundamentally flawed as the OCT reconstructions are not a true (geometrically and dimensionally) representation of the corneal structure due to the distortion introduced by refraction of the illumination and observation beams. The study on the refraction induced distortion will be provided in next chapter.

4.8 Conclusions

In this chapter, a method was developed to measure depth-resolved displacement and strain fields inside a porcine corneal trephinate due to changes in the intraocular pressure. DVC was performed on the reconstructed OCT data volumes for the silicone rubber phantom and porcine cornea samples. Stationary and rigid body translation tests indicate that the strain noise in the absence of deformation is up to 0.08% when a 24^3 voxel sub-volume is used, which leads to a good compromise between the strain resolution and spatial resolution. Reasonable displacement and strain spatial distributions were obtained for both the phantom and the cornea. These results show a good overall qualitative agreement with the results of a simple FE model and suggest that better results should be achievable once refraction correction is implemented.

CHAPTER 5

CORRECTION OF REFRACTION INDUCED DISTORTION IN OCT RECONSTRUCTIONS FOR VOLUME DEFORMATION MEASUREMENTS

5.1 Introduction

Accurate displacement and strain measurements based on DVC require that the reference and deformed data volumes accurately represent the spatial position of all the internal features of reconstructed specimen, i.e. that no geometrical distortions should be present. However, OCT reconstructions usually suffer from different types of geometric distortions.

Refraction induced distortion is one type of these errors. It arises when the sample has a curved surface or the sample has a flat surface which does not lie perpendicular to the scanning beam. In this case the scanning beam changes its propagation direction at the air/sample interface but the OCT system reconstructs the scattered light as if light had propagated without such a change. A consequence of this is that internal features appear to be in a different position in the OCT reconstruction. Apart from this, as the dimension along the propagation direction in an OCT image is optical path rather than physical distance, thus the position of features depends on the knowledge of the refractive index of the medium. Pioneering work on these issues has been done and solutions provided for the correction of 2D OCT images based on Fermat's principle and Snell's law [128, 129].

Another type of distortion is caused by the 'fan' scanning of certain OCT systems [128, 130, 131], in which a fan of scanning rays cause a flat surface to appear curved in the OCT reconstruction, as illustrated in Fig 5.1 [128].

This chapter presents a method to correct the refraction induced distortion in 2D/3D OCT reconstructions based on Fermat's principle [132]. A more computationally efficient way was developed in which a minimization algorithm was only executed on a sub-set of voxels. This method was compared to the point-by-point minimization method in which the algorithm was executed for every voxel. Controlled tilt tests of a flat and a hemispherical

silicone rubber phantom are described, which establish the effect of the refraction induced distortion in the strain fields obtained with DVC.

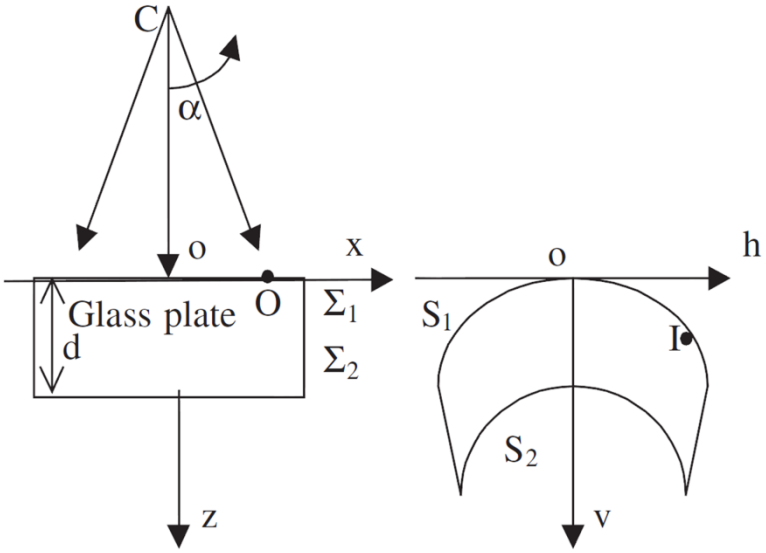

Fig 5.1 Distorted image of a microscope slide when scanned with a fan of rays (Reproduced from reference [128], Podoleanu *et al*). Point *O* and *I* are the object and corresponding image point, respectively. Σ_1, Σ_2 are the top and bottom object surfaces, while S_1, S_2 are the corresponding surfaces in the image.

5.2 Refraction induced distortion in OCT reconstructions

The SS-OCT system used in this work was designed to eliminate fan distortion, and therefore flat surfaces are reconstructed as flat in the OCT data volume. This was done by placing the galvo scanners in the back focal plane of the objective lens so that the beam pivots about it and leaves the lens always parallel to the optical axis. The scanning beam is therefore assumed to be always vertical, which can be confirmed by looking at the reconstructed image for the flat silicone rubber phantom in Fig 3.3. Therefore, if still present, the fan distortion is considered negligible in this work, and the study of geometric distortions will only focus on the refraction induced distortion at the air/sample interface. A further simplification is that we will consider a uniform distribution of refractive index within the sample.

For a sample with a flat top surface, it is free of the distortion problem if the scanning ray is perpendicular to the sample surface. As the scanning ray moves parallel to the optical axis, the reconstructed volume data represent the real configuration of the scanned sample. However, for a sample with curved surface such as cornea in (Fig 4.5), refraction induced

distortion arises. This will cause an error in the actual position of the microstructure features inside the cornea. Fig 5.2 illustrates how this distortion arises. In this figure, let us use *K* to represent the plane of zero optical path difference (a datum surface relative to which distance is measured). *A* is an arbitrary incident point on the top surface at which light, travelling perpendicular to *K*, enters the cornea from the OCT scanning ray. *AC* is the normal to the surface at the incident point *A*. The incident ray *OA* subtends an angle θ_0 to the surface normal at *A*. The refracted ray passes through point *B* within the corneal tissue (object space), subtending angle θ_1 to the surface normal at *A*, following the Snell's law:

$$n_0 \sin\theta_0 = n_1 \sin\theta_1 \tag{5.1}$$

where n_0 and n_1 represent the refractive indices outside and within the cornea (in the air $n_0 = 1$, in the cornea $n_1 = 1.38$), respectively. The OCT system records this refracted optical path in the image as a vertical A-scan line, denoted *OI* in Fig. 5.2, where point *I* is the corresponding point of the object point *B* in the reconstructed image space . As the optical path difference is equal to the physical distance in the medium multiplied by the refractive index, *OI* in the image space is equal to:

$$|OI| = n_0|OA| + n_1|AB| \tag{5.2}$$

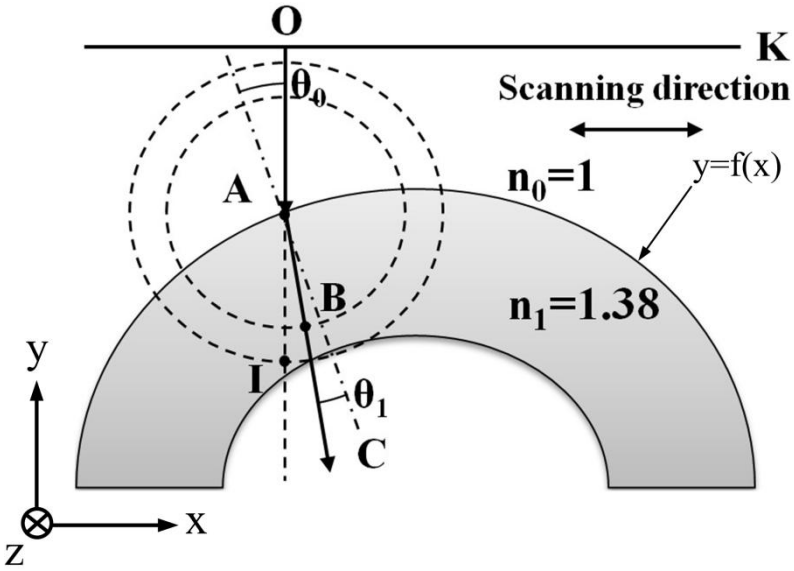

Fig 5.2: Refraction of the incident beam in an OCT scanning system. During a scan, the beam moves parallel to the indicated direction along the *x* and *z* axes.

It can be seen that a point *I* in the image space actually corresponds to the point *B* in the object space. Therefore, the reconstructed volume is actually expanded and deformed outwards compared to the real configuration of the object. The distorted data volume would then introduce errors in the displacement and strain measurements obtained by performing DVC on the OCT reconstructions, leading to spurious values that need to be assessed.

Refraction correction in OCT images has already been dealt with in the literatures using Fermat's principle and Snell's law [128, 129]. The approach based on Fermat's principle, even though computationally demanding, does not require any assumptions on the cornea surface shape (e.g. approximation to a sphere). This principle states that the path taken between two points by a ray of light is the path that can be reached in the least time. Thus, point *B* is reached by a unique ray refracted at point *A*. Therefore, given *B*, point *A* can be found using a minimization algorithm of the optical path defined in equation (5.2). Then, the corresponding point *I* in the image space (to point *B* in object space) can be searched along path *OA* at a distance $n_1|AB|$ from point *A*. Once the exact (non-integer) coordinates of point *I* are determined, the light intensity value at this image point is evaluated through interpolation (bilinear in our case), and the value is associated to the coordinates of point *B*, which belong to a Cartesian grid in object space. By applying the same procedure to all other object points, the corrected images are obtained.

Alternatively, the refraction correction can also be implemented from the image space. In this case, the coordinate x_A for any A-scan is known from the column location in the image. As shown in Fig 5.2, assuming the parametric function of the top interface is known, the incident angle θ_0 for each scanning ray *OA* can be determined after calculating the surface normal at incident point *A*, from which the refractive angle θ_1 can be determined based on the Snell's law as defined in equation (5.1). Then, the parametric function of the refractive ray *AB* can be determined. For each image point *I*, the corresponding object point *B* in the object space can be searched along the path *AB* at a distance $\frac{|AI|}{n_1}$ from point *A*. Once the exact (non-integer) coordinates of point *B* in the object space are determined, the light intensity value at the image point *I* is associated to the coordinates of point *B*. Since the corresponding object points of the image points are at non-integer positions, interpolation is needed to determine the light intensity value at the integer positions defined on a Cartesian grid in the object space.

Both approaches can be used to correct the refraction induced distortion and both involve interpolation: the Fermat's approach interpolates the intensity between grid points in the image space, which is fast and can be done for instance by the 'interp2' function in Matlab®; the direct approach requires interpolation of scattered data (non-integer coordinates in object space) into a regular grid. This can be done using functions like 'griddata' in Matlab®, which fits a surface of the form $v = f(x, y)$ to the scattered data in the vectors (x, y, v). The griddata function interpolates the surface at scattered query points and returns the interpolated values, the surface always passing through the data points defined by x and y.

In the present study, the first approach was implemented, following the steps of previous published work. We attempted the second approach to save computation time, but at the time we were not aware of interpolation functions such as griddata that would solve the problem of given scattered data, interpolate them in a regular grid. It is expected that this second approach would save computation time and we have plans to apply it and compare the performance of both.

It should be pointed out that there can also be internal refraction at the interfaces between the different layers of the cornea considering the slight difference in their refractive indices e.g. 1.401 and 1.373-1.380 for the human corneal epithelium and stroma, respectively, as previously studied by Patel *et al* [133]. This difference in refractive index between different corneal layers is insignificant compared to that between the air and cornea interface (1 and 1.38). Therefore, for the sake of simplicity, the refractive index of the cornea in the present study was assumed to be uniform when performing refraction correction. A detailed approach would require solving refraction at each interface, which position and functional form should be found in the order in which the illuminating beam propagates through them.

5.3 Correction of refraction induced distortion in OCT reconstructions

5.3.1 Refraction correction in 2D

To perform the correction for the refraction induced distortion, the refractive indices of the media and the parametric equation of the interface must be known as a prerequisite. In Fig 5.2, the equation of the top interface of the object can be expressed as

$$y = f(x) \tag{5.3}$$

It should be pointed out that the dc term in $f(x)$ is not critical as refraction only depends on the local gradient. The refractive indices within and outside the medium are n_1 and n_0, respectively. For an arbitrary object point *B*, the coordinates are (x_B, y_B). For the corresponding incident point *A*, the coordinates can be expressed as $(x_A, f(x_A))$. As stated in equation (5.2), the optical path difference (OPD) of a ray is equal to the physical path length multiplied by its refractive index. Thus, OPD can be written as

$$OPD = n_0 f(x_A) + n_1 \left[(x_B - x_A)^2 + (y_B - f(x_A))^2 \right]^{\frac{1}{2}} \tag{5.4}$$

where (x_B, y_B) are known as they are defined in a Cartesian grid in the object space for each point. Therefore, the only unknown in equation (5.4) is x_A. In this case, OPD is a function of x_A. Replacing x_A by x, OPD becomes

$$OPD(x) = n_0 f(x) + n_1 \left[(x_B - x)^2 + (y_B - f(x))^2 \right]^{\frac{1}{2}} \tag{5.5}$$

According to Fermat's principle, for a given point *B* there is only one incident point *A* that can lead to the minimal OPD. Therefore, by minimizing OPD, x of the incident point can be found. Then, the coordinates of point *A* can be decided.

Now the task is to find where in the image space we should look at for this given object point *B*. Let's use (x_I', y_I') to represent the coordinates of the corresponding image point *I*. Since the OCT system registers the optical path in the image as a vertical A-scan, the horizontal coordinate x_I' of point *I* is

$$x_I' = x_A \tag{5.6}$$

The vertical coordinate y_I' is

$$y_I' = n_0 f(x_A) + n_1 |AB| \tag{5.7}$$

where $|AB|$ is

$$|AB| = \left[(x_B - x_A)^2 + (y_B - f(x_A))^2 \right]^{\frac{1}{2}} \tag{5.8}$$

After determining the coordinates of the image point *I*, the intensity value at that point will be associated with the object point *B*. As the coordinates of point *I* can be non-integer values, interpolation is needed to determine the intensity value of that point. Here, linear interpolation was used. The above method was implemented using MatLab® R2007a.

5.3.1.1 Example with a simulated fringe pattern

The first attempt for refraction correction was implemented on an image with a simulated fringe pattern. The idea is to see how these fringes look like after refraction correction. As illustrated in Fig 5.3(a), a 128×128 pixels image was produced. The pattern in the image was created by a 2D cosine function. In Fig 5.3(b), a 1-D cosine function was selected to represent the parametric function of the interface, which is

$$y = 128 - 32 \times \left(1 - \cos\left(\frac{\pi x}{64}\right)\right) \tag{5.9}$$

This cosine function (in pixel units) not only works as the mask for the fringe pattern, but also it is required when calculating the OPD. It should be pointed out that in this simulation the choice of the parametric function for the interface is somewhat arbitrary as long as it is curved.

The masked fringe pattern is shown in Fig 5.3(c). Thus, a simulated sample with curved interface and speckle contrast was produced. The refractive indices within and outside the simulated sample are 1.38 and 1, respectively (selected according to the indices of cornea and air). Then, the refraction correction algorithm as introduced previously was implemented on this simulated image, and the corrected fringe pattern is shown in Fig 5.3(d). Comparing Fig 5.3 (c) and (d), it is clear that after refraction correction the simulated sample becomes thinner. This is not surprising as the vertical axis now represents physical distance instead of optical path. It is also clear that the horizontal and vertical fringes in Fig 5.3(c) now become tilted, indicating how the inner points move to their actual positions after refraction correction.

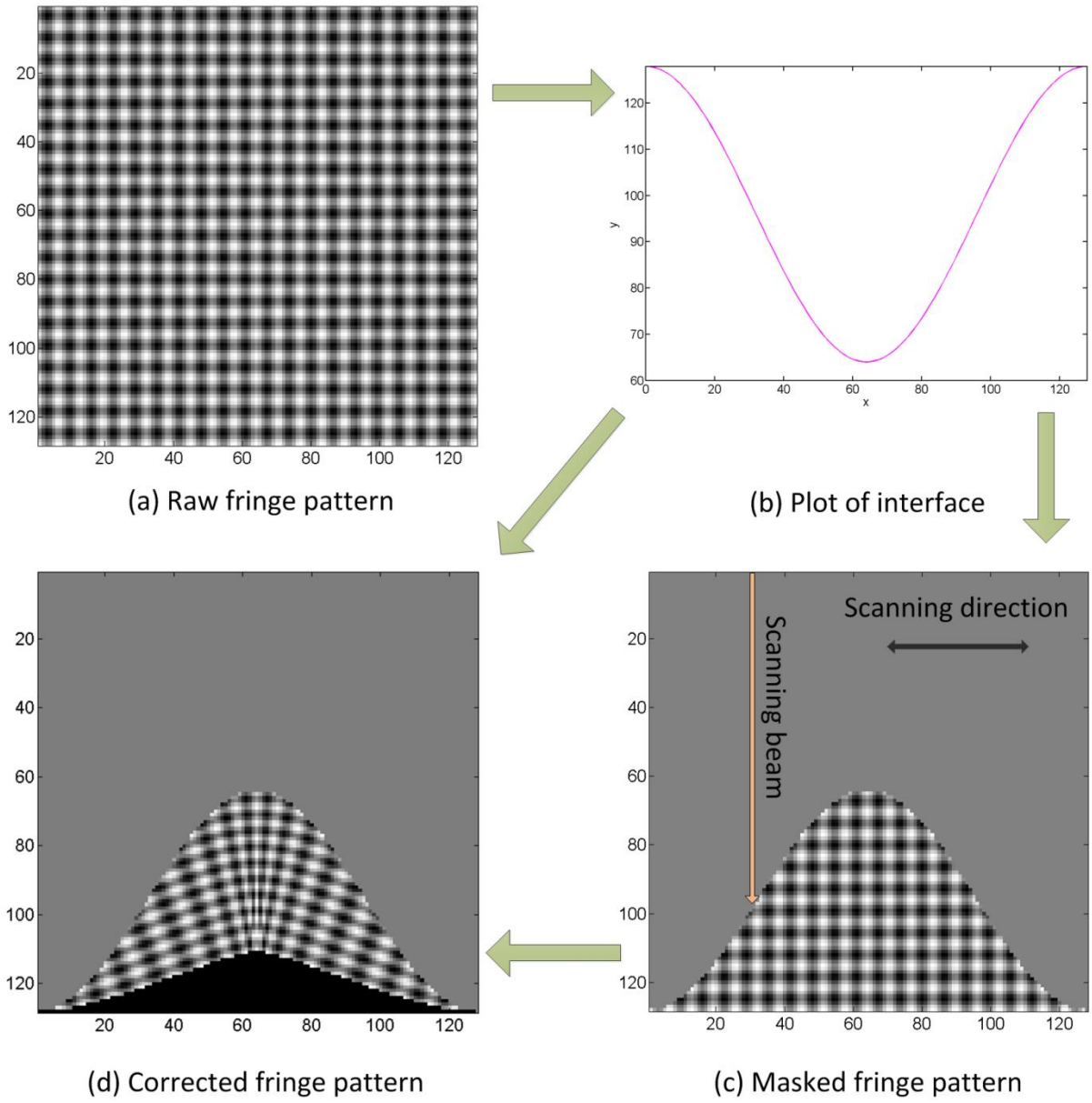

Fig 5.3: Procedure of 2D refraction correction on a simulated fringe pattern

5.3.1.2 2D refraction correction of an OCT image

The example of refraction correction on simulated fringe pattern visually shows how the correction algorithm works. In this section, the correction method was applied to correct a central *z*-slice of the OCT reconstructed volume of the porcine cornea, which is shown in Fig 5.4.

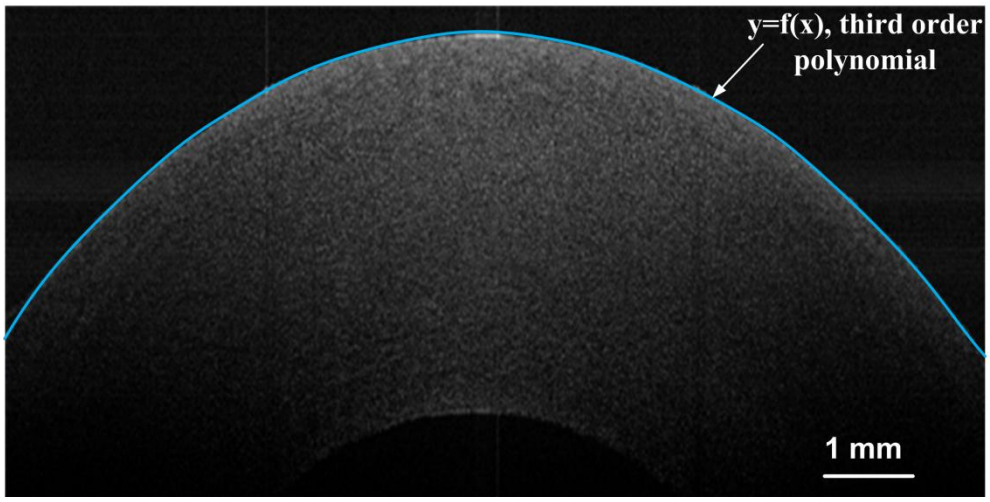

Fig 5.4: Central transverse *z*-slice of the OCT reconstructed volume for porcine cornea

The first step is to decide the parametric function for the interface of the porcine cornea, as already explained in the previous sections. This was implemented by picking points on the top interface (using command 'Ginput' in Matlab) and then fitting a third order polynomial function using these selected points. The fitted polynomial function for the top interface is shown below and the units are pixels.

$$y = -1.5\times\left((x-510)/360\right)^3 + 160\times\left((x-510)/360\right)^2 + 11\times(x-510)/360 + 30 \quad (5.10)$$

In practice, it is very useful to mask out all the unwanted points outside the cornea as this can reduce the number of data points to be corrected thus reducing calculation time. In this case, a third order polynomial function was also fitted for the bottom interface, which is

$$y = -2.1\times\left((x-490)/150\right)^3 + 43\times\left((x-490)/150\right)^2 - 1.3\times(x-490)/150 + 420 \quad (5.11)$$

The masked cornea image is represented in Fig 5.5(a). The refractive indices within and outside the porcine cornea is 1.38 and 1, respectively. Fig 5.5(b) shows the cornea after refraction correction.

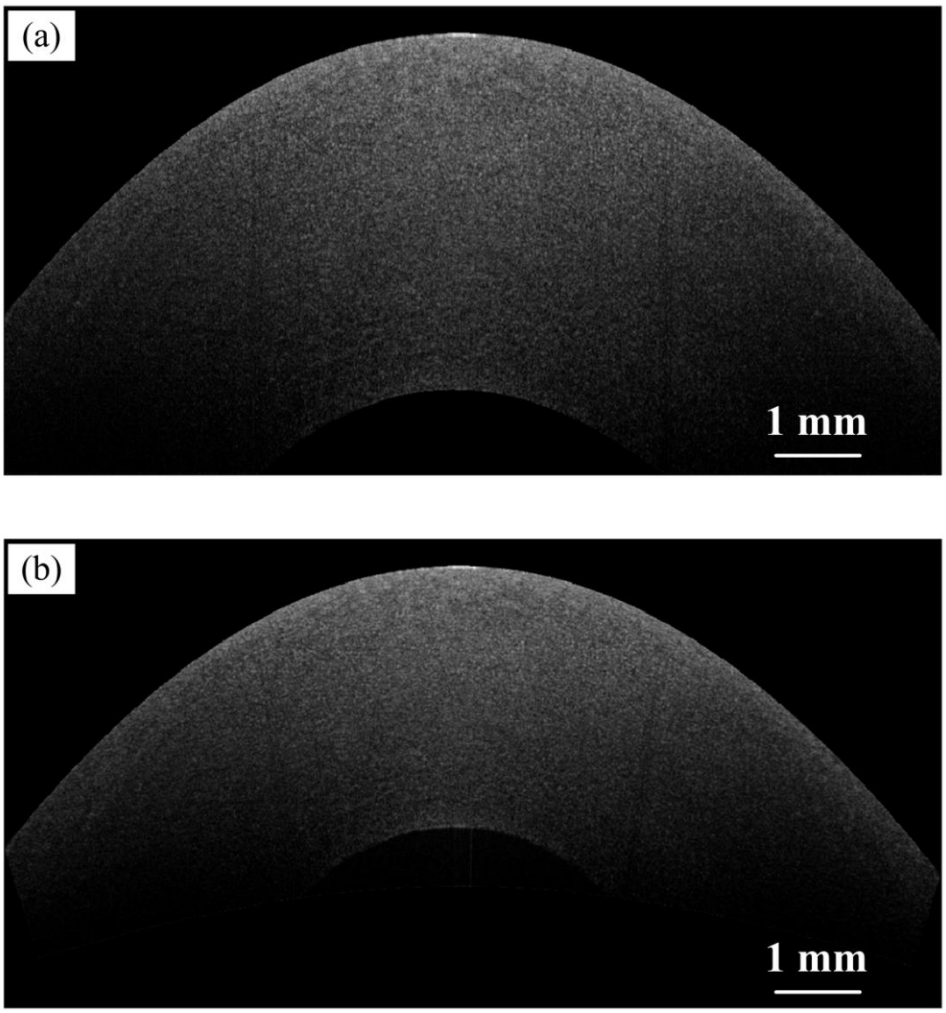

Fig 5.5: Masked OCT images (a) before and (b) after refraction correction

As expected, the corrected cornea now becomes thinner. The materials displace inwards and upwards compared to the uncorrected cornea image. It can be seen that several vertical shadow lines within the cornea in Fig 5.5(a) become tilted after the correction. This is consistent with the correction results for the fringe pattern. It should be pointed out that this correction method has a limitation regarding the calculation time. For this 2D cornea image, the calculation time is about 10 hours, which is rather time-consuming due to the fact that the used '*fminsearch*' (Nelder-Mead simplex direct search algorithm) is not the most efficient minimization algorithm and the minimization algorithm needs to be executed for too many data points. When dealing with a 3D data volume, the calculation time would be amplified thousands of times, making the correction unachievable. In this case, a refraction correction method working in a more computationally efficient way becomes necessary. This will be discussed in the following section.

5.3.1.3 Sub-grid approach

The reason why the refraction correction is very time-consuming is that the minimization algorithm is executed for every point in the object space. For a typical 2D cornea image, the image size is 1024×512 pixels. For a reconstructed 3D volume, the number will raise to $1024 \times 512 \times 1024$ voxels. Such a large number of data points will make the correction time unachievable. Thus, to make the correction method feasible for data volumes, the idea is to reduce the number of data points where the minimization algorithm is performed. In this case, the image space coordinates are computed not for all the object points but in a subset of them arranged in a grid. Here, a grid was defined as $[1:5:1024]$, $[1:5:512]$ along x and y directions, respectively, for the cornea image.

First, the minimization algorithm was performed on these grid points to determine their coordinates in the image space. Then, the coordinates of intermediate object points in the image space were found by interpolating the coordinates of those grid points. Fig 5.6 shows the plots of x and y coordinates in the image space for each object point obtained by using the above mentioned method.

After determining the coordinates (non-integer values) of each object point in the image space, the intensity value at that coordinates was interpolated (linear interpolation) and associated with the corresponding object point. The corrected cornea image then can be obtained, which is shown in Fig 5.7. Using this method, the calculation time for a typical 2D cornea image (1024×512 pixels) was significantly reduced from 10 hours to 73 seconds, which is about 500 times more efficient. This makes the correction for volume achievable.

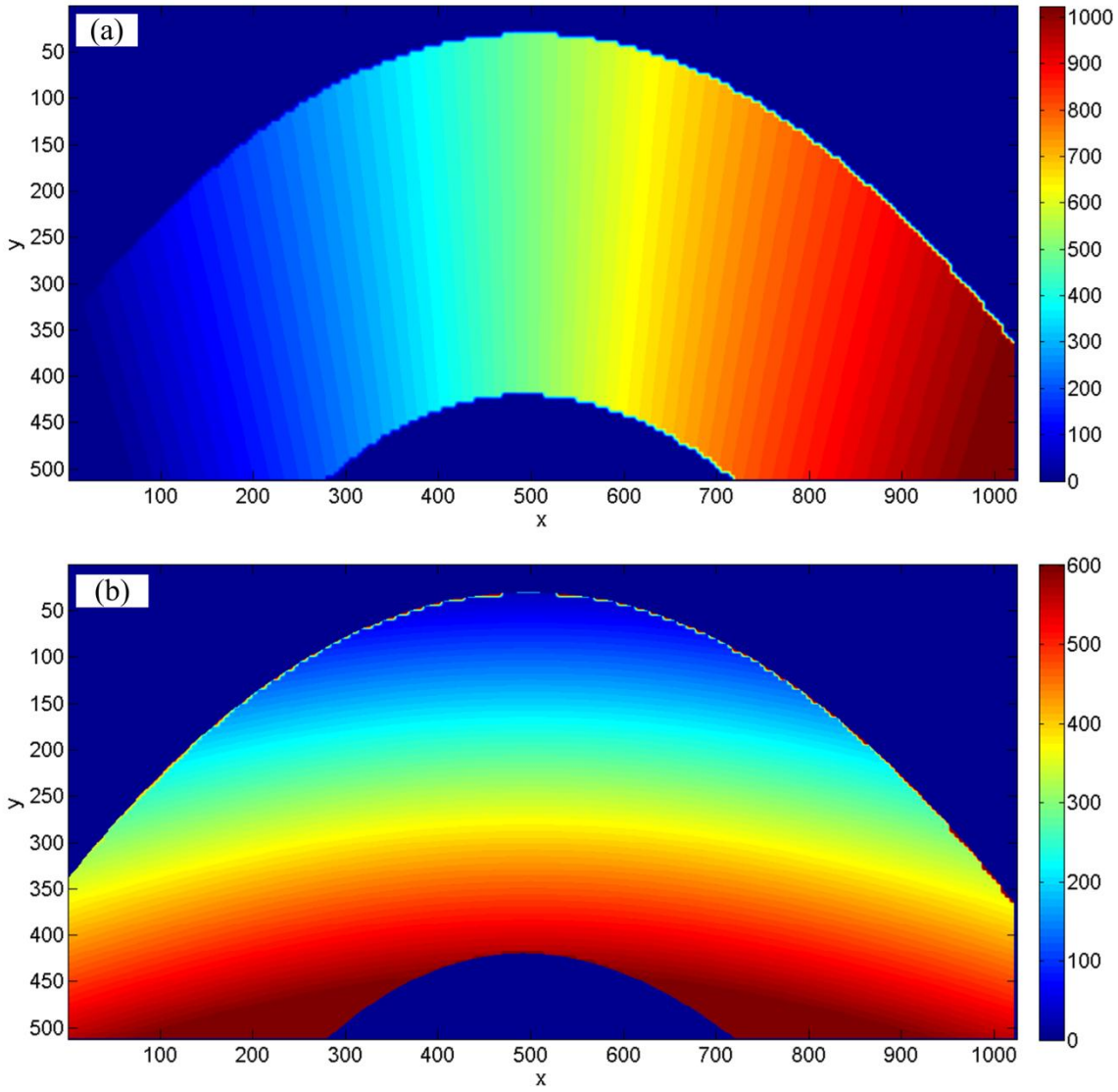

Fig 5.6: Plots of (a) *x* and (b) *y* coordinates in the image space for each object point

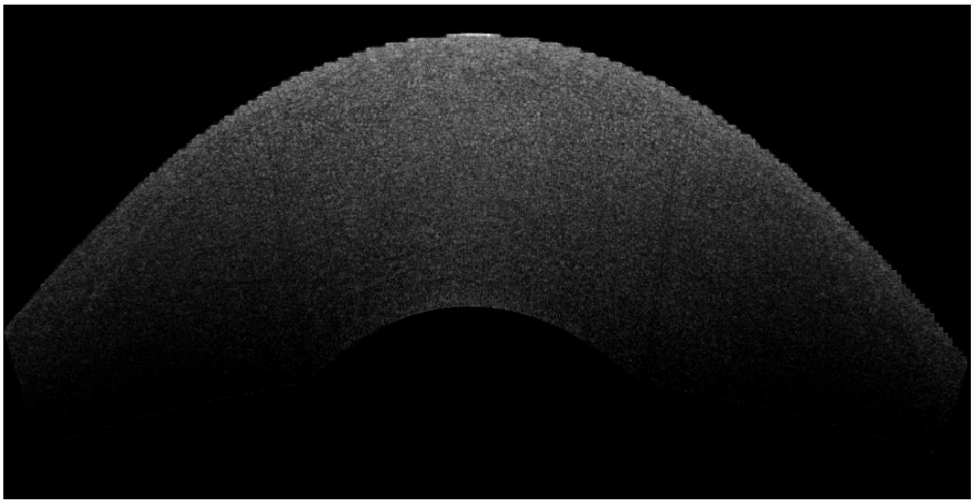

Fig 5.7: Corrected cornea image obtained with minimization on grid points

One question that comes to mind is whether this approach loses refraction correction accuracy as compared with the approach in which minimization is performed for all the object points. To bring an answer to that question, the error map between the corrected cornea image obtained with point by point minimization (Fig 5.5(b)) and the corrected cornea image obtained with minimization on grid points (Fig 5.7) is plotted in Fig 5.8. As can be seen, the difference in intensity values between the two images is very small. The mean and standard deviation values of the difference were computed, which are -5.2×10^{-5} and 0.02, respectively. Compared with the intensity value of the cornea (mean intensity 32), this difference is insignificant.

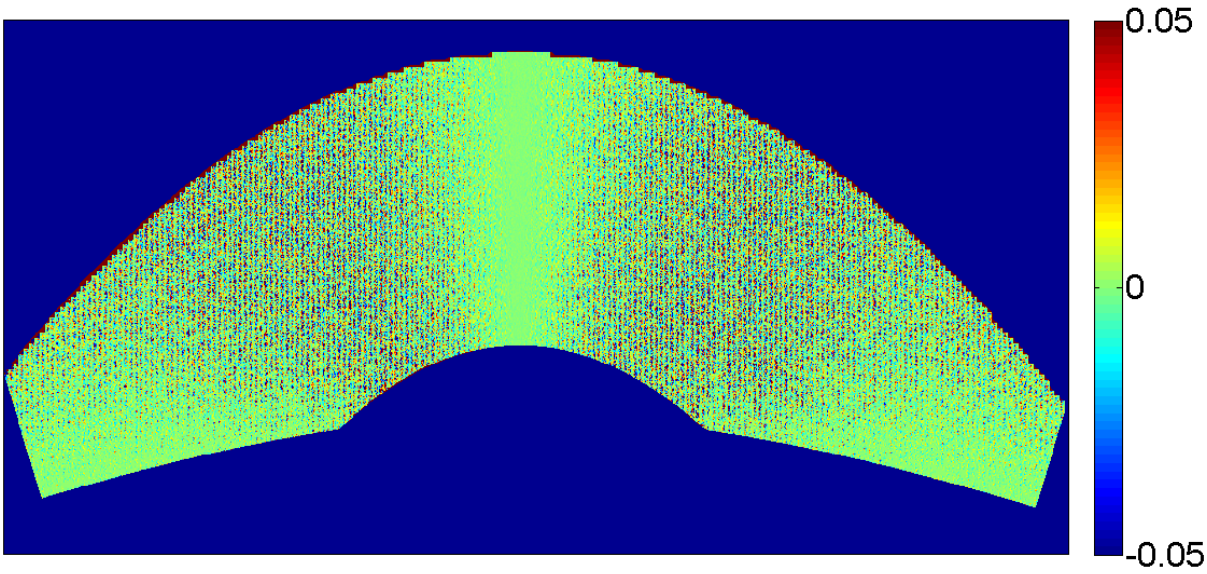

Fig 5.8: Error map between the corrected cornea image obtained with point by point minimization and the corrected cornea image obtained with minimization on grid points

5.3.2 Refraction correction in 3D

The approach of performing minimization on grid points has been proved to be effective in reducing computation time and maintaining refraction correction accuracy compared with the approach in which minimization is executed for all object points. Therefore, in this subsection this approach was applied to correct the refraction induced distortion in 3D volume reconstructions.

5.3.2.1 Functions for refraction correction in a data volume

The refraction correction for a data volume was implemented with the same procedure detailed for a 2D image. The first step is to determine the parametric equation of the top interface, which can be expressed as

$$y = f(x,z) \tag{5.12}$$

For an arbitrary object point *B*, its coordinates are (x_B, y_B, z_B). The coordinates of the corresponding incident point *A* can be expressed as $(x_A, f(x_A, z_A), z_A)$. Then, the OPD can be calculated as

$$OPD = n_0 f(x_A, z_A) + n_1 \left[(x_B - x_A)^2 + (y_B - f(x_A, z_A))^2 + (z_B - z_A)^2 \right]^{\frac{1}{2}} \tag{5.13}$$

where (x_B, y_B, z_B) are known as they are defined in a 3D Cartesian grid in the object space for each object point. Therefore, the unknowns in equation (5.13) are x_A and z_A. In this case, OPD becomes a function of x_A and z_A, which writes

$$OPD(x,z) = n_0 f(x,z) + n_1 \left[(x_B - x)^2 + (y_B - f(x,z))^2 + (z_B - z)^2 \right]^{\frac{1}{2}} \tag{5.14}$$

By minimizing OPD, the coordinates $(x_A, f(x_A, z_A), z_A)$ of the incident point *A* can be found for a given object point *B*. Then, let's use (x_I', y_I', z_I') to represent the coordinates of the corresponding image point *I*. The lateral coordinates x_I' and z_I' of point *I* is

$$x_I' = x_A \tag{5.15a}$$

$$z_I' = z_A \tag{5.15b}$$

The vertical coordinate y_I' is

$$y_I' = n_0 f(x_A, z_A) + n_1 |AB| \tag{5.16}$$

where $|AB|$ is

$$|AB| = \left[(x_B - x_A)^2 + (y_B - f(x_A, z_A))^2 + (z_B - z_A)^2 \right]^{\frac{1}{2}} \tag{5.17}$$

After determining the coordinates of the image point *I*, the intensity value at that point can be calculated for the object point *B* using 3D linear interpolation.

5.3.2.2 Refraction correction of an OCT volume

To determine the parametric function of the top interface of the porcine cornea, a number of points were picked on the top cornea surface using Matlab command 'Ginput'. These points were then used to fit a fourth order polynomial function. Fig 5.9 shows the fitted top surface of the porcine cornea in the reference state. The fitted polynomial function for the top interface is

$$y = p_{00} + p_{10}x + p_{01}z + p_{20}x^2 + p_{11}xz + p_{02}z^2 + p_{30}x^3 + p_{21}x^2z + p_{12}xz^2 + p_{03}z^3 + p_{40}x^4 + p_{31}x^3z + p_{22}x^2z^2 + p_{13}xz^3 + p_{04}z^4 \quad (5.18)$$

where the parameters in the function are listed in Table 5.1.

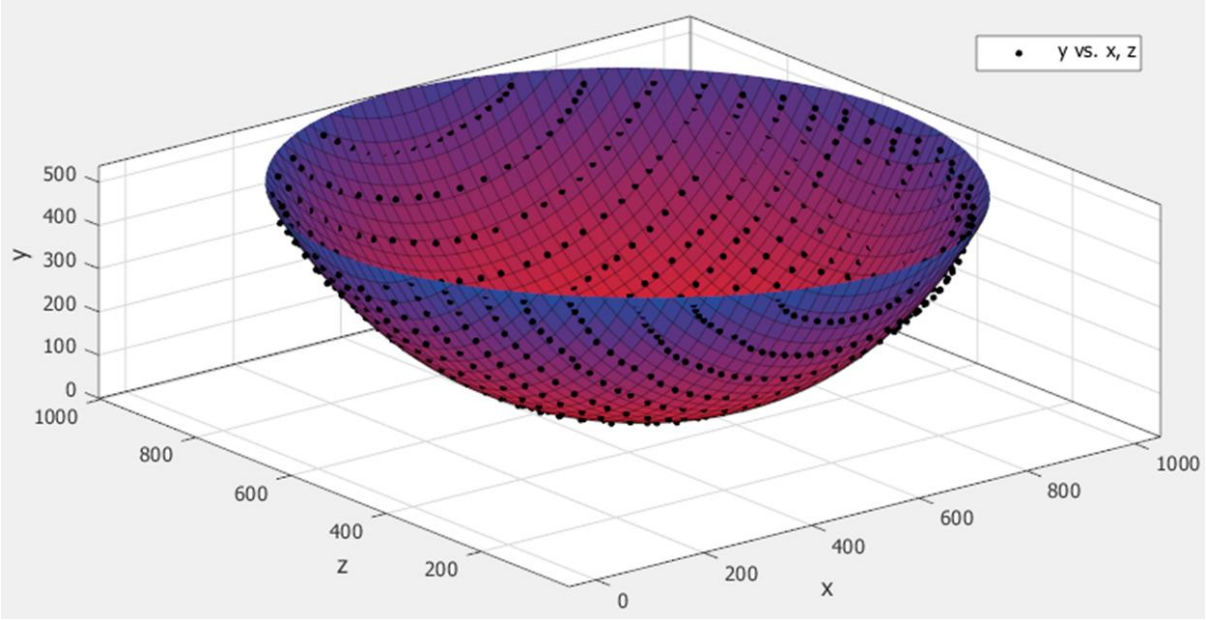

Fig 5.9: Plot of the fitted top surface of the porcine cornea using a forth order polynomial.

Table 5.1: Parameters of the 4th order polynomial function for the top surface of the porcine cornea in the reference state

P_{00}	P_{10}	P_{01}	P_{20}	P_{11}	P_{02}	P_{30}	P_{21}
764.9	-1.885	-2.339	0.002667	0.002941	0.003611	-1.96 $\times 10^{-6}$	-2.299 $\times 10^{-6}$
P_{12}	P_{03}	P_{40}	P_{31}	P_{22}	P_{13}	P_{04}	
-3.176 $\times 10^{-6}$	-2.505 $\times 10^{-6}$	1.198 $\times 10^{-9}$	-5.481 $\times 10^{-10}$	2.895 $\times 10^{-9}$	1.487 $\times 10^{-10}$	1.166 $\times 10^{-9}$	

For the deformed state, another fourth order polynomial function was also fitted, and its parameters are listed in Table 5.2.

Table 5.2: Parameters of the 4th order polynomial function for the top surface of the porcine cornea in the deformed state

P_{00}	P_{10}	P_{01}	P_{20}	P_{11}	P_{02}	P_{30}	P_{21}
859.5	-2.346	-2.774	0.0035	0.004237	0.004376	-2.652 $\times 10^{-6}$	-3.631 $\times 10^{-6}$
P_{12}	P_{03}	P_{40}	P_{31}	P_{22}	P_{13}	P_{04}	
-4.358 $\times 10^{-6}$	-3.171 $\times 10^{-6}$	1.435 $\times 10^{-9}$	-1.553 $\times 10^{-10}$	3.525 $\times 10^{-9}$	4.676 $\times 10^{-10}$	1.412 $\times 10^{-9}$	

A 3D grid was defined as $[1:5:1024]$, $[1:5:512]$, $[1:5:1024]$ along the *x*, *y* and *z* directions, respectively, for the reconstructed cornea volume in each pressure state. The minimization algorithm was then performed on the 3D grid points, as already explained in the previous subsection. Following the subsequent procedures, these distorted cornea volume reconstructions were corrected.

5.3.2.3 DVC results from refraction corrected OCT volumes

As we want to know how the refraction correction affects the deformation measurement, thus, the refraction correction was performed on the reconstructed cornea volumes obtained from the cornea inflation test introduced in chapter 4. DVC was then performed on the corrected

cornea volumes at both load steps to obtain the corrected displacement and strain fields. In Fig 5.10, the displacement maps after refraction correction are represented in column (b) and compared with the corresponding results before correction in column (a). It can be seen that the overall displacement distributions before and after refraction correction are consistent with each other although some differences can be observed. Take u_x displacement for example, it becomes larger after refraction correction with the maximal displacement now located closer to the inner interface compared with the u_x displacement map before correction. Regarding u_y, an increase in value is also observed. The strain maps before and after refraction correction are compared in Fig 5.11 (a) and (b), respectively. As can be seen, apart from the difference in strain values, the strain distribution also becomes more concentrated in the central area after refraction correction. This is more consistent with the strain results of the FE model shown in Fig 4.11(b).

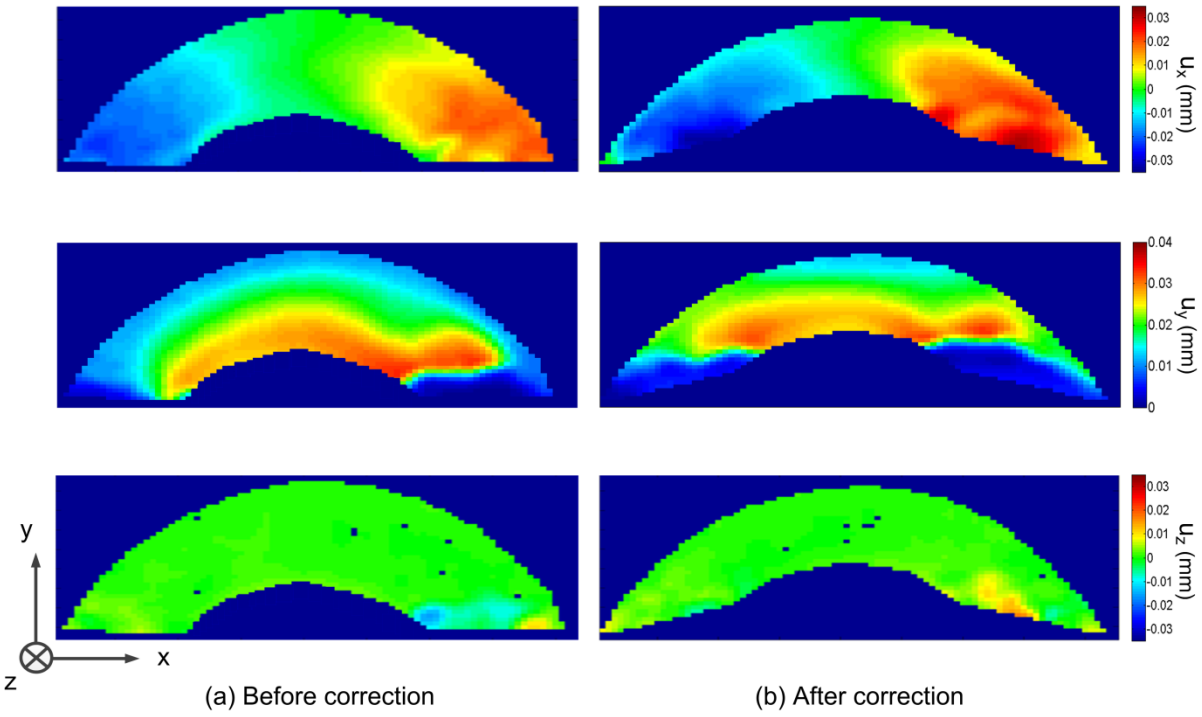

Fig 5.10: Displacement maps for the central *z*-slice 25 of the porcine cornea inflated from 2 to 2.5 kPa: (a) before and (b) after refraction correction.

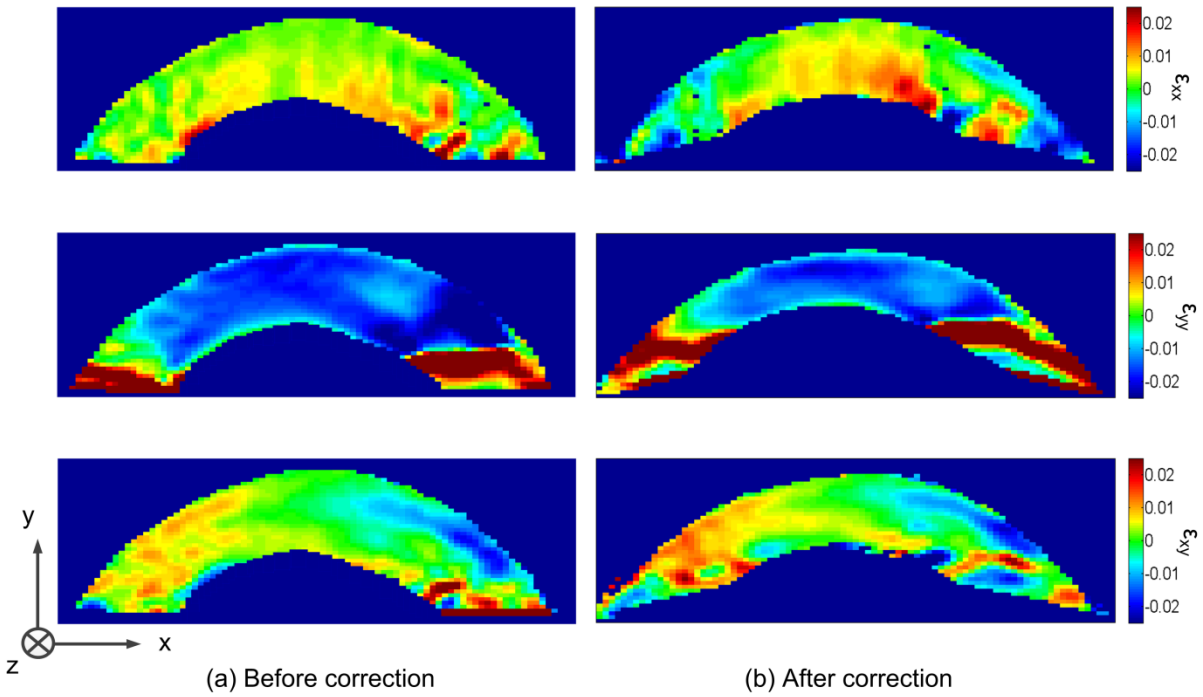

Fig 5.11: Strain maps for the central *z*-slice 25 of the porcine cornea inflated from 2 to 2.5 kPa: (a) before and (b) after refraction correction.

5.4 Validation

In the previous subsections, the refraction correction methods were introduced in detail. Examples were given for the correction of OCT images as well as DVC results obtained with the corrected cornea volumes. These results look very promising. However, one question that naturally arises is whether this correction method really corrects the OCT reconstructions. Does it really improve the DVC deformation measurement? To bring an answer to this question, tilt tests using different phantoms were designed in this section.

5.4.1 Tilt tests

In the tilt tests, stable silicone rubber phantoms were placed on a rotation stage and rotated 0.5 ° in the *xy*-plane. At each state (reference and rotated state), a 3D volume was reconstructed using the SS-OCT system. Then, the reconstructed volumes were brought to perform DVC, and strain and rotation maps were obtained. Ideally, there should be no strain as this is a pure rigid body rotation. The rotation map should show exact input value, which is 0.5 °. The idea is to check how the computed strain and rotation results differ from the reference case. Then, the refraction correction algorithm was applied to the reconstructed

volumes and DVC was performed to obtain the corrected strain and rotation results. By doing so, one can see whether the strain and rotation results are consistent with the reference values after refraction correction.

5.4.2 Sample preparation

Two phantoms with different shapes were fabricated using silicone rubber (MM240-TV). One is a rectangular flat strip while the other is hemispherical, as illustrated in Fig 5.12. Copper particles (with an average particle size of about 1 μm) were seeded into them to provide the speckle contrast. The reason for choosing these two different shapes is that by doing so, one can study the different distortions induced by a uniform refraction angle (here, a tilted flat top surface) and non-uniform refraction angles (hemispherical top surface). Fig 5.13 (a) and (b) show the central *z*-slices of the OCT reconstructed volumes of the flat and hemispherical phantoms, respectively. The dashed lines in the two OCT images illustrate the position of these phantoms after rigid body rotation. It should be pointed out that the quality of the OCT images starts to weaken in deeper regions, especially evident in the hemispherical phantom, where the correlation coefficient values are smaller than 0.8. Therefore, the strain and rotation results in those regions were discarded.

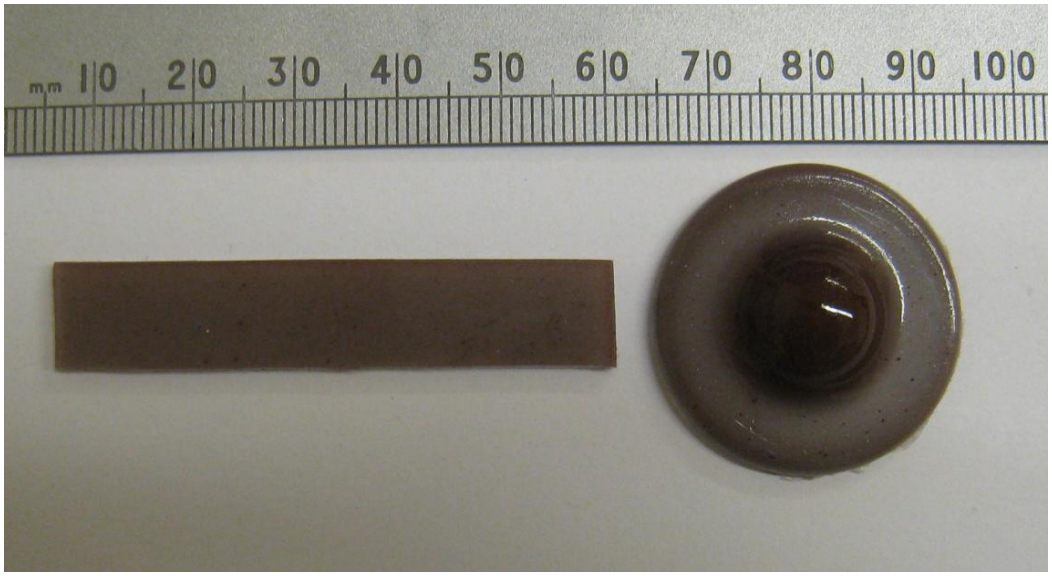

Fig 5.12: Photo of the flat and hemispherical silicone rubber phantoms for tilt tests.

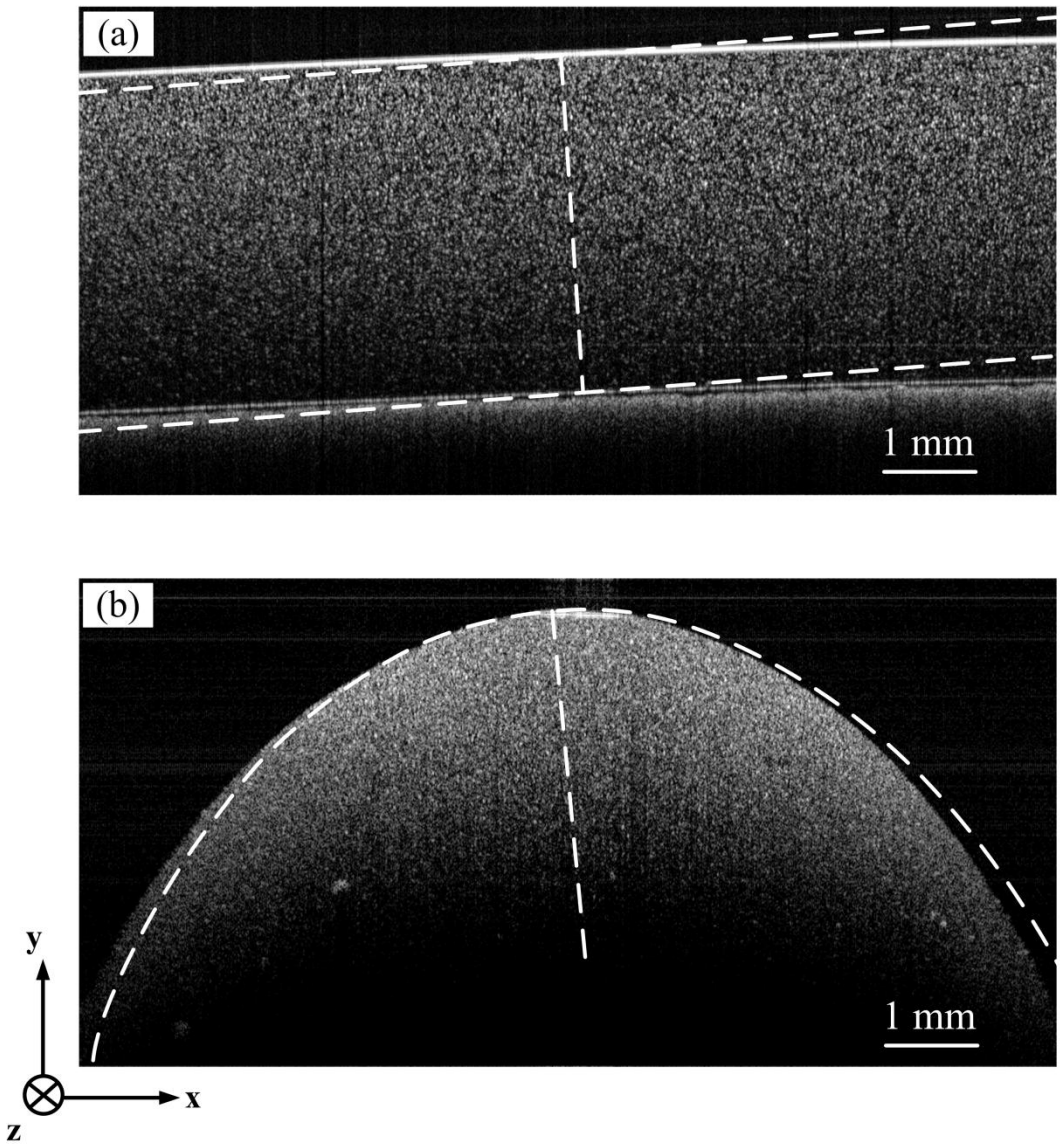

Fig 5.13: Central *z*-slices of the OCT reconstructed volumes of: (a) flat and (b) hemispherical silicone rubber phantoms. Dashed lines indicate the samples interface after rotation.

5.4.3 DVC results for tilt tests

A sub-volume size of 36^3 voxels was selected to strike a balance between the displacement and strain noise as well as the spatial resolution. Each sub-volume had 50% overlap with its six adjacent neighbours. The strains and rotations were derived from the centred finite difference of the calculated displacement fields as follows, without any additional smoothing.

$$\begin{aligned} \varepsilon_{ij} &= \frac{1}{2}\left(u_{i,j} + u_{j,i}\right) \\ \omega_{ij} &= \frac{1}{2}\left(u_{i,j} - u_{j,i}\right) \end{aligned} \tag{5.19}$$

In Fig 5.14, the strain and rotation maps before and after refraction correction are shown for ε_{xx}, ε_{yy}, ε_{xy} and ω_{xy} for a central z-slice of the flat phantom strip. The mean and standard deviation values of these strain and rotation components are listed in Table 5.3. It can be observed from Fig 5.14(a) and Table 5.3 that ε_{xx} and ε_{yy} before refraction correction show values that are close to the strain noise level (According to the noise study of OCT coupled with DVC in chapter 3, section 3.5, the noise level of different strain components is around 4×10^{-4}) while ε_{xy} shows positive values that are larger than the noise level, with a mean value of 1.3×10^{-3}. Regarding rotation, ω_{xy} shows values that are smaller than the input value 0.5 °, with a mean value of 0.32 °. These results indicate that the refraction induced distortion effectively introduces errors to DVC measurements even in the case of flat samples. It mainly affects the shear strain components. After refraction correction, as shown in Fig 5.14(b), one can see that values of ε_{xy} drop to the strain noise level. Regarding the rotation, values of ω_{xy} are now closer to the reference rotation of 0.5 °, with a mean value of 0.49 °, as listed in Table 5.3. These results indicate that the DVC measurements are effectively adjusted after refraction correction.

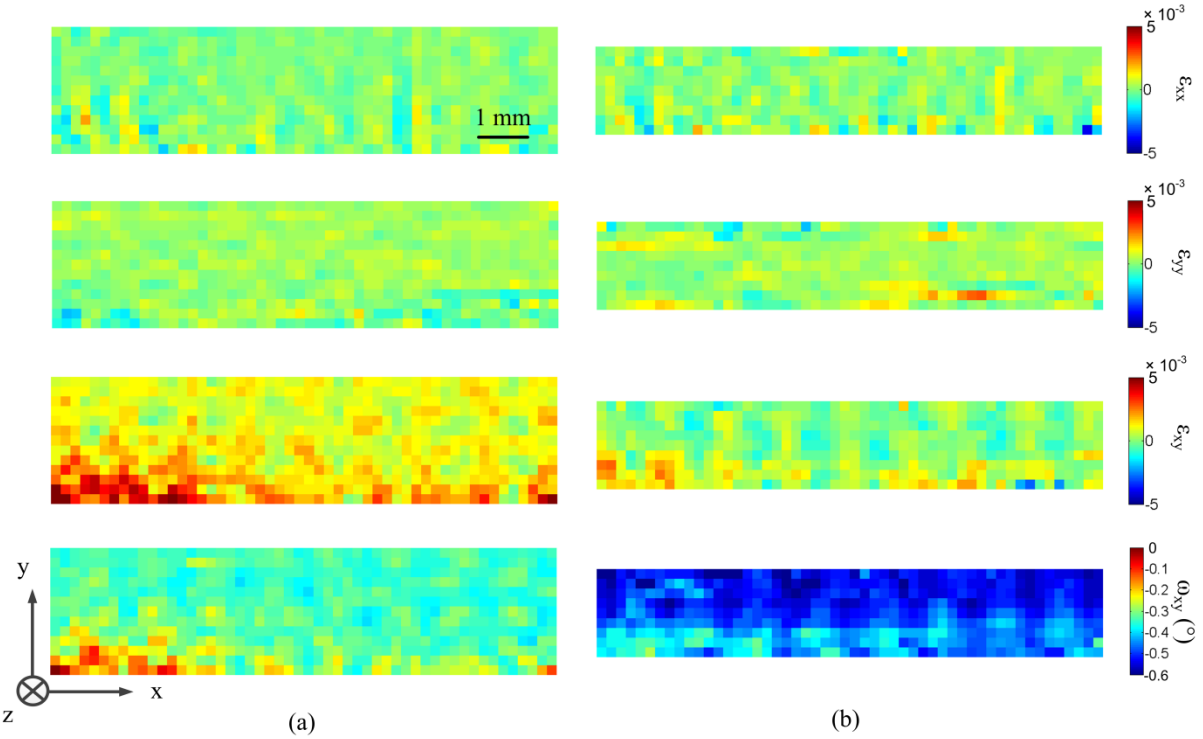

Fig 5.14: Strain and rotation maps for the flat phantom tilt test: (a) before and (b) after refraction correction, 36^3-voxel sub-volume, 50% overlap.

It should be pointed out that there is an increase in standard deviation for the strain and rotation components as can be seen in Table 5.3. This is probably because the refraction correction is based on interpolation. DVC itself is also based on interpolation. Therefore, it is not really surprising that more errors were introduced to the final results after this multi-interpolation process.

Table 5.3: Mean and standard deviation values of the strain and rotation components for the flat phantom tilt test before and after refraction correction.

	Before correction	After correction
ε_{xx}	Mean: -2.8×10^{-5} Std: 4.7×10^{-4}	Mean: 5.9×10^{-5} Std: 5.8×10^{-4}
ε_{yy}	Mean: 1.5×10^{-4} Std: 4.3×10^{-4}	Mean: 2.8×10^{-4} Std: 5.5×10^{-4}
ε_{xy}	Mean: 1.3×10^{-3} Std: 9.2×10^{-4}	Mean: 2.0×10^{-4} Std: 7.4×10^{-4}
ω_{xy}	Mean: -0.32° Std: 0.053°	Mean: -0.49° Std: 0.067°

Similar results were obtained for the hemispherical phantom. The strain and rotation maps before and after refraction correction for ε_{xx}, ε_{yy}, ε_{xy} and ω_{xy} are provided in Fig 5.15 for a central *z*-slice, and their mean and standard deviation values are listed in Table 5.4. Again, as can be seen in Fig 5.15(a), before refraction correction, ε_{xx} and ε_{yy} show distributions close to the strain noise level while ε_{xy} shows large positive values, with a mean of 2.6×10^{-3}, as listed in Table 5.4. Regarding the rotation, ω_{xy} is underestimated, with a mean value of only 0.25°. These results were improved after refraction correction with ε_{xy} dropping to noise level and ω_{xy} increasing to 0.43, closer to the input value 0.5°, as shown in Fig 5.15(b) and Table 5.4. One can also observe in Table 5.4 that there is an increase in the strain and rotation standard deviations after refraction correction. This has already been explained earlier for the flat phantom strip.

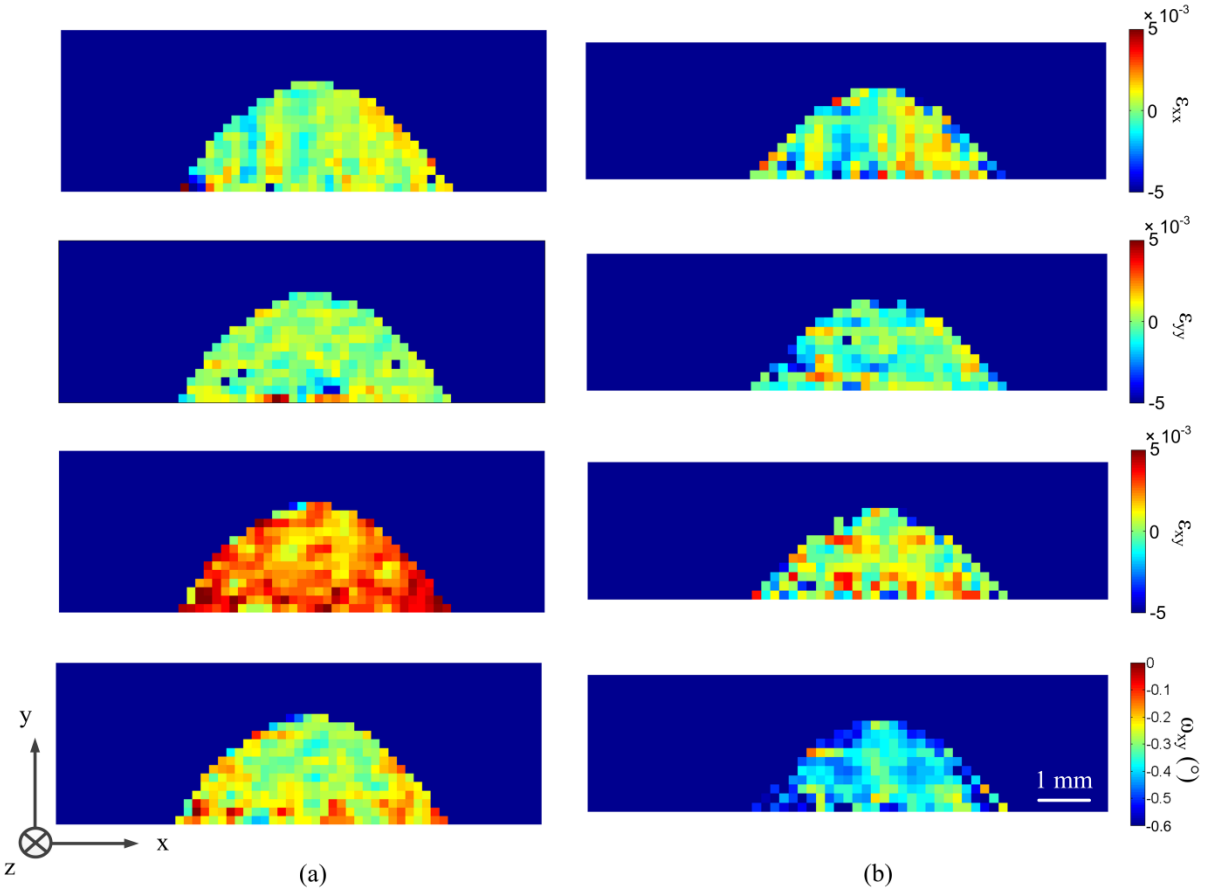

Fig 5.15: Strain and rotation maps for the hemispherical phantom tilt test: (a) before and (b) after refraction correction, 36^3-voxel sub-volume, 50% overlap.

Table 5.4: Mean and standard deviation values of the strain and rotation components for the hemispherical phantom tilt test before and after refraction correction.

	Before correction	After correction
ε_{xx}	Mean: -2.9×10^{-4} Std: 1.2×10^{-3}	Mean: -2.0×10^{-4} Std: 1.7×10^{-3}
ε_{yy}	Mean: 1.9×10^{-4} Std: 9.0×10^{-4}	Mean: -5.6×10^{-4} Std: 1.5×10^{-3}
ε_{xy}	Mean: 2.6×10^{-3} Std: 1.2×10^{-3}	Mean: 1.6×10^{-4} Std: 2.3×10^{-3}
ω_{xy}	Mean: -0.25° Std: 0.069°	Mean: -0.43° Std: 0.13°

5.5 Conclusions

In this chapter, it has been described how the refraction induced distortion arises in OCT reconstructions, which is an error source to DVC deformation measurement. Refraction correction methods for both 2D and 3D cases were developed based on Fermat's principle. A point-by-point minimization algorithm was first developed to correct 2D OCT images. This method however suffers from a shortcoming of long computation time. Therefore, a more computationally efficient way was developed, in which the minimization algorithm was only executed on a sub-set of points. Compared with the point-by-point minimization method, the latter one can significantly reduce the computation time, e.g. from about 10 hours to about 1 minute for a typical OCT image (1024×512 pixels), without a noticeable loss in accuracy. The 3D refraction correction method was applied to correct the reconstructed cornea volumes of the inflation test. The refraction corrected DVC measurements were found to be more consistent with the simulation results presented in Chapter 4. Tilt tests using a flat and a hemispherical silicone rubber phantom were carried out to validate the performance of the refraction correction method. The results show that after correction the refraction distortion induced spurious strain were reduced and the measured local rotation was much closer to the reference value.

CHAPTER 6

CONCLUSIONS AND PERSPECTIVES

6.1 Conclusions

In this thesis, an effective methodology has been developed to measure the depth-resolved 3D deformation of semi-transparent, light scattering materials such as cornea. These 3D deformation measurements can be utilized to identify the material constitutive parameters using the VFM.

The VFM was extended into 3D to accommodate to the now available depth resolved 3D deformation measurements. Both manually defined virtual fields and the optimized piecewise virtual fields were developed. They were validated to be feasible to accurately extract the material constitutive parameters through simple FEM simulations. The manually defined virtual fields were compared with the optimized piecewise virtual fields when the strain data was corrupted by different amounts of Gaussian white noise. The result shows that both methods can yield reasonable identification results. However, when the noise becomes larger, the piecewise optimized virtual fields are much more stable, and can yield more accurate identification results.

DVC can provide, by means of a single channel OCT system, multicomponent displacement fields. From these displacement fields all the strain components required by inversion methods such as the 3D VFM can be determined. A strain uncertainty in the order of $\sim 2\times10^{-4}$ to $\sim 3.5\times10^{-4}$ was observed for the OCT+DVC approach by performing noise analysis. This approach is appropriate for strain as large as ~2% (in the axial direction) above which an incremental approach should be used to avoid speckle decorrelation.

Interpolation bias in the DVC algorithm was found to be the reason for the spurious fringes observed in the strain maps. Two approaches were verified to be feasible to reduce the interpolation bias due to image under-sampling. The first approach is to perform pre-smoothing (e.g. Gaussian low-pass filter) to the volume data prior to correlation. For the second approach, the interpolation bias can be reduced by increasing the sampling density of

the SS-OCT system, even though this leads to a reduction in the field of view. Another option would be to reduce the effective numerical aperture of the OCT imaging optics, to increase the 3D speckle size and maintain large fields of view.

The 3D deformation fields were used to identify the elastic constitutive parameters of silicone rubber phantoms using the 3D VFM. The identification results for the cases of uniform and heterogeneous strain fields were compared with those calculated analytically through the constant uniaxial stress assumption and the micro tensile machine, showing good agreement.

The depth-resolved 3D deformation of the porcine cornea and silicone rubber phantom samples under posterior inflation conditions was measured using OCT+DVC. Reasonable displacement and strain results of the inflation tests were obtained for both phantom and cornea samples. These results show a good overall agreement with the results of a simple FE model.

Correction methods for both 2D and 3D cases were developed based on Fermat's principle to correct the refraction induced distortion in the OCT reconstructions. A computationally efficient way was developed which can significantly reduce the computation time of the correction method without losing correction accuracy. Tilt tests were carried out to evaluate the performance of the refraction correction method. The results show that after correction the refraction distortion induced spurious strain was reduced and the measured rotation results increased closer to the known reference value. Refraction correction was applied to the reconstructed cornea volumes of the inflation test. The DVC results after refraction correction were found to be more consistent with the simulation results and are now suitable and ready for further identification studies of corneal properties with 3D VFM.

6.2 Perspectives

- Due to the time limitation of the present project, added complexity to the calculation of external virtual work in an inflation test with pressure field, and poorer strain results near the bottom regions due to inadequate image quality, constitutive parameters of the porcine cornea have not been identified yet. Future work will be aimed at identifying the constitutive parameters once these issues are solved. To realize this, optimized piecewise VFM can be used. The virtual displacement at the clamped peripheral boundary must be

set to zero so that the external virtual work done by the unknown reaction force can be cancelled out. For each measurement point at the bottom cornea/vitreous interface, the component of virtual displacement along the normal direction of the bottom interface at this point must be determined to calculate the external virtual work at this measurement point. Based on this, the total external virtual work done by the inflation pressure can be determined by the integral of the external virtual work at individual measurement points. Then, the constitutive parameters of the cornea can be identified following the same procedure as for the examples in section 2.7.

- The present deformation measurements are based on single layer specimens such as the introduced silicone rubber phantoms. Even though the cornea is composed of five layers, the stroma consists of over 90% of the corneal thickness. Therefore, it would be interesting to create a phantom with multi-layers (e.g. double-layers with the same thickness and different stiffness), and measure the heterogeneous deformation fields of each layer using OCT+DVC. It would be useful to develop a 3D VFM which takes into account of the material heterogeneity. This 3D VFM could be used to extract the material constitutive parameters of each layer from the heterogeneous deformation fields of a single test. This recommended future study could significantly advance the applicability of the proposed methodology.

- One limitation of the current OCT+DVC system for identifying the different mechanical properties of different corneal layers from the inflation test is the limited spatial resolution of the OCT system compared to the very small thickness of each layer, especially for epithelium, Bowman's layer, Descemet's membrane, and endothelium. Due to this limitation, the current OCT system cannot provide OCT images with sufficient independent measurement points in each corneal layer. Therefore, in the future, an OCT system with improved spatial resolution should be used to obtain OCT images with sufficient measurement points in each corneal layer, from which the different strain distribution in each layer (due to the difference in material mechanical properties for each layer) of the inflation test can be measured. It should be pointed out that, as in a tensile test configuration, the strain distributions in layers with different material mechanical properties should show differences even though they are loaded equally in the inflation configuration. Based on this strain measurement, constitutive parameters of each layer should be identified using the 3D VFM developed specifically for material heterogeneity.

- The methodology (Inflation Test+OCT+DVC) presented in chapter 4 can be used in the future to study the corneal deformation behaviour at different pressure range (from low pressure to high pressure) to fully address the linear and non-linear mechanical properties of the cornea.

- Due to light reflection and absorption, current volume data tend to have weak quality in deeper regions of the sample, which leads to inaccurate DVC results there, and affects the identification of the constitutive parameters. Thus, efforts can be targeted at the improvement of image quality and depth range of the OCT system in the future. In order to reduce refraction distortions the illumination path could be adjusted by adding a negative lens close to the cornea to make the illumination beam perpendicular to the interface so that refraction can be reduced. This would require an OCT system with deeper penetration depth and reduced spectral roll-off.

- Other soft tissues such as artery, skin, esophagus, *etc*. could also be studied using the proposed methodology to study their deformation behaviour and material properties. It will be interesting to measure the depth-resolved full-field deformation of these tissues under high pressure to study their non-linear properties and failure response (e.g. aneurysm rupture).

- In the present work, the 3D VFM has been implemented for linear elasticity. However, considering the non-linear behaviour of the biological tissues in large deformation, it will be useful to develop a 3D non-linear VFM. Different non-linear models can be used such as hyper-elasticity. These models could serve to a more comprehensive identification of the material constitutive parameters.

REFERENCES

[1] R. Ambekar, K. C. Toussaint Jr, A. W. Johnson. The effect of keratoconus on the structural, mechanical, and optical properties of the cornea, *Journal of the Mechanical Behavior of Biomedical Materials*, 4(3), 223-236, 2011

[2] I. Fatt. *Physiology of the eye: An introduction to the vegetative functions*. Butterworth-Heinemann, 1992

[3] D. A. Atchison, G. Smith. *Optics of the human eye*. Butterworth-Heinemann, 2000

[4] M. Notara, A. Alatza, J. Gilfillan, A. R. Harris, H. J. Levis, *et al*. In sickness and in health: Corneal epithelial stem cell biology, pathology and therapy. *Experimental Eye Research*, 90(2), 188-195, 2010

[5] A. C. Browning, A. Bhan, A. P. Rotchford, S. Shah, H. S. Dua. The effect of corneal thickness on intraocular pressure measurement in patients with corneal pathology. *The British Journal of Ophthalmology*, 88(11), 1395-1399, 2004

[6] A. Tarkkanen, L. Merenmies. Corneal pathology and outcome of keratoplasty in autoimmune polyendocrinopathy-candidiasis ectodermal dystrophy. Acta Ophthalmologica Scandinavica, 79(2), 204-207, 2001

[7] J. B. Robin, D. J. Schanzlin, S. M. Verity, B. A. Barron, R. C. Arffa, *et al*. Peripheral corneal disorders. *Survey of Ophthalmology*, 31(1), 1-36 1986

[8] J. H. Krachmer, R. S. Feder, M. W. Belin. Keratoconus and related noninflammatory corneal thinning disorders. *Survey of Ophthalmology*, 28(4), 293-322, 1984

[9] M. J. Mannis, W. A. Segal, J. K. Darlington. Making sense of refractive surgery in 2001: why, when, for whom, and by whom?. *Mayo Clinic Proceedings*, 76(8), 823-829, 2001

[10] M. R. Bryant, P. J. McDonnell. Constitutive laws for biomechanical modeling of refractive surgery. *Journal of Biomechanical Engineering*, 118(4), 473-481, 1996

[11] M. Asejczyk-Widlicka, W. Srodka, R. A. Schachar, B. K. Pierscionek. Material properties of the cornea and sclera: A modelling approach to test experimental analysis. *Journal of Biomechanics*, 44(3), 543-546, 2011

[12] R. E. Norman, J. G. Flanagan, I. A. Sigal, S. M. Rausch, I. Tertinegg, C. R. Ethier. Finite element modeling of the human sclera: Influence on optic nerve head biomechanics and connections with glaucoma. *Experimental Eye Research*, 93(1), 4-12, 2011

[13] T. H. Kwon, J. Ghaboussi, D. A. Pecknold, Y. M. Hashash. Effect of cornea material stiffness on measured intraocular pressure. *Journal of Biomechanics*, 41(8), 1707-1713, 2008

[14] Y. Komai, T. Ushiki. The 3-dimensional organization of collagen fibrils in the human cornea and sclera. *Investigative Ophthalmology & Visual Science*, 32(8), 2244-2258, 1991

[15] R. S. Snell, M. A. Lemp. *Clinical Anatomy of the Eye, 2nd Edition*. Wiley-Blackwell, 1998

[16] W. Radner, M. Zehetmayer, R. Aufreiter, R. Mallinger. Interlacing and cross-angle dstribution of collagen lamellae in the human cornea. *Cornea*, 17(5), 537-543, 1998

[17] J. E. Scott. Proteoglycan: collagen interactions and corneal ultrastructure. *Biochemical Society Transactions*, 19, 877-881, 1991

[18] H. Studer, X. Larrea, H. Riedwyl, P. Buchler. Biomechanical model of human cornea based on stromal microstructure. *Journal of Biomechanics*, 43(5), 836-842, 2010

[19] S. Deokule, R. N. Weinreb. Relationships among systemic blood pressure, intraocular pressure, and open-angle glaucoma. *Canadian Journal of Ophthalmology*, 43(3), 302-307, 2008

[20] M. Kass, M. L. Sears. Hormonal regulation of intraocular pressure. *Survey of Ophthalmology*, 22(3), 153-176, 1977

[21] Y. Shiose. Intraocular pressure: New perspectives. *Survey of Ophthalmology*, 34(6), 413-435, 1990

[22] Y. Shiose, Y. Kawasc. A new approach to stratified normal intraocular pressure in a general population. *American Journal of Ophthalmology*, 101 (6), 714-721, 1986

[23] J. Caprioli, R. Varma. Intraocular pressure: modulation as treatment for glaucoma. *American Journal of Ophthalmology*, 152(3), 340-344, 2011

[24] D. Wang, W. Huang, Y. Li, Y. Zheng, P. J. Foster, *et al*. Intraocular pressure, central corneal thickness, and glaucoma in Chinese adults: The Liwan eye study. *American Journal of Ophthalmology*, 152(3), 454-462, 2011

[25] G. O. Waring, M. M. Rodriques, P. R. Laibson. Corneal dystrophies. *Survey of Ophthalmology*, 23(2), 71-122, 1978

[26] J. Y. Niederkorn, H. Alizadeh, H. Leher, J. P. McCulley. The pathogenesis of Acanthamoeba keratitis. *Microbes and Infection*, 1(6), 437-443, 1999

[27] C. C. Powell. Chapter 41-Vision-Threatening corneal ulcers. *Veterinary Emergency Medicine Secrets, 2nd Edition*, Elsevier Health Sciences, 2001

[28] K. Anderson, A. El-Sheikh, T. Newson. Application of structural analysis to the mechanical behaviour of the cornea. *Journal of the Royal Society Interface*, 1(1), 3-15, 2004

[29] A. El-sheikh, D. Alhasso, P. Rama. Biomechanical properties of human and porcine corneas. *Experimental Eye Research*, 86(5), 783-790, 2008

[30] S. L. Woo, A. S. Kobayashi, W. A. Schlegel, C. Lawrence. Nonlinear material properties of intact cornea and sclera. *Experimental Eye Research*, 14 (1), 29-39, 1972

[31] A. El-sheikh, D. Alhasso, P. Rama. Assessment of the epithelium's contribution to corneal biomechanics. *Experimental Eye Research*, 86(2), 445-451, 2008

[32] B. L. Boyce, J. M. Grazier, R. E. Jones, T. D. Nguyen. Full-field deformation of bovine cornea under constrained inflation conditions. *Biomaterials*, 29(28), 3896-3904, 2008

[33] K. M. Myers, B. Coudrillier, B. L. Boyce, T. D. Nguyen. The inflation response of the posterior bovine sclera. *Acta Biomaterialia*, 6(11), 4327-4335, 2010

[34] A. El-sheikh, K. Anderson. Comparative study of corneal strip extensometry and inflation tests. *Journal of the Royal Society Interface*, 2(3), 177-185, 2005

[35] D. R. Lari, D. S. Schultz, A. S. Wang, O. T. Lee, J. M. Stewart. Scleral mechanics: Comparing whole globe inflation and uniaxial testing. *Experimental Eye Research*, 94(1), 128-135, 2012

[36] B. L. Boyce, R. E. Jones, T. D. Nguyen, J. M. Grazier. Stress-controlled viscoelastic tensile response of bovine cornea. *Journal of Biomechanics*, 40(11), 2367-2376, 2007

[37] Y. Zeng, J. Yang, K. Huang, Z. Lee, X. Lee. A comparison of biomechanical properties between human and porcine cornea. *Journal of Biomechanics*, 34(4), 533-537, 2001

[38] Y. J. Jordan, J. E. Jordan, J. B. Lightfoote, K. D. Ragland. Quality outcomes of reinterpretation of brain CT studies by subspecialty experts in stroke imaging. *American Journal of Roentgenology*, 199(6), 1365-1370, 2012

[39] F. Watarai, M. Takahashi, T. Hosoya, K. Murata. Congenital lung abnormalities: A pictorial review of imaging findings. *Japanese Journal of Radiology*, 30(10), 787-797, 2012

[40] A. R. Zeina, B. Kessel, A. Mahamid, J. Gazmawi, A. Shrim, *et al*. Computed tomographic diagnosis of traumatic fetal subdural hematoma. *Emergency Radiology*, 20(2), 169-172, 2013

[41] F. Pierron, S. A. McDonald, D. Hollis, J. Fu, P. J. Withers, et al. Comparison of the mechanical behaviour of standard and auxetic foams by x-ray computed tomography and digital volume correlation. *Strain*, 49(6), 467-482, 2013

[42] P. Leplay, J. Réthoré, S. Meille, M. C. Baietto, J. Adrien, *et al*. Three-dimensional analysis of an in situ double-torsion test by X-ray computed tomography and digital volume correlation. *Experimental Mechanics*, 53(7), 1265-1275, 2013

[43] J. J. Bock, A. M. Jacobi. X-ray micro-computed tomography imaging of open-cell metal foams. *Journal of Heat Transfer*, 134(8), 080911, 2012

[44] J. R. Helliwell, C. J. Sturrock, K. M. Grayling, S. R. Tracy, R. J. Flavel, *et al*. Applications of X-ray computed tomography for examining biophysical interactions and structural development in soil systems: A review. *European Journal of Soil Science*, 64(3), 279-297, 2013

[45] R. W. Y. Lee, S. K. Conley, A. Gropman, F. D. Porter, E. H. Baker. Brain magnetic resonance imaging findings in smith-lemli-opitz syndrome. *American Journal of Medical Genetics, Part A*, 161(10), 2407-2419, 2013

[46] G. Sommer, J. Bremerich, G. Lund. Magnetic resonance imaging in valvular heart disease: clinical application and current role for patient managemen. *Journal of Magnetic Resonance Imaging*, 35(6), 1241-1252, 2012

[47] A. Pan, R. Kumar, P. M. MacEy, G. C. Fonarow, R. M. Harper, *et al*. Visual assessment of brain magnetic resonance imaging detects injury to cognitive regulatory sites in patients with heart failure. *Journal of Cardiac Failure*, 19(2), 94-100, 2013

[48] P. Glover, P. Mansfield. Limits to magnetic resonance microscopy. *Reports on Progress in Physics*, 65(10), 1489-1511, 2002

[49] B. Larson, S. Abeytunge, E. Seltzer, M. Rajadhyaksha, K. Nehal. Detection of skin cancer margins in Mohs excisions with high-speed strip mosaicing confocal microscopy: A feasibility study. *British Journal of Dermatology*, 169(4), 922-926, 2013

[50] J. L. Thomason, A. Knoester. Application of confocal scanning optical microscopy to the study of fibre-reinforced polymer composites. *Journal of Materials Science Letters*, 9(3), 258-262, 1990

[51] C. M. St Croix1, S. H. Shand, S. C. Watkins. Confocal microscopy: comparisons, applications, and problems. *Biotechniques*, 39(6) SUPPL, S2-S5, 2005

[52] G. McConnell. Improving the penetration depth in multiphoton excitation laser scanning microscopy. *Journal of Biomedical Optics*, 11(5), 054020, 2006

[53] A. F. Fercher. Optical coherence tomography - development, principles, applications. *Zeitschrift fur Medizinische Physik*, 20(4), 251-276, 2010

[54] T. Gambichler, V. Jaedicke, S. Terras. Optical coherence tomography in dermatology: technical and clinical aspects. *Archives of Dermatological Research*, 303(7), 457-473, 2011

[55] B. J. Kaluzy, J. J. Kaluzny, A. Szkulmowska, I. Gorczynska, M. Szkulmowski, *et al*. Spectral optical coherence tomography: a novel technique for cornea imaging. *Cornea*, 25(8), 960-965, 2006

[56] D. F. Kiernan, W. F. Mieler, S. M. Hariprasad. Spectral-domain optical coherence tomography: a comparison of modern high-resolution retinal imaging systems. *American Journal of Ophthalmology*, 149(1), 18-31, 2010

[57] N. Hutchings, T. L. Simpson, C. Hyun, A. A. Moayed, S. Hariri, *et al*. Swelling of the human cornea revealed by high-speed, ultrahigh-resolution optical coherence tomography. *Investigative Ophthalmology and Visual Science*, 51(9), 4579-4584, 2010

[58] J. Welzel, E. Lankenau, R. Birngruber, R. Engelhardt. Optical coherence tomography of the human skin. *Journal of the American Academy of Dermatology*, 37(6), 958-963, 1997

[59] K. Ishibashi, N. Ozawa, J. Tagami, Y. Sumi. Swept-source optical coherence tomography as a new tool to evaluate defects of resin-based composite restorations. *Journal of Dentistry*, 39(8), 543-548, 2011

[60] J. P. Dunkers, R. S. Parnas, C. G. Zimba, R. C. Peterson, K. M. Flynn, *et al*. Optical coherence tomography of glass reinforced polymer composites. *Composites: Part A*, 30(2), 139-145, 1999

[61] K. Wiesauer, M. Pircher, E. Götzinger, C. K. Hitzenberger, R. Oster, *et al*. Investigation of glass-fibre reinforced polymers by polarization-sensitive, ultra-high resolution optical

coherence tomography: Internal structures, defects and stress. *Composites Science and Technology*, 67(15-16), 3051-3058, 2007

[62] B. Bista, A. Sadr, A. Nazari, Y. Shimada, Y. Sumi, *et al*. Nondestructive assessment of current one-step self-etch dental adhesives using optical coherence tomography. *Journal of Biomedical Optics*, 18(7), 076020, 2013

[63] A. Safrani, I. Abdulhalim. Ultrahigh-resolution full-field optical coherence tomography using spatial coherence gating and quasi-monochromatic illumination. *Optics Letters*, 37(4), 458-460, 2012

[64] T. D. Nguyen, B. L. Boyce. An inverse finite element method for determining the anisotropic properties of the cornea. *Biomechanics and Modeling in Mechanobiology*, 10(3), 323-337, 2011

[65] A. Pandolfi, F. Manganiello. A model for the human cornea: constitutive formulation and numerical analysis. *Biomechanics and Modeling in Mechanobiology*, 5(4), 237-246, 2006

[66] A. Pandolfi, G. A. Holzapfel. Three-dimensional modeling and computational analysis of the human cornea considering distributed collagen fibril orientations. *Journal of Biomechanical Engineering*, 130(6), 061006, 2008

[67] F. Pierron, M. Grédiac. *The virtual fields method*. Springer New-York, 2012

[68] M. Grédiac, F. Pierron, S. Avril, E. Toussaint. The virtual fields method for extracting constitutive parameters from full-field measurements: a review. *Strain*, 42(4), 233-253, 2006

[69] S. Avril, F. Pierron. General framework for the identification of constitutive parameters from full-field measurements in linear elasticity. *International Journal of Solids and Structures*, 44(14-15), 4978-5002, 2007

[70] M. Grédiac, F. Pierron. Numerical issues in the virtual fields method. *International Journal for Numerical Methods in Engineering*, 59(10), 1287-1312, 2004

[71] S. Avril, M. Bonnet, A. S. Bretelle, M. Grédiac, F. Hild, *et al*. Overview of identification methods of mechanical parameters based on full-field measurements. *Experimental Mechanics*, 48(4), 381-402, 2008

[72] F. Pierron, S. Zhavoronok, M. Grédiac. Identication of the through-thickness properties of thick laminated tubes using the virtual fields method. *International Journal of Solids and Structures*, 37(32), 4437-4453, 2000

[73] M. Grédiac, F. Pierron, Y. Surrel. Novel procedure for complete in-plane composite characterization using a single T-shaped specimen. *Experimental Mechanics*, 39(2), 142-149, 1999

[74] M. Grédiac, F. Pierron, A. Vautrin. The Iosipescu in-plane shear test applied to composites: a new approach based on displacement field processing. *Composites Science and Technology*, 51(3), 409-417, 1994

[75] M. Grédiac. On the direct determination of invariant parameters governing the bending of anisotropic plates. *International Journal of Solids and Structures*, 33(27), 3969-3982, 1996

[76] M. Grédiac, F. Auslender, F. Pierron. Applying the virtual fields method to determine the through-thickness moduli of thick composites with a nonlinear shear response. *Composites Part A*, 32(12), 1713-1725, 2001

[77] H. Chalal, F. Meraghni, F. Pierron, M. Grédiac. Direct identification of the damage behaviour of composite materials using the virtual fields method. *Composites Part A*, 35(7-8), 841-848, 2004

[78] T. Guélon, E. Toussaint, J. B. Le Cam, N. Promma, M. Grediac. A new characterisation method for rubber. *Polymer Testing*, 28(7), 715-723, 2009

[79] M. Grédiac, F. Pierron. Applying the virtual fields method to the identification of elasto-plastic constitutive parameters. *International Journal of Plasticity*, 22(4), 602-627, 2006

[80] Y. Pannier, S. Avril, R. Rotinat, F. Pierron. Identification of elasto-plastic constitutive parameters from statically undetermined tests using the virtual fields method. *Experimental Mechanics*, 46(6), 735-755, 2006

[81] S. Avril, F. Pierron, Y. Pannier, R. Rotinat. Stress reconstruction and constitutive parameter identification in plane-stress elasto-plasticity problems using surface measurements of deformation fields. *Experimental Mechanics*, 48(4), 403-419, 2008

[82] S. Avril, P. Badel, A. Duprey. Anisotropic and hyperelastic identification of in vitro human arteries from full-field optical measurements. *Journal of Biomechanics*, 43(15), 2978-2985, 2010

[83] J. Kim, S. Avril, A. Duprey, J. Favre. Experimental characterization of rupture in human aortic aneurysms using a full-field measurement technique. *Biomechanics and Modeling in Mechanobiology*, 11(6), 841-853, 2012

[84] Y. Surrel. Moire and grid methods: a signal-processing approach. *Proceedings of SPIE - The International Society for Optical Engineering*, 2342, 118-127, 1994

[85] F. Pierron, B. Green, M. R. Wisnom. Full-field assessment of the damage process of laminated composite open-hole tensile specimens. Part I: Methodology. *Composites Part A*, 38(11), 2307-2320, 2007

[86] S. Avril, E. Ferrier, A. Vautrin, P. Hamelin, Y. Surrel. A full-field optical method for the experimental analysis of reinforced concrete beams repaired with composites. *Composites Part A*, 35(7-8), 873-884, 2004

[87] P. D. Ruiz, J. M. Huntley, R. D. Wildman. Depth-resolved whole-field displacement measurement by wavelength-scanning electronic speckle pattern interferometry. *Applied Optics*, 44(19), 3945-3953, 2005

[88] P. D. Ruiz, Y. Zhou, J. M. Huntley, R. D. Wildman. Depth-resolved whole-field displacement measurement using wavelength scanning interferometry. *Journal of Optics A*, 6(7), 679-683, 2004

[89] S. Chakraborty, P. D. Ruiz. Measurement of all orthogonal components of displacement in the volume of scattering materials using wavelength scanning interferometry. *Journal of the Optical Society of America A*, 29(9), 1776-1785, 2012

[90] I. Cespedes, J. Ophir, H. Ponnekanti, N. Maklad. Elastography: Elasticity imaging using ultrasound with application to muscle and breast in vivo. *Ultrasonic Imaging*, 15(2), 73-88, 1993

[91] A. Manduca, T. E. Oliphant, M. A. Dresner, J. L. Mahowald, S. A. Kruse, *et al.* Magnetic resonance elastography: Non-invasive mapping of tissue elasticity. *Medical Image Analysis*, 5(4), 237-254, 2001

[92] R. K. Wang, S. Kirkpatrick, M. Hinds. Phase-sensitive optical coherence elastography for mapping tissue microstrains in real time. *Applied Physics Letters*, 90(16), 164105, 2007

[93] V. Y. Zaitsev, L. A. Matveev, A. L. Matveyev, G. V. Gelikonov, V. M. Gelikonov. Elastographic mapping in optical coherence tomography using an unconventional approach based on correlation stability. *Journal of Biomedical Optics*, 19(2), 021107, 2014

[94] S. J. Kirkpatrick, R. K. Wang, D. D. Duncan. OCT-based elastography for large and small deformations. *Optics Express*, 14(24), 11585-11597, 2006

[95] C. Sun, B. Standish, V. X. D. Yang. Optical coherence elastography: Current status and future applications. *Journal of Biomedical Optics*, 16(4), 043001, 2011

[96] T. C. Chu, W. F. Ranson, M. A. Sutton, W. H. Peters. Applications of digital-image-correlation techniques to experimental mechanics. *Experimental Mechanics*, 25(3), 232-244, 1985

[97] E. Parsons, M. C. Boyce, D. M. Parks. An experimental investigation of the large-strain tensile behavior of neat and rubber-toughened polycarbonate. *Polymer*, 45(8), 2665-2684, 2004

[98] F. Hild, S. Roux. Comparison of local and global approaches to digital image correlation. *Experimental Mechanics*, 52(9), 1503-1519, 2012

[99] V. Libertiaux, F. Pascon, S. Cescotto. Experimental verification of brain tissue incompressibility using digital image correlation. *Journal of the Mechanical Behavior of Biomedical Materials*, 4(7), 1177-1185, 2011

[100] Q. Z. Fang, T. J. Wang, H. G. Beom, H. P. Zhao. Rate-dependent large deformation behavior of PC/ABS. *Polymer*, 50(1), 296-304, 2009

[101] Y. Wang, A. M. Cuitino. Full-field measurements of heterogeneous deformation patterns on polymeric foams using digital image correlation. *International Journal of Solids and Structures*, 39(13-14), 3777-3796, 2002

[102] E. M. Parsons, M. C. Boyce, D. M. Parks, M. Weinberg. Three-dimensional large-strain tensile deformation of neat and calcium carbonate-filled high-density polyethylene. *Polymer*, 46(7), 2257-2265, 2005

[103] B. K. Bay, T. S. Smith, D. P. Fyhrie, M. Saad. Digital volume correlation: Three-dimensional strain mapping using x-ray tomography. *Experimental Mechanics*, 39(3), 217-226, 1999

[104] F. Forsberg, R. Mooser, M. Arnold, E. Hack, P. Wyss. 3D micro-scale deformations of wood in bending: Synchrotron radiation μCT data analyzed with digital volume correlation. *Journal of Structural Biology*, 164 (3), 255-262, 2008

[105] F. Gillard, R. Boardman, M. Mavrogordato, D. Hollis, I. Sinclair, *et al.* The application of digital volume correlation (DVC) to study the microstructural behaviour of trabecular bone during compression. *Journal of the Mechanical Behavior of Biomedical Materials*, 29, 480-499, 2014

[106] F. Forsberg, C. R. Siviour. 3-D deformation and strain analysis in compacted sugar using X-ray microtomography and digital volume correlation. *Measurement Science and Technology*, 20(9), 095703, 2009

[107] K. Madi, G. Tozzi, Q. H. Zhang, J. Tong, A. Cossey, *et al.* Computation of full-field displacements in a scaffold implant using digital volume correlation and finite element analysis. *Medical Engineering and Physics*, 35(9), 1298-1312, 2013

[108] N. Limodin, J. Réthoré, J. Y. Buffière, F. Hild, S. Roux, *et al.* Influence of closure on the 3-D propagation of fatigue cracks in a nodular cast iron investigated by X-ray tomography and 3-D volume correlation. *Acta Materialia*, 58(8), 2957-2967, 2010

[109] R. Brault, A. Germaneau, J. C. Dupré, P. Doumalin, S. Mistou, *et al.* In-situ analysis of laminated composite materials by X-ray micro-computed tomography and digital volume correlation. *Experimental Mechanics*, 53(7), 1143-1151, 2013

[110] C. Franck, S. Hong, S. A. Maskarinec, D. A. Tirrell, G. Ravichandran. Three dimensional full-field measurements of large deformations in soft materials using confocal microscopy and digital volume correlation. *Experimental Mechanics*, 47(3), 427-438, 2007

[111] S. Avril, M. Grédiac, F. Pierron. Sensitivity of the virtual fields method to noisy data. *Computational Mechanics*, 34(6), 439-452, 2004

[112] H. E. Coules, L. D. Cozzolino, P. Colegrove, S. Ganguly, S. Wen, *et al.* Residual strain measurement for arc welding and localised high-pressure rolling using resistance strain gauges and neutron diffraction. *Journal of Strain Analysis for Engineering Design*, 47(8), 576-586, 2012

[113] C. Fernández-Valdivielso, I. R. Matías, F. J. Arregui. Simultaneous measurement of strain and temperature using a fiber Bragg grating and a thermochromic material. *Sensors and Actuators A: Physical*, 101(1-2), 107-116, 2002

[114] W. An, T. E. Carlsson. Speckle interferometry for measurement of continuous deformations. *Optics and Lasers in Engineering*, 40(5-6), 529-541, 2003

[115] D. Post, W. A. Baracat. High-sensitivity moiré interferometry-A simplified approach. *Experimental Mechanics*, 21(3), 100-104, 1981

[116] J. Fu, M. Haghighi-Abayneh, F. Pierron, P. D. Ruiz. Assessment of corneal deformation using optical coherence tomography and digital volume correlation. *Conference*

Proceedings of the Society for Experimental Mechanics, Springer, New York , 5, 155-160, 2013

[117] M. A. Sutton, J. J. Orteu, H. W. Schreier. *Image correlation for shape, motion and deformation measurements*. Springer, New York, 2009

[118] J. Coupland, J. Lobera. Optical tomography and digital holography. *Measurement Science and Technology*, 19(7), 070101, 2008

[119] P. D. Ruiz, J. M. Huntley, J. M. Coupland. Depth-resolved imaging and displacement measurement techniques viewed as linear filtering operations. Experimental Mechanics, 51(4), 453-465, 2011

[120] T. Astarita, G. Cardone. Analysis of interpolation schemes for image deformation methods in PIV. *Experiments in Fluids*, 38(2), 233-243, 2005

[121] G. Besnard, F. Hild, S. Roux. Finite-element displacement fields analysis from digital images: application to Portevin-Le Châtelier bands. *Experimental Mechanics*, 46(6), 789-803, 2006

[122] P. Lava, S. Cooreman, S. Coppieters, M. De Strycker, D. Debruyne. Assessment of measuring errors in DIC using deformation fields generated by plastic FEA. *Optics and Lasers in Engineering*, 47(7-8), 747-753, 2009

[123] B. Pan. Bias error reduction of digital image correlation using Gaussian pre-filtering. *Optics and Lasers in Engineering*, 51(10), 1161-1167, 2013

[124] R. K. Wang, V. V. Tuchin (Editors). *Advanced biophotonics: tissue optical sectioning*. Taylor & Francis, 2013

[125] B. F. Kennedy, S. H. Koh, R. A. McLaughlin, K. M. Kennedy, P. R. T. Munro, *et al.* Strain estimation in phase-sensitive optical coherence elastography. *Biomedical Optics Express*, 3(8), 1865-1879, 2012

[126] S. MacRae, J. Schwiegerling, R. W. Snyder. Customized and low spherical aberration corneal ablation design. *Journal of Refractive Surgery*, 12(2) SUPPL, S246-S248, 1999

[127] K. E. Hamilton, D. C. Pye. Young's modulus in normal corneas and the effect on applanation tonometry. *Optometry and Vision Science*, 85(6), 445-450, 2008

[128] A. Podoleanu, I. Charalambous, L. Plesea, A. Dogariu, R. Rosen. Correction of distortions in optical coherence tomography imaging of the eye. *Physics in Medicine and Biology*, 49(7), 1277-1294, 2004

[129] V. Westphal, A. M. Rollins, S. Radhakrishnan, J. A. Izatt. Correction of geometric and refractive image distortions in optical coherence tomography applying Fermat's principle. *Optics Express*, 10(9), 397-404, 2002

[130] S. Ortiz, D. Siedlecki, L. Remon, S. Marcos. Optical coherence tomography for quantitative surface topography. *Applied Optics*, 48(35), 6708-6715, 2009

[131] S. Van der Jeught, J. A. N. Buytaert, A. Bradu, A. GH. Podoleanu, J. J. J. Dirckx. Real-time correction of geometric distortion artefacts in large-volume optical coherence tomography. *Measurement Science and Technology*, 24(5), 057001, 2013

[132] A. Schuster. An *introduction to the theory of o*ptics. Edward Arnold, London, 1904

[133] S. Patel, J. Marshall, F. W. Fitzke. Refractive index of the human corneal epithelium and stroma. *Journal of Refractive Surgery*, 11(2), 100-105, 1995

RÉSUMÉ EN FRANÇAIS

L'étude de la cornée de l'œil vertébré est un sujet interdisciplinaire qui implique la médecine, la biologie, la mécanique, la science des matériaux, etc. L'étude des propriétés biomécaniques de la cornée a une importance considérable dans l'ophtalmologie, et a également le potentiel d'application dans d'autres domaines de high-tech. Par conséquent, pendant des décennies de nombreux chercheurs se sont consacrés à ce domaine de recherche.

Pour étudier les propriétés biomécaniques de la cornée, premièrement il est nécessaire d'avoir une bonne compréhension de la composition et de l'anatomie de l'œil et sa cornée. Les effets internes tels que la pression intraoculaire sont également essentiels car ils influencent le comportement biomécanique de la cornée de façon significative. Ces propriétés fondamentales devraient être étudiées comme des conditions préalables à la construction de méthodes expérimentales appropriées et de modèles numériques représentatifs afin d'étudier et de prédire le comportement biomécanique de la cornée. Actuellement, les chercheurs ont développé de nombreuses méthodes expérimentales qui permettent de représenter la réponse physiologique de la cornée sous pression et évalué ses propriétés biomécaniques telles que l'élasticité, la viscoélasticité, etc. Basé sur les méthodologies pour l'identification du problème inverse, les paramètres constitutifs de la cornée peuvent être identifiés en utilisant des mesures expérimentales telles que la mesure du champ de déplacement/déformation. Ces propriétés identifiées ont une grande valeur car elles peuvent être utilisées pour étudier la pathologie de la cornée, dans laquelle les propriétés

des cornées pathologiques diffèrent de celles normales. Elles peuvent également être appliquées à développer les modèles d'éléments finis pour simuler et prévoir le comportement biomécanique de la cornée.

Actuellement, la plupart des travaux de recherche qui ont été faits pour caractériser les propriétés biomécaniques de la cornée sont basés sur les tests de traction uniaxiale ou les mesures de surface telles que le test de l'inflation conjugué à la corrélation d'images numériques. Cependant, la mesure du champ de déformation total en 3-D avec résolution en profondeur n'a pas encore été entreprise, ce qui est essentiel pour mieux comprendre le comportement biomécanique interne de la cornée. En outre, l'identification actuelle des paramètres constitutifs des matériaux est généralement basée sur la mise à jour du modèle par éléments finis, qui souffre souvent d'optimisation locale et d'un long temps de traitement. La méthode des champs virtuels a été développée en remplacement de cette méthode d'identification, surmontant les lacunes de la mise à jour du modèle d'éléments finis. Cette méthode peut être appliquée pour l'identification des paramètres des matériaux dans la présente étude.

Le travail présent vise à développer une méthodologie qui peut être appliquée pour mesurer le champ de déformation total en 3-D des matériaux semi-transparents et diffusant la lumière, tels que la cornée. Ensuite, l'idendificationdes paramètres constitutifs de ces mesures de déformation 3-D est réalisée en utilisant la méthode des champs virtuels. Les problèmes spécifiques qui seront abordés comprennent:

- Extension de la méthode des champs virtuels en 3-D.
- Développer les montages expérimentaux pour les tests de traction et les

tests d'inflation pour les spécimens de fantôme en caoutchouc de silicone et de cornée porcine.

- Détermination du champ de déformation total en 3-D avec profondeur résolue utilisant la tomographie par cohérence optique (OCT) couplée avec la corrélation volumique numérique (DVC).
- Développer une méthode pour corriger les distorsions induites par réfraction dans les reconstitutions obtenues par OCT.

Cette thèse est organisée comme suit. Le chapitre 1 présente une revue bibliographique sur les connaissances de base de la cornée tels que la structure, la composition et la pression intraoculaire, etc. L'état de l'art dans l'étude expérimentale des propriétés biomécaniques de la cornée est introduit. Ensuite, diverses techniques d'imagerie volumique sont examinées en vue de l'analyse de la structure interne de la cornée. Après cela, différentes méthodes pour identifier les paramètres constitutifs sont introduites. Et enfin, les méthodes d'obtention des mesures du champ de déformation sont également introduites.

Le chapitre 2 présente en détail l'établissement de la méthode des champs virtuels en 3-D pour des champs virtuels définis manuellement et des champs virtuels optimisés par morceaux. Ensuite, de simples modèles par éléments finis sont introduits pour valider la faisabilité de ces champs virtuels en 3-D. Enfin, les champs virtuels définis manuellement sont comparés avec les champs virtuels optimisés par morceaux en ajoutant aux données de déformation une gamme de bruits pour comparer leurs performances respectives à récupérer les paramètres constitutifs de ces données polluées par le bruit.

Le chapitre 3 présente les mesures du champ de déformation 3-D avec résolution en profondeur pour les fantômes en caoutchouc de silicone sous tension, obtenues en effectuant la tomographie par cohérence optique couplée avec la corrélation volumique numérique. L'étude de l'effet du bruit et des incertitudes de reconstructions ainsi que de la décorrélation des mouchetures (speckles) induits par la déformation est d'abord introduite. Le biais d'interpolation est ensuite analysé. Enfin, les paramètres élastiques constitutifs des fantômes sont identifiés.

Dans le chapitre 4, le champ de déformations 3-D du fantôme de cornée en caoutchouc de silicone et de la cornée porcine dans les conditions d'inflation postérieure sont mesurées. Un modèle d'éléments finis avec les mêmes conditions d'inflation de la cornée est introduit et comparé aux résultats expérimentaux.

Une méthode pour corriger les distorsions induites par réfraction des reconstructions 2-D/3-D de la tomographie par cohérence optique est présentée dans le chapitre 5. Cette méthode de correction est appliquée à corriger les images en volume reconstruites à partir de la cornée porcine. Des tests d'inclinaison des différents fantômes en caoutchouc de silicone sont introduits pour évaluer la performance de la méthode pour corriger les reconstructions distordues.

Dans le dernier chapitre, les conclusions et perspectives sont présentées.

Chapitre 1

La cornée est localisée sur la face externe du globe oculaire et possède une structure multi-couches et semi-transparente. Elle protège l'œil contre l'environnement extérieur, absorbe l'oxygène et les nutriments du film lacrymal et maintient la forme et la stabilité de l'œil en résistant à la pression intraoculaire. Elle joue également un rôle important dans la formation de l'image par réfraction de la lumière à l'arrière de l'œil. La cornée est composée de cinq couches, à savoir l'épithélium, la couche de Bowman, le stroma, la membrane de Descemet et l'endothélium. Le stroma constitue 90% de l'épaisseur de la cornée et domine la performance structurelle de la cornée. Il est constitué de lamelles empilées de fibrilles de collagène disposées régulièrement et noyées dans une matrice hydratée. Parce que la fibrille de collagène est le composant le plus rigide de la cornée, son agencement et sa distribution déterminent essentiellement les propriétés mécaniques et la transparence lumineuse de la cornée.

Plusieurs études expérimentales ont été réalisées afin de caractériser les propriétés biomécaniques de la cornée. Généralement, il existe deux types de test qui sont souvent adoptés pour examiner la réponse mécanique de la cornée sous pression, qui sont le test d'inflation et le test de traction, respectivement. Le test d'inflation est une méthode physiologiquement représentative pour déterminer les propriétés mécaniques de la cornée. Par conséquent, cette méthode a été sélectionnée dans notre projet pour étudier le comportement mécanique avec résolution en profondeur des cornées ex-vivo.

Parce que la cornée a une structure composite complexe, en plus du fait que certaines pathologies peuvent changer les propriétés biomécaniques internes de la cornée localement, les études basées sur la mesure d’un point

ou de surface ne sont pas suffisantes pour examiner complètement le comportement mécanique de la cornée. Par conséquent, il serait utile de développer une méthode qui puisse utilisée pour caractériser les propriétés biomécaniques internes et le champ de déformation total en 3-D de la cornée.

L'analyse de la microstructure interne d'un matériau est importante pour l'étude des propriétés mécaniques du matériau. Au lieu de l'imagerie traditionnelle de surface, des techniques d'imagerie qui peuvent regarder à l'intérieur des matériaux sont nécessaires, englobées dans le terme Tomographie. Diverses techniques tomographiques basées sur différents mécanismes ont été développées, telles que la tomographie à rayons X (X-CT), l'imagerie par résonance magnétique (MRI), la microscopie confocale (CM), la tomographie par cohérence optique (OCT), etc.

Par rapport aux X-CT, MRI et CM, l'OCT est plus appropriée pour l'imagerie 3-D des tissus biologiques tels que les cornées, les peaux, les artères, etc. L'X-CT exige que les objets détectés aient suffisamment de contraste d'absorption des rayons X pour une imagerie efficace. L'X-CT est généralement appropriée pour l'imagerie de solides. Bien que la MRI soit utilisée pour l'imagerie de tissus biologiques, elle n'est pas autant appropriée que l'OCT à l'imagerie des tissus morphologiques en raison de sa résolution relativement faible. En outre, le coût élevé de MRI réduit aussi l'applicabilité de cette technique. CM peut fournir des images de la structure interne des tissus biologiques minces à haute résolution. Toutefois, la profondeur de pénétration de cette technique est beaucoup moins grande que l'OCT. Par conséquent, dans la présente étude, OCT est sélectionnée pour la reconstruction des tissus biologiques.

La mise à jour de modèle par éléments finis est l'approche la plus utilisée pour l'identification des paramètres constitutifs, qui présente toutefois des limites telles que qu'une optimisation locale et un long temps de traitement. La méthode des champs virtuels basée sur le principe du travail virtuel est une solution de remplacement spécialement développée à des fins d'identification. Elle élimine ces inconvénients. Pour cela, le champ de déformation actuel, l'information sur la charge appliquée, et l'information d'accélération sont fournis par l'expérimentation. Les composantes de contrainte peuvent être exprimées par les paramètres constitutifs des matériaux et les composantes de déformation par une équation constitutive appropriée. Un bon choix des champs de déplacement virtuels permet l'extraction des paramètres constitutifs inconnus.

L'acquisition du champ de déformation est un préalable à l'identification des paramètres constitutifs. Les récents progrès dans les techniques de mesure de la déformation de la surface/du volume telles que la méthode de la grille, l'interférométrie, la corrélation d'image/de volume numérique, etc. fournissent la mesure du champ de déformation en 2-D et en 3-D.

La corrélation volumique d'images (DVC) est effectivement une extension en 3-D de la corrélation d'images numériques (DIC). La DVC a été développée pour mesurer la déformation interne en 3-D des matériaux en faisant le suivi de points caractéristiques internes semblables à des speckles 3-D contenues dans les volumes reconstruits.

Bien que la DVC soit principalement appliquée aux données X-CT volumiques, les matériaux sont limités par la nécessité de présenter un

contraste d'absorption des rayons X. Pour certains matériaux souples et semi-transparents tels que les tissus biologiques (cornées, peaux, artères, etc.), des techniques plus appropriées doivent être sélectionnées. La CM est une option, qui peut fournir des données de volume de haute résolution (inférieure au micron). Elle a été couplée avec la DVC pour mesurer la déformation interne en 3-D. Cependant, son application est limitée par la faible portée de la région détectée. En effet, la profondeur de pénétration de la CM est généralement limitée en dessous du millimètre, pour les spécimens plus épais tels que les cornées, les peaux, les artères, etc. cette technique n'est pas suffisante pour mapper champ de déformation dans toute l'épaisseur. Il a été introduit dans les sections précédentes que l'OCT est capable d'obtenir une plus grande profondeur de pénétration par rapport à CM. L'OCT est largement utilisée pour l'imagerie des tissus biologiques. Pour mesurer le champ de déformation en 3-D des tissus biologiques tels que la cornée, la DVC sera appliquée aux données volumiques reconstruites par OCT. Ceci, cependant, n'a pas encore été entrepris au mieux de notre connaissance.

Chapitre 2

Différents ensembles de champs virtuels 3-D définis manuellement ont été sélectionnés pour l'identification des paramètres constitutifs de matériaux. Le cas simple d'un cube en compression a été conçu pour illustrer la mise en œuvre de la méthode des champs virtuels en 3-D. L'élasticité linéaire isotrope a été choisie dans un but de simplicité. Les résultats montrent que ces ensembles de champs virtuels ont une sensibilité différente au bruit sur

la déformation. Par conséquent, le choix des champs virtuels peut être critique.

La VFM 3-D optimisée a été développée en détail. Des champs virtuels par morceaux ont été sélectionnés dans ce cas-ci. L'optimisation a été réalisée en utilisant des multiplicateurs Lagrangien aux conditions limites qui éliminent la contribution des forces de réaction au niveau des supports et des conditions particulières fournissant directement les paramètres constitutifs. Cette VFM 3-D optimisée par morceaux a été validée en utilisant des modèles d'éléments finis simples avec élasticité isotrope et élasticité orthotrope. Similaire à la VFM 3-D définie manuellement, les paramètres constitutifs identifiés par la VFM 3-D optimisée par morceaux sont pratiquement identiques aux valeurs d'entrées, montrant donc la faisabilité de cette méthode.

Une gamme de bruits blancs Gaussiens a été ajoutée aux données exactes de déformation simulée. La VFM définie manuellement a été comparée à la VFM optimisée par morceaux. L'objectif est de comparer les performances de ces champs virtuels dans la récupération de paramètres constitutifs des données polluées par le bruit. Les résultats montrent que les deux méthodes peuvent fournir de bons résultats d'identification. Toutefois, lorsque le bruit devient plus grand, la VFM optimisée par morceaux est plus stable et peut fournir des résultats d'identification plus précis.

Chapitre 3

Deux bandes plates rectangulaires de fantômes ont été fabriquées en utilisant du gel de silicone (MM240-TV), dont l'une d'elles avec des

encoches. Le module d'Young nominal du caoutchouc de silicone est de 1.88 MPa, pouvant changer avec la proportion du durcisseur. Le montage expérimental est constitué d'un appareil de test en traction et un système de tomographie par cohérence optique à source de signal balayé (SS-OCT). Pour les deux états de référence et déformés, une séquence d'images en volume du spécimen a été acquise à l'aide du système SS-OCT. Ensuite, la DVC a été utilisée pour calculer les champs de déplacement en 3-D des reconstructions obtenues par SS-OCT.

Avant les tests de traction, l'effet combiné du bruit et des incertitudes de reconstruction a été étudié par l'exécution d'un test stationnaire et un test de de corps rigide en translation du fantôme. L'effet de décorrélation des speckles induite par déformation a été étudié par une simulation numérique. Une incertitude sur la déformation de l'ordre de $\sim 2\times10^{-4}$ à $\sim 3.5\times10^{-4}$ a été observée pour les tests stationnaire et de translation. L'OCT+DVC couplées sont jugées appropriées pour la mesure de déformations jusqu'à ~2% (dans le sens axial), valeur au-dessus de laquelle une approche incrémentale devrait être utilisée pour éviter la décorrélation des speckles.

Des valeurs raisonnables des champs de déplacement et de déformation ont été obtenues pour le fantôme rectangulaire et pour le fantôme avec encoches. Les franges parasites observées dans les champs de déformation ont été analysées, et sont causées par le repliement d'image (aliasing). Ceci est confirmé par l'exécution d'un test de traction en doublant la charge sur le fantôme rectangulaire.

Deux approches ont été prouvées faisables pour réduire le biais d'interpolation causé par l'aliasing. Dans la première approche, le

pré-lissage avec un filtre passe-bas de Gaussien a été appliqué aux images volumiques avant la corrélation. Les résultats montrent que le pré-lissage est efficace pour réduire le biais d'interpolation mais il cause une légère augmentation des écarts-types sur les déformations (le niveau de bruit augmente de $\sim 4\times10^{-4}$ à $\sim 8\times10^{-4}$ après pré-lissage). Dans la deuxième approche, il n'y a pas de franges parasites observées dans les champs de déformation lorsque la densité d'échantillonnage du système SS-OCT a été doublée. Ceci indique que l'augmentation de la densité d'échantillonnage est une approche efficace pour réduire le biais d'interpolation causé par l'aliasing.

Les champs de déformation 3-D uniformes et non uniformes obtenus par OCT+DVC ont été utilisés pour identifier les paramètres constitutifs élastiques Q_{ij} du fantôme rectangulaire et du fantôme avec encoches en utilisant la VFM 3-D définie manuellement. Les modules élastiques (le module d'Young E et le coefficient de Poisson ν) extraits de cette approche sont compatibles avec ceux calculés par l'approche de contrainte uniaxiale constante et les résultats obtenus avec une machine de traction micro. Une autre VFM 3-D a également été développée pour identifier le module de compression K et le module de cisaillement G en utilisant les données de déformation obtenues à partir du test de traction du fantôme avec encoches. Cela offre une autre option pour mesurer les paramètres rigidité du matériau quand ν est très proche de 0.5.

Chapitre 4

Une cornée porcine a été utilisée dans cette étude en raison de la difficulté d'obtenir une cornée humaine intacte. Les globes oculaires frais ont été recueillis auprès de l'abattoir local dans les 6 heures après leur abattage et testés dans les 12 heures post-mortem. Un fantôme artificiel de cornée humaine a été fabriqué en utilisant le gel de silicone.

Le montage expérimental contient un appareil d'inflation et le système SS-OCT. Les spécimens ont été montés et fixés sur une chambre antérieure artificielle. La cornée et le fantôme ont été gonflés de 2 kPa à 2.5 kPa. A chaque état de pression, une séquence d'images en volume du spécimen a été acquise par le système SS-OCT. Les reconstructions volumiques ont été enregistrées pour l'exécution de la DVC. Ensuite, les champs de déplacement et de déformation ont été calculés.

L'analyse du bruit a été effectuée avant les tests d'inflation, montrant que le sous-volume de 24×24×24 voxels est un bon compromis entre la résolution spatiale et la résolution de déformation pour la cornée et le fantôme.

Le modèle éléments finis du test d'inflation de la cornée porcine a été développé en utilisant le progiciel commercial ABAQUS 6.11®. Il aide à comprendre les distributions de déplacement et de déformation de la cornée en condition d'inflation. Les résultats de la simulation sont comparés à ceux mesurés par DVC afin de voir s'ils ont une bonne cohérence.

Après avoir exécuté la DVC, de bons résultats de déplacement et de déformation pour les tests d'inflation ont été obtenus pour les deux spécimens du fantôme et de la cornée. Ces résultats montrent un bon accord

avec les résultats du modèle EF et montrent la faisabilité de cette méthode appliquée aux études de la déformation interne de la cornée humaine.

Chapitre 5

Pour un spécimen avec une surface supérieure plate, on est exempt du problème de distorsions si le rayon de balayage est perpendiculaire à la surface du spécimen. Cependant, pour un spécimen avec une surface courbe telle que la cornée, une distorsion induite par la réfraction se produit. Cela introduit des erreurs de détermination de la position réelle de la microstructure dans la cornée. Les images volumiques distordues introduisent ensuite des erreurs dans les mesures de déplacement et de déformation.

Des méthodes de correction de réfraction pour les cas 2-D et 3-D ont été développées basées sur le principe de Fermat. Un algorithme de minimisation point-par-point a été développé d'abord pour corriger les images 2-D distordues obtenues par OCT. Cette méthode présente cependant l'inconvénient d'un long temps de traitement. Par conséquent, une méthode plus efficace a été développée, dans laquelle l'algorithme de minimisation est exécuté uniquement sur les points définis d'une grille. Ensuite, les coordonnées des points objets intermédiaires dans l'espace d'image sont obtenues en interpolant les coordonnées de ces points de grille. Par rapport à la méthode avec minimisation point-par-point, cette dernière permet de réduire le temps de traitement considérablement, par exemple, de ~10 heures à ~1 minute pour une image typique d'OCT (1024×512 pixels),

sans perte de précision de correction. Cela rend la correction du volume réalisable.

La correction des distorsions a été effectuée sur les reconstructions volumiques de la cornée obtenues à partir du test d'inflation introduit dans le chapitre 4. La DVC a ensuite été effectuée sur les volumes corrigés de la cornée pour obtenir les champs corrigés des déplacements et des déformations. Il montre que les résultats de DVC après correction des distorsions sont plus compatibles avec les résultats de la simulation.

Des tests d'inclinaison sur des fantômes ont été effectués pour évaluer la performance de la méthode de correction à corriger les reconstructions distordues et les mesures de déformation obtenues par DVC. Deux fantômes ont été fabriqués. L'un est une bande plate tandis que l'autre est hémisphérique.

Les fantômes ont été placés sur un plateau de rotation et tournés de 0.5 ° dans le plan *xy*. A chaque état, un volume a été reconstruit par le système SS-OCT. La DVC a été appliquée aux reconstructions volumiques. Les champs de déformation et de rotation ont été obtenus. Ensuite, la méthode de correction des distorsions a été effectuée sur reconstructions volumiques, et une DVC a été effectuée pour obtenir les déformations et rotations corrigées. L'objectif est de voir si les résultats de déformation et de rotation sont améliorés après la correction des distorsions.

Les résultats montrent que, après la correction la déformation parasite induite par la distorsion de réfraction a été réduite, et la mesure de rotation s’est rapprochée de la valeur d'entrée. Ceci indique que la méthode peut

corriger les reconstructions distordues d'OCT à leur configuration réelle. Ceci permettra d'améliorer la précision de mesure par OCT couplée avec DVC lors de la mesure en 3-D des déformations des spécimens avec surface courbée.

Chapitre 6

Conclusions

Dans cette thèse, une méthode efficace a été mise au point pour mesurer le champ de déformation total en 3-D de matériaux semi-transparents et diffusant la lumière tels que la cornée. Ces mesures de déformation 3-D peuvent être utilisées pour identifier les paramètres constitutifs de matériaux, au moyen de la VFM.

La VFM a été étendue en 3-D pour accueillir les mesures du champ total de déformation en 3-D. Les champs virtuels définis manuellement et les champs virtuels optimisés par morceaux ont été développés. Leur capacité à extraire les paramètres constitutifs précisément des simulations FEM simples a été montrée faisable. Les champs virtuels définis manuellement ont été comparés avec les champs virtuels optimisés par morceaux en ajoutant à leurs données de déformation une gamme de bruits blancs Gaussiens afin de comparer leurs résultats respectifs. Les résultats montrent que toutes les méthodes peuvent fournir les bons résultats d'identification. Toutefois, lorsque le bruit devient plus grand, les champs virtuels optimisés par morceaux sont beaucoup plus stables et peuvent fournir des résultats d'identification plus précis.

La DVC peut fournir, au moyen d'un système d'OCT avec un seul canal, les champs de déplacement multi-composants. De ces champs de déplacement tous les composants de déformation requis par les méthodes d'inversion telles que la VFM 3-D peuvent être déterminés. Une incertitude sur la déformation de l'ordre de ~2×10^{-4} à ~3.5×10^{-4} a été observée pour l'approche OCT+DVC en effectuant une analyse de bruit. L'approche OCT+DVC est appropriée pour des déformations n'allant pas au-delà de de ~2% (dans le sens axial), point au-dessus duquel une approche incrémentale devrait être utilisée pour éviter la décorrélation des speckles.

L'aliasing s'est montré la raison des franges parasites observées dans les champs de déformation. Deux approches ont montré être possible pour réduire le biais d'interpolation en raison de l'aliasing. La première approche consiste à effectuer le pré-lissage (par exemple un filtre passe-bas de Gaussien) aux images volumiques avant la corrélation. Pour la deuxième approche, le biais d'interpolation peut être réduit en augmentant la densité d'échantillonnage du système SS-OCT.

Les champs 3-D de déformation ont été utilisés pour identifier les paramètres constitutifs élastiques des fantômes en caoutchouc de silicone en utilisant la VFM 3-D. Les résultats de l'identification des cas des champs de déformation uniformes et hétérogènes ont été comparés avec ceux calculés analytiquement dans l'hypothèse de contrainte uniaxiale constante et ceux mesurés par la machine de traction micro, montrant de bons accords.

Les champs de déformation 3-D dans la profondeur de la cornée porcine et du fantôme de silicone dans les conditions d'inflation postérieure ont été mesurés en utilisant OCT+DVC. De bons résultats de déplacement

et déformation des tests d'inflation ont été obtenus pour les spécimens du fantôme et la cornée. Ces résultats montrent un bon accord avec ceux du modèle FE.

Des méthodes de correction pour les deux cas 2-D et 3-D ont été développées basées sur le principe de Fermat pour corriger la distorsion induite par la réfraction dans les reconstructions d'OCT. Un moyen plus efficace a été développé qui permet de réduire considérablement le temps de calcul sans perte de précision de correction. Les tests d'inclinaison ont été effectués pour évaluer la performance de la méthode de correction. Les résultats montrent que, après la correction des distorsions les déformations parasites ont été réduites, et les mesures de rotation ont été augmentées, devenant plus proches des valeurs d'entrée. Ceci indique que la correction des distorsions peut corriger les reconstructions distordues d'OCT par rapport à leur configuration réelle. La méthode de correction a été appliquée pour corriger les reconstructions volumiques de la cornée du test d'inflation. Les résultats de DVC après correction sont plus cohérents avec ceux de la simulation.

Perspectives

Les mesures actuelles de déformation sont basées sur les spécimens avec une seule couche tels que les fantômes de silicone introduits. Même si la cornée est composée de cinq couches, le stroma constitue plus de 90% de l'épaisseur de la cornée. Par conséquent, il serait intéressant de créer des fantômes avec multi-couches (par exemple, double-couches avec la même épaisseur et les rigidités différentes), et de mesurer les champs de déformation hétérogènes de chaque couche dans le même temps en utilisant

OCT+DVC. Il serait utile de développer une VFM 3-D qui prend en compte l'hétérogénéité des matériaux. Cette VFM 3-D peut être utilisée pour extraire les paramètres constitutifs de chaque couche en utilisant des champs de déformation hétérogènes et un seul test. Cette étude future recommandée pourrait améliorer considérablement l'applicabilité de la méthodologie proposée.

En raison de la réflexion et de l'absorption de la lumière, les images volumiques actuelles tendent à avoir une mauvaise qualité dans les régions inférieures. Cela conduit à des résultats de DVC inexacts à cet endroit, et affecte l'identification des paramètres constitutifs. Ainsi, des efforts peuvent être entrepris en l'amélioration de la qualité des images à l'avenir. Cela peut être effectué en ajustant le trajet d'illumination, tel que par l'ajout d'une lentille appropriée pour rendre le faisceau d'illumination perpendiculaire à l'interface afin que la réflexion puisse être réduite (Cela peut aussi réduire la distorsion induite par la réfraction). Autrement, un système OCT avec une plus grande profondeur de pénétration est également une solution.

D’autres tissus biologiques tels que les artères, les peaux, etc. peuvent aussi être étudiés en utilisant la méthodologie proposée pour étudier leur comportement de déformation et propriétés de matériaux. Il serait intéressant de mesurer les champs de déformation de ces tissus sous haute pression pour étudier leurs propriétés non linéaires et réponse aux dommages (par exemple la rupture de l'anévrisme).

Dans le présent travail, la VFM 3-D a été mise en œuvre en élasticité linéaire. Cependant, en considérant le comportement non linéaire des tissus biologiques sous grandes déformations, il serait utile d'élaborer une VFM

3-D non linéaire. Différents modèles non linéaires peuvent être utilisés tels que l'hyperélasticité. Ces modèles peuvent servir à une identification plus complète des paramètres constitutifs des matériaux.

LIST OF PUBLICATIONS AND HONOURS

- J. Fu, F. Pierron, P. D. Ruiz. Elastic stiffness characterization using three-dimensional full-field deformation obtained with optical coherence tomography and digital volume correlation. *Journal of Biomedical Optics*, 18(12), 121512, 2013.

- F. Pierron, S. A. McDonald, D. Hollis, J. Fu, P. J. Withers, A. Alderson. Comparison of the mechanical behaviour of standard and auxetic foams by x-ray computed tomography and digital volume correlation, *Strain*, 49(6), 467-482, 2013.

- J. Fu, M. Haghighi-Abayneh, F. Pierron and P. D. Ruiz. Assessment of corneal deformation using optical coherence tomography and digital volume correlation, *Conf. Proc. SEM.*, 5, 155-160, Springer, New York, 2013.

- J. Fu, F. Pierron, and P. D. Ruiz. Correction of refraction induced distortion in optical coherence tomography corneal reconstructions for volume deformation measurements, *Proceedings of the Photomechanics 2013 Conference, Montpellier*, France, 2013.

- Third prize winner in “2012 Young Stress and Vibration Analyst Competition” held in University of Glasgow, UK, 2012

IDENTIFICATION OF CORNEAL MECHANICAL PROPERTIES USING OPTICAL TOMOGRAPHY AND DIGITAL VOLUME CORRELATION

ABSTRACT: This work presents an effective methodology for measuring the depth-resolved 3D full-field deformation of semitransparent, light scattering soft tissues such as vertebrate eye cornea. This was obtained by performing digital volume correlation on optical coherence tomography volume reconstructions of silicone rubber phantoms and porcine cornea samples. Both the strip tensile tests and the posterior inflation tests have been studied. Prior to these tests, noise effect and strain induced speckle decorrelation were first studied using experimental and simulation methods. The interpolation bias in the strain results has also been analyzed. Two effective approaches have been introduced to reduce the interpolation bias. To extract material constitutive parameters from the 3D full-field deformation measurements, the virtual fields method has been extended into 3D. Both manually defined virtual fields and the optimized piecewise virtual fields have been developed and compared with each other. Efforts have also been made in developing a method to correct the refraction induced distortions in the optical coherence tomography reconstructions. Tilt tests of different silicone rubber phantoms have been implemented to evaluate the performance of the refraction correction method in correcting the distorted reconstructions.

Keywords: Soft tissue; Depth-resolved strain; Optical coherence tomography; Constitutive parameters identification; Deformation measurement.

IDENTIFICATION DE LA MÉCANIQUE DE LA CORNÉE PAR LA TOMOGRAPHIE OPTIQUE ET LA CORRÉLATION DE VOLUME NUMÉRIQUE

RÉSUMÉ: Ce travail présente une méthodologie efficace pour mesurer le champ de déformation total en 3D des tissus mous semi-transparents et diffusant la lumière, tels que la cornée de l'œil vertébré. Cela a été obtenu en utilisant la tomographie par cohérence optique couplée avec la corrélation volumique numérique sur des fantômes en caoutchouc de silicone et de la cornée porcine. Des tests de traction et des tests d'inflation postérieure ont été étudiés. Avant ces tests, l'effet du bruit et la décorrélation des speckles due à la déformation sont d'abord étudiés en utilisant des méthodes expérimentales et numériques. Le biais d'interpolation dans les résultats de déformation a été analysé. Deux approches efficaces ont été prises pour réduire le biais d'interpolation. Pour extraire les paramètres constitutifs des mesures de déformation 3D, la méthode des champs virtuels a été étendue en 3D. Les champs virtuels définis manuellement et les champs virtuels optimisés par morceaux ont été développés et comparés entre eux. Des efforts ont également été déployés pour corriger les distorsions induites par réfraction dans les reconstructions de la tomographie par cohérence optique. Des tests d'inclinaison des différents fantômes de silicone ont été introduits afin d’évaluer la performance de la méthode pour corriger les reconstructions distordues.

Mots clés: Tissu mou; Déformations (mécanique); Tomographie en cohérence optique; Identification; Contraintes (mécanique).

Jiawei FU

Doctorat : Systèmes Mécaniques et Matériaux

Année 2014

Identification de la mécanique de la cornée par la tomographie optique et la corrélation de volume numérique

Ce travail présente une méthodologie efficace pour mesurer le champ de déformation total en 3-D des tissus mous semi-transparents et diffusant la lumière, tels que la cornée de l'œil vertébré. Cela a été obtenu en utilisant la tomographie par cohérence optique couplée avec la corrélation volumique numérique sur des fantômes en caoutchouc de silicone et de la cornée porcine. Des tests de traction et des tests d'inflation postérieure ont été étudiés. Avant ces tests, l'effet du bruit et la décorrélation des speckles due à la déformation sont d'abord étudiés en utilisant des méthodes expérimentales et numériques. Le biais d'interpolation dans les résultats de déformation a été analysé. Deux approches efficaces ont été prises pour réduire le biais d'interpolation. Pour extraire les paramètres constitutifs des mesures de déformation 3-D, la méthode des champs virtuels a été étendue en 3-D. Les champs virtuels définis manuellement et les champs virtuels optimisés par morceaux ont été développés et comparés entre eux. Des efforts ont également été déployés pour corriger les distorsions induites par réfraction dans les reconstructions de la tomographie par cohérence optique. Des tests d'inclinaison des différents fantômes de silicone ont été introduits afin d'évaluer la performance de la méthode pour corriger les reconstructions distordues.

Mots clés : tissu mou - déformations (mécanique) - tomographie en cohérence optique – identification – contraintes (mécanique).

Identification of Corneal Mechanical Properties Using Optical Tomography and Digital Volume Correlation

This work presents an effective methodology for measuring the depth-resolved 3-D full-field deformation of semitransparent, light scattering soft tissues such as vertebrate eye cornea. This was obtained by performing digital volume correlation on optical coherence tomography volume reconstructions of silicone rubber phantoms and porcine cornea samples. Both the strip tensile tests and the posterior inflation tests have been studied. Prior to these tests, noise effect and strain induced speckle decorrelation were first studied using experimental and simulation methods. The interpolation bias in the strain results has also been analyzed. Two effective approaches have been introduced to reduce the interpolation bias. To extract material constitutive parameters from the 3-D full-field deformation measurements, the virtual fields method has been extended into 3-D. Both manually defined virtual fields and the optimized piecewise virtual fields have been developed and compared with each other. Efforts have also been made in developing a method to correct the refraction induced distortions in the optical coherence tomography reconstructions. Tilt tests of different silicone rubber phantoms have been implemented to evaluate the performance of the refraction correction method in correcting the distorted reconstructions.

Keywords: soft tissue - depth-resolved strain - optical coherence tomography - constitutive parameters identification – deformation measurement.

Thèse réalisée en partenariat entre :

Loughborough University

CHINA SCHOLARSHIP COUNCIL

utt université de technologie Troyes

Ecole Doctorale "Sciences et Technologies"